THE CITY UNIVERSITY

OPTIMUM ROTOR BLADE CONFIGURATIONS FOR MINIMUM OSCILLATORY ROOT BENDING MOMENT

A Thesis Submitted for the Degree of

Doctor of Philosophy

in

Mechanical Engineering

by

Mohamed Ibrahim Abd-El Rahman Khattab

January 1985

CONTENTS

Page No.

Page No.

LIST OF SYMBOLS

Symbol	Definition
A	element cross sectional area, (in^2)
A_r	area of rotor disc, (in^2)
A_c, A_s	longitudinal and lateral cyclic pitch amplitudes, (o)
$\{A\}$	unknown constant vector; equation (1)
$[A]$	transformation matrix; equation (27)
a_{sn}, a_{cn}	n th harmonic of sine and cosine of Fourier series.
$[B]$	transformation matrix; equation (27)
C	blade chord, (in)
C_ℓ	local blade lift slope
c_n	n th harmonic amplitude; $((a_{sn}^2 + a_{cn}^2)^{\frac{1}{2}})$
D_o	depth of the cantilever root, (in)
D_i	cantilever depth at the i th station, (in)
$EI_{yy}(x)$, $EI_{zz}(x)$	flatwise and edgewise stiffness of the blade, ($lbf\text{-}in^2$)
$\underset{\sim}{e}$	steepest descent direction
$F_\ell(x)$	aerodynamic load, equation (62.a), (lbf/in)
F_o	exciting force amplitude, (lbf)
$\{F\}$	aerodynamic pressure vector w.r.t. fixed axes, (lbf/in^2)
$F_x(i)$	centrifugal force acting on any section at distance x from left end of the i th element, (lbf)
$f_{\beta i}(x)$	flapping deflection of the i th mode, (in)
$f_{\beta j}^{(i)}(x)$	mode shape function at distance x from the left end of the i th element and j th mode.

$[G_i]$	centrifugal stiffness matrix of the i th element, (lbf/in)
$GJ(x)$	blade torsional rigidity, ($lbf\text{-}in^2$)
H_i	nondimensional i th depth parameter; D_i/D_o
H_o	nondimensional root depth parameter of the cantilever; $H_o = 1$
h_i	ratio of the rotating hub radius to the i th element length; r_o/ℓ_i
$[k_i]$	stiffness matrix of the i th element, (lbf/in)
$[K]$	overall assembly stiffness matrix, (lbf/in)
L	blade length, (in)
$L(x)$	instantaneous aerodynamic lift per unit length,(lbf/in)
$L_{tot}(\psi)$	rotor total lift, (lbf)
$L_{tot)av}$	average total lift over one revolution, (lbf)
ℓ_i	length of the i th element, (in)
$M_{bi}(\psi)$, $M_{fi}(\psi)$	flapping root bending moment of i th blade based on aerodynamic loading and flapping displacement respectively, (lbf-in)
$M_x(\psi), M_y(\psi)$	rolling and pitching moments based on the aerodynamic loading,(lbf-in)
$M_{fx}(\psi)$, $M_{fy}(\psi)$	rolling and pitching moments based on the flapping displacement, (lbf-in)
$M_{x)av}, M_{y)av}$	average rolling and pitching moments over one revolution based on the aerodynamic loading, (lbf-in)
M_{fx}^*, M_{fy}^*	average rolling and pitching moment over one revolution based on the flapping displacement, (lbf-in)
M_{xp}, M_{yp}	peak to peak value of the rolling and pitching moments based on the flapping displacement, (lbf-in)

$[M]$	overall assembly mass matrix, (chug)
$[M_i]$	i th generalised mass, equation (83.a)
$m_i(x)$	mass per unit length at distance x from the left end of the i th element, (chug/in)
$m_d(i)$	mass per unit length at the i th station (chug/in)
$m_L(i), m_R(i)$	mass per unit length at the left and right end respectively of the i th element, (chug/in)
$[m_i]$	mass matrix of the i th element, (chug)
N_b	number of blades
N_d	number of structural nodes (stations) along the blade
N_E	number of blade finite elements
N_{mo}	number of flapping modes
N_{rev}	number of blade revolutions to attain steady state response
N_x	number of radial divisions within the beam element
N_ψ	number of azimuthal divisions around the rotor disc
N_τ	number of interpolations within the 1st azimuth division
$O_{bj}(H)$	modified objective function; equation (98)
$[p_m]$	inertia matrix, (chug)
$\{p\}$	aerodynamic pressure vector w.r.t. local blade axes, (lbf/in^2)
p_i	ratio of the total length of all elements (before and not including the i th element under consideration) to the i th element length; $(\sum_{k=1}^{i-1} \ell_k)/\ell_i$

$\{Q_a\}$	aerodynamic damping vector
$\{Q_i\}$	aerodynamic generalised force vector of the i th mode
$\{Q_m\}$	gyrodynamic matrix; equation (40)
q_i	generalised co-ordinate of the i th mode
$\{R\}$	position vector of a point in the system with reference to fixed axes, (in)
$\{R_m\}$	centrifugal stiffness matrix, (lbf/in)
r	nondimensional radial position; $(\frac{xk}{L})$
r_o	rotating hub radius, (in)
SF	shearing force at the cantilever root, (lbf)
$\{S_{mi}\}$	steady state mass contribution to the equation of motion for the i th mode, (lbf)
$s_i(x)$	flatwise stiffness at distance x from the left end of the i th element, (lbf-in^2)
$s_L^{(i)}, s_R^{(i)}$	flatwise stiffness at the left and right end of the i th element respectively, (lbf-in^2)
u	induced velocity down through the rotor disc, (in/sec)
u_o	induced velocity at the rotor centre, (in/sec)
$\{u\}$	local air mass velocity vector, (in/sec)
VBM	vibration bending moment at the root of the cantilever beam, (lbf-in)
V_f	helicopter flight speed, (knots)
$\{V_r\}$	relative velocity vector at the blade section w.r.t. fixed axes, (in/sec)
v	instantaneous local (relative) airspeed, (in/sec)
v_x, v_y, v_z	relative local air velocity components (in/sec)
W	helicopter weight (lb)
$W_b(H)$	basic objective function (blade mass or cantilever mass), (lb)

w_{ni}	natural frequency of the i th mode (c/s)
w_{di}	damped natural frequency of the i th mode, (c/s)
w_f	exciting frequency, (c/s)
w_{sep}	absolute difference between the exciting frequency and the natural frequency of the modified cantilever beam, (c/s)
$w_{\gamma o_1}$, $w_{\gamma o_2}$	first and second natural frequencies of the cantilever beam of minimum weight penalty, (c/s)
w_{si}	i th initial frequency separation, ($w_{si} = w_f - w_{\gamma oi}$; i = 1,2), (c/s)
x_k	co-ordinate of the k th structural node (station) along the blade, (in)
α_i	flatwise stiffness slope within the i th element, (lbf-in)
$\alpha(x)$	blade section incidence
β_o	coning angle
$\beta(x)$	sectional flapping angle
β_c, β_s	first harmonic longitudinal and lateral flapping amplitude respectively
γ	penalty parameter
γ_i	slope of the mass distribution within the i th element, (chug/in^2)
$\{\delta\}$	vector listing the nodal displacement
ε_o	pre-determined minimum bending moment, (lbf-in)
ε_i	damping ratio of the i th mode
Θ	applied collective pitch
$\theta(x)$	local blade section pitch, (equation 25) or cross-section rotation
θ_s	local blade section pitch at the feathering bearing

$\theta_t(x)$	built-in twist along the blade
$\theta_o(x)$	applied collective pitch plus built-in twist
λ	descent steplength
λ_i	i th frequency ratio; $(\frac{w_{ni}}{\Omega})$
$\lambda_{mi}, \lambda_{ki}, \lambda_{\theta i}$	i th estimated descent steplength for the blade mass, flatwise stiffness and built-in twist distributions respectively
μ	advance ratio
ν	inflow ratio
$[\phi]$	modal matrix
ϕ_n	phase angle of n th harmonic $(\tan^{-1}\frac{a_{sn}}{a_{cn}})$
$\{\phi_i^{(j)}\}$	j th mode shape vector of the i th element
ψ	azimuth position
ψ_{step}	azimuthal increment
Ω	rotational speed

LIST OF FIGURES

LIST OF TABLES

ACKNOWLEDGEMENTS

The author offers his deep appreciation to his supervisor, Professor G.T.S. Done for many valuable discussions and continuous advice and encouragement throughout this project.

Thanks are due in particular to [redacted] in Structures Department, Royal Aircraft Establishment (Farnborough-London), who provided the Vortex Ring Model computer program and also considerable help and encouragement in discussion.

The author would also like to thank [redacted] for his generous help during the preparation of the test rig, and [redacted] who typed the manuscript.

The author remains greatly indebted to his country (Egypt) for the financial support.

SUMMARY

Vibration is a continuing problem in helicopters. It can be particularly severe for the modern type of rotor head (hingeless rotor blade helicopters) in which the flap and lag hinges are replaced by flexible elements, unless a considerable effort is made at the design stage to keep it within reasonable limits. This type of helicopter is usually characterised by a relatively high peak to peak value of the hub non-rotating co-ordinate moments transmitted to the fuselage, e.g. on the pre-production Lynx helicopter. Part of the design process consists of manipulating the rotor (which is the major source of this vibration), by means of altering the blade structural and mass configuration, in order to minimise the overall vibration transmitted to the fuselage. Many of these adjustments are generally made on the basis of experience and intuition.

In this research project, the structural optimization technique is used to formalise the process with the desire to find the optimum configurations of the rotor blades (mass, flatwise stiffness and built-in twist distributions along the blade), in forward flight conditions, such that the oscillatory rolling and pitching moment is minimised. This problem is one of a general class which involves optimization by so-called "blade dynamic tailoring". It is a linear programming problem and the sequential unconstrained minimization technique (SUMT)

which uses an algorithm based on the steepest descent method is utilised.

The results follow an orderly sequence leading to a substantial reduction in the oscillatory rolling and pitching moments peak values (up to 48.5% and 28.8% respectively) with small changes in the blade configuration. Therefore, optimum design of rotor blades provides substantial benefits with small penalties, so it is suggested that use of structural optimization as a design tool by industry could lead to improved rotors.

1. INTRODUCTION

The high vibration level in the helicopters which is an inherent characteristic is becoming an increasingly important design consideration because of stringent requirements for crew/passenger comfort and also for increased reliability of structural components and on-board electronic equipment. On some military helicopters there is a need for a stable platform for firing weapons and target acquisition. The major source of this vibration, the main effects of which are evident in the fuselage, is the rotor. The main rotor vibration is at fundamentally N_b per rev. (where N_b is the number of rotor blades) and is due to the aeroelastic response of the rotor blades. The role of this vibration and the importance of its control in helicopters are clearly emphasised in the literature survey in Section 2.

One of the foremost considerations in the design of helicopter rotors is the reduction of oscillatory hub loads together with the fuselage vibration caused by these loads through judicious blade design.

The unprecedented developments in computational capability over the last decade have fostered equally impressive developments in structural optimization schemes in all disciplines of engineering. Of particular importance is the emergence of the finite element method for the solution of continuum problems. It provided the necessary motivation for the perfection of

matrix manipulation techniques, linear and non-linear equation solution methods, and for eigenproblem analysis and numerical integration schemes. The introduction of optimization schemes into the design of complex structures (e.g. helicopters) then followed quite naturally. It provides a means of not only saving weight and cost but also of allowing sensitivity studies to be made which can lead to improved structural integrity.

The motivation of the present research is aimed at using recent advances in the field of structural optimization to develop a rational design procedure for the rotor blades. In this design procedure, the blade mass, flatwise stiffness and built-in twist distributions are to be dynamically tailored such that an objective function based on the oscillatory rolling and pitching moments is minimised. The mass per unit length, flatwise stiffness and built-in twist at 19 spanwise stations along the blade are used as design variables. Upper and lower bounds on these design variables are prescribed to prevent them from reaching impractical values. An arbitrary initial design variable (base-line design) of the blade under consideration is selected to start the optimization process.

An analytical model for prediction of the rotor aeroelastic performance in trimmed forward flight conditions has been developed using a modal approach. The blade is represented aerodynamically by a blade element model, the rotor wake being simulated first by a Glauert downwash distribution (uniform inflow) and then by a series of vortex rings (non-uniform inflow),

using up to 12 rings and 2 filaments which are situated at the root and tip blade section. Only flapping deflection was considered and the finite element method has been used to estimate the dynamic characteristics for both rotating and non-rotating blades, 4-degrees of freedom elements (in which the mass per unit length and flatwise stiffness vary linearly with distance along the beam element) being used. Blade displacements are expressed as a summation of rotating orthogonal flatwise modes (four modes) and the modal co-ordinates are calculated numerically using the azimuthal convolution integral. Finally, the flapping root bending moment as well as the resultant non-rotating co-ordinate moments (objective function), based on the engineers theory of bending, were also computed.

The problem is then cast as a non-linear programming problem and a sequential unconstrained minimisation technique incorporating an algorithm based on the steepest descent technique is used. The problem has been formulated so that a straight forward optimization takes place with respect to change of the design variable from an arbitrary initial blade configuration.

Due to the unacceptably long computation times for each change of such huge number of design variables, the major computational effort being in the evaluation of the objective function, a preliminary exercise was firstly carried out to demonstrate the feasibility of the optimization procedure.

The solutions of the optimum configurations of a cantilever beam, excited by an oscillatory force of constant amplitude at its tip, for minimum oscillatory root bending moment have been obtained. These solutions are worked out in detail with the excitation frequency rather less than, and also rather greater than both first and second natural frequencies. In addition, a laboratory experimental investigation has been carried out on a simple non-rotating cantilever beam model and doubts about assumptions made in mathematical modelling resolved.

The understanding gained from the optimization results of the optimum configurations of the above cantilever beam, led to the development of a more refined optimization procedure for the rotor blade tailoring configurations. In this procedure the optimum modified mass flatwise stiffness and built-in twist distributions along the blade, for minimum oscillatory rolling and pitching moments, are obtained. The numerical optimization results are discussed and the appropriate conclusions are also drawn.

2. REVIEW OF LITERATURE

The literature pertaining to helicopter vibration problems is reviewed in the following sections as well as the vibration control methods. Applicabilities of these control methods are also emphasised.

2.1. Vibration of Helicopters

One characteristic of helicopters is that they are subject to severe vibration. Such undesirable excessive vibration can cause structural fatigue of helicopter components, damage to armaments and equipment on board the helicopter, passenger discomfort and control difficulties of the crew.

From the point of view of dynamics, the helicopter is often treated as consisting of two coupled systems: the rotor and the fuselage. The major source of vibration, the main effects of which are evident in the fuselage, is the rotor. The tail rotor and gearbox also contribute smaller, but often quite important, excitations. The vibration of any part of the fuselage depends not only on these excitations but on the elastic response of the fuselage. The role of vibration in helicopter dynamics has recently been summarised [1,2]:

The high vibration levels in a helicopter are due to loads generated by the rotor which in turn depend on the airloads generated by the blades as well as the dynamic characteristics of the whole rotor system. Continuous rotation of the rotor

creates a periodic asymmetry of the geometric configuration of the helicopter. On the other hand, the primary source of this vibration is the non-uniform flow passing through the rotor causing oscillatory loads on the rotor blades. These air loads produce time varying forces and moments at the rotating hub which are periodic in nature. Subsequently these forces and moments are transmitted from the rotating hub system to the fixed fuselage system, where they act as exciting forces and moments on the fuselage with various integer multiples of rotor speed (Ω). Thus the helicopter vibration is characterised by harmonic excitation in the fixed system.

Unfortunately, the airframe is a highly complex structure and calculation of mode shapes and natural frequencies, for example, is extremely difficult. Nevertheless, it is most important that the acceptable vibration characteristics are achieved at the design stage to avoid the costly and lengthy business of having to alleviate excessive vibration by modifying production aircraft. However, alleviation of such excessive vibration may require structural modification of the airframe and/or the fitting of some form of vibration control as follows:

2.2. Respective Vibration Control Methods

The stringent vibration requirements of modern helicopters necessitates special methods and devices to control and reduce vibration to an acceptable level. These stringent requirements have led to extensive research and development programs, by

helicopter manufacturers, aimed at substantial reduction of excessive vibration. The various vibration control methods used in helicopters fall broadly into the following categories [3, 4, 5]:

2.2.1. Vibration Isolation:

On most helicopters the main gearbox taking the drive from the engine or engines to the rotor is normally mounted directly beneath the rotor. The possibility of using the rotor/transmission unit for alleviating fuselage vibration has been explored in many designs as follows:

(i) Passive Isolators:

On a conventional helicopter the fuselage is usually isolated from the rotor/transmission unit by means of flexible mounting isolator system. This isolator system requires that the natural frequency of the system be below the isolated frequency for obtaining minimum transmissibility of the force into the fuselage. For common rotor generated frequencies relatively low stiffness ("soft" springs) must therefore be used. Drawbacks of this isolator system are that continuous mechanical control across the interface is difficult and then the maneouvering response will be lost. Furthermore, this isolator is often designed to suit a particular helicopter model and to achieve only partial alleviation of transmitted vibration. While this method has proved its effectiveness for two bladed teetering rotors, it has enjoyed only limited success in the case of multi-blade rotor systems. These

days, the simple flexible mounting is no longer used, but has been replaced by the direct isolation system.

One particular method of isolation uses the nodalisation concept. The basic principle of this method is that a flexible beam (which may carry a mass at its midpoint) has two nodes when vibrating in the fundamental free-free lateral normal mode. If the beam is supported at these nodes, no vibration is transmitted from the beam to the supports. Thus, a beam mounting arrangement (between the gearbox and the airframe) is designed from the node points of the beam system when it responds to rotor hub forcing.

Shipman [6] describes the development and application of such a nodalisation concept to helicopters.

Kidd et al [7] reported on the occurrence of in-flight nodal points in the fuselage and showed the added benefit of placing one of these nodal points in the cabin area. This method falls short of producing a ±0.05 g ride throughout the cabin over the entire flight envelope.

Another patented device is the "Dynamic Anti-resonance Vibration Isolator" or DAVI invented by Flannelly [8] . This device, which counteracts spring forces with inertia forces possesses low frequency isolation with low static deflection, was developed to isolate the rotor system and also crew seats. It is claimed to obviate the obvious disadvantage of the conventional soft mounting isolator, i.e. the effects of variability of the sprung mass and excessive quasi-steady deflections. The rotor/transmission unit in this case is mounted on the fuselage using such isolators.

These isolators consist of spring elements to which pendulums are attached as illustrated in Figure (1.a). At the tuned or anti-resonance frequency the inertia forces from the inertia bar cancel forces from the spring and produce nearly 100% isolation. The main advantage of the DAVI is that the suspension is still rather than stiff. The transmitted force in the absence of damping is approximately equal to zero at a frequency somewhat higher than the natural frequency. When damping is present the transmitted force is small and finite. DAVI devices could be fitted as part of the gearbox-engine rotor head suspension system.

The application of anti-resonance theory has been developed by Bartlett and Flannelly [9]. They presented a solution of an anti-resonance eigenvalue problem in which the anti-resonance can be determined by matrix iteration. They also studied the anti-resonance nodes introduced by dynamic absorbers and anti-resonance isolators.

Rita et al [10] describe and illustrate some of the basic concepts, analysis and ground tests to demonstrate the feasibility of DAVI isolation system. The fuselage was isolated from the in-plane force of the main rotor. A substantial reduction in vertical 2/rev vibration load was achieved. They concluded that the DAVI isolation system could be designed for about 1.5 per cent of the gross weight of the helicopter.

Desjardins and Hooper [11] describe a system based on DAVI units called IRIS (Improved Rotor Isolation System) with a spring mass beyond the linkage as shown in Figure (1.b). The spring

(a) Conventional DAVI (b) Improved DAVI

Figure 1 DAVI .... "Dynamic Antiresonance Vibration Isolator"

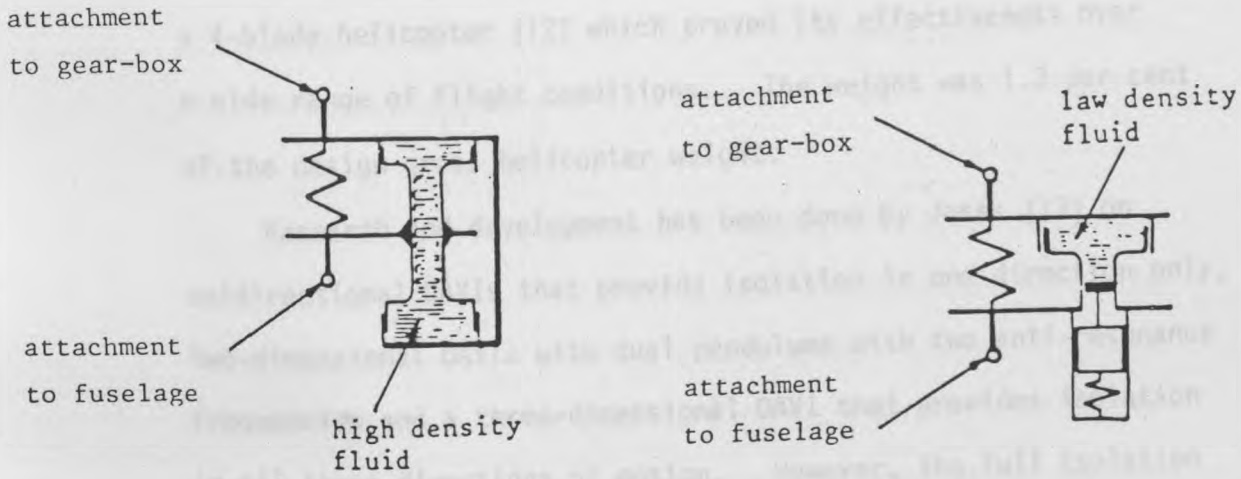

(a) LIVE Isolator (b) Hydraulic Antiresonance Isolator.

Figure 2 Antiresonance Isolator

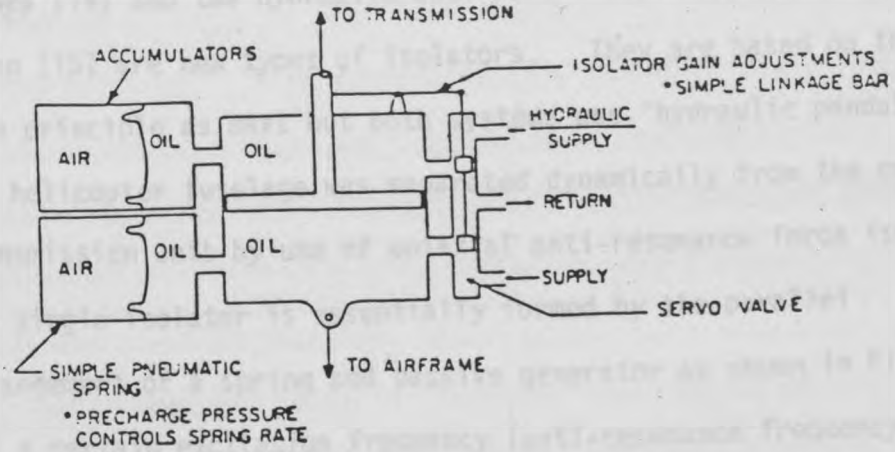

Figure 3 Schematic Illustration of Hydropenumatic Active Isolator.

mass allows force isolation at two distinct frequencies. This is because the device has two main degrees of freedom. Deliberately introduced damping was not beneficial. This IRIS has been used for 4-blade hingeless rotor helicopters. Vibration levels were kept below 0.05 g for most flight conditions. They also designed, built and flew an experimental improved IRIS for a 4-blade helicopter [12] which proved its effectiveness over a wide range of flight conditions. The weight was 1.3 per cent of the design gross helicopter weight.

Research and development has been done by Jones [13] on unidirectional DAVIs that provide isolation in one direction only, two-dimensional DAVIs with dual pendulums with two anti-resonance frequencies and a three-dimensional DAVI that provides isolation in all three directions of motion. However, the full isolation of the rotor requires isolation in all axes, and this makes the system rather complicated. Furthermore, for maintenance and reliability the many additional bearings seem to be problematic.

The LIVE (Liquid Inertia Vibration Eliminator) developed by Halwes [14] and the hydraulic anti-resonance isolator evolved by Braun [15] are new types of isolators. They are based on the same principle as DAVI but both systems use 'hydraulic pendulums'. The helicopter fuselage was separated dynamically from the rotor/transmission unit by use of uniaxial anti-resonance force isolators. The single isolator is essentially formed by the parallel arrangement of a spring and passive generator as shown in Figure 2, for a certain excitation frequency (anti-resonance frequency) the

spring force and the hydraulic force generator which produced by the relative movement between fuselage and rotor-transmission unit are opposite and equal at the fuselage side attachment of the isolator element.

Passive isolators are now at the stage of development that they are often used for helicopters, they add mechanical complexity to the helicopter and get even more complex if more than one frequency has to be isolated.

(ii) Active Isolators:

The progress of the overall understanding, of modern control, of electronics and of modern servohydraulics enables an efficient active isolation system to be realised. These active isolators can be used as a force isolator; this means in comparison to passive systems that the pendulum is replaced by an electrohydraulic actuator in which its dynamic characteristics are provided by the active closed loop control system.

An active isolation system described by Kidd et al [7] is a SAVSS (Servo-Active Vibration Suppression System). This SAVSS employs an actuator to oscillate a mass which produces a reaction on the fuselage. This force acts at a chosen harmonic frequency of the rotor to reshape the fuselage mode produced by rotor forces at the same harmonic. The presented results indicated that a significant reduction in 2/rev vibration levels was achieved for pilot and co-pilot stations.

Hardenberg and Saltanis [16] have investigated an active transmission isolation system. This isolation system was used

to isolate the vertical and in-plane rotor head vibratory forces from a helicopter fuselage without introducing deflection. This was achieved by using a hydropneumatic, servo-centred isolation system installed at the transmission-airframe interface. Shake tests showed that an overall reduction of approximately 70 per cent in the fuselage response to main rotor 6/rev excitation was achieved.

Kuczynski and Madden [17] have described a system in which low and high frequency loads are reacted actively and passively respectively. The primary elements in the isolation system are hydropneumatic servo-controlled actuators. A schematic representation of the unit is shown in Figure 3. The unit is basically a hydraulic piston reacting against captured air chambers with a relatively low gain mechanical displacement feedback servo valve. The captured air bulk modulus provides a spring restoring force with piston displacement. Also when the piston displaces, the servo valve feeds hydraulic fluid into the piston chamber in the direction of motion, compressing the air and creating a restoring force on the piston 90^{o} out of phase with piston displacement. The net result is that for static or transient loads on the isolator, the displacement servo feature keeps the unit centred in midstroke, whilst for high frequency motion the units act as soft air springs, as insufficient fluid flow through the servo occurs to create appreciable forces. This means that its basic principle is passive isolation but with active trim. Shakedown flight test

results which were carried out on a S-61 rotor indicated that a considerable reduction in vibration levels has been achieved.

These active isolation systems may be used to isolate at more than one frequency but at the expense of fluid power and mechanical complexity. However, they have not yet achieved general acceptance in the helicopter industry.

2.2.2. Rotor-Borne Vibration Absorbers:

Centrifugal pendulum absorbers mounted on rotor blades have already been in use for a long time. These devices can be used to reduce the response of particular flapping or in-plane modes of rotor blades with the object of reducing root shear or root bending moment. However, the absorber assembly rotates with the rotor. It has a mass mounted as a pendulum and restoring force for the pendulum mass is provided by centrifugal force. The system is most effective if it is tuned, i.e. its natural frequency equals the excitation frequency to be absorbed. Consider the simple system shown in Figure (4.a) in which the pendulum swings in the plane of rotation. The natural frequency is $\Omega\sqrt{R/r}$; it is linearly related to the speed of rotation (Ω). The advantage of the system is that the absorber, after it has been tuned to a given frequency, remains in tune regardless of the rotor speed. So the absorber is effective at high frequency only if the ratio r/R is small. Thus, there is a practical difficulty in applying a simple pendulum for cancelling higher orders of vibration, because the small length of pendulum required

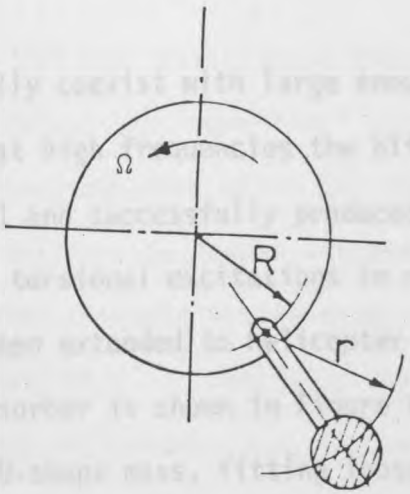

(a) Simple Pendulum Absorber

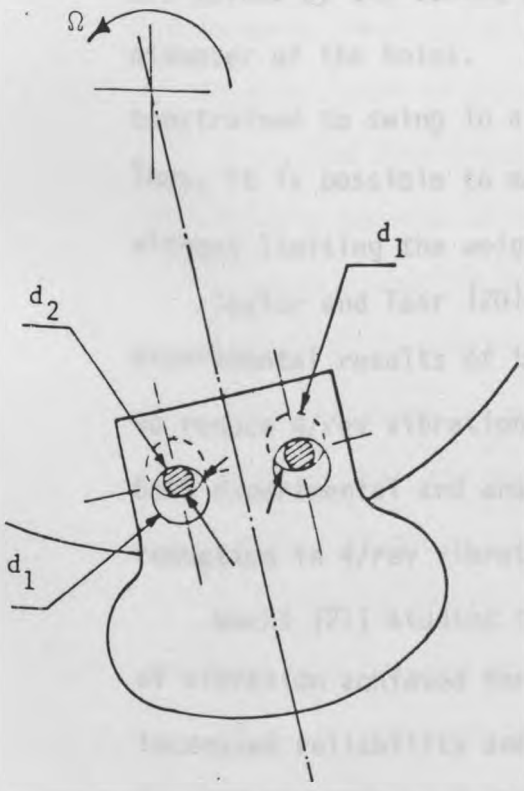

(b) Bifilar Absorber

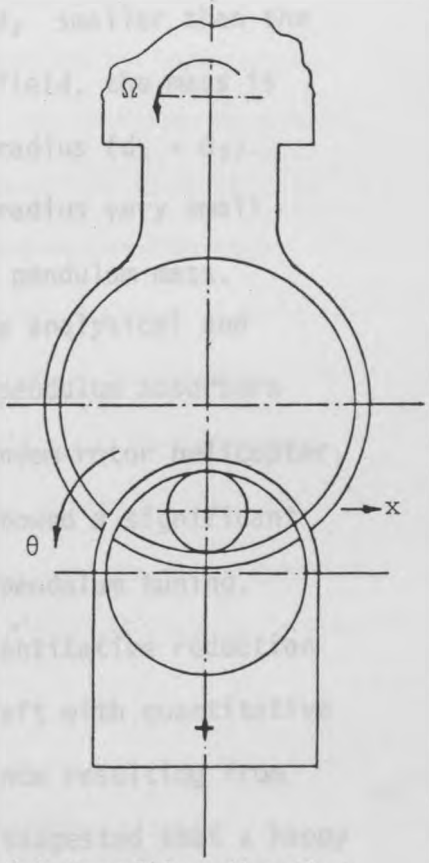

(c) Monofilar Absorber

Figure 4 Pendulum Absorber

cannot physically coexist with large enough mass to be effective. Nevertheless, at high frequencies the bifilar absorber, invented by Chilton [18] and successfully produced in practice for cancelling the torsional excitations in reciprocating aircraft engines, has been extended to helicopter applications by Paul [19]. The bifilar absorber is shown in Figure (4.b). Its pendulum mass is normally a U-shape mass, fitting loosely around an arm projecting from the centre of rotation. The arm has two circular holes of the same diameter d_1. This arm and the pendulum mass are joined by two tuning pins of diameter d_2 smaller than the diameter of the holes. In a centrifugal field, the mass is constrained to swing in a circular arc of radius $(d_1 - d_2)$. Thus, it is possible to make the pendular radius very small without limiting the weight or size of the pendulum mass.

Taylor and Tear [20] have reported the analytical and experimental results of the blade mounted pendulum absorbers to reduce 4/rev vibration on a 4-bladed tandem-rotor helicopter. Both experimental and analytical results showed a significant reduction in 4/rev vibration with optimum pendulum tuning.

Wachs [21] studied the relation of quantitative reduction of vibration achieved throughout the aircraft with quantitative increased reliability and reduced maintenance resulting from the application of bifilar absorber. He suggested that a happy meeting ground exists between two approaches: making components more tolerant of vibration and making the whole helicopter less of a vibrating machine by installing a bifilar vibration absorber.

Mouzakis [22] has investigated theoretically a new pendulum-type absorber called the "monofilar" as shown in Figure (4.c). It is a rotor head absorber which has the ability, unlike the more familiar bifilar, to reduce vibration simultaneously at two frequencies using a single active mass. This is because the monofilar dynamic mass can rotate as well as translate, giving two main degrees of freedom, i.e. two natural frequencies. He concluded that the monofilar design offers potential benefits relative to bifilar absorbers in terms of simplicity, reductions in weight, parts count, maintenance and production costs. Furthermore, it is possible to achieve reduction in hub forces of the same order as those achievable with two bifilar absorbers.

A problem with these above types of pendulum absorbers is that a large portion of the installed weight is ineffective. Furthermore, operation relies upon sliding or rolling of metal surfaces which is practically unacceptable where maintainability and reliability are of paramount consideration. On the other hand each troublesome mode needs a separate absorber, and this would make a complete, combined system, too complex and expensive. Perhaps, this is the reason why the blade pendulum absorbers are not used in a broader application.

Thus, an interesting new centrifugal pendulum absorber which has been investigated analytically and experimentally by Viswanathan and McClure [23] is the Mercury Pendulum Absorber (MPA). This employs mercury as the tuning weight that works inside a totally sealed cylindrical container. The MPA concept is that

the motion of mercury resembles that of a simple pendulum mass when the rotating hub is subjected to an oscillatory motion as illustrated schematically in Figure 5. Also, the MPA has an additional advantage in that it has no surfaces undergoing any wear. But the disadvantage is that should the mercury ever leak out, it could corrode aircraft parts and hence the installation should redundantly ensure against the possibility of any mercury leakage. The authors presented a mathematical model to analyse the rotor response, MPA response and the fuselage vibration while the helicopter is in the transitional flight from forward to hover. They also concluded that the cabin vibration level has been reduced by about 60% and more flights should be anticipated to complete the search for optimum tuning.

Another interesting new absorber, is, in effect, a spring mass mounted on the rotor head that operates in a plane parallel to the rotor; it is shown in Figure 6. This absorber which was developed by White [24] is a fixed-frequency rotor hub vibration absorber. The operational characteristics are very similar to the bifilar pendulum, but, of course, it is not self tuning. It is claimed to obviate the obvious disadvantages of bifilar absorbers, i.e. overcoming any potential reliability and maintenance problems. An ingenious design of spirally-wrapped fibre composite springs allows sufficient displacement amplitude but does not endanger fatigue life. The distance of the absorber from the centre of mass of the helicopter allows it effectively to counteract the vibratory moment resultants induced at the rotor

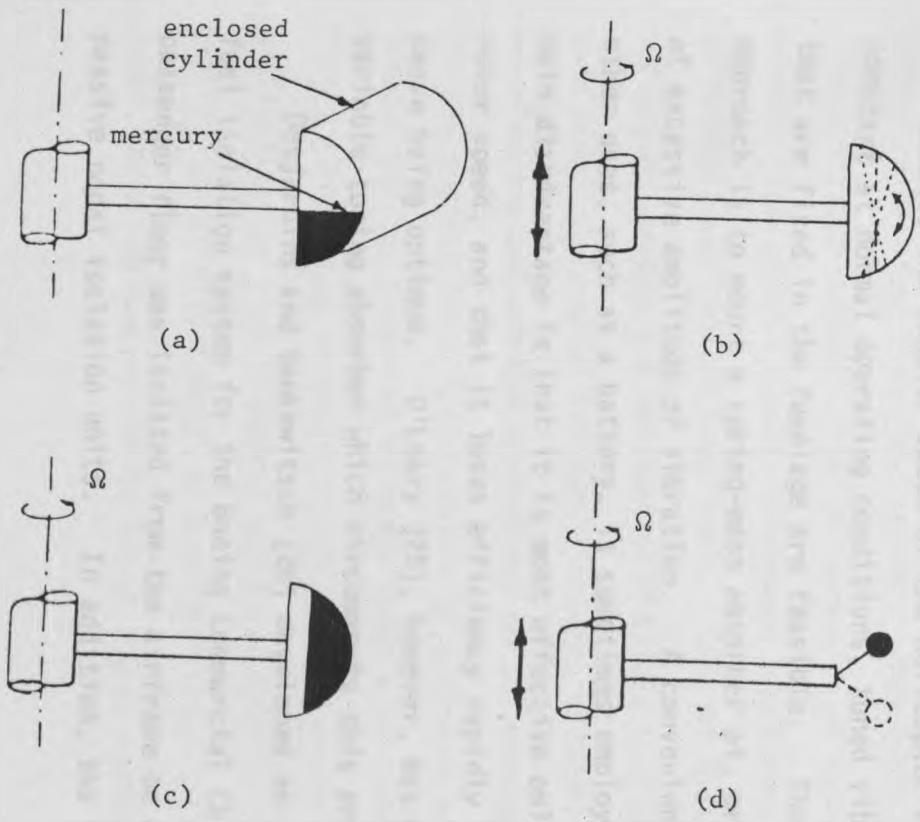

Figure 5 Concept of a Mercury Pendulum Absorber (MPA)

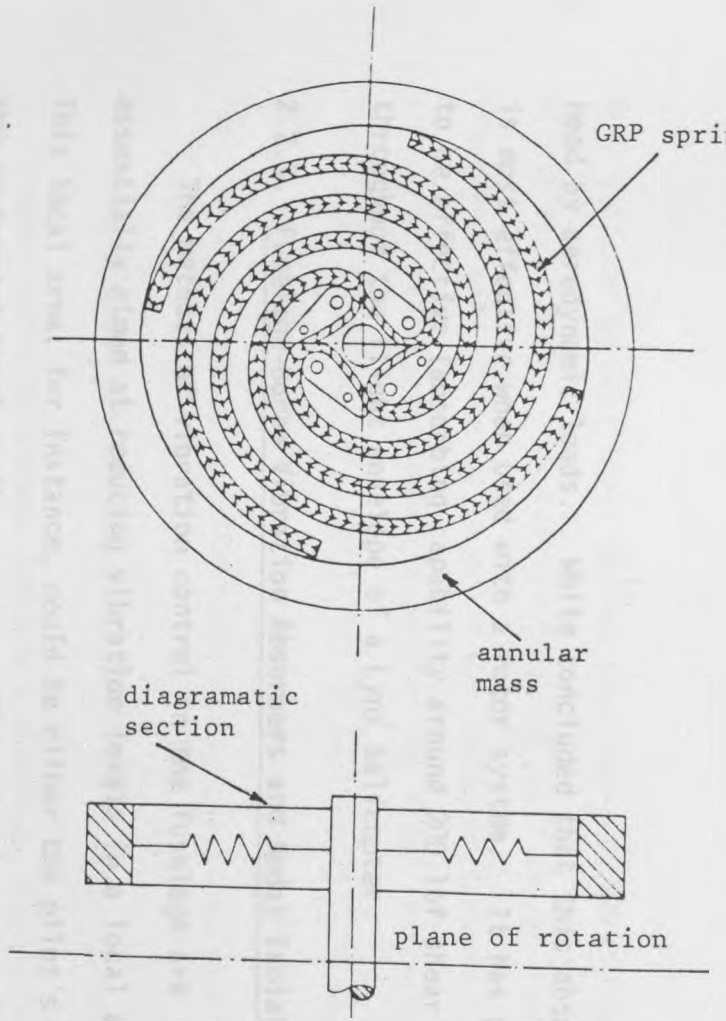

Figure 6 Rotor Head Vibration Absorber.

head by aerodynamic loads. White concluded that this absorber is most effective when used with a rotor system. It has proved to be effective (absorbing capability around 200 lbf shear force) throughout the flight envelope of a Lynx helicopter.

2.2.3. Fuselage-Borne Vibration Absorbers and Nodal Isolation:

The methods of vibration control in the fuselage are essentially aimed at reducing vibration levels in a local area. This local area, for instance, could be either the pilot's seat, the instrument panel or the passenger floor in the case of commercial helicopters. Classical vibration absorbers and nodal isolation may adequately serve this purpose.

Because the angular speed of the helicopter rotor is almost constant at normal operating conditions, tuned vibration absorbers that are fixed in the fuselage are feasible. The fairly simple approach is to mount a spring-mass absorber at, or near, a point of excessive amplitude of vibration. A convenient mass that has other uses, such as a battery, is sometimes employed [3]. The main disadvantage is that it is most effective only at one particular rotor speed, and that it loses efficiency rapidly if the conditions cease being optimum. O'Leary [25], however, has made use of a variable tuning absorber which circumvents this problem.

Desjardins and Sankewitsch [26] developed an integrated floor/fuel isolation system for the Boeing Commercial Chinook. The passenger floor was isolated from the airframe on a series of passive nodal isolation units. In addition, the fuel tanks

were isolated so that their dynamic mass was effectively nulled at all fuel levels. Analysis, component tests and an aircraft shake test were conducted to prove the isolation system. The aircraft flight tests demonstrated that the floor isolation lowers the airframe vibration levels to an average of 0.05 g on the passenger floor. Furthermore, the effectiveness of the fuel isolation system was also confirmed by the shake test.

2.2.4. Higher Harmonic Blade Pitch Control:

Higher Harmonic Control (HHC) is a promising active control method of reducing helicopter vibration by controlling its primary source, the exciting airloads on the rotor blades. These airloads are periodic at frequencies equal to the fundamental and higher harmonics of rotor rotational speed. They cause both rigid and flexible blade motion, also at harmonics of rotor rotational speed. The overall result is harmonic blade root loads with both aerodynamic and inertia components. Some of these harmonic loads are phased amongst the various rotor blades such that they cancel when added together at the hub. Others, however, reinforce each other at the hub and are transmitted to the fuselage. Therefore one may suggest that it is possible to influence and minimise them through various orders of harmonic blade pitch control. However, recent advances in automatic control system design with the availability of high frequency actuators have facilitated the application of this concept to practical rotor systems. Using small amounts of swashplate motion at higher harmonic frequencies

of blade cyclic pitch once every rotor revolution. Theoretical results were presented for a non-linear 4-bladed single rotor helicopter simulation which demonstrated the effectiveness of the active control system, and 4/rev fuselage vibration reductions of the order of 80-90 per cent were achieved. The rotor performance penalty (torque increases) associated with this level of vibration reduction was about 1-3 per cent but more studies are needed to determine the impact of active control on performance.

Hammond [31] presented the results of a wind tunnel test using a dynamically-scaled helicopter rotor model to evaluate the use of HHC for reducing helicopter vibration levels. Significant reductions in the rotor vibratory vertical force and vibratory pitching moment were achieved over a wide range of advance ratios tested. But simultaneous reduction of vibratory rolling moment was not achieved at all advance ratios. Hammond left the reason for these results as an open issue.

However, use of an active control system to alleviate helicopter vibration implies an additional weight penalty due to introduction of apparently redundant and relatively complex control systems. Furthermore, the design and manufacture of such control systems will be added to the overall cost.

2.2.5. Structural Modification:

The respective methods and devices for the helicopter vibration control, may be ingenious though all suffer a significant weight penalty. These methods and devices do not, and cannot, suppress

or remove all fuselage vibration, and it is accepted that this will always be present to some extent. On the other hand, the unprecedented development in computational capability in the last decade has fostered equally impressive development in structural optimization schemes in all disciplines of engineering.

The design of complex structures to satisfy dynamic response restrictions is hampered by the inherent difficulty and computational cost of dynamic analysis. These limitations impose a ceiling on the number of trial designs which can be analysed. Furthermore, from analysis alone it is not usually clear how a design should be modified if it is desired to improve or maintain its dynamic properties. However, structural optimization provides a means of not only saving weight and cost but also allows sensitivity studies to be made which can improve structural integrity.

Research in structural optimization follows one of the several approaches which have recently been classified [32,33] as follows:

(a) One approach is to invoke the "Variational Calculus method" and to find a function or a number of functions which will extremize the objective function subject to the constraints. This approach is referred to as the continuous model. Unfortunately, only relatively simple problems can be solved by this approach, since the calculation of variations becomes intractable when complex engineering structures are considered.

(b) Another approach is to cast the problem in a "mathematical programming form" and to directly search for a set of discrete variables which will extremize the objective function subject to several equality and inequality constraints. This approach is referred to as the discrete model. Fortunately, several improvements developed over the last few years appear to have significantly extended the capability of the mathematical programming approach, and, as a result, it is a more practical approach.

(c) In yet another approach, a criterion related to the behaviour of the structure is derived such that, when the structure is sized to satisfy this criterion the objective function automatically attains an optimum. This approach is usually denoted in the literature of structure synthesis as the optimality criteria method.

A great deal has been written on structural optimization under dynamic constraints in recent years as the recent comprehensive survey by Rangacharyulu and Done [34] indicates. A portion of the research work that has been done is concerned with the general methods of structural optimization using continuous and discrete models for free vibration problems, forced vibration problems and non-conservative problems.

The need to reduce structure weight without compromising structural integrity is all important in aerospace applications and much of the motivation behind the development of structural optimization methods has been due to this factor. Minimum weight

design subject to a specified natural frequency was considered by Turner [35], using Lagrange multipliers to introduce the free vibration equations as constraints. The problem considered was that of axial vibration of a cantilever rod carrying an end mass. The numerical solution was given for the case of a continuously varying cross-section rod as well as for the case of a stepped rod with three prismatic segments. The procedure consisted essentially of starting with a given mass distribution and hence with a given natural frequency and then obtaining a series of corrections to the mass distribution until minimum mass was achieved.

Rubin [36] presented an analytical procedure of a minimum weight design for a frequency constrained problem. This optimization procedure follows two alternating cycles. Separate gradient equations were used first to obtain the correct structural frequency (called the frequency modification mode). Then, with the frequency held constant, the weight is minimised, (called the weight minimisation mode), using a steepest descent algorithm. Occasional correction steps using the frequency modification mode are needed to maintain the desired frequency change. The finite element method was used in deriving the equations of motion of the modelled structure. In the finite element model only one parameter was allowed to vary in each element. Furthermore, this parameter must occur as a linear factor in the element matrices. Numerical results were presented to demonstrate the feasibility of the dynamic optimization procedure.

Fox and Kapoor [37] studied the minimum weight design problem with constraints on dynamic response and frequency characteristics of a structure due to shock loading. The resulting optimization problem, posed as a mathematical programming problem, was solved using the feasible direction methods. They used the finite element method with standard beam type elements to analyise the general planar-truss frame structure. The eigenvalue problem was solved by minimizing the Rayleigh quotient in a sequence of subspaces for as many eigenvectors and eigenvalue as desired. This method is particularly advantageous in a design process. As the design is evolved the natural frequency may change drastically but mode shapes for previous designs are good candidates for the starting point of a new design. The presented results indicated that a considerable reduction in the computing time had been achieved.

The problem of maximising the lowest eigenvalue, with a constraint on the total mass has been investigated by Taylor [38]. The equations of motion are written in terms of kinetic and potential energies. A variational method was used to obtain the minimum mass distribution of an axially vibrating rod. This problem was also solved by Zarghamee [39] using the non-linear mathematical programming technique. The procedure is based on gradient equations which express the rate of change of frequency with respect to the design parameters. Numerical results of the optimized cantilever truss were given to demonstrate the method

of solution.

McCart et al [40] have investigated a method for the minimum weight design problem of structures subject to constraints on strength and specified natural frequencies. A steepest descent boundary value method was used to obtain the solution of a portal-frame structure. In this method an initial estimate is made for the material distribution (mass distribution) along the members of the structure. A small change in the material distribution is then determined which reduces the given objective function and also satisfies the constraints. This small change in material distribution is taken as an improved estimate of the optimal structure. The process is repeated until there is no change in the objective function due to successive iteration.

Elwany and Barr [41] have recently studied some optimization problems in flexural vibration of beams. This study is an extension of their earlier work [42,43] on the optimization problem relating to torsional vibration of beams. The problem was stated in variational form with a view to show the duality of the two problems of maximising the natural frequency for a given weight, and minimising the weight for a given frequency.

Joseph and Lucien [44] dealt with the minimum weight optimum design of planar frames including an optional mode frequency constraint used to prevent system buckling. The influence of member axial force on frame stiffness was taken into consideration. The mathematical programming problem was solved numerically using

the sequential unconstrained minimisation technique. An interior extended penalty formulation using the Davidon-Fletcher-Powell minimisation algorithm was implemented and numerical results were given.

Niordson [45] used a variational method to find the best possible tapering of a simply supported beam of fixed volume to achieve the highest possible value of natural frequency in the fundamental mode of lateral vibration. The resulting non-linear eigenvalue problem consisted of homogeneous fourth order non-linear differential equations with boundary conditions and was solved numerically.

Text books [46, 47] provide lucid expositions of various algorithms in which the structural design is treated as a problem of mathematical extremization of an objective function in an "n" dimensional design variable space, behavioural functions constraining the search for the extremum, this being carried out by methods of linear and non-linear programming techniques. Some examples of mathematical programming methods are the gradient projection, steepest descent, feasible directions and various unconstrained minimisation techniques in conjunction with so called penalty functions to account for constraints.

Moe [48] presented a survey of mathematical programming methods with special emphasis on penalty function techniques.

Done [49] studied the possibility of adjusting the mathematical model of a system in order to achieve the coincidence between the computed natural frequencies and those measured

experimentally. This was achieved by using an optimization technique in which the system parameter deviation providing the basic objective function and the dynamic property requirements (natural frequency changes) providing the constraints. These constraints were added to the basic objective function, using Lagrange multipliers, to give the overall objective function. This type of problem may be classified under "system identification". A laboratory turbine-rotor was modelled mathematically using Timoshenko beam elements and the six lowest natural frequencies in bending were considered. The rates of change of natural frequency (frequency sensitivities or gradients) with the various stiffness properties were presented. The problem was manipulated; firstly, using Young's modulus and modulus of rigidity as design variables. Changes of the moduli from standard values represented overall stiffness deficiencies in the mathematical model. In this case, a best fit to the lowest six natural frequencies was made. Secondly, "stiffness" diameters were used as design variables, thereby allowing for deficiencies in the mathematical model near the discontinuous changes of section. The overall measure of the difference between the actual and the stiffness diameter was minimised using the gradient projection method. The computed lowest six natural frequencies were matched exactly with those measured experimentally.

Kim et al [50] have developed non-linear perturbation method for dynamic model redesign. The modal analysis method is often

applied for the complex structures with general purpose finite element codes. It is a generalisation of the mathematical treatment presented by Stetson [51,52] and is based on a perturbation of the eigensystem, and all non-linear terms, to achieve large changes in the natural frequencies and mode shapes. A penalty function was implemented in which the penalty parameter was chosen to equally emphasise minimum weight (or least change) and minimum error in nodal energy. The resulting optimization (perturbation) problem, posed as a non-linear mathematical programming, was solved using the conjugate gradient method. To demonstrate this method of analysis, the authors considered the flexural vibration of a rectangular uniform cantilever beam (shear deformation and axial displacement were not included). The method has been discussed and numerical results were given for one mode only.

During the development stage of the helicopter there occur many possibilities for reducing the vibrational response of important parts of the helicopter. One possible method is to adjust, modify or initially design the elastic elements of the structure appropriately. For instance, the rotor blades may be structurally "tailored" in order to minimise the oscillatory input to the fuselage from the rotor head, and likewise the fuselage itself may be designed in such a way as to minimise response in local areas (e.g. crew and passenger areas). Optimization routines tend to use a great deal of computer time when many variables are involved. Thus, it is necessary to

establish the sensitivity of the predicted response to structural changes in order to select the relatively few sensitive structural parameters out of the overall set.

One way of doing this is to compute the rate of change of response at particular point on the structure under consideration with changes in all the variable parameters. The larger of these "gradients" would indicate those parameters which have the greater effectiveness [53]. A drawback with this is that only small perturbations are considered. Thus some "sensitive" parameters or elements would be missed.

Another way of sorting out the best structural elements or parameters in controlling vibration is the strain energy density approach which has been developed by Sciarra [54]. This approach was used for defining which structural elements in the fuselage should be modified in order to achieve the desired results. Modal strain energy is calculated for each structural element using the mode shape for the natural frequency to be modified. It is assumed that elements with highest strain energy density are the best candidates for modification (kinetic energy is not considered). These elements are changed so that natural frequencies of the fuselage are moved away from the excitation frequency of the main rotor, thereby reducing dynamic amplification. It is also assumed that such change will have beneficial effect over all response. Examination of a twin-rotor helicopter has provided confirmation.

The response of a vibrating structure as a function of structural parameters has been described by Done and Hughes [55]. They used the Vincent circle approach [56] to identify the best parameters to use for the optimization. This approach is based on the fact that if a linear structure is excited by a sinusoidal force at a constant frequency, then if either the mass at a point or stiffness between two points (as represented by spring) is varied, the response in the complex plane traces out a circular locus. The larger size circle indicates that the associated parameter has a greater effect on the response than a parameter producing a small circle. Accordingly, a simple yardstick based on circle diameter may be used for deciding on the best parameters. Done, et al [57] and Walker [58] have performed some simple experimental verification of the Vincent circle approach method.

Based on this study, Done and Hughes [59] provided a simple structure modification by inserting a linear spring between two points on the Lynx helicopter fuselage model. The relative effectiveness of changing the elemental stiffness was studied using various criteria as illustrated in Figure 7. This analysis was applied to the problem of determining which part of the helicopter fuselage structure is most effective in reducing the rotor induced vibrational response in the region of pilot's seat.

The application of a mathematical optimization process to helicopter vibration control by structural modification has been reported by Done and Rangacharyulu [60]. A non-linear programming

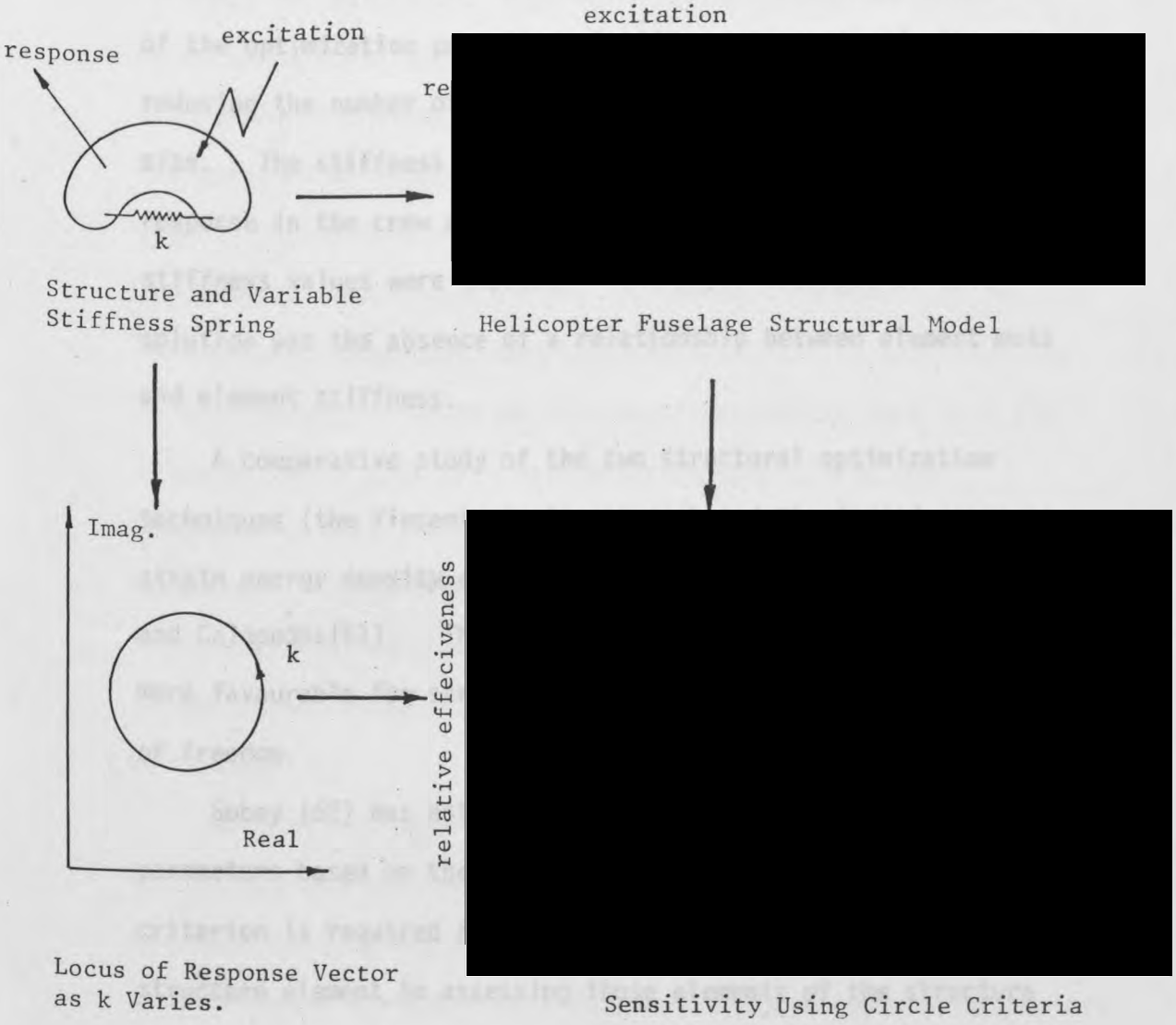

Figure 7 Relative Effectiveness of Changing Stiffness.

problem and a sequential unconstrained minimisation technique incorporating an algorithm based on the methods of Davidon, Fletcher and Powell was used to determine the precise values of the optimization parameters (stiffness parameters), thereby reducing the number of available design variables to tractable size. The stiffness parameters were used in controlling the response in the crew area. Realistic bounds on the elemental stiffness values were imposed. The major drawback of this solution was the absence of a relationship between element mass and element stiffness.

A comparative study of the two structural optimization techniques (the Vincent circle approach and the forced response strain energy density approach) has been discussed by Hanson and Calapodas[61]. They concluded that the second approach is more favourable for structures with a large number of degrees of freedom.

Sobey [62] has established a criterion for selecting parameters based on the circular response property. This criterion is required for determing the importance of each structure element in assessing those elements of the structure which are most effective in reducing helicopter vibration response. The main advantage of using such a criterion is that once the receptance matrix for the structure is obtained, any geometric property relating to circular loci can be relatively easily computed. Sobey also conducted an exercise in which mass was varied simultaneously with stiffness. He concluded

that for realistic values of mass and stiffness the effects of mass addition are small enough to be ignored.

For the purposes of testing out a particular parameter selection process combined with an optimization procedure, Done [63] employed a mathematical model of the helicopter fuselage. The selected stiffness parameters (as design variables) were used in controlling the response in the crew and passenger area. The penalty function method was implemented and numerical results were given. Done concluded that the optimization technique can be used to obtain values of structural parameters such that the response over a part of a helicopter is greatly reduced. Furthermore, only a relatively few variables need to be adjusted to achieve a satisfactory result in terms of response. This highlights the importance of the initial selection process, and suggests that these methods of parameter selection would be worthwhile.

An efficient numerical method based on local modification of the fuselage was applied to problem of helicopter alleviation has been investigated by Wang, et al [64]. The frequency response of a vibrating structure as a function of its structural properties which is a generalisation of the approach by Done, et al [55, 57] was presented. The sensitivity analysis has been used to determine which structural element changes are responsible for vibration reduction. The entire helicopter (the rotor, the rotor-fuselage interface and the fuselage) was analysed once using a finite element idealization. The rotor was made up of ten

identical beam elements. Each beam element had four degrees of freedom. The interface between the rotor and the fuselage was modelled as a stiff linear spring. Ten beam elements of varying mass and stiffness made up the fuselage. When structural parameters (mass and stiffness) were changed, minimum response was obtained by solving linear algebraic systems. The usefulness of this method was demonstrated by the given numerical results.

King [65] derives a simple algorithm to estimate the changes in the normal modes and natural frequencies of a dynamical system when the system is modified by the addition of mass, stiffness or mass-spring absorber. The effect of fitting a dynamic absorber to the main rotor head of the helicopter was also estimated. Flight test results have demonstrated the usefulness of the algorithm in estimating the efficacy of vibration reduction techniques.

In the early stages of the development of the helicopter, it was believed that helicopter vibrations could be reduced by the correct choice of rotor blade mass and stiffness distributions. Hirsch et al [66] have described earlier the development of the XH-17 helicopter in which 300 lb weight was added to each blade in order to change the spanwise and chordwise mass distribution and thereby reduce vibrations. The cyclic stresses were reduced 35 to 45 per cent in all flight regimes tested. This was accomplished by adding the concentrated weight to the blade leading edge outboard of the second mode nodal point. They tentatively concluded that the blade was operating near resonance

with the third harmonic forcing function, and that its "effective damping" was greatly reduced by the blade twist. This adverse effect of the twist was a major factor contributing to the large 3/rev stresses. This was based on the belief that the aerodynamic load due to the increment of the twist caused by added weight would lag the bending displacement and hence damp the bending motion. The authors showed that the additional weight would increase the second mode bending natural frequency from 3.11/rev to 3.13/rev.

Recent studies [67 - 70] are aimed at modifying the blade properties (mass and stiffness distributions) to reduce vibration levels in forward flight. Taylor [67] has treated the vibration reduction problem of an articulated rotor blade by modifying the mass distribution, and to a lesser extent the stiffness distribution of the blade, using a so called "modal shaping parameter". It is hypothesised that changing the mode shape such that it is orthogonal to the forcing function is a way to lower vibration. In this analytical design method, Taylor represented the 4/rev airloading distribution by a cubic polynomial weighted by a tip loss factor starting at 95 per cent radius. The sensitivity of the modal shaping parameter to blade design variables was investigated by making variations in blade flatwise stiffness and mass from the baseline design. From this parametric study, Taylor concluded that blade mass distribution rather than total blade mass or flatwise stiffness, is the prime variables controlling the modal shaping parameter. The second flatwise

mode is the prime vibration contributor for the baseline 4-bladed rotor. Significant vibration reductions (70 per cent reduction in 4/rev vertical root shear) were achieved when 4 per cent blade mass was added at the tip of a S-76 blade.

Blackwell [68] considered the addition of mass to the UH-60A blade of a 4-bladed articulated rotor. Using the CH-53A airload distribution, the effects on vibratory hub loads of changes in spanwise mass distribution were examined. Modal analysis was performed to identify regions of the blade in which added mass would be beneficial and to assist in understanding the basic mechanism involved. This analysis was run at two flight conditions. However, the analysis predicted that mass added at midspan of the blade reduced the vibratory root shears (of the order of 10 - 35 per cent) which were not as large as those projected by Taylor [67]. Blackwell concluded that the best mass distribution depends upon other properties of the blade and flight conditions. It is premature to speculate on what types of mass distribution will be appropriate for a given high speed rotor blade, but he suggests that it is a parameter which may afford significant vibration benefits. Blackwell also explored the effects on the UH-60A rotor vibratory hub loads to change in blade twist and blade bending stiffness. The presented results show a very small effect of twist on vibratory loads. So he suggests that high twist blades (which are desirable for good hover performance) are not detrimental to vibration. He also concluded that the reductions in root shears achieved by

detuning blade modes from (N_b-1), N_b and (N_b+1) per rev (where N_b is the number of blades) were not as large as the changes predicted for changes in mass distribution.

Bennet [69] presents a simple approach to rotor blade design in which vertical hub shears due to flapping only were minimised, using mathematical programming techniques. The vertical shear forces which are functions of the blade spanwise mass and stiffness distributions were calculated using a classical modal approach (the effect of blade dynamics on the airloads was neglected). For the optimal design techniques the blade was divided into 15 radial segments with design variables being the mass and out-of-plane stiffness at each segment. After 130 iterations the resultant optimum mass and stiffness distributions were obtained which reduced the vertical hub shears by about 50 per cent. Bennet also studied the optimum rotor blade geometric pitch distribution such that it will generate a specified thrust with minimum hovering power. He suggests that applying the non-linear programming algorithms to conventional helicopter engineering analysis will improve the detail design process.

Another modern structural optimization technique applied to the vibration reduction of helicopter rotor blades in forward flight has been investigated by Friedmann and Shanthakumaran [70]. In this optimization problem, the objective function minimised the oscillatory vertical hub shears or the hub rolling moments at one particular advance ratio. The aeroelastic stability

margins in hover together with blade fundamental frequency placement were used as constraints. The aeroelastic stability and response analysis based on a fully coupled flap-lag-torsional analysis for the hingeless rotor blade was utilised. Two uncoupled modes were used to represent each of the elastic degrees of freedom. Furthermore, the structural part of the blade cross-section was represented by a thin walled, single cell, rectangular box section. The dimensions of this box (breadth, height and thickness of each side) at each span station of the blade were treated as a design variable. The non-structural masses at three outboard segments were considered as additional design variables. The sequence of unconstrained minimisation techniques based on extended interior penalty function formulation was used for the optimization algorithm. The optimization results for the hingeless rotor indicated conclusively that non-structural mass located in the outboard one third portion of the blade and distributed along the elastic axis provides a good practical means for vibration reduction. This reduction of the order of 15 - 40 per cent was achieved by a relatively small modification of the original design. The authors also concluded that the use of structural optimization techniques can yield substantial practical benefits in the blade design process which can be easily implemented by helicopter companies.

2.2.6. Remarks Concerning Literature Survey:

As indicated by the previous literature review, no substantial research on designing rotor blades for minimum vibration levels exists. The major portion of the current research effort to reduce successive helicopter vibration levels has been directed towards the use of various control devices. These control devices may be ingenious though all suffer a significant weight penalty. Furthermore, the design and manufacture of such control systems will be added to the overall cost.

The current state of expertise in helicopter technology today is that the rotor blades could be structurally "tailored" in order to minimise the oscillatory input to the fuselage from the rotor head. There are several reasons for this possibility as follows. Firstly, helicopter rotor blades for both main rotors and tail rotors are now being fabricated from composite material [71]. This implies that the designer can choose, with certain restrictions, the optimum EI-distribution. Furthermore, the lightness of the composite material for the main rotor blades usually necessitates the addition of weight to give sufficient autorotational blade inertia. Thus, there is a considerable amount of flexibility as to how this weight may be distributed. Secondly, the methods of structural optimization and parameter identification which are reviewed in the last section are now refined to the point where they can be efficiently applied to the blade structure. However, the aim of the present study is

to utilise recent advances of these structural optimization methods to develop a rational design procedure for the rotor blades. In this design procedure, the mass and stiffness distributions are to be tailored in such a way so that the oscillatory inputs from the rotor head to the fuselage (pitching and rolling moments) are minimised. Clearly, this method does not require any expenditure for hardware design and installation, such as required by the previous control devices.

3. THE ROTOR BLADE FINITE ELEMENT FLAPPING MODEL

The blade is assumed to be rigid chordwise so that its motion is represented by the bending and rotation of a slender beam. To prevent the coupling between bending and torisonal vibration it can be assumed that the mass centre and shear centre coincide. Therefore the deformation is limited to bending only in the direction of the principal axes of the cross-section. The transverse shear and rotatory inertia have been neglected.

3.1. Non-Rotating Blade

The hingeless rotor is considered as a cantilever beam rigidly attached to the hub. A finite beam element sub-division is shown in Figure 8 and the beam element considered is shown in Figure 9. It has two structural nodes, each possessing two degrees of freedom, and the nodal variables are the transverse displacement $v(x)$ and the cross-section rotation $\theta(x)$.

3.1.1. Element stiffness and Mass Matrices:

The derivation of the element stiffness and mass matrices are based on the beam element properties (mass and flatwise stiffness distribution) and it is assumed to vary linearly with distance along the axis of the beam element. The transverse displacement may be represented approximately by

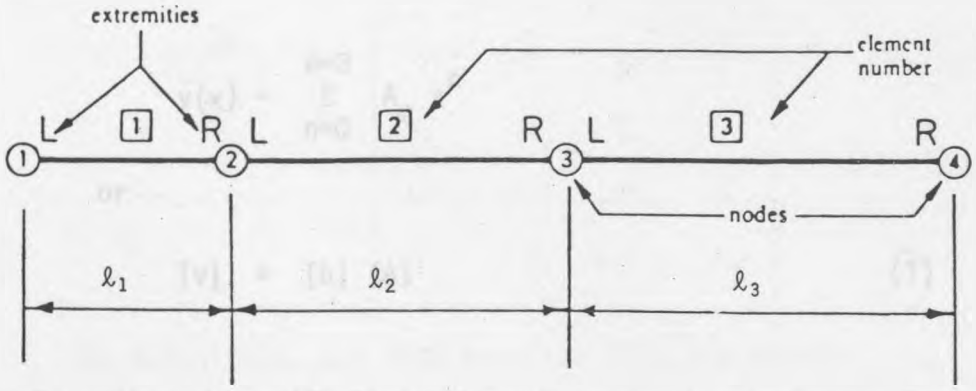

Figure 8 Finite Element Model

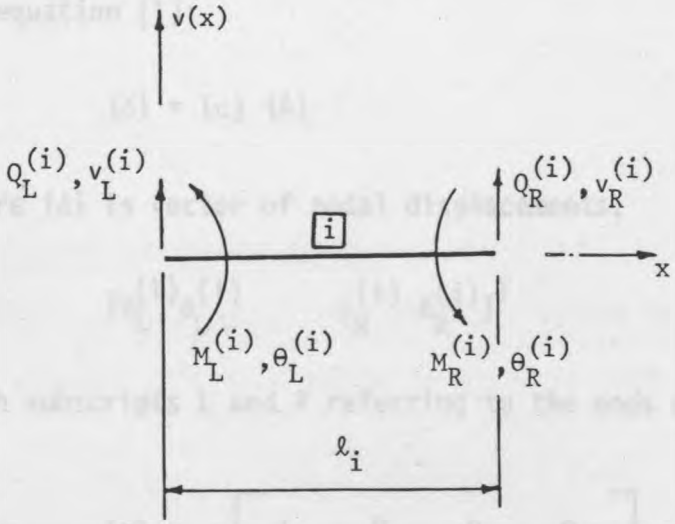

Figure 9 Forces and Displacements at the Extremities of the Beam Element.

a cubic polynomial, that is:

$$v(x) = \sum_{n=0}^{n=3} A_n x^n$$

or

$$[v] = [b] \{A\} \qquad (1)$$

where the vector {A} lists the unknown constants $A_o \ldots\ldots A_3$.

The cross section rotation is approximately equal to the slope $\partial v(x)/\partial x$ of the transverse displacement, i.e.:

$$[\theta] = [Y] \{A\} \qquad (2)$$

The extremity displacements of i <u>th</u> element are now obtained by substituting the co-ordinate of the extremities in equation (1):

$$\{\delta\} = [c] \{A\} \qquad (3)$$

where $\{\delta\}$ is vector of nodal displacements,

$$[v_L^{(i)} \theta_L^{(i)} \quad v_R^{(i)} \theta_R^{(i)}]^T$$

with subscripts L and R referring to the ends x = 0 and $x = \ell_i$ and

$$[c] = \begin{bmatrix} 1 & 0 & 0 & 0 \\ 0 & 1 & 0 & 0 \\ 1 & \ell_i & \ell_i^2 & \ell_i^3 \\ 0 & 1 & 2\ell_i & 3\ell_i^2 \end{bmatrix} \qquad (4)$$

whose inverse is:

$$[c]^{-1} = \frac{1}{\ell_i^3} \begin{bmatrix} \ell_i^3 & 0 & 0 & 0 \\ 0 & \ell_i^3 & 0 & 0 \\ -3\ell_i & -2\ell_i^2 & 3\ell_i & -\ell_i^2 \\ 2 & \ell_i & -2 & \ell_i \end{bmatrix} \qquad (5)$$

By definition, and from equation (1), the strain $d^2v(x)/dx^2$ can be written as:

$$\{\varepsilon\} = [0 \quad 0 \quad 2 \quad 6x] \{A\}$$

Introducing $[H] = [0 \quad 0 \quad 2 \quad 6x]$

then equation (3) is given by:

$$\{\varepsilon\} = [B_i] \{\delta\}$$

where

$$[B_i] = [H][c]^{-1} \qquad (6)$$

i) Element Stiffness Matrix:

In standard formulation of plain stress or strain the i th element stiffness matrix is given by [72] as:

$$[k_i] = \int_{vol} [B_i]^T [D_i] [B_i] \, d(vol) \qquad (7)$$

where $[D_i]$ is the elasticity matrix which relates the stress to the strain.

For an element in which the flatwise stiffness $s_i(x)$ varies linearly with distance along the beam one may write:

$$s_i(x) = s_L^{(i)} + \alpha_i x \tag{8}$$

where

$$\alpha_i = \frac{s_R^{(i)} - s_L^{(i)}}{\ell_i}$$

Since the strain within a beam in bending is defined through its curvature, the elasticity matrix yields:

$$[D_i] = s_i(x) \tag{9}$$

Substituting the matrices of equations (6) and (9) into equation (7), it can be verified by matrix multiplication that the bending stiffness of the i <u>th</u> element is given by:

$$k_i = \frac{1}{\ell_i^3} \begin{bmatrix} k_{11} & & \text{Symm.} & \\ k_{21} & k_{22} & & \\ k_{31} & k_{32} & k_{33} & \\ k_{41} & k_{42} & k_{43} & k_{44} \end{bmatrix} \tag{10}$$

where

$$k_{11} = (12\, s_L^{(i)} + 6\alpha_i \ell_i)$$

$$k_{21} = (6\, s_L^{(i)} + 2\alpha_i \ell_i)\ell_i$$

$$k_{31} = -(12\, s_L^{(i)} + 6\alpha_i \ell_i)$$

$$k_{41} = (6\ s_L^{(i)} + 4\alpha_i \ell_i)\ell_i$$

$$k_{22} = (4\ s_L^{(i)} + \alpha_i \ell_i)\ell_i^2$$

$$k_{32} = -(6\ s_L^{(i)} + 2\alpha_i \ell_i)\ell_i$$

$$k_{42} = (2\ s_L^{(i)} + \alpha_i \ell_i)\ell_i^2$$

$$k_{33} = (12\ s_L^{(i)} + 6\alpha_i \ell_i)$$

$$k_{43} = -(6\ s_L^{(i)} + 4\alpha_i \ell_i)\ell_i$$

$$k_{44} = (4\ s_L^{(i)} + 3\alpha_i \ell_i)\ell_i^2$$

ii) Element Mass Matrix:

For an element subjected to a distributed force, the virtual work done by this force is equal to that done by an equivalent external nodal force vector $\{p_e\}$ in moving through a nodal displacement $\{\Delta\delta\}$. Consequently $\{p_e\}$ is given by [72] as:

$$\{p_e\} = [m_i]\{\ddot{\delta}\}$$

in which

$$[m_i] = [c^{-1}]^T \int_0^L [b]^T m_i(x)[b]\, dx [c^{-1}] \qquad (11)$$

The mass distribution $m_i(x)$ varies linearly with distance along the beam element, therefore:

$$m_i(x) = m_L^{(i)} + \gamma_i\, x \qquad (12)$$

where

$$\gamma_i = \frac{m_R^{(i)} - m_L^{(i)}}{\ell_i}$$

Substituting the matrix [b] of equation (1) and equation (12) into equation (11) and carrying out the indicated matrix multiplication, the i th element mass matrix can be written as:

$$[m_i] = \frac{1}{40320}\begin{bmatrix} m_{11} & & & \\ m_{21} & m_{22} & \text{Symm.} & \\ m_{31} & m_{32} & m_{33} & \\ m_{41} & m_{42} & m_{43} & m_{44} \end{bmatrix} \quad (13)$$

where

$$m_{11} = (14976m_L^{(i)} + 3456\gamma_i\ell_i)\ell_i$$

$$m_{21} = (2112m_L^{(i)} + 672\gamma_i\ell_i)\ell_i^2$$

$$m_{31} = (5184m_L^{(i)} + 2592\gamma_i\ell_i)\ell_i$$

$$m_{41} = -(1248m_L^{(i)} + 576\gamma_i\ell_i)\ell_i^2$$

$$m_{22} = (384m_L^{(i)} + 144\gamma_i\ell_i)\ell_i^3$$

$$m_{32} = (1248m_L^{(i)} + 672\gamma_i\ell_i)\ell_i^2$$

$$m_{42} = -(288m_L^{(i)} + 144\gamma_i\ell_i)\ell_i^3$$

$$m_{33} = (14976m_L^{(i)} + 11520\gamma_i\ell_i)\ell_i$$

$$m_{43} = -(2112m_L^{(i)} + 1440\gamma_i\ell_i)\ell_i^2$$

$$m_{44} = (384m_L^{(i)} + 240\gamma_i\ell_i)\ell_i^3$$

3.2. Rotating Rotor Blade

The rotor blade is now considered as a cantilever beam mounted on the periphery of a rotating hub of radius r_o as shown in Figure 10. For a beam undergoing lateral vibration, v(x) is the deflection in the vertical direction of an arbitrary point at a distance x from the hub, on the middle plane of the beam. The hub is assumed to be rigid.

Under the effect of rotational speed (Ω) the blade is stiffened due to additional stresses created by centrifugal forces.

3.2.1. Centrifugal Forces Acting on the Blade

Consider the finite element as shown in Figure 11. The centrifugal force acting on any section at distance x from the left end of i th element is given by [73] as:

$$F_x^{(i)} = \int_x^{\ell_i} \Omega^2 m_i(x)(r_o + p_i \ell_i + x)dx + \int_{(p_i+1)\ell_i}^{L} \Omega^2 m_i(x')(r_o + x')dx' \qquad (14)$$

where

$p_i = \left(\sum_{K=1}^{K=i-1} \ell_K\right)/\ell_i$, is the ratio of total length of all elements (before, and not including, the i th element under consideration), to the i th element length.

In the above equation, the first term represents the centrifugal force associated with the portion of the element

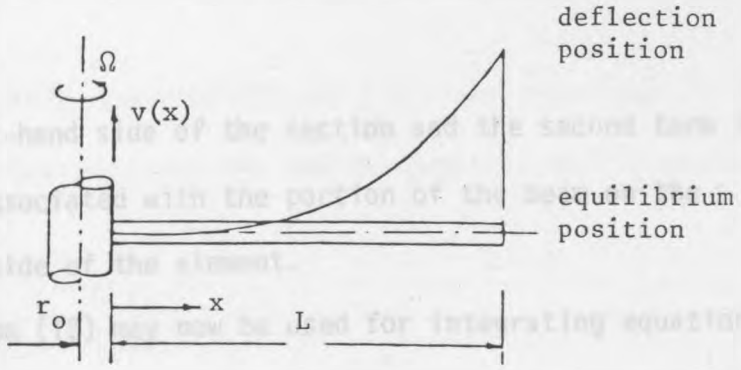

Figure 10 Rotating Radial Beam.

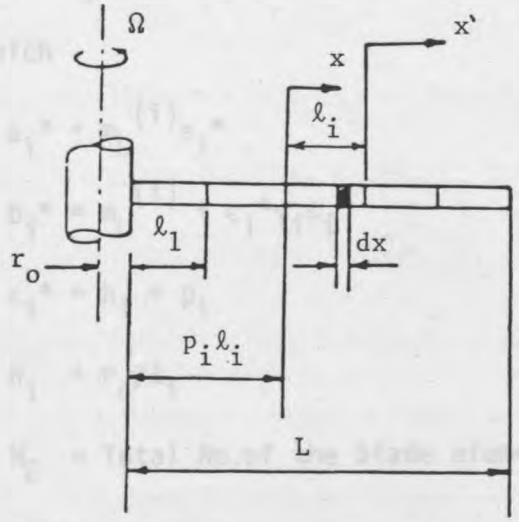

Figure 11 Schematic Representation of the Finite Element Location.

on the right-hand side of the section and the second term is the force associated with the portion of the beam on the right-hand side of the element.

Equation (12) may now be used for integrating equation (14):

$$F_x^{(i)} = \Omega^2 [-a_i^* \ell_i x - \frac{1}{2} b_i^* x^2 - \frac{1}{3} \gamma_i x^3 + c_i] \qquad (15)$$

where

$$c_i = [a_i^* + \frac{1}{2} b_i^* - \frac{1}{3} \gamma_i \ell_i] \ell_i^2 + \sum_{p=i+1}^{p=N_E} [a_p^* + \frac{1}{2} b_p^* + \frac{1}{3} \gamma_p \ell_p] \ell_p^2$$

in which

$$a_i^* = m_L^{(i)} \varepsilon_i^*$$

$$b_i^* = m_L^{(i)} + \varepsilon_i^* \gamma_i \ell_i$$

$$\varepsilon_i^* = h_i + p_i$$

$$h_i = r_o / \ell_i$$

and N_E = Total No.of the blade elements.

3.2.2. Centrifugal Element Stiffness Matrix

For the slender beam the centrifugal stiffness of the i th element can be written as [73] :

$$[G_i] = [c^{-1}]^T \int_0^{\ell_i} [Y]^T F_x^{(i)} [Y] dx [c^{-1}] \qquad (16)$$

Substituting equation (2) and (15) into the above equation and carrying out the indicated matrix multiplication yields:

$$[G_i] = \frac{\Omega^2 \ell_i}{12600} \begin{bmatrix} G_{11} & & & \\ G_{21} & G_{22} & & \\ G_{31} & G_{32} & G_{33} & \\ G_{41} & G_{42} & G_{43} & G_{44} \end{bmatrix} \tag{17}$$

where

$$G_{11} = (-7560a_i^* - 2160b_i^* - 900\gamma_i\ell_i + 15120c_i^*)$$

$$G_{21} = (-1260a_i^* - 450b_i^* - 210\gamma_i\ell_i + 1260c_i^*)\ell_i$$

$$G_{31} = (7560a_i^* + 2160b_i^* + 900\gamma_i\ell_i - 15120c_i^*)$$

$$G_{41} = (180b_i^* + 150\gamma_i\ell_i + 1260c_i^*)\ell_i$$

$$G_{22} = (-420a_i^* - 120b_i^* - 55\gamma_i\ell_i + 1680c_i^*)\ell_i^2$$

$$G_{32} = (1260a_i^* + 450b_i^* + 210\gamma_i\ell_i - 1260c_i^*)\ell_i$$

$$G_{42} = (210a_i^* + 90b_i^* + 55\gamma_i\ell_i - 420c_i^*)\ell_i^2$$

$$G_{33} = (-7560a_i^* - 2160b_i^* - 900\gamma_i\ell_i + 15120c_i^*)$$

$$G_{43} = (-180b_i^* - 150\gamma_i\ell_i - 1260c_i^*)\ell_i$$

$$G_{44} = (-1260a_i^* - 540b_i^* - 325\gamma_i\ell_i + 1680c_i^*)\ell_i^2$$

in which

$$c_i^* = c_i/\ell_i^2$$

3.3. Assembly of the Overall Mass and Stiffness Matrices

Having calculated the mass and stiffness (structural plus centrifugal) matrices of the individual elements into which the blade is subdivided, the next step is to assemble these to form the overall mass and stiffness matrices for the entire discretized rotor blade.

The overall matrices can be automatically assembled using the computer, according to the sequence of the structural node numbering on the blade, making use of the fact that the nodal displacements must be compatible and the external forces applied at the nodes must be equal to the reactions set up at the extremities attached to those nodes.

In general it is easily verified that, if the discretized structure has a total of n nodes and m degrees of freedom per node, it will have a symmetric overall assembly matrix of order (nm * nm).

Obviously, to prevent the rigid body motion the boundary conditions for the hingeless rotor (as a cantilever beam) under consideration must be applied, i.e.:

$$\{\delta_1\} = 0 \qquad (18)$$

So one may exclude, from the overall assembly matrices, the rows and columns which refer to zero prescribed displacement, equation (18), to obtain the non-singular overall assembly mass and stiffness matrices denoted by [M] and [K] respectively.

A simple, effective and general method that is easily programmed for the computer was written; the "WHBEVS" subroutines listed in Appendix (9) are used, for this purpose.

3.4. Eigenvalues and Eigenvectors of the Rotor Blade

Consider an undamped freely vibrating, linear system given by the homogeneous equations:

$$[M]\{\ddot{\delta}\} + [K]\{\delta\} = 0 \qquad (19)$$

where $\{\delta\}$ is the geometric displacement vector (translational and angular) of the rotor structural nodes. Solving equation (19) leads to the eigenvalues w_{n1}^2, w_{n2}^2..... and eigenvectors $\{\phi^{(1)}\}$, $\{\phi^{(2)}\}$.....

where w_{nj} and $\{\phi^{(j)}\}$ are the j th natural frequency and the corresponding modal shape respectively. These are expressed in the form of a modal matrix $[\phi]$:

$$[\phi] = [\{\phi^{(1)}\}\ \{\phi^{(2)}\},...] \qquad (20)$$

and frequency matrix $[w_{n2}^2]$;

$$[w_n^2] = \text{diag}\,[w_{n1}^2, w_{n2}^2,.....] \qquad (21)$$

The frequency matrix and corresponding modal matrix are calculated by means of a computer program (Appendix (9)) using standard NAG library routines. The routines F01ABF and F02ABF are used for this purpose.

3.5. Mode Shape Function

Rearranging the j th blade mode shape $\{\phi^{(j)}\}$ to have the j th mode shape for the i th element of the blade, say, $\{\phi_i^{(j)}\}$, then for the element no.1 the j th mode shape is:

$$\{\phi_1^{(j)}\} = [v_1 \theta_1 \quad v_2 \theta_2]^T$$

Similarly, for elements nos. 2, 3, ...

$$\{\phi_2^{(j)}\} = [v_2 \theta_2 \quad v_3 \theta_3]^T$$

and

$$\phi_3^{(j)} = [v_3 \theta_3 \quad v_4 \theta_4]^T \text{ , ...}$$

Now, one may write the calculated $\{\phi_i^{(j)}\}$ instead of $\{\delta\}$ of equation (3), i.e.:

$$[c]\{A_i^{(j)}\} = \{\phi_i^{(j)}\} \qquad (22)$$

The above equations are now solved for $\{A_i^{(j)}\}$ to obtain the unknown constants $(A_0 - A_3)$ of the i th element and j th mode.

Then, substituting these values into equation (1), the mode shape function at any distance x of the i th element and j th mode can be determined as:

$$f_{\beta j}^{(i)}(x) = \{1 \quad x \quad x^2 \quad x^3\} \{A_i^{(j)}\} \qquad (23)$$

A block diagram for the calculation sequences is shown in Figure 12 and a subroutine (GAUSEL) is written in Appendix (9) in order to compute the mode shape function of the above equation.

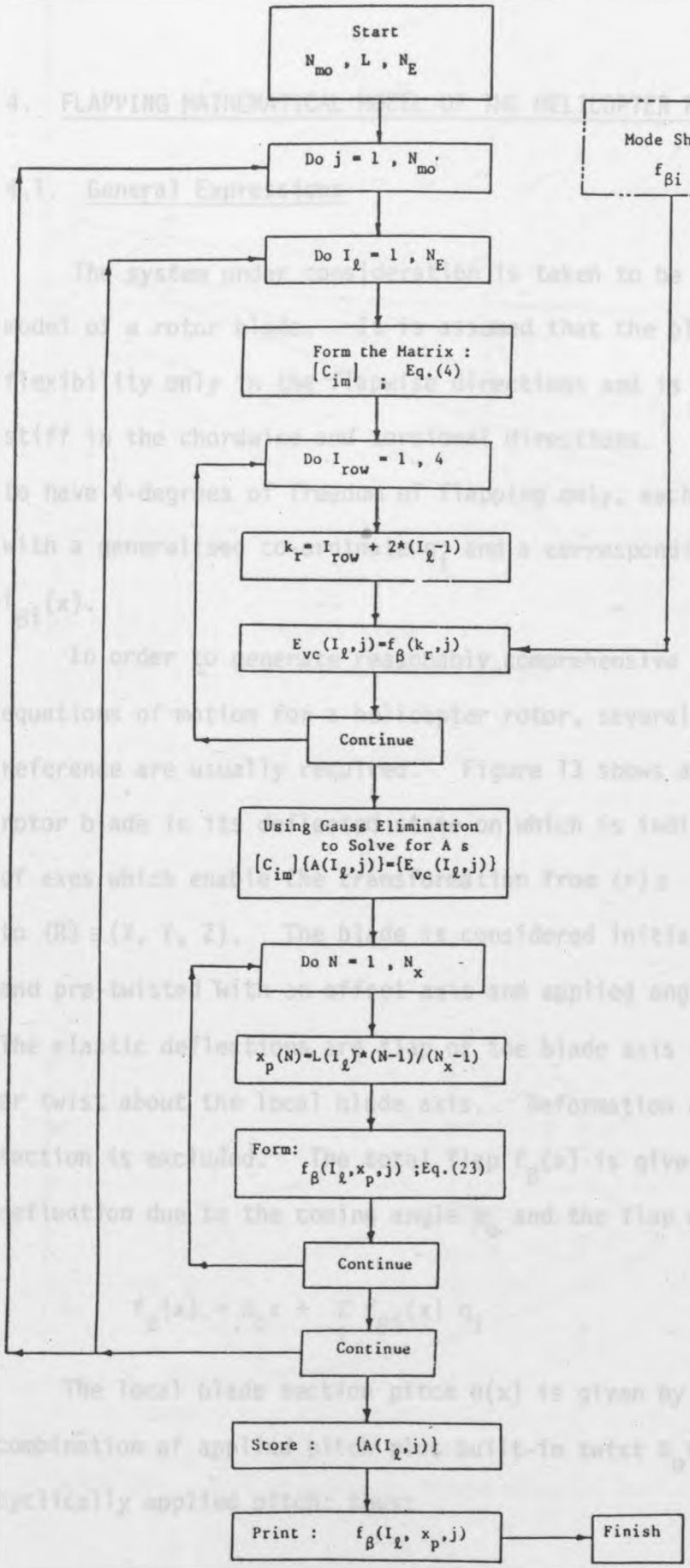

Figure 12 A Block Diagram for Calculating the Mode Shape Function.

4. FLAPPING MATHEMATICAL MODEL OF THE HELICOPTER ROTOR BLADE

4.1. General Expressions

The system under consideration is taken to be a mathematical model of a rotor blade. It is assumed that the blade has flexibility only in the flapwise directions and is infinitely stiff in the chordwise and torsional directions. It is allowed to have 4-degrees of freedom of flapping only, each associated with a generalised co-ordinate q_i and a corresponding mode shape $f_{\beta i}(x)$.

In order to generate reasonably comprehensive aeroelastic equations of motion for a helicopter rotor, several axes of reference are usually required. Figure 13 shows a 'semi-rigid' rotor blade in its deflected state on which is indicated sets of axes which enable the transformation from $\{r\} \equiv (X_3, Y_3, Z_3)$ to $\{R\} \equiv (X, Y, Z)$. The blade is considered initially coned and pre-twisted with an offset axis and applied angle of pitch. The elastic deflections are flap of the blade axis and pitch or twist about the local blade axis. Deformation of the cross section is excluded. The total flap $f_\beta(x)$ is given by the deflection due to the coning angle β_o and the flap modes, i.e.:

$$f_\beta(x) = \beta_o x + \sum_i f_{\beta i}(x)\, q_i \qquad (24)$$

The local blade section pitch $\theta(x)$ is given by a combination of applied pitch plus built-in twist $\theta_o(x)$ and cyclically applied pitch; thus:

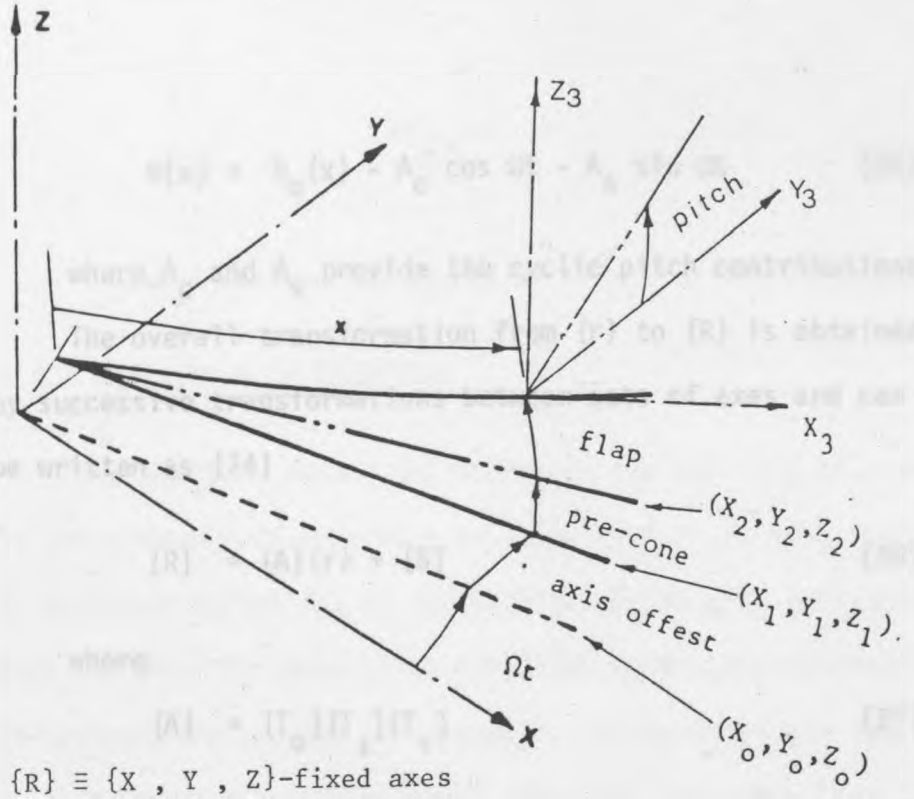

{R} ≡ {X , Y , Z}-fixed axes

{r} ≡ {X_3 , Y_3 , Z_3}-blade coordinates

Figure 13 Sets of Axes

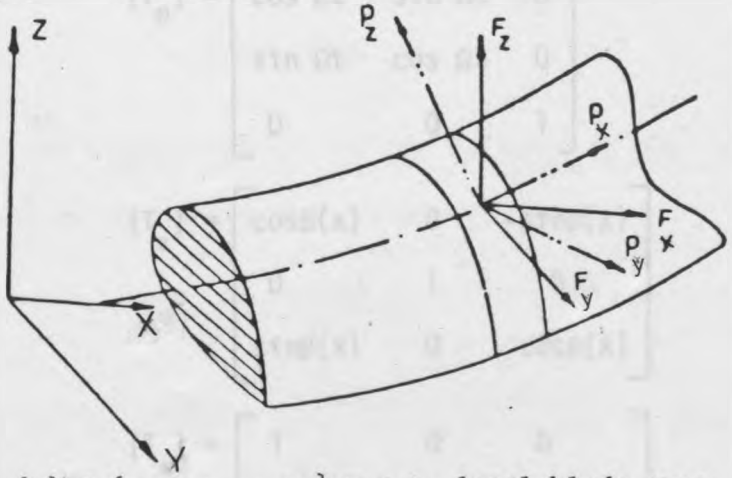

{p} ≡ {p_x , p_y , p_z} w.r.t. local blade axes

{F} ≡ {F_x , F_y , F_z} w.r.t. fixed axes.

Figure 14 Aerodynamic Force Components.

$$\theta(x) = \theta_0(x) - A_c \cos \Omega t - A_s \sin \Omega t \qquad (25)$$

where A_c and A_s provide the cyclic pitch contributions.

The overall transformation from {r} to {R} is obtained by successive transformations between sets of axes and can be written as [74] :

$$[R] = [A]\{r\} + [B] \qquad (26)$$

where

$$[A] = [T_0][T_2][T_4] \qquad (27)$$

$$[B] = [T_0]\{c\} \qquad (28)$$

in which

$$\{c\} = \begin{bmatrix} X - \frac{1}{2}\int_0^X \beta(x)^2 dx \\ Y_0 \\ Z_0 + f_\beta(x) \end{bmatrix} \qquad (29)$$

$$[T_0] = \begin{bmatrix} \cos \Omega t & -\sin \Omega t & 0 \\ \sin \Omega t & \cos \Omega t & 0 \\ 0 & 0 & 1 \end{bmatrix} \qquad (30)$$

$$[T_2] = \begin{bmatrix} \cos\beta(x) & 0 & -\sin\beta(x) \\ 0 & 1 & 0 \\ \sin\beta(x) & 0 & \cos\beta(x) \end{bmatrix} \qquad (31)$$

$$[T_4] = \begin{bmatrix} 1 & 0 & 0 \\ 0 & \cos\theta(x) & -\sin\theta(x) \\ 0 & \sin\theta(x) & \cos\theta(x) \end{bmatrix} \qquad (32)$$

$$\beta(x) = \beta_o + \sum_i \frac{\partial f_{\beta i}(x)}{\partial x} q_i \qquad (33)$$

Y_o and Z_o define the amount of offset of the blade axes.

4.2. Derivation of Equations

The position vector {R} expresses the position of a point in the system with reference to fixed axes. It is a function of position vector {r} of the material point with reference to axes suitable for describing the given modes, the generalised co-ordinate vector {q} corresponding to the modes and the time t. The external instantaneous force per unit area (i.e. aerodynamic pressure in the present case) {F} is a vector with reference to fixed axes. It is a function of {r}, {q}, {$\dot{q}$} and t. Lagrange's equations provide:

$$\frac{d}{dt}\left(\frac{\partial T}{\partial \dot{q}_i}\right) - \frac{\partial T}{\partial q_i} + \frac{\partial u}{\partial q_i} = Q_i, \quad i = 1,\ldots 4 \qquad (34)$$

where

$$T = \tfrac{1}{2}\int \{\dot{R}\}.\{\dot{R}\}dm \qquad (35)$$

is the kinetic energy and the integral is over all elemental mass dm comprising the system.

$$Q_i = \int \{F\}. \frac{\partial \{R\}}{\partial q_i} ds \qquad (36)$$

is the aerodynamic generalised force and is given by the integral over the surface, s, of the system.

u is the potential energy. Structural damping is neglected.

4.2.1. Respective Contributions to the Equation of Motion

The coefficient matrices of the equations of motion contain contributions deriving from the mass and stiffness distributions, and from the aerodynamic force distribution. The evaluation of the separate contributions is described in the following sections. Since the data relating to the blade mass, stiffness and aerodynamic properties are not analytical, it follows that the final evaluation which involves a spanwise integration must be performed numerically. However, unlike a totally computational approach [74, 75], the simplification of the blade mode deflection to pure flapping has permitted a certain amount of analytical treatment, e.g. as in equation (68) below.

(a) Mass Contributions:

The kinetic energy contribution, equation (34) can be shown as:

$$\frac{d}{dt}\left(\frac{\partial T}{\partial \dot{q}_i}\right) - \frac{\partial T}{\partial q_i} = \int\left[\frac{d}{dt}\left(\{\dot{R}\}.\frac{\partial \{\dot{R}\}}{\partial \dot{q}_i}\right) - \{\dot{R}\}.\frac{\partial \{\dot{R}\}}{\partial q_i}\right] dm \qquad (37)$$

Applying the Taylor series expansion and substituting for the operator $\frac{d}{dt}$ by:

$$\frac{d}{dt} = \left[\frac{\partial}{\partial t} + \sum_i \dot{q}_i \frac{\partial}{\partial q_i}\right],$$

gives:

$$[p_m]\{\ddot{q}_i\} + [Q_m]\{\dot{q}_i\} + [R_m]\{q_i\} + \{S_{mi}\} \qquad (38)$$

where

$[p_m]$, $[Q_m]$, $[R_m]$ and $\{S_{mi}\}$ are the mass, gyrodynamic, centrifugal stiffness matrices and contributions to steady state respectively. They are found to be [74]:

$$[p_m] = \int[(\frac{\partial \{R\}}{\partial q_i}) \cdot (\frac{\partial \{R\}}{\partial q_j})]\, dm \tag{39}$$

$$[Q_m] = 2\int[(\frac{\partial \{R\}}{\partial q_i}).(\frac{\partial^2 \{R\}}{\partial q_j \partial t})]\, dm \tag{40}$$

$$[R_m] = \int[(\frac{\partial \{R\}}{\partial q_i}).(\frac{\partial^3 \{R\}}{\partial q_j \partial^2 t}) + (\frac{\partial^2 \{R\}}{\partial q_i \partial q_j}).(\frac{\partial^2 \{R\}}{\partial t^2})]\, dm \tag{41}$$

$$\{S_{mi}\} = \int[(\frac{\partial \{R\}}{\partial q_i}).(\frac{\partial^2 \{R\}}{\partial t^2})]\, dm \tag{42}$$

Inspection of equations (39) to (42) shows that the integral of the elemental mass dm times the dot product of two vectors has a particular differential of $\{R\}$. If the cyclic pitch is not applied (i.e. fixed blade pitch) $[T_o]$ is the only time varying component in matrices [A] and [B] of equations (27) and (28).

So $\partial\{R\}/\partial t$ and $\partial^2\{R\}/\partial t^2$ can be written as:

$$\frac{\partial \{R\}}{\partial t} = \frac{\partial [T_o]}{\partial t}\{c\}$$

$$= \Omega[S_1]\{c\} \tag{43}$$

and

$$\frac{\partial^2 \{R\}}{\partial t^2} = \Omega^2[S_2]\{c\} \tag{44}$$

where

$$[S_1] = \begin{bmatrix} -\sin \Omega t & -\cos \Omega t & 0 \\ \cos \Omega t & -\sin \Omega t & 0 \\ 0 & 0 & 1 \end{bmatrix} \tag{45}$$

$$[S_2] = \begin{bmatrix} -\cos \Omega t & \sin \Omega t & 0 \\ -\sin \Omega t & -\cos \Omega t & 0 \\ 0 & 0 & 1 \end{bmatrix} \tag{46}$$

Now, the mass point in the blade under investigation is taken to be concentrated at the origin of the blade axes; thus, position vector {r} is zero, and all contributions to {R} and its differentials involving [A] disappear. Thus, one may consider only the [B] part of equation (26), i.e.:

$$\frac{\partial \{R\}}{\partial q_i} = [T_o] \frac{\partial \{c\}}{\partial q_i} \tag{47}$$

From equation (44) and equation (47)

$$\left(\frac{\partial \{R\}}{\partial q_i}\right).\left(\frac{\partial^2 \{R\}}{\partial t^2}\right) = \Omega^2 [S_2]^T \{c\}^T [T_o] \frac{\partial \{c\}}{\partial q_i} \tag{48}$$

Ignoring the blade offsets Y_o, Z_o and neglecting the second order quantities, the differentials $\partial\{c\}/\partial q_i$ and $\partial^2\{c\}/\partial q_i \partial q_j$ can be written as:

$$\frac{\partial \{c\}}{\partial q_i} = \left[\left(-\int_o^x \beta(x) \frac{\partial f\beta_i(x)}{\partial x}\right), 0, f_{\beta i}(x)\right]^T \tag{49}$$

and

$$\frac{\partial^2\{c\}}{\partial q_i \partial q_j} = [(-\int_0^x \frac{\partial f_{\beta i}}{\partial x}\frac{\partial f_{\beta j}}{\partial x}),\ 0,\ 0]^T \qquad (50)$$

i) Inertia Matrix $[p_m]$:

Substituting equation (47) into equation (39) leads to

$$[p_m] = \int_0^L \{\frac{\partial\{c\}}{\partial q_i}\}^T [T_o]^T [T_o]\{\frac{\partial\{c\}}{\partial q_i}\}dx$$

The inertia matrix can be obtained by using equation (49) and carrying out the indicated matrix multiplication for the above equation.

$$[p_m] = \int_0^L m(x)\ f_{\beta i}(x) f_{\beta j}(x)\ dx \qquad (51)$$

ii) Gyrodynamic Matrix $[Q_m]$:

Using equations (43) and (47) and performing the scalar product given by equation (40), the gyrodynamic matrix can be written as:

$$[Q_m] = 2\Omega\int_0^L \{\frac{\partial\{c\}}{\partial q_i}\}^T [T_o]^T [S_1]\{\frac{\partial\{c\}}{\partial q_j}\}\ dm$$

Substituting equations (30), (45) and (49) into the above equation and neglecting the second order quantities yields:

$$[Q_m] = 0 \qquad (52)$$

This simply confirms that in deflections involving only pure flapping modes, there are no Coriolis couplings.

iii) Centrifugal Stiffness Matrix $[R_m]$:

Introduction of equations (46) to (50) in the centrifugal stiffness equation (41) leads to:

$$[R_m] = \Omega^2 \int_0^L m(x) \{\frac{\partial \{c\}}{\partial q_i}\}^T [T_o]^T [S_2] \{\frac{\partial \{c\}}{\partial q}\} dx$$

$$+\Omega^2 \int_0^L m(x) \{\frac{\partial^2 \{c\}}{\partial q_i \partial q_j}\}^T [T_o]^T [S_2] \{c\} dx$$

Neglecting the second order in q_i, the centrifugal stiffness matrix becomes:

$$[R_m] = \Omega^2 \int_0^L m(x) \times (\int_0^x \frac{\partial f_{\beta i}}{\partial x} \frac{\partial f_{\beta j}}{\partial x} dx) dx \qquad (53)$$

iv) Steady State Mass Contribution $\{S_{mi}\}$:

The steady state terms may be taken as the steady displacement case or the pre-cone rotating configuration, i.e. $q_i = 0$.

Substituting equations (44) and (47) into equation (42) the steady state contribution becomes:

$$\{S_{mi}\} = \Omega^2 \int_0^L \{\frac{\partial \{c\}}{\partial q_i}\}^T [T_o]^T [S_2] \{c\} m(x) \, dx$$

Applying $q_i = 0$ to equations (29) and (49) and substituting into the above equation. Neglecting the second order terms in β_o, the steady state term in the i th equation due to mass can

be written as:

$$\{S_{mi}\} = \Omega^2 \int_0^L m(x) \times \beta_o f_{\beta i}(x)\, dx \qquad (54)$$

(b) Structural Stiffness Contributions:

Usually in helicopter dynamic analyses, it is a relatively simple matter to form an expression for the strain energy u in terms of the generalised co-ordinates q_i.

It is assumed that the blade properties are provided as spanwise distributions of bending flexibility ($EI_{yy}(x)$) in flatwise direction whilst the blade is infinitely stiff in the edgewise and torsional senses.

For a symmetric blade section the principal axes are aligned with the flat and edgewise blade axes, but the flap and lagwise directions are not normally coincident, so it is necessary to resolve the modal contributions through the local blade pitch angle in order to build up the strain energy terms. This leads to difficulties, which are explained and resolved in Appendix (1). As a result the bending strain energy in terms of the given mode shapes may be written in the much simplified form:

$$u = \tfrac{1}{2} \int_0^L EI_{yy}(x)\, f''_{\beta i}(x)^2 dx \qquad (55)$$

The structural stiffness contribution to the equations of motion is given by [74]:

$$[R_s] = \frac{\partial^2 u}{\partial q_i \partial q_j} \qquad (56)$$

So the differentiations necessary are with respect to the mode shapes themselves, and it follows that:

$$[R_s] = [\int_0^L EI_{yy}(x) f''_{\beta i}(x) f''_{\beta j}(x)\, dx] \qquad (57)$$

(c) Aerodynamic Contributions:

Equation (36) is an expression for the generalised force in terms of the dot product of two vectors. One is a certain differential of {R} and the other is a pressure vector {F} with reference to fixed axes. The pressure components with respect to local blade axes are shown in Figure 14. The required transformation between {F} and {p} is made through the matrix [A] of equation (26), i.e.:

$$\{F\} = [A]\,\{p\}$$

Therefore, equation (36) becomes:

$$Q_i = [\int \{p\}^T\, [A]^T \{\frac{\partial \{R\}}{\partial q_i}\}\, ds] \qquad (58)$$

The taper on the blade is usually very small, so the component p_x of the pressure vector is assumed zero. Thus the above equation can be written as:

$$Q_i = [\int D_y^{01} \int p_y dy dx + \int D_z^{01} \int p_z dy dx] \qquad (59)$$

where the integrals are over the lifting surface and the $\{D^{01}\}$ coefficients are given by:

$$\{D^{01}\} = [A]^T \left\{\frac{\partial \{R\}}{\partial q_i}\right\}$$

$$= [T_4]^T [T_2]^T \left\{\frac{\partial \{c\}}{\partial q_i}\right\}$$

Using equations (30), (31) and (49) gives:

$$\begin{bmatrix} D_x^{01} \\ D_y^{01} \\ D_z^{01} \end{bmatrix} = \begin{bmatrix} \sin \beta(x)\ f_{\beta i}(x) \\ \sin \theta(x)\ \cos\beta(x)\ f_{\beta i}(x) \\ \cos \theta(x)\ \cos\beta(x)\ f_{\beta i}(x) \end{bmatrix} \qquad (60)$$

The aerodynamic force would normally be provided as a lift, drag and moment on a (non-deformable) aerofoil section as shown in Figure 15. For the sake of simplicity, the lift may be assumed to act at the reference axis and the drag may be neglected. The dy integrals (over the chord) are identified as:

$$\begin{aligned} \int p_z dy &= L(x) \cos \alpha(x) \\ \int p_y dy &= L(x) \sin \alpha(x) \\ \int p_z y dy &\cong 0 \end{aligned} \qquad (61)$$

where

$\alpha(x)$ is the section incidence

and $L(x)$ is the section instantaneous aerodynamic lift.

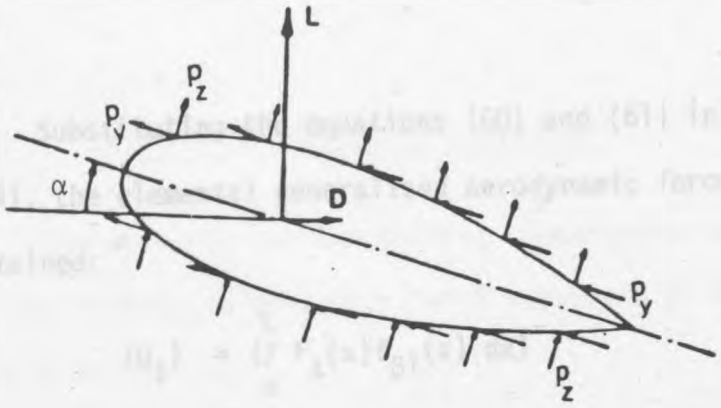

Figure 15 Aerodynamic Resultants.

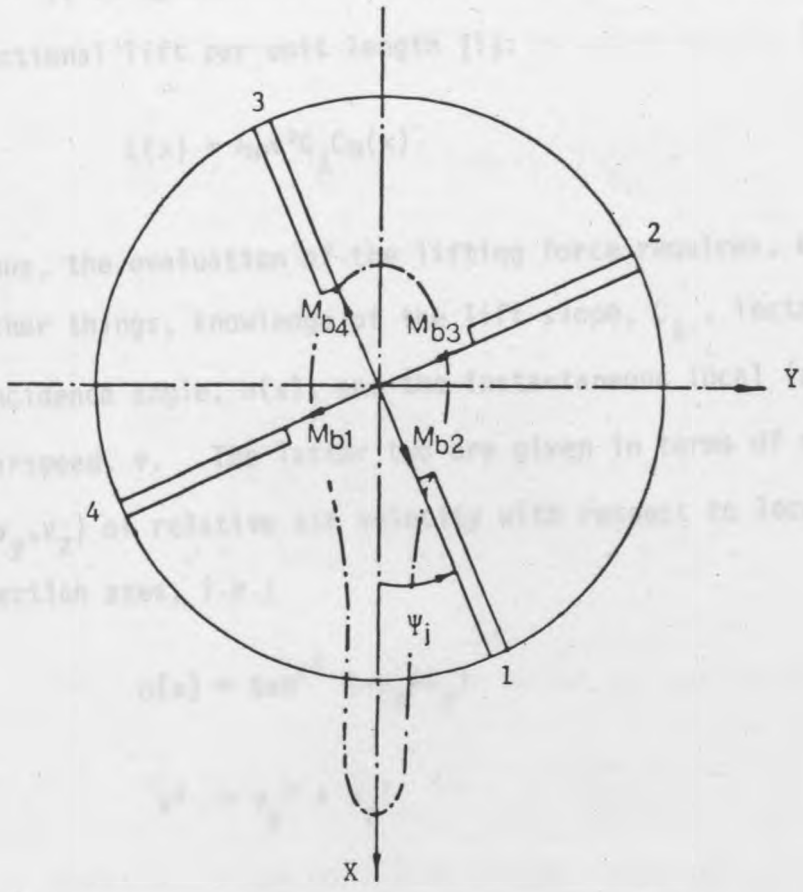

Figure 16 Blades Root Moment Decomposition.

Substituting the equations (60) and (61) into equation (59), the elemental generalised aerodynamic force can be obtained:

$$\{Q_i\} = \{\int_0^L F_\ell(x) f_{\beta i}(x)\, dx\} \qquad (62)$$

where

$$F_\ell(x) = L(x)\cos\beta(x)\cos(\alpha(x)-\theta(x)) \qquad (62a)$$

4.3. Use of Strip Theory

It is convenient to apply strip theory in obtaining the sectional lift per unit length [1]:

$$L(x) = \tfrac{1}{2}\rho v^2 C_\ell C\alpha(x) \qquad (63)$$

Thus, the evaluation of the lifting force requires, amongst other things, knowledge of the lift slope, C_ℓ, instantaneous incidence angle, $\alpha(x)$, and the instantaneous local (relative) airspeed, v. The latter two are given in terms of components (v_y, v_z) of relative air velocity with respect to local blade section axes, i.e.:

$$\alpha(x) = \tan^{-1}(-v_z/v_y)$$

$$v^2 = v_y^2 + v_z^2 \qquad (64)$$

4.3.1. Relative Air Velocity Components

The absolute section velocity components, at the origin of the section co-ordinates, with reference to fixed axes can be written as:

$$\frac{d}{dt}\{R\} = \frac{d}{dt}[[A]\{r\} + [B]]$$

For the point of interest, i.e. $\{r\} = 0$

$$\frac{d}{dt}\{R\} = [\frac{\partial}{\partial t} + \sum_i \dot{q}_i \frac{\partial}{\partial q_i}] [B]$$

Substituting equation (28) in the above equation, gives:

$$\frac{d}{dt}\{R\} = [\dot{T}_o]\{c\} + \sum_i \{\dot{q}_i\}[T_o]\{\frac{\partial \{c\}}{\partial q_i}\}$$

Using equation (49) and neglecting the higher order terms leads to:

$$\{\dot{R}\} = \begin{bmatrix} -\Omega \times \sin \Omega t \\ \Omega \times \cos \Omega t \\ \sum_i \dot{q}_i f_{\beta i}(x) \end{bmatrix} \qquad (65)$$

The local air mass velocity vector {u} can be written as:

$$\{u\} = [V_f \quad 0 \quad -u]^T \qquad (66)$$

where V_f is the helicopter flight speed and

u is the induced velocity down through the rotor.

Then, the total relative velocity $\{V_r\}$ at the blade section with respect to fixed axes is:

$$\{V_r\} = \{u\} - \{\dot{R}\}$$

Substituting equations (65) and (66) into the above equation yields:

$$\{V_r\} = \begin{bmatrix} V_f + \Omega x \sin \Omega t \\ - \Omega x \cos \Omega t \\ - u - \sum_i \dot{q}_i f_{\beta i}(x) \end{bmatrix} \tag{67}$$

The total relative velocity with reference to blade axes is denoted by the vector $\{v\}$. Then, the required transformation between $\{v\}$ and $\{V_r\}$ is made through the matrix [A], i.e.:

$$\{v\} = [A]^T \{V_r\}$$

Performing the matrix multiplication of equation (27) and substituting the result and equation (67) into the above equation provides the relative air velocity components as:

$$\begin{bmatrix} v_x \\ v_y \\ v_z \end{bmatrix} = \begin{bmatrix} V_f \cos \Omega t \cos \beta(x) - u_f \sin \beta(x) \\ -v_1(x) \cos \theta(x) - v_2(x) \sin \theta(x) \\ v_1(x) \sin \theta(x) - v_2(x) \cos \theta(x) \end{bmatrix} \tag{68}$$

where

$$v_1(x) = V_f \sin \Omega t + \Omega x$$

$$v_2(x) = V_f \cos \Omega t \sin \beta(x) + u_f \cos \beta(x)$$

$$u_f = u + \sum_i \dot{q}_i f_{\beta i}(x)$$

$$\theta(x) = \theta_t(x) + \Theta - A_c \cos \Omega t - A_s \sin \Omega t$$

in which Θ, A_c and A_s can be obtained by solving the trim case.

Finally, to summarise, knowledge of v_x, v_y and v_z enables v and $\alpha(x)$ to be formed using equation (64), and hence L(x) in equation (63), and subsequently the vector of generalised aerodynamic forces in equation (62).

4.4. The Trim Calculations

The trimmed flight condition of the helicopter is determined when the control setting is such as to achieve equilibrium of the net forces and moments acting on the helicopter.

Owing to the complexity of the trim case [77] the problem will be examined through quantitative calculations based on a specific rotor system and simplifying assumptions. These assumptions are as follows [78]:

1. The helicopter is in straight and level steady flight.
2. The rotor hub and helicopter centre of gravity coincide, i.e. the whole aircraft is represented by

a point mass coinciding with the hub.

3. The average pitch and roll moments are zero (averaged over one revolution).
4. The effect of lead-lag degree of freedom on the trim state of the rotor is neglected.
5. Tail, fuselage moments and side force components are neglected.
6. Various forces used are considered to be average forces over one revolution.
7. The total geometric pitch angle is assumed to be given by equation (25).

Consequently, there are two types of trim calculation which are commonly used [78]. The first type simulates the actual forward flight conditions; the weight of the helicopter is approximately equal to the total thrust and vertical and horizontal force equilibrium is maintained. In addition, zero pitching and rolling moments on the rotor are maintained. The second type simulates conditions under which a rotor would be tested in the wind tunnel. Horizontal and vertical force equilibrium is not required because the rotor is mounted on a supporting structure. Only the requirement of zero pitching and rolling moments on the rotor is imposed.

In calculating the trim state of the rotor, inplane forces and the fuselage drag have been neglected. The requirements of equilibrium for trim may be given simply as follows:

The average total lift of the rotor must equal the helicopter weight over one revolution, i.e.:

$$L_{tot)av} = W \tag{69}$$

and the average rolling and pitching moments must equal zero;

$$\begin{aligned} M_{x)av} &= 0 \\ M_{y)av} &= 0 \end{aligned} \tag{70}$$

In order to calculate the expressions for the total lift, L_{tot}, rolling moment M_x and pitching moment M_y one may write:

$$L_i(\psi_j) = \int_0^L L(x)\, dx, \quad j = 1,....N_\psi \tag{71}$$

and

$$M_{bi}(\psi_j) = \int_0^L L(x)\, dx \qquad j = 1,....N_\psi \tag{72}$$

where

$L_i(\psi_j)$ and $M_{bi}(\psi_j)$ are the i <u>th</u> blade total lift and root bending moment respectively.

The integration on the right hand side of the above two equations can be obtained numerically based on the blade stations (x_k, k = 1,2,...N_d). These values will be calculated at discrete azimuth angles ψ_j, into which the cycle is divided; that is:

$$\psi_j = 2\pi(j-1)/N_\psi \qquad j = 1,2,....N_\psi$$

The total lift for 4-blade rotor can be written as:

$$L_{tot}(\psi_j) = L_1(\psi_j) + L_2(\psi_j + \frac{\pi}{2}) + L_3(\psi_j + \pi) + L_4(\psi_j + \frac{3\pi}{2})$$

$$j = 1,2,....N_\psi \qquad (73)$$

then, the average total lift over one revolution is:

$$L_{tot)av} = \frac{1}{N_\psi} \sum_{j=1}^{N_\psi} L_{tot}(\psi_j) \qquad (74)$$

Pitching and rolling moments are obtained by a simple vector decomposition of the root moment for each blade as shown in Figure 16, i.e.:

$$M_y(\psi_j) = (-M_{b_1} + M_{b_3}) \cos \psi_j + (-M_{b_2} + M_{b_4}) \sin \psi_j$$

$$j = 1,2,...N_\psi \qquad (75)$$

and

$$M_x(\psi_j) = (M_{b_1} - M_{b_3}) \sin \psi_j + (M_{b_2} - M_{b_4}) \cos \psi_j$$

$$j = 1,2,....N_\psi \qquad (76)$$

For trim purposes, the average value of these quantities, per revolution, are as follows:

$$M_{y)av} = \frac{1}{N_\psi} \sum_{j=1}^{N_\psi} M_y(\psi_j) \qquad (77)$$

and

$$M_{x)av} = \frac{1}{N_\psi} \sum_{j=1}^{N_\psi} M_x(\psi_j) \qquad (78)$$

4.4.1. The Method of Solution:

The trim state can be evaluated iteratively to simulate the actual forward flight conditions. The initial data required is the blade geometry, aerodynamic constants (ρ, C_ℓ) and the operating flight condition. A block diagram of iteration process is shown in Figure 17.

As a first approximation the induced velocity down through the rotor is assumed to be uniform. It can be calculated using the trapezoidal Glauert formula [1]:

$$u = u_o \left[1 + \S \frac{x_k}{L} \cos \psi\right] \tag{79}$$

where

$$u_o = \frac{W}{2\rho A_r V_f}$$

is the induced velocity at the rotor centre and A_r is rotor area.

$\S$ is a factor chosen to be slightly greater than unity (in the present case a typical value taken for $\S$ is 1.2).

Starting with an initial small value of collective pitch Θ, longitudinal cyclic pitch A_c and lateral cyclic pitch A_s, the aerodynamic force is assumed to be independent of q_i and $\dot{q}_i$ ($q_i, \dot{q}_i = 0$). The relative air velocity components can be computed at each blade station, equation (68). Consequently, the sectional blade lift is calculated from equation (63). Then, the total i th blade lift and moment at the j th discrete azimuth angle can be calculated by the respective integration

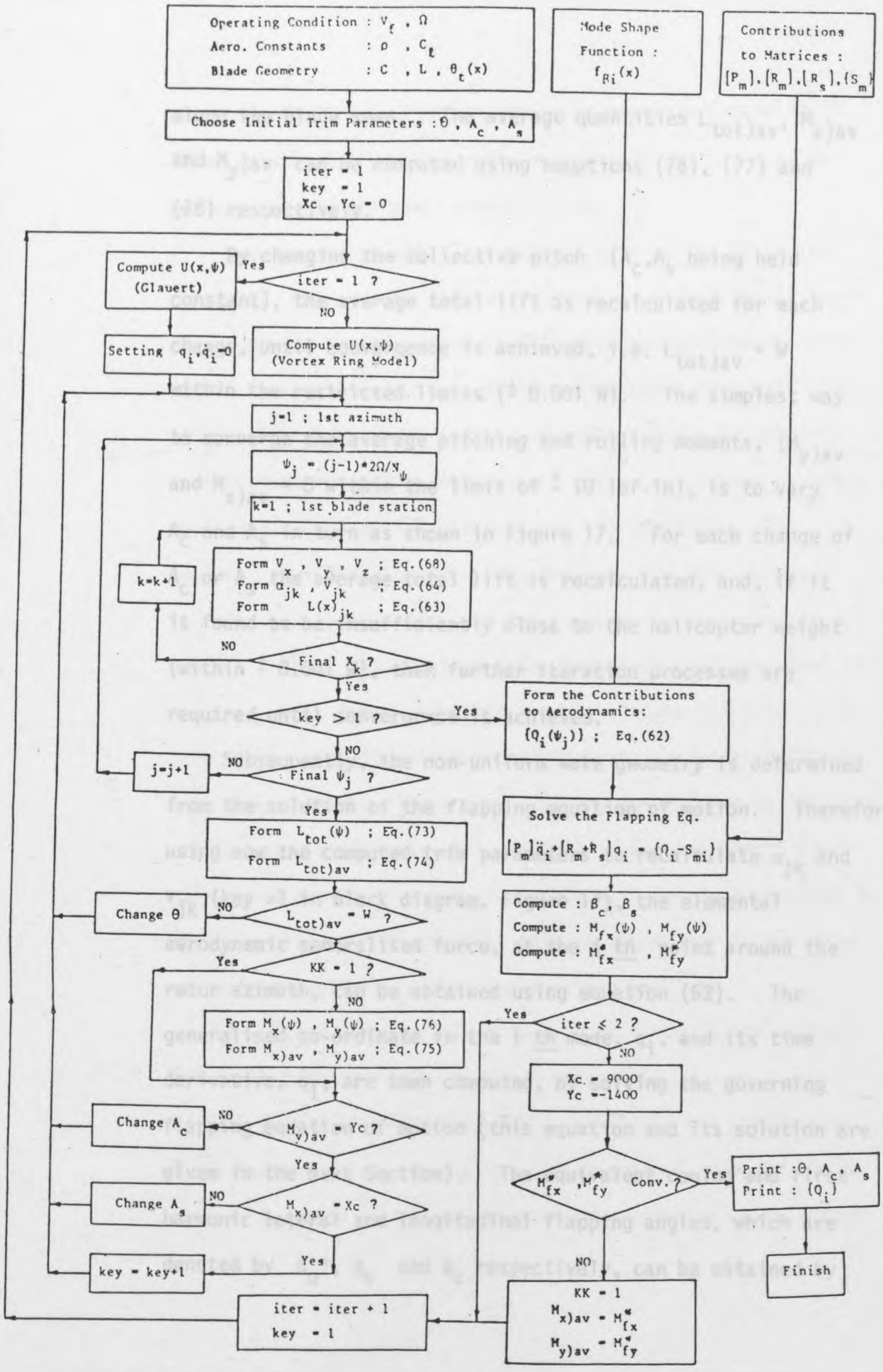

Figure 17 Block Diagram of Trim Iterations and Forming the Aerodynamic Contributions.

along the blade span. The average quantities $L_{tot)av}$, $M_{x)av}$ and $M_{y)av}$ can be computed using equations (74), (77) and (78) respectively.

By changing the collective pitch (A_c,A_s being held constant), the average total lift is recalculated for each change, until convergence is achieved, i.e. $L_{tot)av} = W$ within the restricted limits ($\pm$ 0.001 W). The simplest way to converge the average pitching and rolling moments, ($M_{y)av}$ and $M_{x)av} = 0$ within the limit of $\pm$ 10 lbf-in), is to vary A_c and A_s in turn as shown in Figure 17. For each change of A_c or A_s the average total lift is recalculated, and, if it it found to be insufficiently close to the helicopter weight (within $\pm$ 0.001 W), then further iteration processes are required until convergence is achieved.

Subsequently, the non-uniform wake geometry is determined from the solution of the flapping equation of motion. Therefore, using now the computed trim parameters to recalculate α_{jk} and v_{jk} (key >1 in block diagram, Figure 17), the elemental aerodynamic generalised force, at the j th point around the rotor azimuth, can be obtained using equation (62). The generalised co-ordinate in the i th mode, q_i, and its time derivative, $\dot{q}_i$, are then computed, by solving the governing flapping equation of motion (this equation and its solution are given in the next Section). The equivalent coning and first harmonic lateral and longitudinal flapping angles, which are denoted by β_0*, β_s and β_c respectively, can be obtained by

representing q_i in a Fourier series as given in Appendix (3). These values will be used with the previous initial data to perform the non-uniform induced inflow.

Now, the rotor wake is simulated by a series of vortex rings [81, 82] and the induced velocity is calculated by means of a computer program using the RAE (Farnborough) vortex ring model. In this model the wake is represented by a half ring originating at the reference blade and typically 12 complete vortex rings extending downstream. Only two systems of rings were used, representing the root and tip vortices. The routines VORTEXRM (Appendix (9)) are used for this purpose.

The aerodynamic force is now taken to be dependent on q_i and $\dot{q}_i$. Then, the obtained trim parameters (uniform wake) are now used, as a first approximation, to compute the final trim parameters. The iteration processes are repeated as before, with computing the pitching and rolling moments due to flapping displacement (equations (92) and (93) in Section 5) and their average values (M_{fy}^* and M_{fx}^*), until M_{fy}^* and M_{fx}^* converge to constant values. Physically, this is equivalent to assuming no aerodynamic moments from the fuselage and tail.

A written program (HTRIMC) which is given in the Appendix (9) is used to solve the previous trim state.

It should be noted that approximation to the steady and first harmonic flapping motions are determined from the above process and used in the non-uniform wake geometry calculations.

Quantities such as the desired lift as used in the preliminary calculations, e.g. for trim, may not be the same as the computed lift from this program. This is a result of blade motion effects due to flexibilities and the non-uniform wake induced velocities.

4.5. The Flapping Equation of Motion Formulation:

Having calculated the contributions of aerodynamic force $\{Q_i\}$ to the i th equations of motion, at j points around the rotor azimuth, as shown in the block diagram in Figure 17, the second step is to build up the flapping motion by summing the individual respective contributions of kinetic energy (mass) and elastic potentials (structure stiffness). The required integrations are performed numerically, (analytical expressions are also given in the Appendix (2)), using standard NAG-library routines (D01GAF). The input data, i.e. mass and stiffness distributions, are given and the mode shapes are calculated, at chosen spanwise (integration point) stations.

A written computer program ALLMATS is given in the Appendix (9) and is used to perform the respective contributions to the equations of motion.

Consequently, the flapping equation of motion for the i th blade flatwise mode becomes:

$$[p_m]\{\ddot{q}_i\} + [R_m + R_s]\{q_i\} = \{Q_i - S_{mi}\} \qquad (80)$$

Solving the characteristic equation (left-hand side) of the above equation leads to the natural frequency matrix $[w_i^2]$ and the corresponding modal matrix $[\phi^*]$. The resultant natural frequencies are used to establish confidence in the numerical methods by comparing these values with those obtained by the previous finite element model of the rotating blade. On the other hand, the resultant modal matrix $[\phi^*]$ is used as a transformation to uncouple the equation (80). This linear transformation is given by [83] as:

$$\{q_i\} = [\phi^*]\{\eta_i\} \tag{81}$$

Substituting the above equation into equation (80) and premultiplying by $[\phi^*]^T$ leads to a set of uncoupled equations for the i th mode, i.e.:

$$\{\ddot{\eta}_i\} + [w_i^2]\{\eta_i\} = \{G_i\} \tag{82}$$

where

$$\{G_i\} = [\phi^*]^T \{Q_i\}/[M_i] \tag{83}$$

in which

$$[M_i] = [\phi^*]^T [p_m][\phi^*] \tag{83.a}$$

To avoid the singularity of resonant response at the harmonics near the natural frequency, it is necessary to include the damping terms on the left-hand side of equation (82). Thus the term $\{2\zeta_i w_i \dot{\eta}_i\}$ is added to both sides, giving:

$$\{\ddot{\eta}_i\} + [2\zeta_i w_i]\{\dot{\eta}_i\} + [w_i^2]\{\eta_i\} = F_i(\psi_j) \qquad (84)$$

where

$$F_i(\psi_j) = \{G_i\} + \{2\zeta_i w_i \dot{\eta}_i\} \qquad (85)$$

is a function of η_i, $\dot{\eta}_i$ and t. This function being evaluated at j points around the rotor azimuth.

ζ_i is the damping ratio for i th mode.

For good convergence the damping ratio used should be close to the actual damping of particular degrees of freedom, including structural, mechanical and aerodynamic damping sources. In fact, since the actual damping in the forcing function $\{G_i\}$ will often be time-varying and even non-linear, the viscous damping ratio has to be an approximation. It should be stressed that the sole function of this damping term is to avoid divergence of the solution; the value ζ_i has no influence on the final converged solution. Thus, the damping ratio up to 35% may be used for the fundamental flap mode of the blade [1].

4.5.1. Integration of the Equation of Motion:

The solution of equation (84), assuming periodicity of both forcing function $F_i(t)$ and response, is obtained numerically using the convolution integral. The generalised co-ordinate $\eta_i(t)$ and its first derivative $\dot{\eta}_i(t)$, for zero initial conditions ($\eta_i(o) = 0$ and $\dot{\eta}_i(o) = 0$), are given explicitly [84] as:

$$\eta_i(t) = \frac{1}{w_{di}} \int_0^t F_i(\tau) e^{-\zeta_i w_{ni}(t-\tau)} \sin w_{di}(t-\tau)\, d\tau \quad (86)$$

$$\dot{\eta}_i(t) = -\zeta_i w_{ni} \eta_i(t) + \int_0^t F_i(\tau) e^{-\zeta_i w_{ni}(t-\tau)} \cos w_{di}(t-\tau) d\tau \quad (87)$$

where

$$w_{di}^2 = w_{ni}^2 (1 - \zeta_i^2)$$

The iterative solution proceeds as shown in the block diagram Figure 18. The aerodynamic contribution $\{Q_i\}$ is calculated at j points around the azimuth for the case in which the aerodynamic force is assumed independent of q_i and $\dot{q}_i$ (q_i and $\dot{q}_i = 0$). The assumed damping term ($2\zeta_i w_{ni} \dot{\eta}_i$) is introduced in the left-hand side of equation (84) to avoid the divergence of the solution near resonance and to achieve the steady state motion after only a few revolutions of the rotor blade. Thus,at a given azimuth angle ψ_j, the blade motion is calculated using equations (86) and (87). This calculation proceeds around the azimuth with increasing time (or ψ) until the steady-state response is achieved.

In the last revolution of the rotor blade, the steady state motion ($\eta_i(t)$) and $\dot{\eta}_i(t)$ is used as a first approximation to generate the assumed damping term ($F_d = 2\zeta_i w_{ni} \dot{\eta}_i$) and to evaluate q_i and $\dot{q}_i$ using equation (81). Now, the aerodynamic force is considered to be dependent on q_i and $\dot{q}_i$ and its contribution $\{Q_i\}$ may be recalculated using the current estimates of q_i and $\dot{q}_i$.

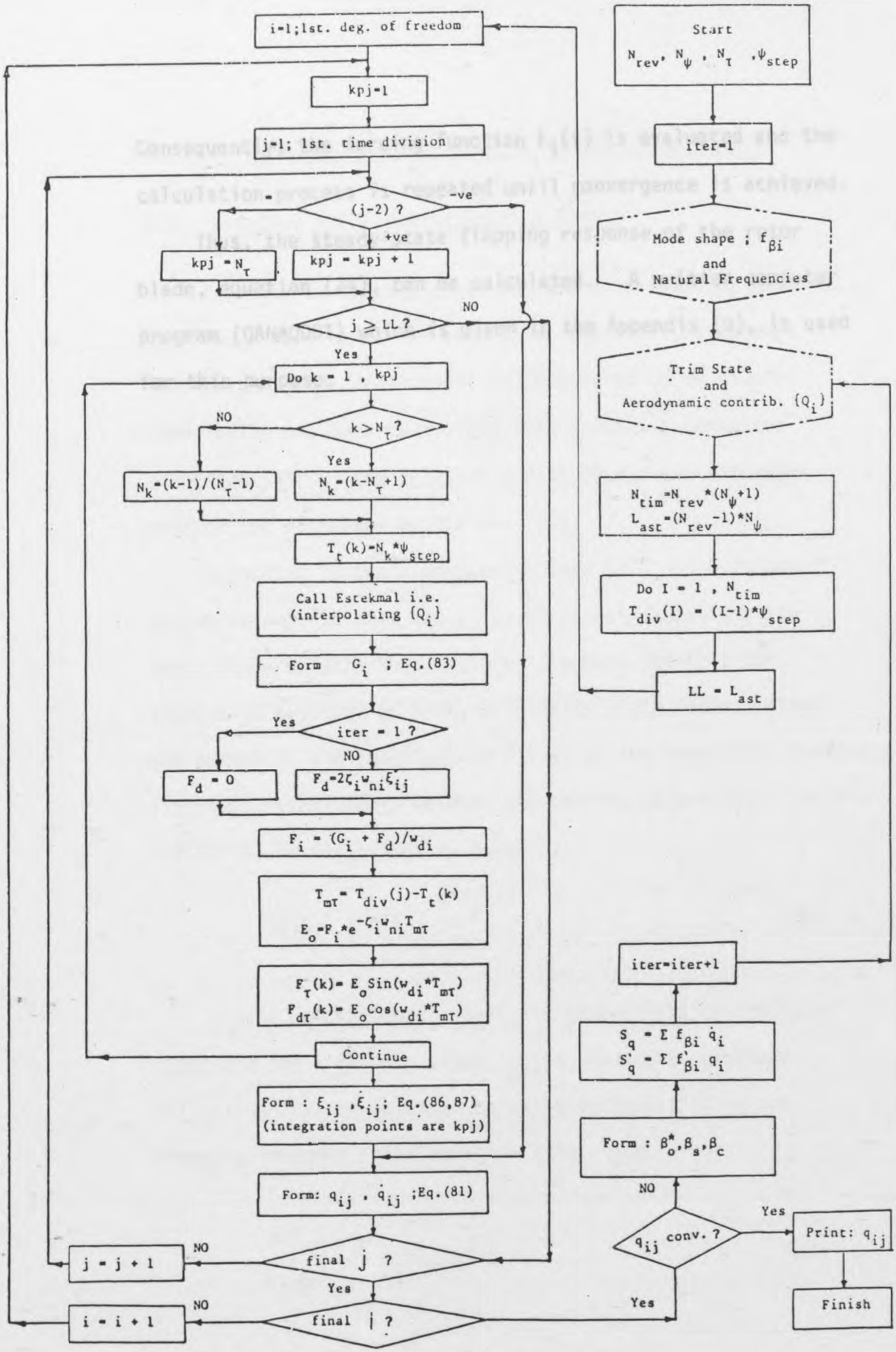

Figure 18 Block Diagram of the Iteration Process to Solve the Flapping Equation of Motion

Consequently, the forcing function $F_i(t)$ is evaluated and the calculation process is repeated until convergence is achieved.

Thus, the steady-state flapping response of the rotor blade, equation (24), can be calculated. A written computer program (QANAQDOT) which is given in the Appendix (9), is used for this purpose.

5. HUB VIBRATION FLAPWISE BENDING MOMENT CALCULATIONS

5.1. Rotating Hub Flapwise Bending Moment

In order to calculate the hub vibration bending moments it is necessary to derive values for the modal curvatures. This method (mode deflection) is considered to be simpler numerically and more convenient than a force integration technique [85]. The relative merits of the two different methods are discussed by Bielawa [86].

According to the elementary theory [87] which is based on the assumption that the cross-sectional dimensions are small compared with the length of the beam and that the transverse sections of beam, originally plane, remain plane and normal to the longitudinal fibres of the beam after bending, the usual relationship between the bending moment $M_f^*(x)$ and the curvature $d^2f_\beta(x)/dx^2$ is given by:

$$M_f^*(x) = EI(x) \frac{d^2f_\beta(x)}{dx^2} \tag{88}$$

Having calculated the periodic generalised co-ordinate $q_i(t)$ and the i th mode shape $f_{\beta i}(x)$ the modal curvature $d^2f_\beta(x)/dx^2$ can be obtained by twice differentiating the flapping response $f_\beta(x)$ equation (24), i.e.:

$$\frac{d^2f_\beta(x)}{dx^2} = \sum_i f''_{\beta i}(x)\, q_i(t) \tag{89}$$

Substituting the above equation into equation (88) the flapwise bending moment at the root of the blade can be written as:

$$M_f = EI)_0 \sum_i f''_{\beta i}(0)\, q_i(t) \qquad (90)$$

Accordingly, the j th rotating hub moment mode contribution at the root of the blade is given by:

$$M_f^{(j)} = EI)_0 f''_{\beta j}(0)\, q_j(t) \qquad (91)$$

5.2. Non-Rotating Hub Flapwise Bending Moment

The problem of helicopter vibration reduction in forward flight is often formalised either by minimising the oscillatory hub shears, or hub moments, or the blade root stresses due to oscillatory loads, or some combination of these. In the present study, only the hub rolling and pitching moments are considered for minimisation to achieve the vibration reduction. These moments are obtained by resolving the rotating flapwise bending moment in the hub fixed non-rotating co-ordinate system and summing over all four blades of the rotor in exactly the same manner as mentioned in Section (4.4.).

By writing M_f instead of M_b in equations (75) and (76) the pitching and rolling moments, respectively, can be written as:

$$M_{fy}(\psi_j) = (M_{f_3} - M_{f_1})\cos\psi_j + (M_{f_4} - M_{f_2})\sin\psi_j \qquad j=1,2,\ldots N_\psi \qquad (92)$$

$$M_{fx}(\psi_j) = (M_{f_1} - M_{f_3}) \sin \psi_j + (M_{f_2} - M_{f_4}) \cos \psi_j$$

$$j = 1,2,....N_\psi \quad (93)$$

Now, the periodic moments which are transmitted through the hub to the aircraft, act as excitation moments on the fuselage. These moments are at the frequencies of $N_b\Omega$, $2N_b\Omega$,..... determined by the number of blades N_b and the rotational frequency Ω of the rotor (the harmonic contents of these moments are derived in Appendix (4)). Basically, the rotor hub acts as a filter which only transmits oscillatory moments with harmonics per revolution of N_b, $2N_b$,..... to the fuselage. This result is based on the assumption that all the blades are identical and have the same periodic motion.

6. THE OPTIMIZATION PROBLEM FORMULATION

In terms of mathematical programming, the blade tailoring problem is in effect the minimisation of the pitching and rolling moments (objective function) by means of changing the mass and stiffness distributions of the blade (design variables). This helicopter vibration reduction problem, expressed as a general class of structural synthesis problems, may be stated in the following form: given the pre-assigned properties and the helicopter performance parameters, find the vector of design variables $\underset{\sim}{H}$ such that:

$$g_j(\underset{\sim}{H}) > 0, \qquad j = 1,.....J$$

$$H_i^{(L)} \leqslant H_i \leqslant H^{(u)}, \qquad i = 1,.....N_d$$

and

$$J(\underset{\sim}{H}) \rightarrow \min$$

where

$g_j(\underset{\sim}{H})$ is the j th constraint function,

H_i is the i th design variable and

subscripts L and u denote lower and upper bounds respectively, and

J(H) is the objective function in terms of the design variables.

The blade tailoring problem is illustrated in the closed loop block diagram, Figure 19. However, it is required to minimise an objective function based on the pitching and rolling moments driven by the aerodynamic forces of the rotor blade. These forces are dependent on the blade response, both these being calculated, in trimmed flight, as described in Section (4). The mass per unit length and the flexural stiffness (EI) at each structural blade node are used as design variables. Restrictions on these design variables are enforced during the optimization process to prevent them from reaching impractical values. Thus, constraints in the form of upper and lower bounds are used. The lower bounds are taken as the baseline design of the blade. The upper bounds are meant to constrain the values of the design variables within 10% of the blade baseline design. Then the two basic objective functions considered are:

$$\begin{aligned} M_o(\underset{\sim}{H}) &= M_{yp} \\ M_o(\underset{\sim}{H}) &= M_{xp} \end{aligned} \qquad (94)$$

where M_{yp} and M_{xp} are the peak to peak values of the oscillatory pitching and rolling moments respectively. The relation between the objective function and the aeroelastic analysis is presented in equations (92) and (93) (Section 5).

Obviously, an increase in the blade nodal design variables normally implies an increase in blade weight and ideally one may seek the solution which provides the least weight penalty.

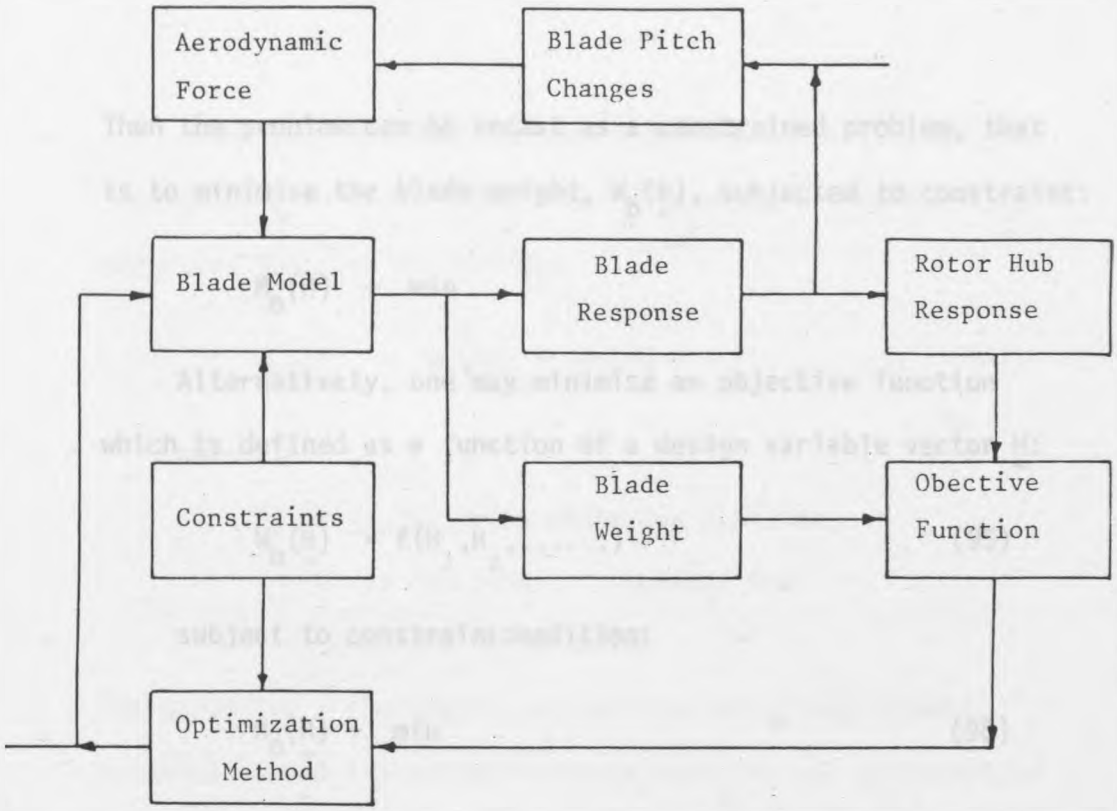

Figure 19 Blade Tailoring Problem Closed Loop Block Diagram.

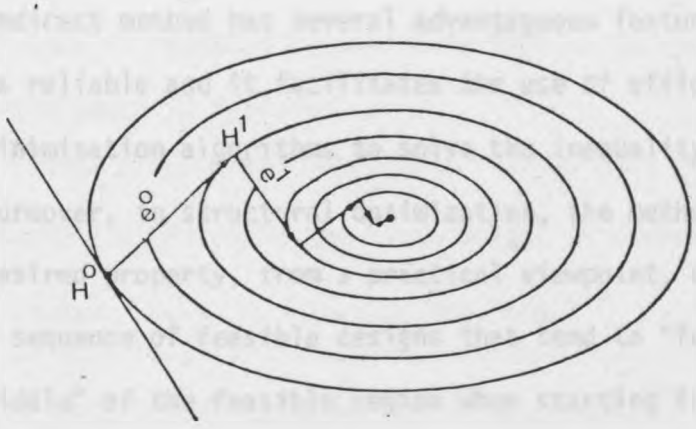

Figure 20 Diagrammatic View of Minimization ; Based on Steepest Descent Technique.

Then the problem can be recast as a constrained problem, that is to minimise the blade weight, $W_b(\underset{\sim}{H})$, subjected to constraint:

$$M_o(H) \rightarrow \min$$

Alternatively, one may minimise an objective function which is defined as a function of a design variable vector $\underset{\sim}{H}$:

$$W_b(\underset{\sim}{H}) = f(H_1, H_2, \ldots\ldots) \tag{95}$$

subject to constraint condition:

$$M_o(\underset{\sim}{H}) \rightarrow \min \tag{96}$$

and

$$H_i^{(L)} \leqslant H_i \leqslant H_i^{(u)}, \quad i = 1, \ldots\ldots N_d \tag{97}$$

The above inequality constrained minimisation problem can be transformed into a sequence of unconstrained minimisation tasks by using an extended interior penalty function. This indirect method has several advantageous features [88]: it is reliable and it facilitates the use of efficient unconstrained minimisation algorithms to solve the inequality problem. Moreover, in structural optimization, the method exhibits the desired property, from a practical viewpoint, of generating a sequence of feasible designs that tend to "funnel down the middle" of the feasible region when starting from a feasible interior point. This keeps the optimum design path away from the constraints, thus causing even a sub-optimal solution to be a feasible solution.

Therefore, the optimization algorithm which is used sequentially in the present problem is based on the modified objective function defined by:

$$O_{bj}(\underset{\sim}{H}) = W_b(\underset{\sim}{H}) + \gamma M_o(\underset{\sim}{H}) \qquad (98)$$

where

$W_b(\underset{\sim}{H})$ is the basic objective function,

$\gamma M_o(\underset{\sim}{H})$ is the penalty function, and

γ is the penalty parameter.

The parameter γ represents the relative weighting between minimisation of the objective function $W_b(\underset{\sim}{H})$ and satisfaction of the constraints $M_o(\underset{\sim}{H}) \rightarrow \min$.

Starting with an initial small value γ (i.e. $\gamma = 0$) and initial design variable vector $\underset{\sim}{H}$, the objective function $O_{bj}(\underset{\sim}{H})$ is minimised (using an algorithm based on steepest technique as given below) to produce a new design variable $\underset{\sim}{H}^{(0)}$; with this $\underset{\sim}{H}^{(0)}$ taken as the new initial design variable vector the process is repeated sequentially with an increased γ until convergence is achieved.

The sequentially increasing values of γ ensure the minimum possible $M_o(\underset{\sim}{H})$ while the blade weight is increased, that is:

for $\gamma \rightarrow 0$, then $O_{bj}(\underset{\sim}{H}) = W_b^{\min}$

for $\gamma \rightarrow \infty$, then $W_b^{\min} \leqslant O_{bj}(\underset{\sim}{H}) \leqslant W_b^{\max}$

Hence, there will be a variety of solutions according to the different values of γ. As a result of this, the penalty parameter γ can be taken to represent the "trade-off" between the weight penalty and minimum fixed axes moments. Thus, at a given advance ratio, and for different values of γ, optimization tables (or curves) for the rotor blade can be drawn up which contain:

$$\text{weight penalty (\% Mass Inc)} = \frac{W_b(\underset{\sim}{H}) - W_b^{\min}(\underset{\sim}{H})}{W_b^{\min}(\underset{\sim}{H})} \times 100 \quad (99)$$

$$\text{Percentage bending moment decrement (\% BM decr)} = \frac{M_o(\underset{\sim}{H})\big|_{\text{at } \gamma=0} - M_o(\underset{\sim}{H})}{M_o(\underset{\sim}{H})\big|_{\text{at } \gamma=0}} \times 100 \quad (100)$$

6.1. Theoretical Background of Steepest Descent Technique

The practical aspects of steepest descent technique are now discussed. It does not require calculation of second derivatives, but involves only direct calculation of the objective function and its first derivatives. The overall computational efficiency of this technique is generally high compared with that of other techniques, and convergence to a solution in relatively fewer steps can be expected [89, 90]. The descent technique involves iterations which consist essentially of three parts. First, a direction of descent is found, then a descent steplength is estimated and finally the descent step is performed as follows:

6.2. Explanation of the Method

It will be convenient to think of the design variable vector $\underset{\sim}{H}$ as a point in Euclidean space and e_i as a set of direction numbers emanating from $\underset{\sim}{H}$. However, one may start at a point $\underset{\sim}{H}^{(o)}$ and determine the direction in which the objective function $O_{bj}(\underset{\sim}{H})$, decreases most rapidly. This direction is given by [89] as:

$$\underset{\sim}{e} = - \nabla O_{bj}(\underset{\sim}{H}) \tag{101}$$

in which $\nabla O_{bj}(\underset{\sim}{H})$ is a vector whose direction is normal to a level surface $O_{bj}(\underset{\sim}{H})$ = constant, and whose magnitude is the direction derivative of $O_{bj}(\underset{\sim}{H})$ in the direction of this normal. It can be written as:

$$\nabla O_{bj}(\underset{\sim}{H}) = \frac{\partial O_{bj}(\underset{\sim}{H})}{\partial H_1} \hat{e}_1 + \frac{\partial O_{bj}(\underset{\sim}{H})}{\partial H_2} \hat{e}_2 + \ldots.$$

where $\hat{e}_i$ is the unit vector of i th direction.

So, the direction of steepest descent technique will take the form:

$$e_i = \left(\frac{\partial O_{bj}(\underset{\sim}{H})}{\partial H_i}\right) \Big/ \left\{\sum_{i=1}^{N_d} \left(\frac{\partial O_{bj}(\underset{\sim}{H})}{\partial H_i}\right)^2\right\}^{\frac{1}{2}},$$

$$i = 1, \ldots.N_d \tag{102}$$

where e_i are the components of a unit vector $\underset{\sim}{e}$, i.e.:

$$\underset{\sim}{e} = \{e_1, e_2, \ldots.\}^T \tag{103}$$

The gradients of $O_{bj}(\underset{\sim}{H})$ can be obtained numerically by evaluating $O_{bj}(\underset{\sim}{H})$ at two neighbouring points and using, for example:

$$\frac{\partial O_{bj}(\underset{\sim}{H})}{\partial H_1} = \frac{O_{bj}(H_1+\Delta H, H_2, \ldots) - O_{bj}(H_1, H_2, \ldots)}{\Delta H}$$

Here, ΔH must be small enough so that $\frac{(\Delta H^2)}{2}\frac{\partial^2 O_{bj}(\underset{\sim}{H})}{\partial H^2}, \ldots$ in the Taylor series, can be neglected.

The gradients $\frac{\partial O_{bj}(\underset{\sim}{H})}{\partial H_i}$ can be calculated for i = 1,2,... and hence the direction of steepest descent can be obtained at any current design point.

Now the objective function $O_{bj}(\underset{\sim}{H} + \lambda\underset{\sim}{e})$, has a negative derivative at $\lambda = 0$, in which λ is the estimated steplength. It is therefore possible to find $\lambda > 0$ such that:

$$O_{bj}(\underset{\sim}{H} + \lambda\underset{\sim}{e}) < O_{bj}(\underset{\sim}{H}) \qquad (104)$$

with such a value of λ, one can take:

$$\underset{\sim}{H}^{(1)} = \underset{\sim}{H}^{(o)} + \lambda\underset{\sim}{e} \qquad (105)$$

as a new starting point and repeat the operation to obtain a sequence of points $\underset{\sim}{H}^{(o)}, \underset{\sim}{H}^{(1)}, \ldots\ldots$, as shown in Figure 20, such that:

$$O_{bj}(\underset{\sim}{H}^{(k+1)}) < O_{bj}(\underset{\sim}{H}^{(k)}) \qquad (106)$$

under suitable restrictions (bounds) the sequence will attain

or converge to a stationary value of $O_{bj}(\underset{\sim}{H})$.

The determination of steplength λ can be accomplished by trials [47]. If the first trial fails to satisfy equation (104), the chosen value of λ is too large; the steplength is reduced by a half for second trial, and so on as shown in the block diagram of the optimization iteration process, Figure 21.

6.3. Preliminary Exercise to Demonstrate the Optimization Procedure

Due to the length and complexity of the dynamic analysis, and the corresponding sensitivity analysis, of the blade tailoring problem, a preliminary exercise was firstly carried out to demonstrate the feasibility of the above optimization procedure. The vibrating bending moment at the root of a cantilever beam (rotating and non-rotating) subjected to an oscillatory force at its tip, was minimised, the design variables being beam depths at certain spanwise positions. In addition, a laboratory experimental investigation was carried out on a simple non-rotating cantilever beam model to resolve any doubts about assumptions made in mathematical modelling. Both the mathematical and experimental model are described as follows:

6.3.1. Optimum Cantilever Configuration for Minimum Oscillatory Bending Moment

Evidently, the optimization procedures that have been described in Section (6) can be applied to both rotating and

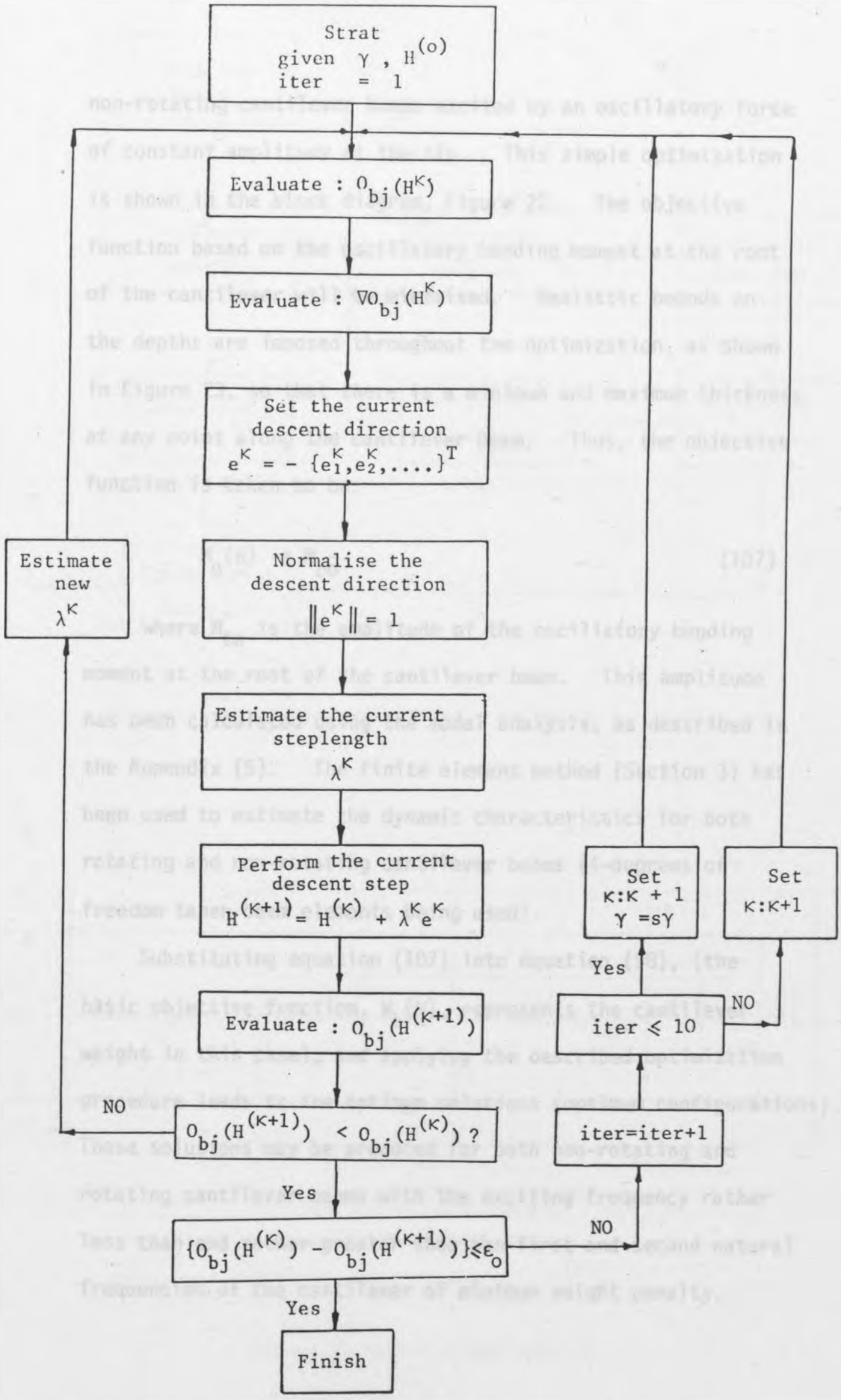

Figure 21 Block Diagram of the Optimization Iteration Process

non-rotating cantilever beams excited by an oscillatory force of constant amplitude at the tip. This simple optimization is shown in the block diagram, Figure 22. The objective function based on the oscillatory bending moment at the root of the cantilever will be minimised. Realistic bounds on the depths are imposed throughout the optimization, as shown in Figure 23, so that there is a minimum and maximum thickness at any point along the cantilever beam. Thus, the objective function is taken to be:

$$M_o(\underset{\sim}{H}) = M_{bo} \tag{107}$$

where M_{bo} is the amplitude of the oscillatory bending moment at the root of the cantilever beam. This amplitude has been calculated using the modal analysis, as described in the Appendix (5). The finite element method (Section 3) has been used to estimate the dynamic characteristics for both rotating and non-rotating cantilever beams (4-degrees of freedom taper beam elements being used).

Substituting equation (107) into equation (98), (the basic objective function, $W_b(\underset{\sim}{H})$, represents the cantilever weight in this case), and applying the described optimization procedure leads to the optimum solutions (optimum configurations). These solutions may be produced for both non-rotating and rotating cantilever beams with the exciting frequency rather less than and rather greater than the first and second natural frequencies of the cantilever of minimum weight penalty.

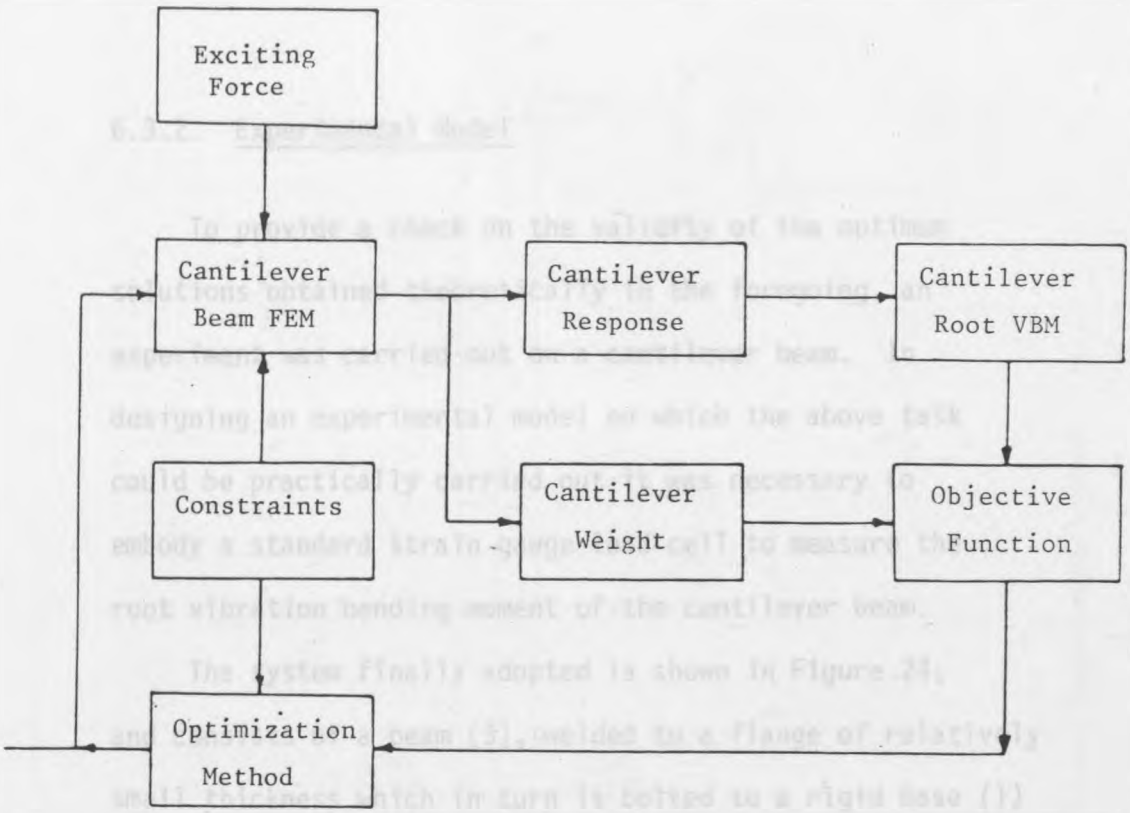

Figure 22 Block Diagram of Simple Optimization Problem.

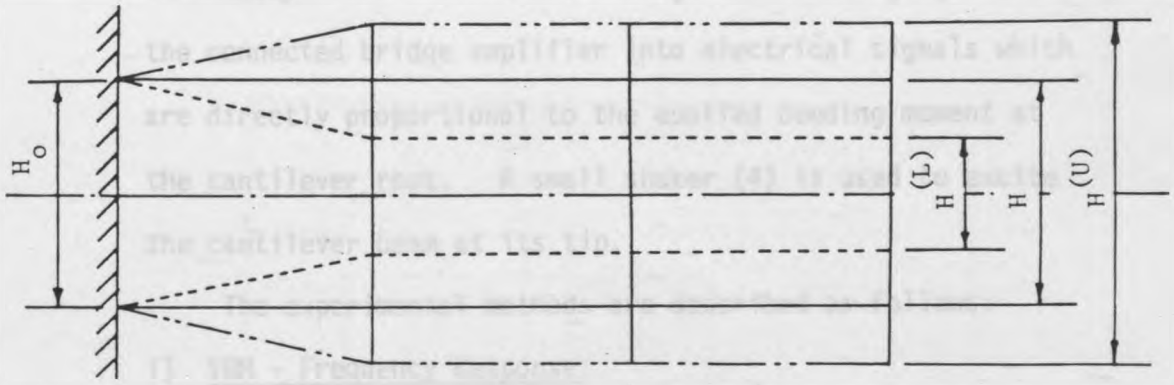

-------- Minimum Weight Solution ; $H^{(L)}=0.5$

———— Beam to be Modified , $H = H_o = 1.0$

—·—·— Maximum Weight Solution ; $H^{(U)}=1.5$

Figure 23 Optimization Model

6.3.2. Experimental Model

To provide a check on the validity of the optimum solutions obtained theoretically in the foregoing, an experiment was carried out on a cantilever beam. In designing an experimental model on which the above task could be practically carried out it was necessary to embody a standard strain gauge load cell to measure the root vibration bending moment of the cantilever beam.

The system finally adopted is shown in Figure 24, and consists of a beam (3), welded to a flange of relatively small thickness which in turn is bolted to a rigid base (1) through two studs, so that the end conditions approximate to those of a cantilever beam. Four strain gauges (2) are cemented in the longitudinal direction on the studs and connected in full bridge fashion. The resulting strains in the bolts are transformed through the strain gauges and the connected bridge amplifier into electrical signals which are directly proportional to the applied bending moment at the cantilever root. A small shaker (4) is used to excite the cantilever beam at its tip.

The experimental methods are described as follows:

i) VBM - Frequency Response

An electrodynamic shaker driven by an automatic vibration exciter control through the power amplifier was used to excite the cantilever beam at its tip. A force transducer of 3.6

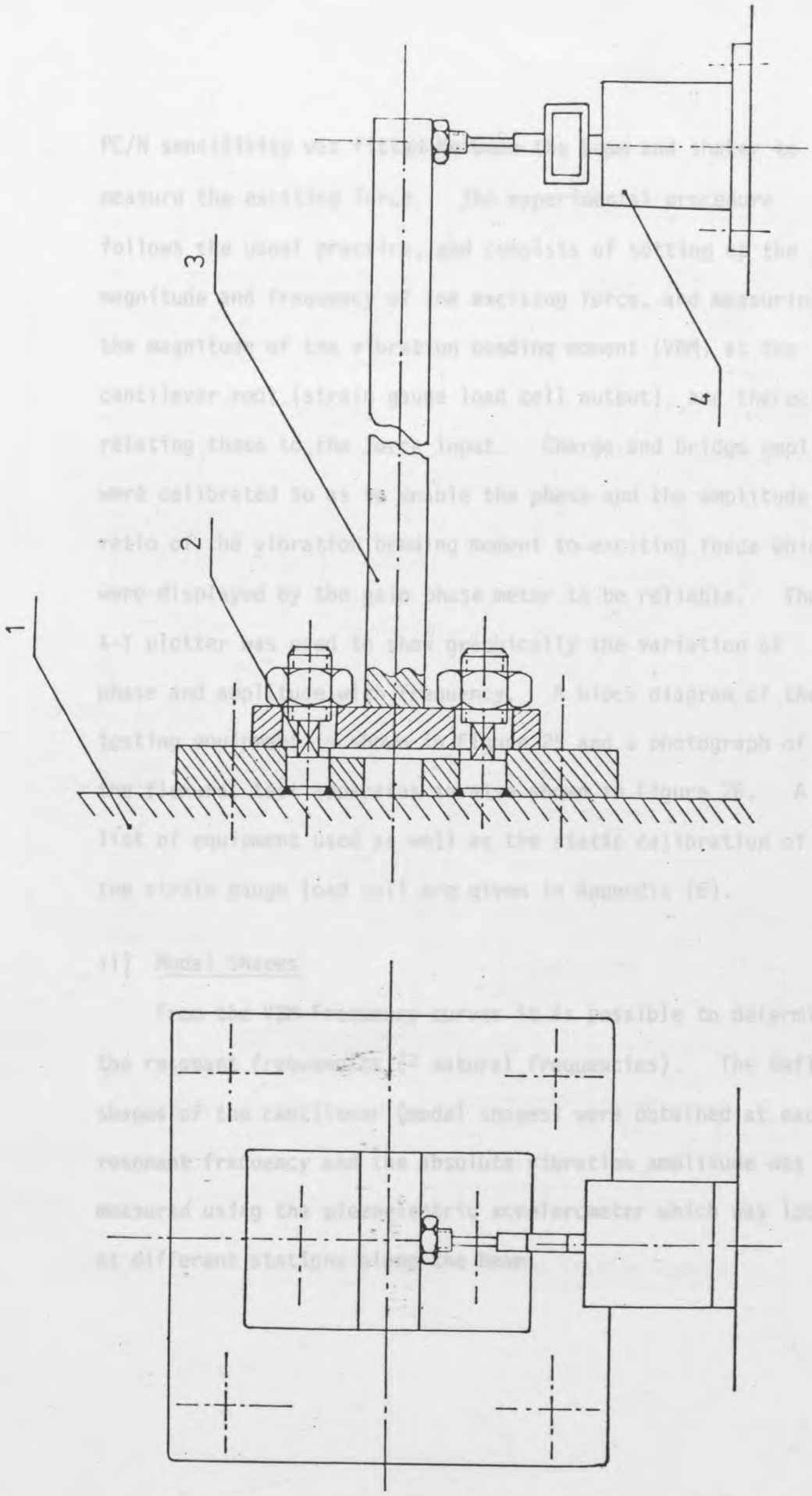

Figure 24 Diagram of the Complete Experimental Model

PC/N sensitivity was fitted between the beam and shaker to measure the exciting force. The experimental procedure follows the usual practice, and consists of setting up the magnitude and frequency of the exciting force, and measuring the magnitude of the vibration bending moment (VBM) at the cantilever root (strain gauge load cell output), and thereafter relating these to the force input. Charge and bridge amplifiers were calibrated so as to enable the phase and the amplitude of ratio of the vibration bending moment to exciting force which were displayed by the gain phase meter to be reliable. The X-Y plotter was used to show graphically the variation of phase and amplitude with frequency. A block diagram of the testing equipment is shown in Figure 25 and a photograph of the flexural test apparatus is also shown in Figure 26. A list of equipment used as well as the static calibration of the strain gauge load cell are given in Appendix (6).

ii) Modal Shapes

From the VBM-Frequency curves it is possible to determine the resonant frequencies ($\cong$ natural frequencies). The deflected shapes of the cantilever (modal shapes) were obtained at each resonant frequency and the absolute vibration amplitude was measured using the piezoelectric accelerometer which was located at different stations along the beam.

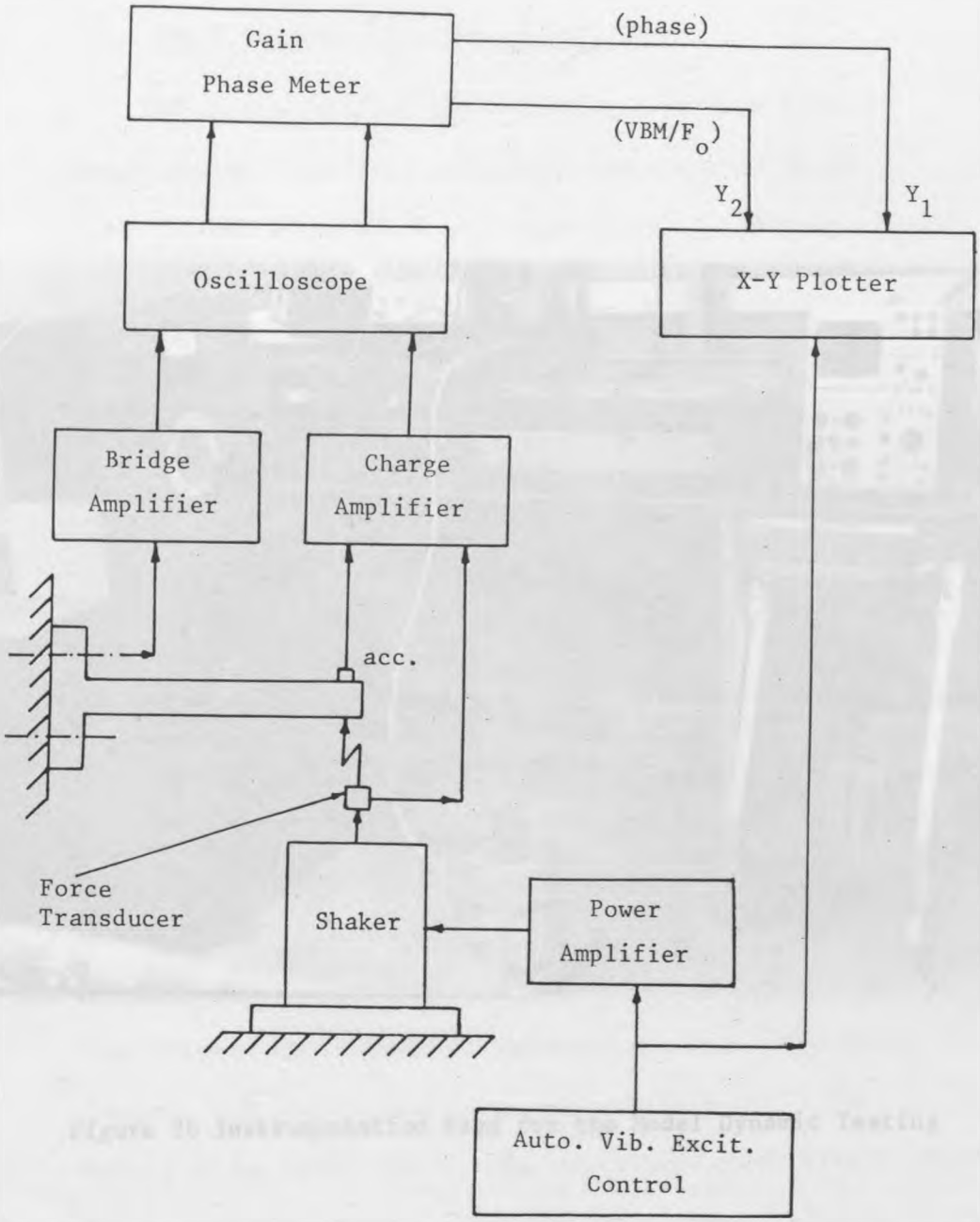

Figure 25 Block Diagram for the Dynamic Testing Equipment

Figure 26 Instrumentation Used for the Model Dynamic Testing

7. RESULTS AND DISCUSSION

7.1. The Preliminary Exercise Results

The cantilever beam considered is a uniform beam, of length 600 mm (23.6 in), with depth and width of 20 mm (0.88 in) and 60 mm (2.36 in) respectively. This cantilever beam was excited by an harmonic exciting force of constant amplitude of 1 N (0.225 lbf) at its tip. In our calculation, only three finite elements are used, with three depths as design variables (H_1, H_2, H_3). These design variables are dimensionless with respect to the depth at the root of the cantilever (held constant). The other initial data are given in Appendix (7). Both the computational and experimental work are described in the following sections.

7.1.1. VBM - Frequency Response

The vibration bending moment (VBM) response of the cantilever root was obtained experimentally and theoretically and the results are compared in Figure 27. It can be seen that the measured natural frequencies are lower than those obtained from theoretically by approximately 10%. This is thought to be partly due to the flange-base joint flexibility of the cantilever model; since in the mathematical model, it is assumed to have zero flexibility. Another source of inaccuracy of the calculated natural frequencies could be due to the use of a value of Young's modulus for the steel beam material as published in the text book, (a tensile test

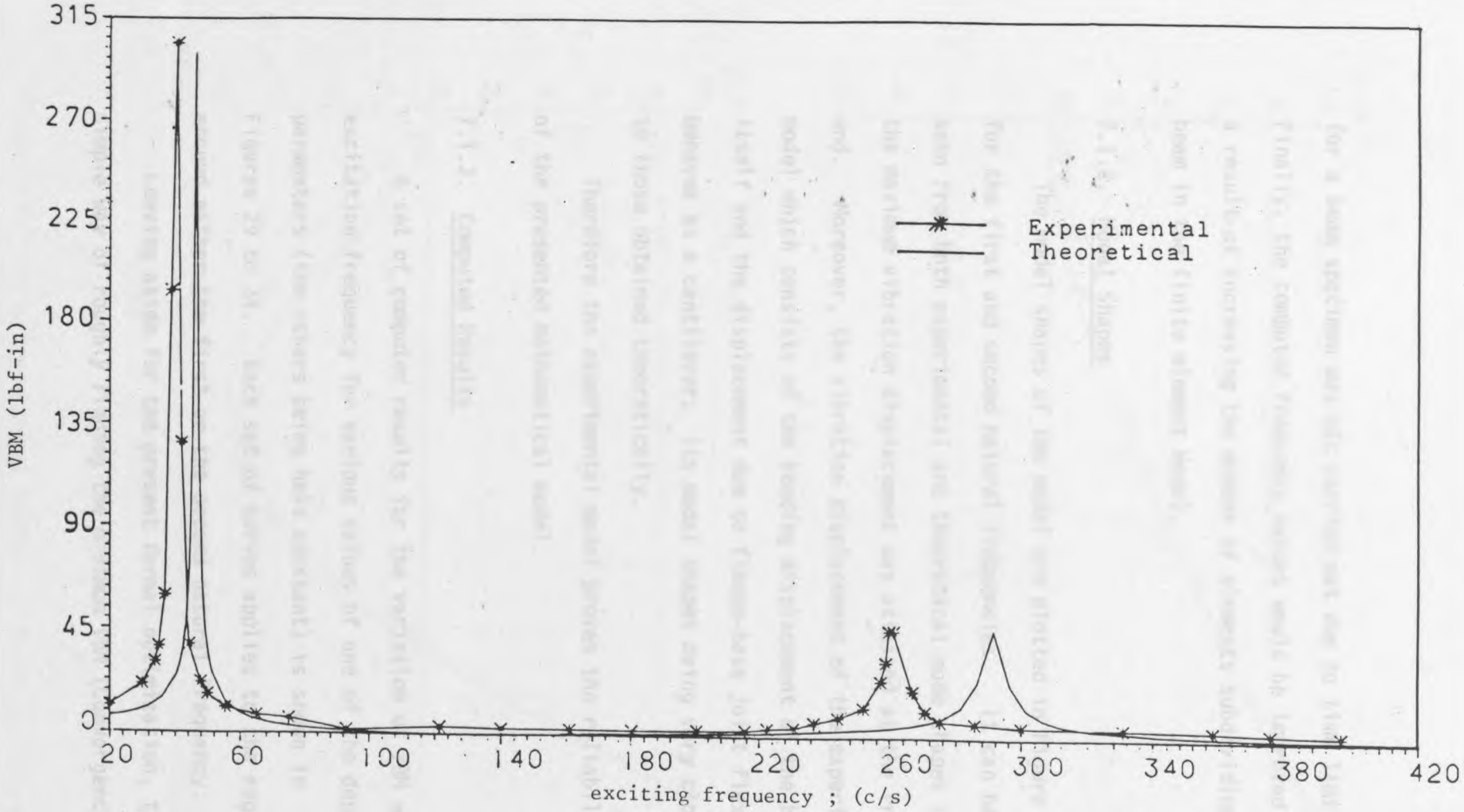

Figure 27 VBM-Frequency Response at the Root of Uniform Cantilever Beam.

for a beam specimen was not carried out due to time limitation). Finally, the computed frequency values would be improved as a result of increasing the number of elements subdividing the beam in the finite element model.

7.1.2. Modal Shapes

The modal shapes of the model are plotted in Figure 28 for the first and second natural frequencies. It can be seen from both experimental and theoretical mode shapes that the maximum vibration displacement was attained at the free end. Moreover, the vibration displacement of the experimental model which consists of the bending displacement of the beam itself and the displacement due to flange-base joint flexibility, behaves as a cantilever; its modal shapes being very close to those obtained theoretically.

Therefore the experimental model proves the reliability of the presented mathematical model.

7.1.3. Computed Results

A set of computer results for the variation of VBM with excitation frequency for various values of one of the depth parameters (the others being held constant) is shown in Figures 29 to 34. Each set of curves applies to the region around either the first or the second natural frequency.

Leaving aside for the present formal optimization, the simple way of roughly finding the minimum VBM (Convergence

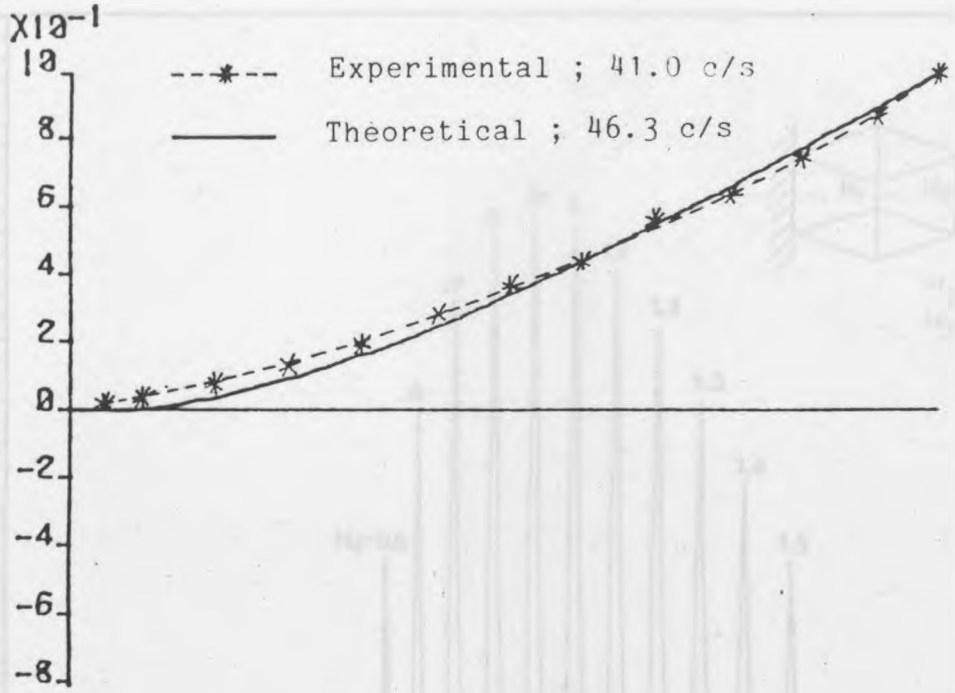

(a) 1 st Mode

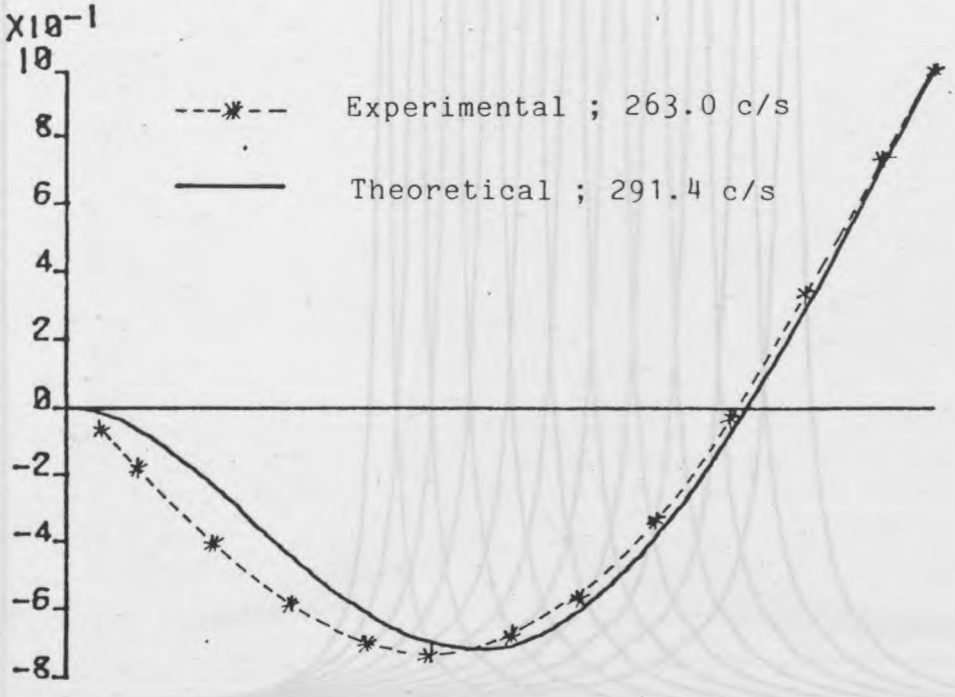

(b) 2 nd Mode

Figure 28 First Two Normal Modes of Bending Vibration of Uniform Cantilever Beam.

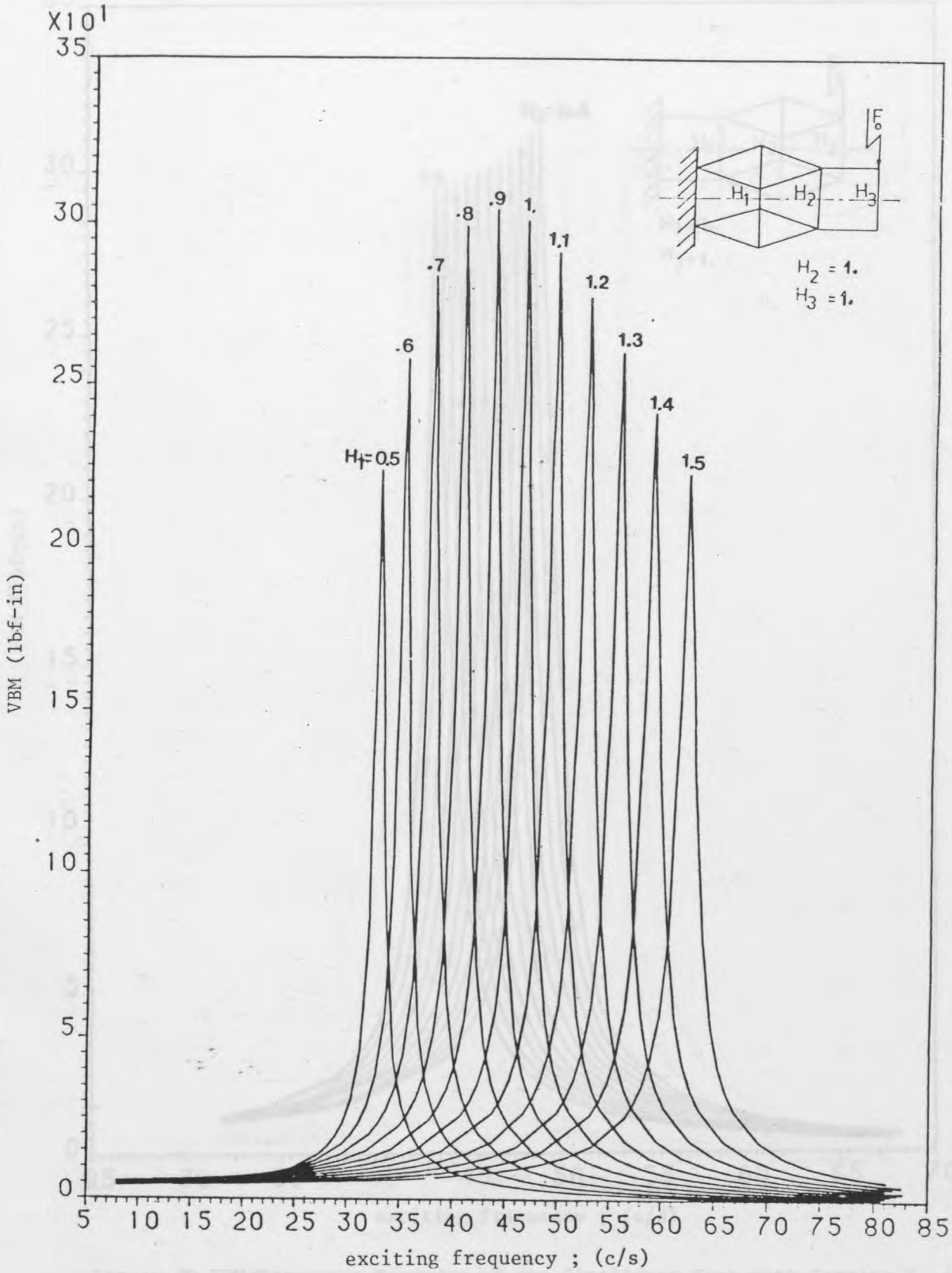

Figure 29 VBM-Frequency Response of the Cantilever Root with Varying H_1 ; (1st Mode).

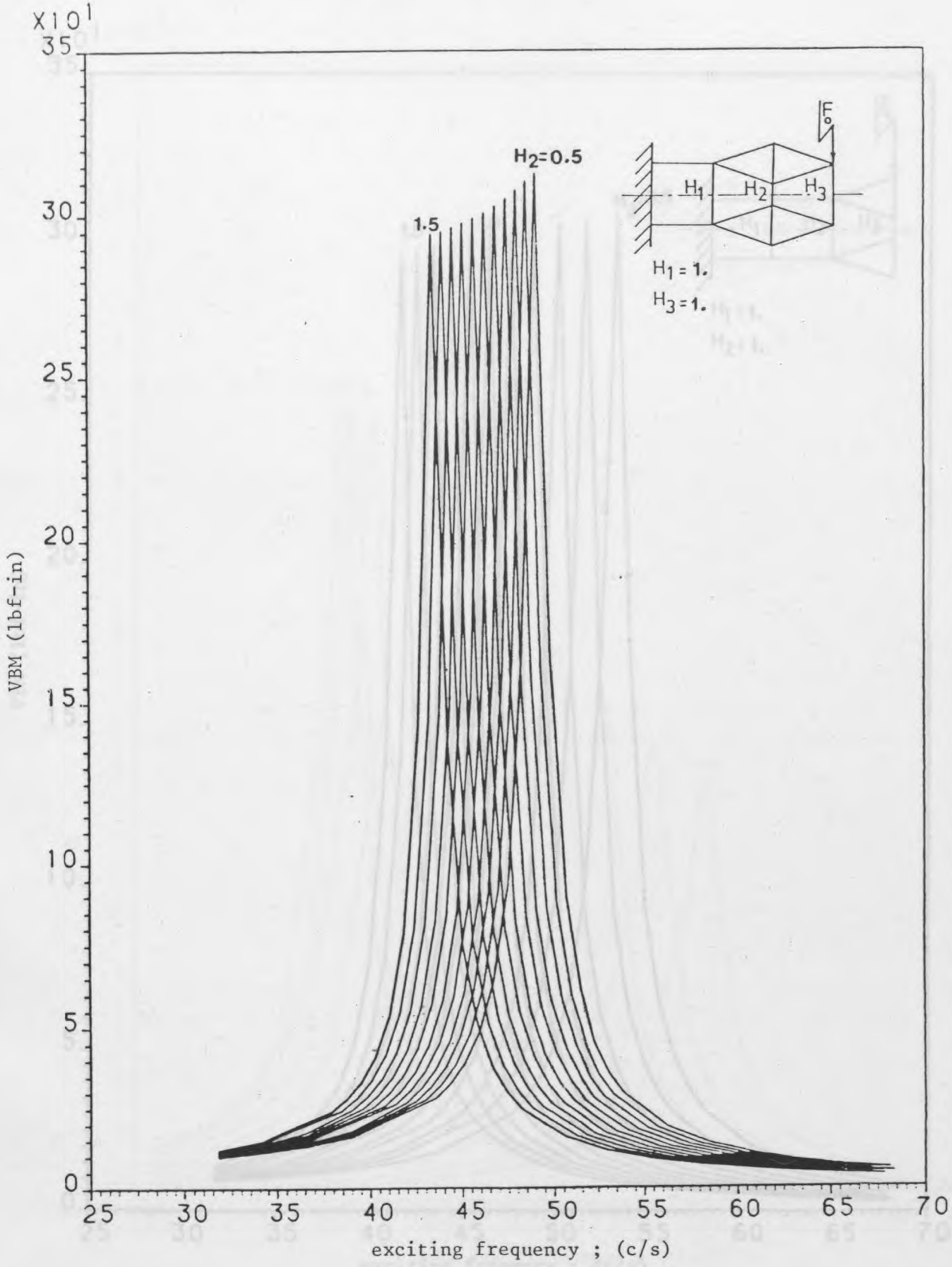

Figure 30 VBM-Frequency Response of the Cantilever Root with Varying H_2 ; (1st Mode).

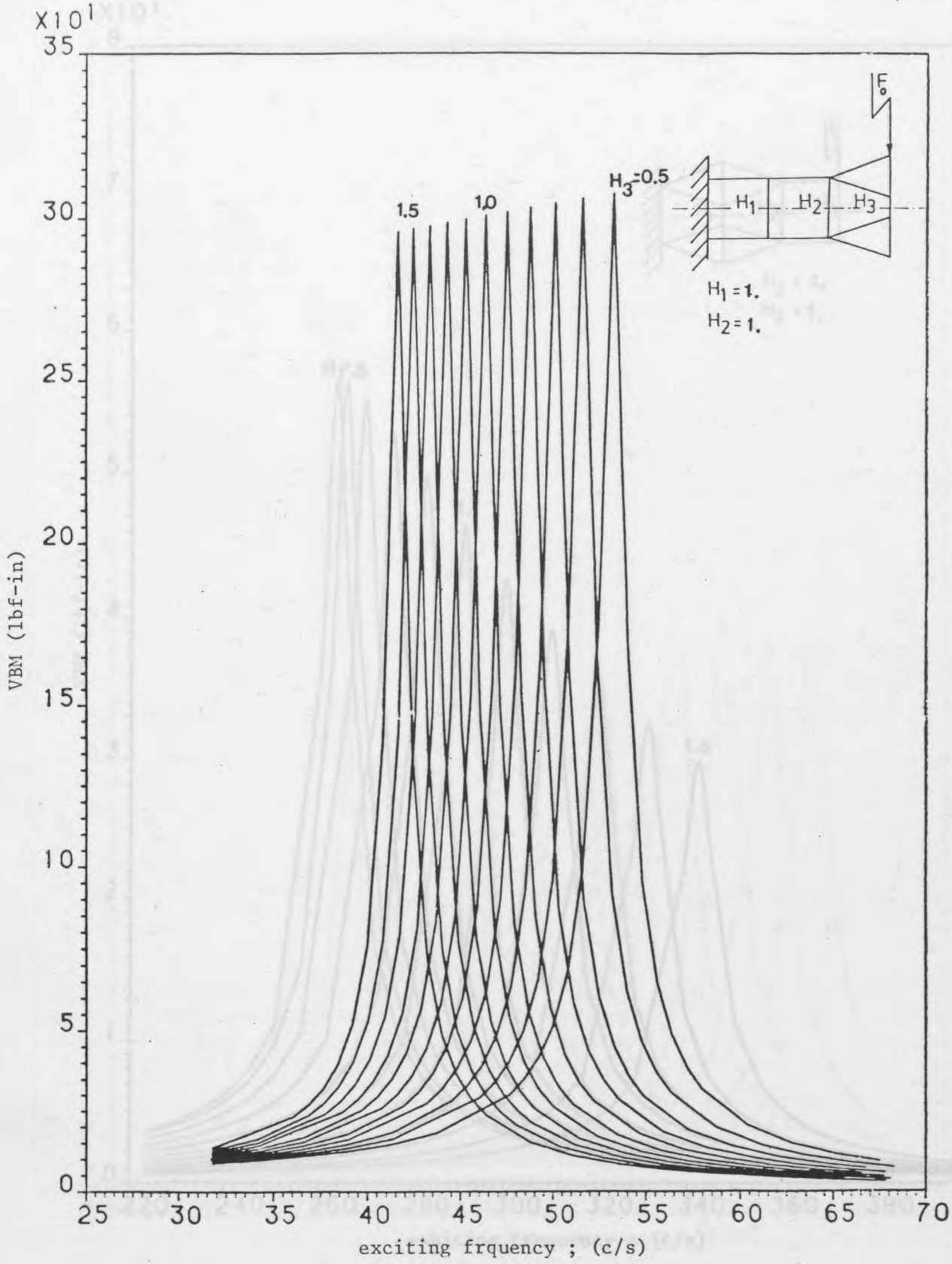

Figure 31 VBM-Frequency Response of the Cantilever Root with Varying H_3 ; (1st Mode).

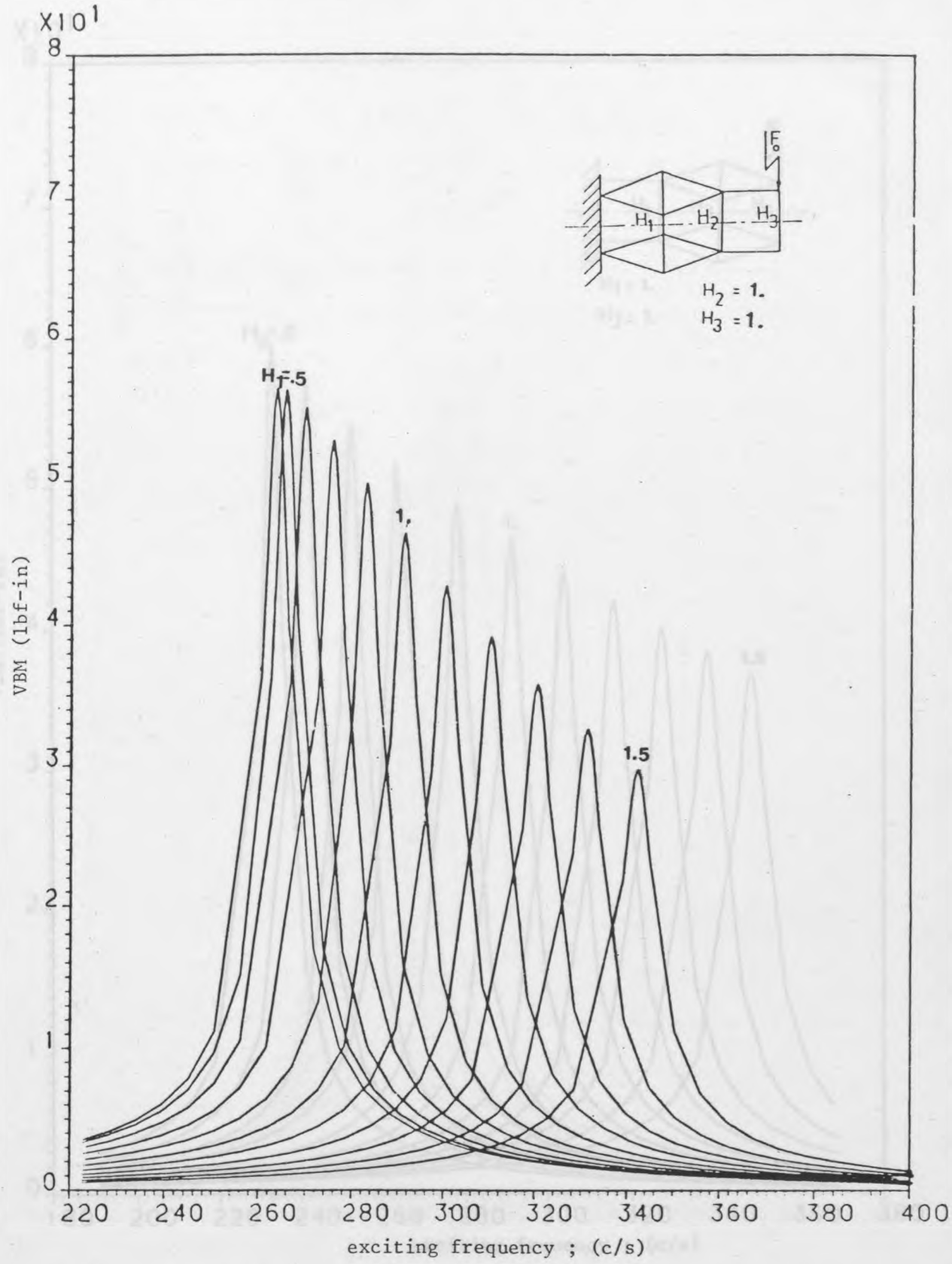

Figure 32 VBM-Frquency Response of the Cantilever Root with Varying H_1 ; (2nd Mode).

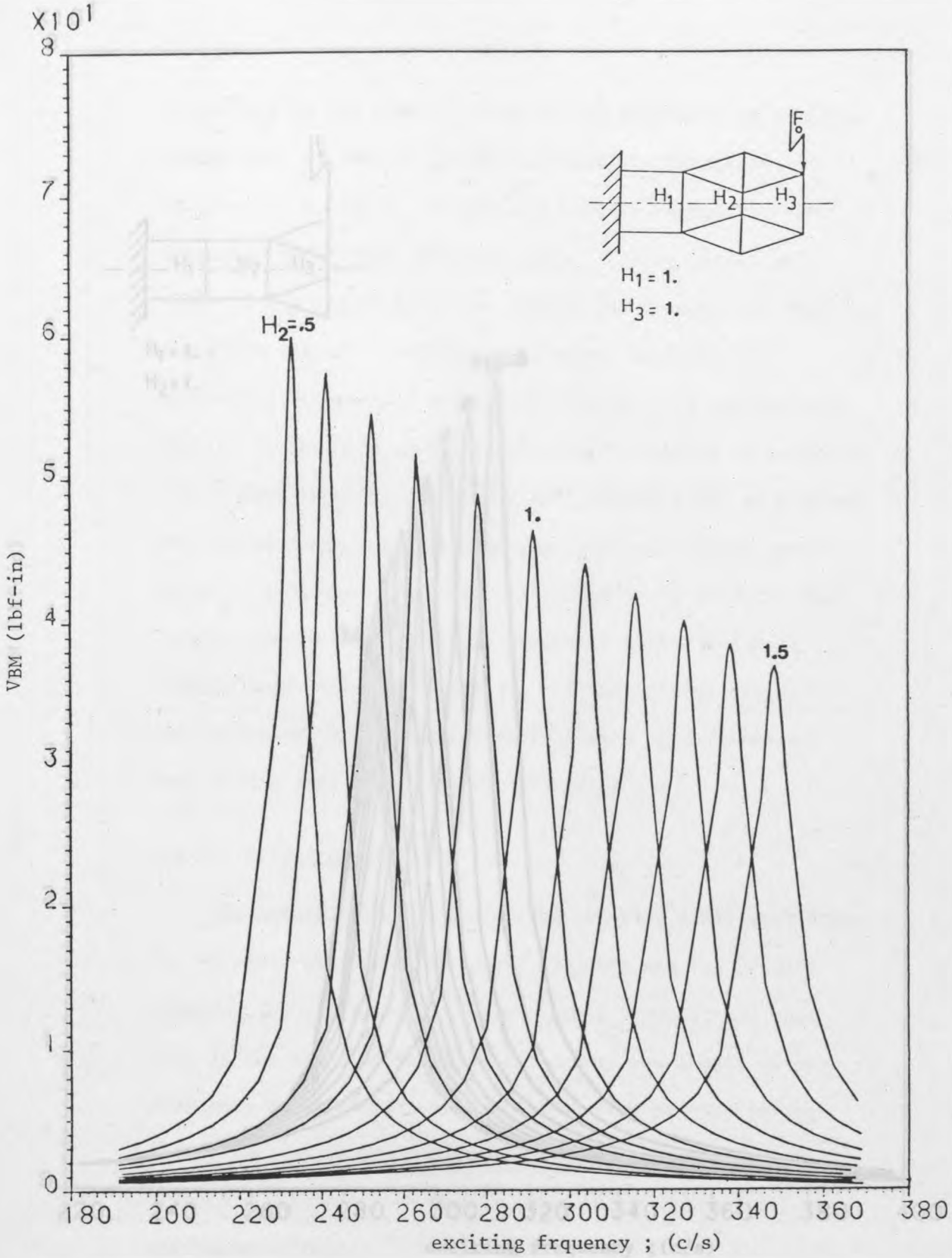

Figure 33 VBM-Frequency Response of the Cantilever Root with Varying H_2 ; (2nd Mode).

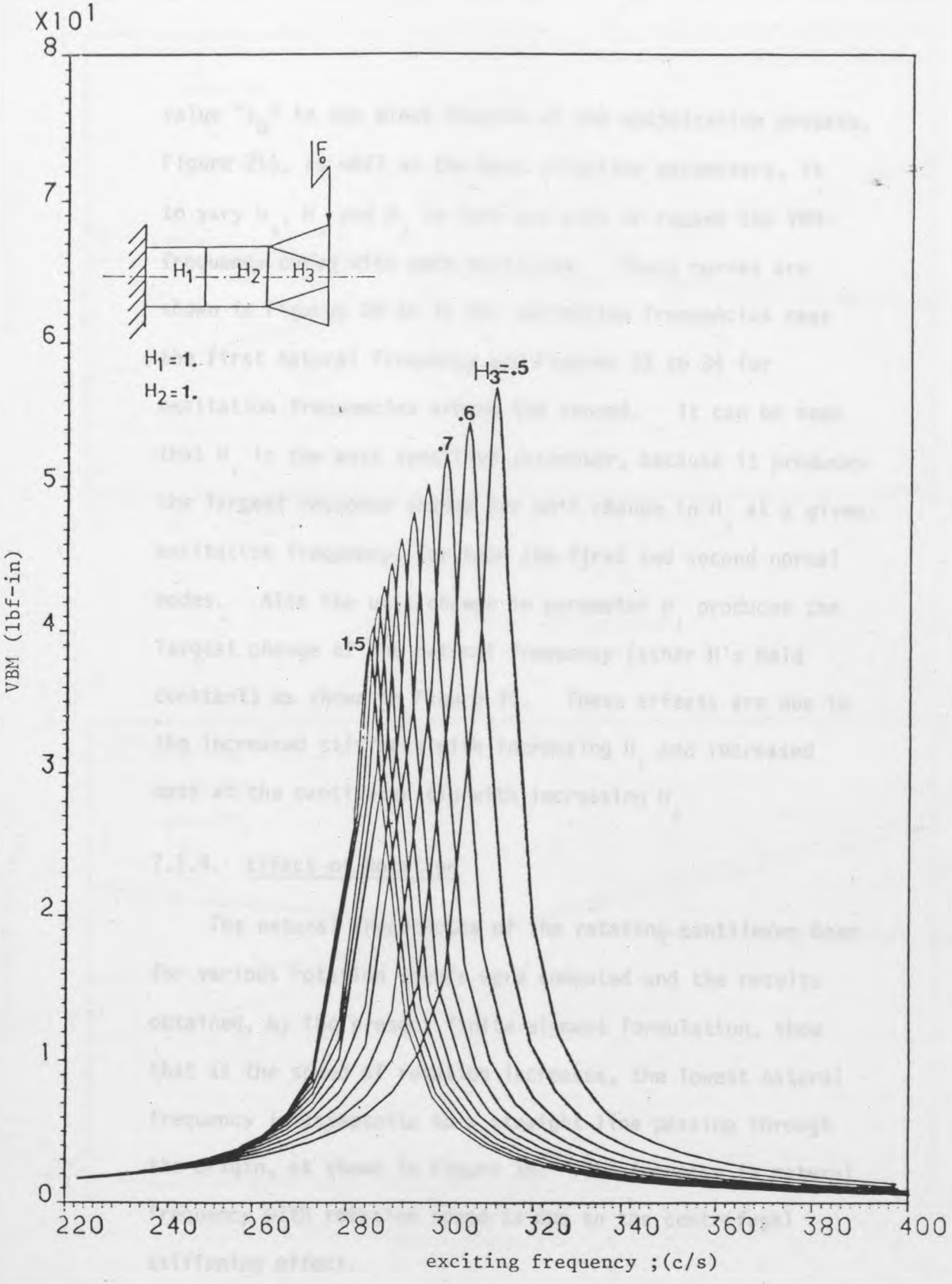

Figure 34 VBM-Frequency Response of the Cantilever Root with Varying H_3 ; (2nd Mode).

value "ε_o" in the block diagram of the optimization process, Figure 21), as well as the most effective parameters, is to vary H_1, H_2 and H_3 in turn and plot or record the VBM-frequency curve with each variation. These curves are shown in Figures 29 to 31 for excitation frequencies near the first natural frequency and Figures 32 to 34 for excitation frequencies around the second. It can be seen that H_1 is the most sensitive parameter, because it produces the largest response change per unit change in H_1 at a given excitation frequency, for both the first and second normal modes. Also the unit change in parameter H_1 produces the largest change of the natural frequency (other H's held constant) as shown in Figure 35. These effects are due to the increased stiffness with increasing H_1 and increased mass at the cantilever tip with increasing H_3.

7.1.4. Effect of Rotation

The natural frequencies of the rotating cantilever beam for various rotation speeds were computed and the results obtained, by the present finite element formulation, show that as the speed of rotation increases, the lowest natural frequency is asymptotic to a straight line passing through the origin, as shown in Figure 36. The increase in natural frequency with rotation speed is due to the centrifugal stiffening effect.

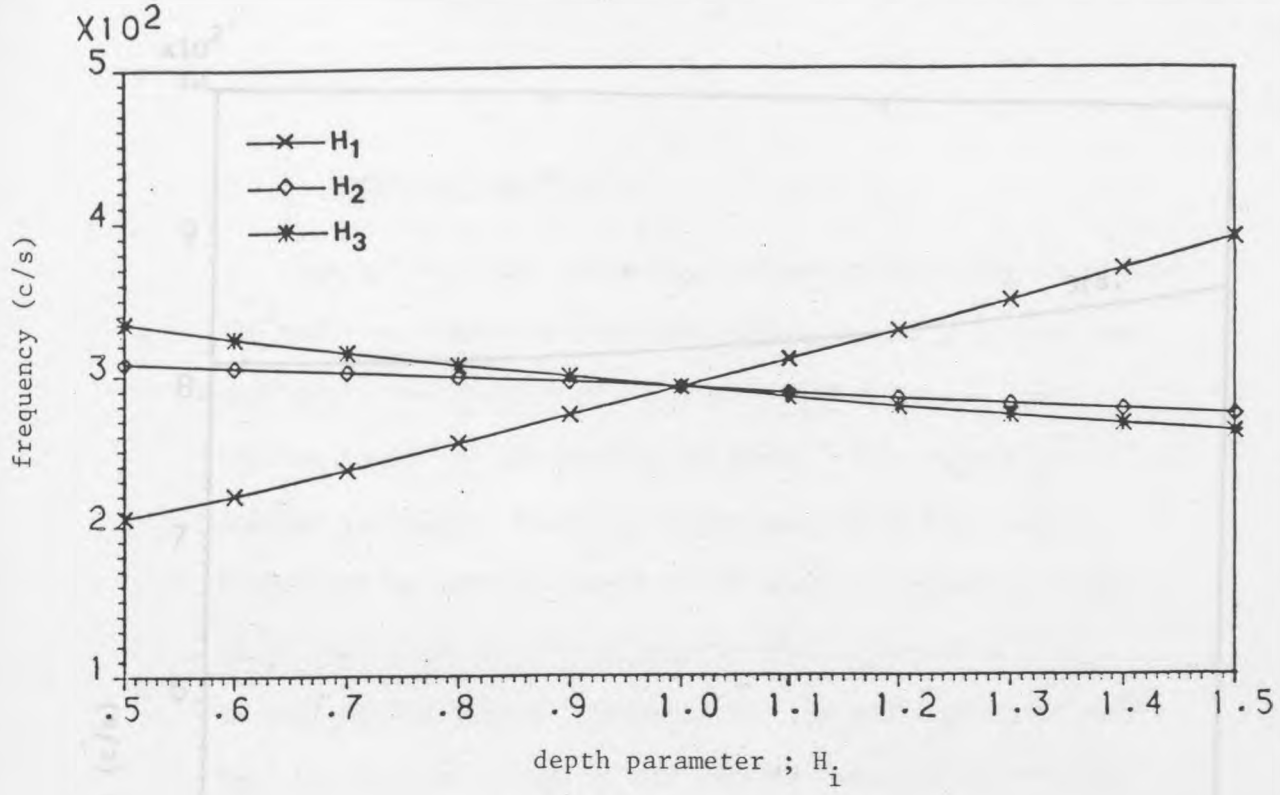

(a) 1st Natural Frequencies

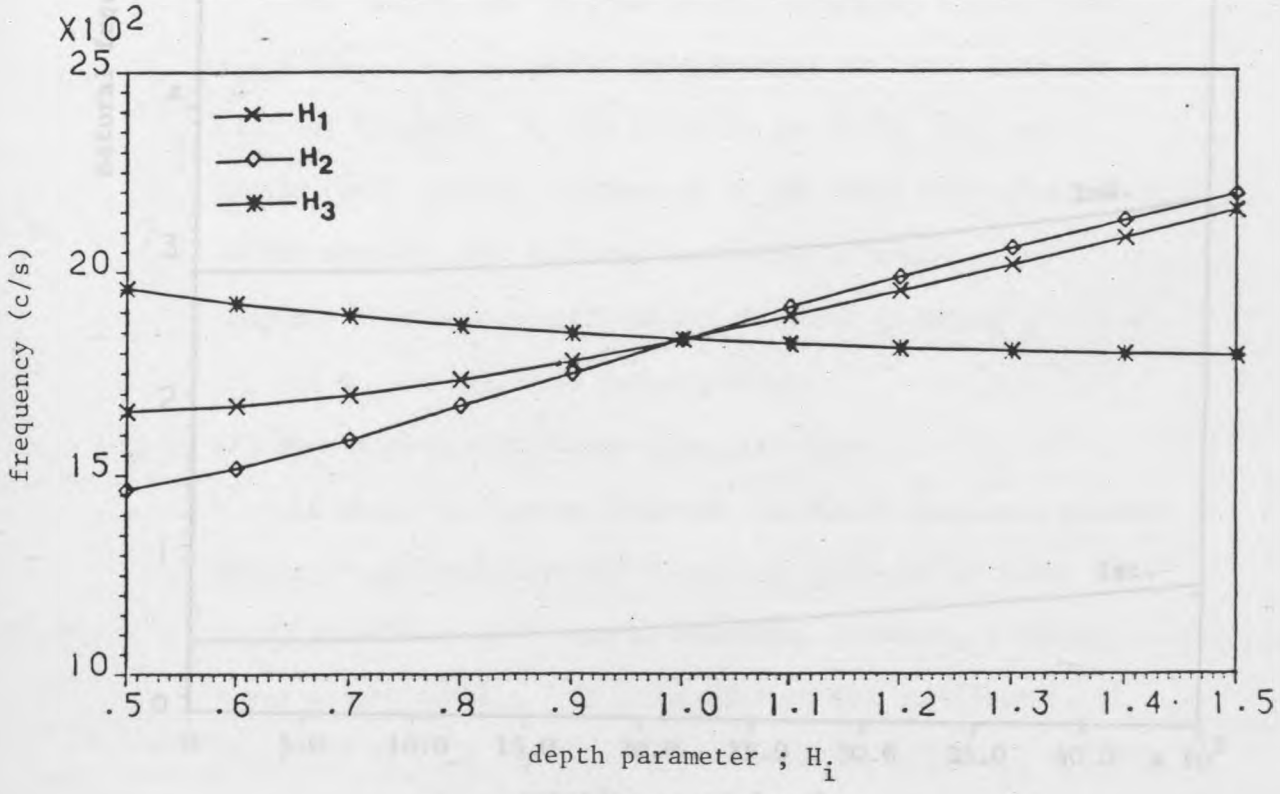

(b) 2nd Natural Frequencies

Figure 35 Change of the Natural Frequencies with Varying H_i ; Other H's being Held Constant.

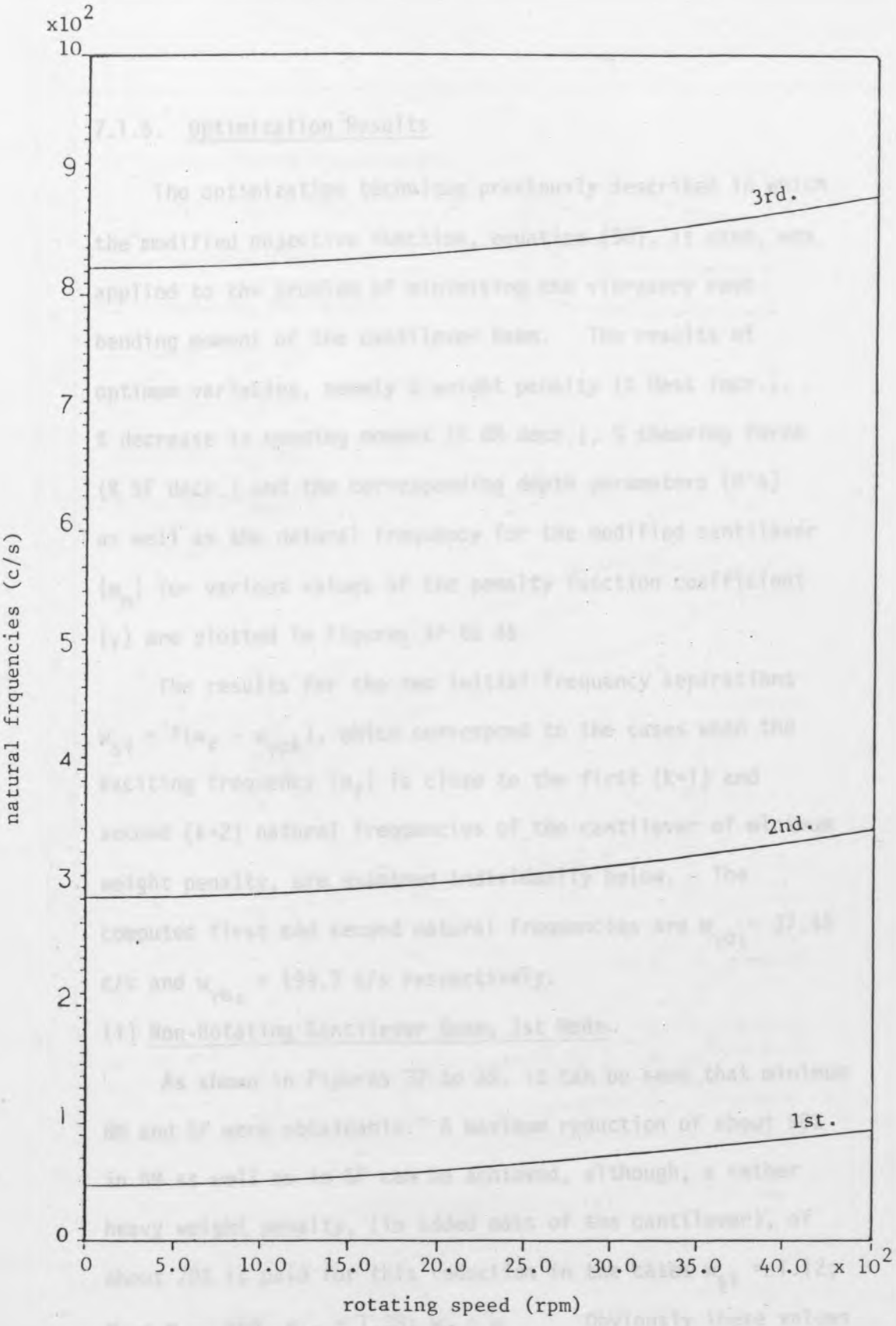

Figure 36 Rotating Cantilever Beam Natural Frquencies Vs. Rotating Speed.

7.1.5. Optimization Results

The optimization technique previously described in which the modified objective function, equation (98), is used, was applied to the problem of minimising the vibratory root bending moment of the cantilever beam. The results of optimum variables, namely % weight penalty (% Mass Incr.), % decrease in bending moment (% BM decr.), % shearing force (% SF decr.) and the corresponding depth parameters (H's) as well as the natural frequency for the modified cantilever (w_n) for various values of the penalty function coefficient (γ) are plotted in Figures 37 to 46.

The results for the two initial frequency separations $w_{si} = \pm(w_f - w_{\gamma ok})$, which correspond to the cases when the exciting frequency (w_f) is close to the first (k=1) and second (k=2) natural frequencies of the cantilever of minimum weight penalty, are examined individually below. The computed first and second natural frequencies are $w_{\gamma o_1} = 37.45$ c/s and $w_{\gamma o_2} = 199.7$ c/s respectively.

(i) Non-Rotating Cantilever Beam; 1st Mode

As shown in Figures 37 to 39, it can be seen that minimum BM and SF were obtainable. A maximum reduction of about 90% in BM as well as in SF can be achieved, although, a rather heavy weight penalty, (in added mass of the cantilever), of about 70% is paid for this reduction in the cases $w_{si} = 1.12$; $w_f < w_{\gamma o1}$ and $w_{si} = 1.38$; $w_f > w_{\gamma o_2}$ Obviously these values

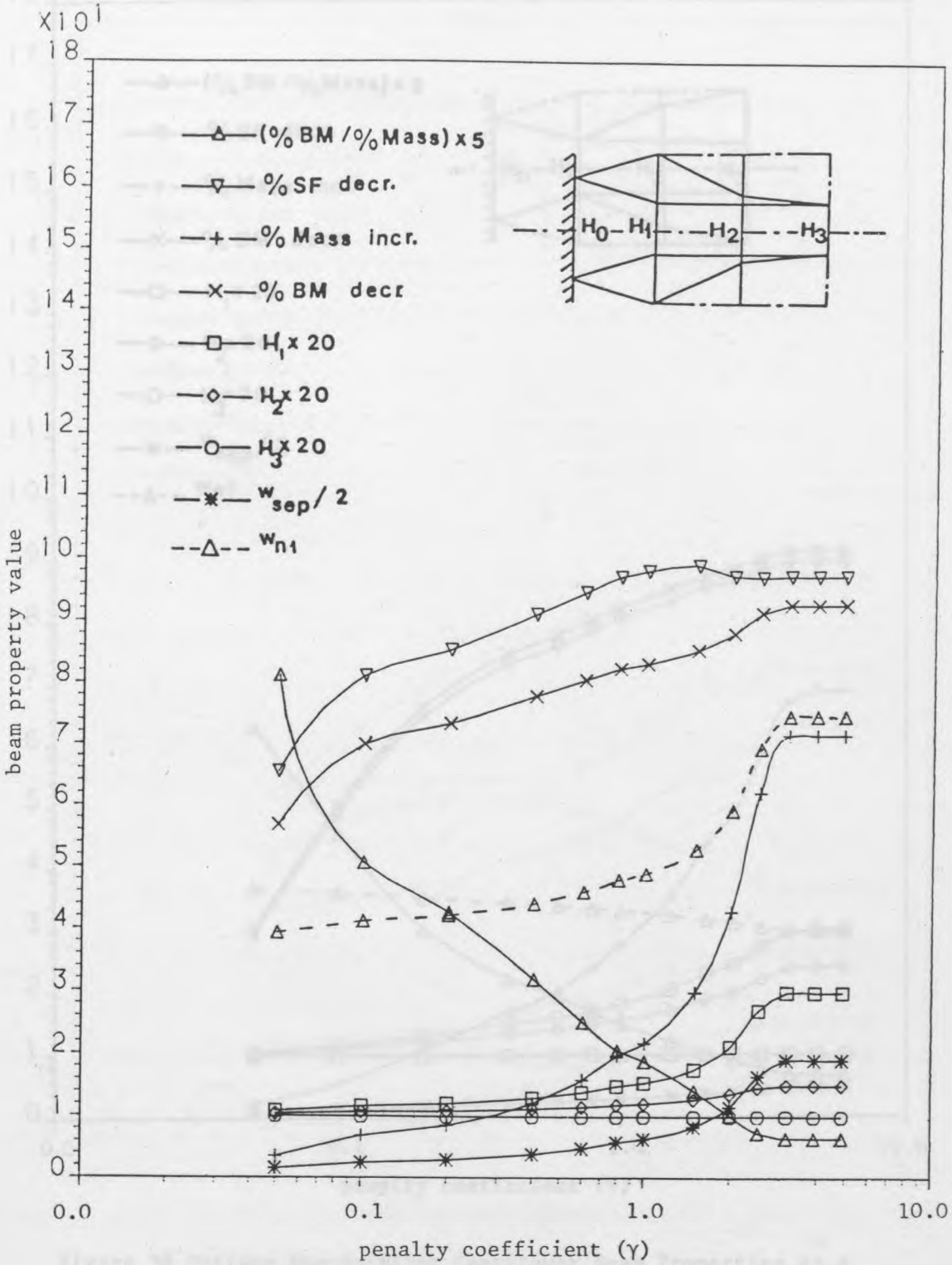

Figure 37 Optimum Non-Rotating Cantilever Beam Properties as a Function of penalty Coefficient ; 1st Mode, $w_{si} = 1.12$ and $w_f < w_{\gamma 01}$

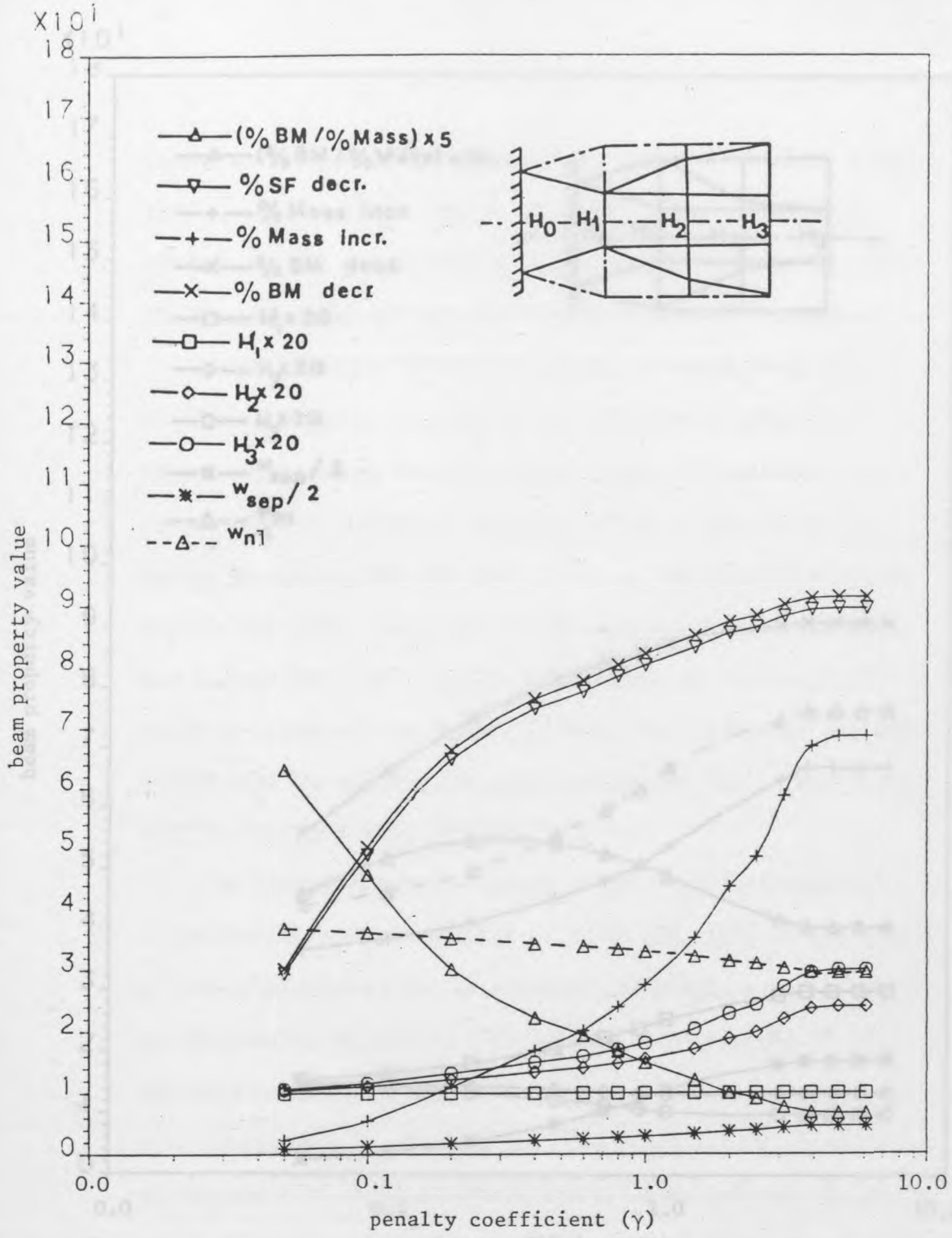

Figure 38 Optimum Non-Rotating Cantilever Beam Properties as a Function of penalty Coefficient ; 1st Mode , $w_{si} = 1.38$ and $w_f > w_{\gamma_{01}}$

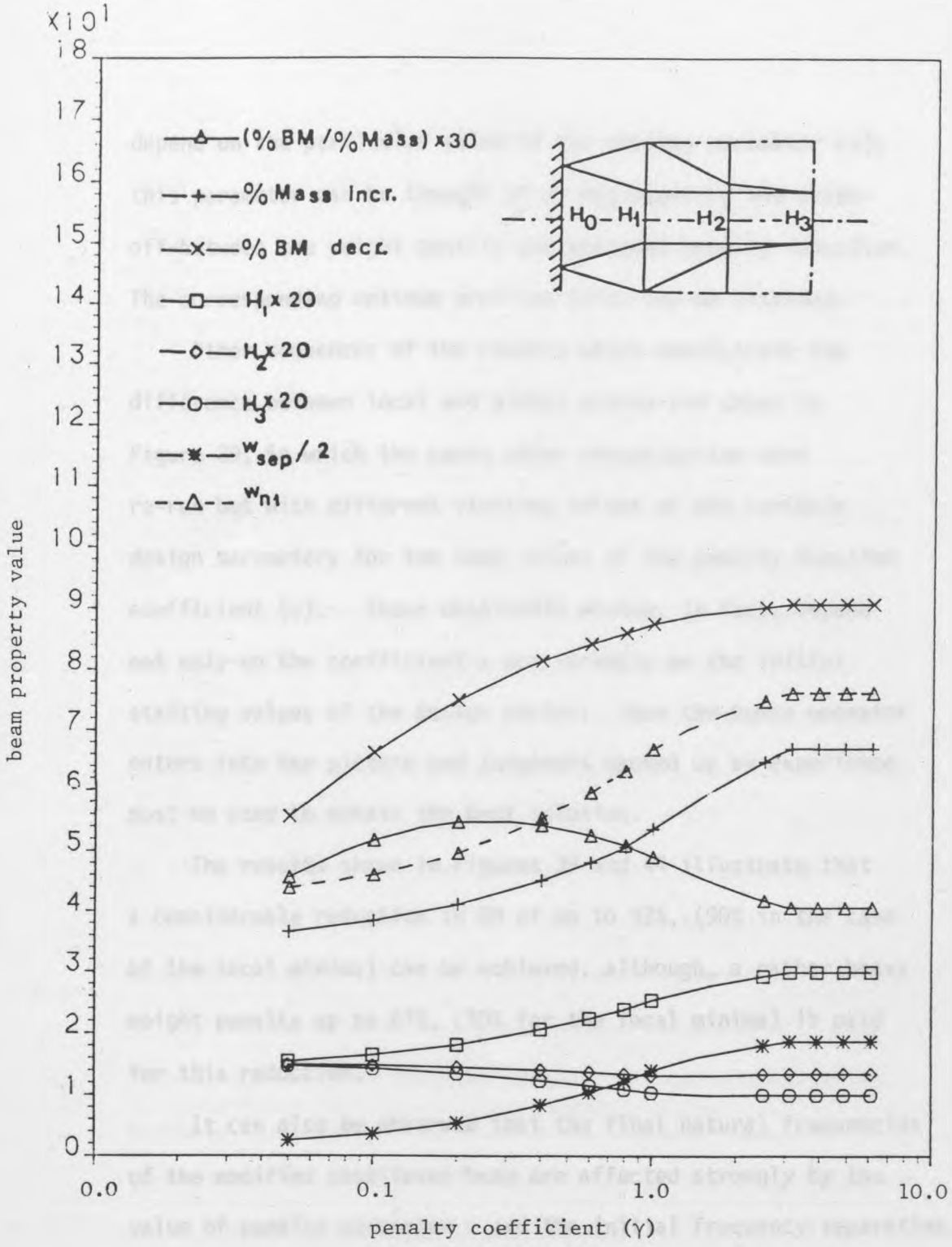

Figure 39 Optimum Non-Rotating Cantilever Beam Properties as a Function of Penalty Coefficient ; 1st Mode , $w_{si} = 1.38$ and $w_f > w_{\gamma_{01}}$ - Global Minima

depend on the particular value of the penalty parameter (γ); this parameter can be thought of as representing the trade-off between the weight penalty and achieved bending reduction. The corresponding optimum profiles (H's) can be attained.

Other sequences of the results which demonstrate the difference between local and global minima are shown in Figure 39, in which the cases under investigation were re-run but with different starting values of the variable design parameters for the same values of the penalty function coefficient (γ). These obtainable minima, in fact, depend not only on the coefficient γ but strongly on the initial starting values of the design vector; thus the human operator enters into the picture and judgement backed up by experience must be used to obtain the best solution.

The results shown in Figures 39 and 44 illustrate that a considerable reduction in BM of up to 92%, (90% in the case of the local minima) can be achieved, although, a rather heavy weight penalty up to 67%, (70% for the local minima) is paid for this reduction.

It can also be observed that the final natural frequencies of the modified cantilever beam are affected strongly by the value of penalty parameter γ and the initial frequency separation. With an increase of γ the frequency separation w_{sep}, (which is equal to the absolute difference between the exciting frequency and the natural frequency of the modified cantilever), was found to be increased. For the case in which $w_{si} = 1.12$;

$w_f < w_{\gamma o1}$ the natural frequency was increased by an amount 105%. On the other hand it was found to be decreased by an amount 21%, for the case in which $w_{si} = 1.38$; $w_f > w_{\gamma o1}$. These effects are due to increased stiffness, (the increase of H_1) in the first case and the increased mass on the cantilever tip, (the increase of H_3) in the second case.

ii) Non-Rotating Cantilever Beam; 2nd Mode

Computed results for this case are presented in Figures 40 and 41. The exciting frequency was changed around the second natural frequency $w_{\gamma o_2}$, i.e. $w_{si} = 1.16$; $w_f < w_{\gamma o2}$ and $w_{si} = 1.34$; $w_f > w_{\gamma o2}$ and it may be seen that compared with first case (i) for the same values of penalty parameter (γ) the design variable required 18 stages to converge. Also a 80% to 98% reduction in BM (as well as in SF) can be achieved. On the other hand the cantilever mass must be increased by about 4% to 11% respectively. It can also be observed that with the change of initial frequency separation, from $w_{si} = 1.16$ to $w_{si} = 1.34$, around the second natural frequency $w_{\gamma o2}$ the resultant changes in computed profiles are quite small which suggests that one configuration might usefully represent an approximate solution for different cases of exciting frequency which are very close to the second natural frequency (199.7 c/s).

iii) Rotating Cantilever Beam; 1st Mode

The results are plotted in Figures 42 to 44 for the cantilever rotating at 500 r.p.m., when the exciting frequency

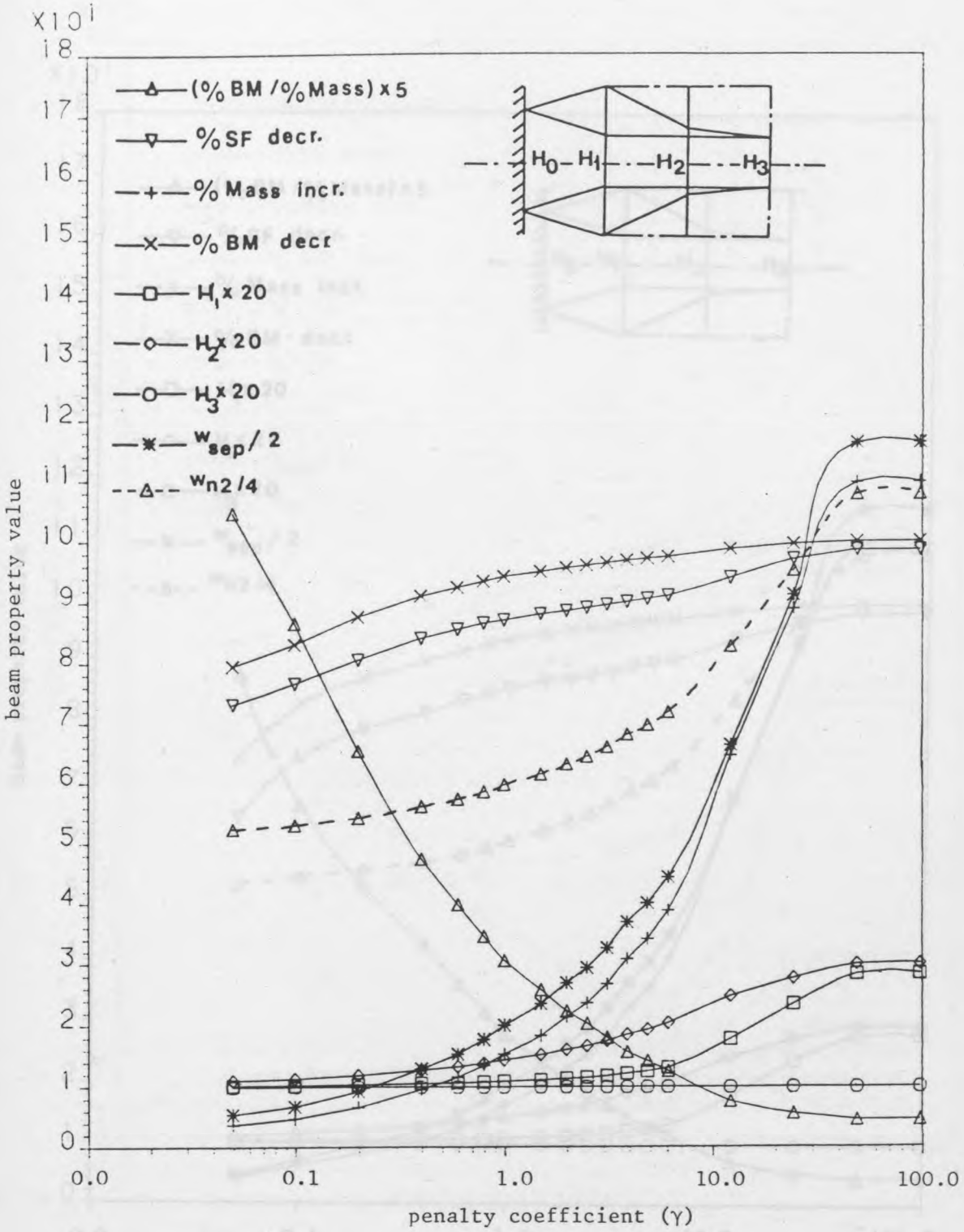

Figure 40 Optimum Non-Rotating Cantilever Beam Properties as a Function of Penalty Coefficient ; 2nd Mode , $w_{si} = 1.16$ and $w_f < w_{\gamma_0 2}$

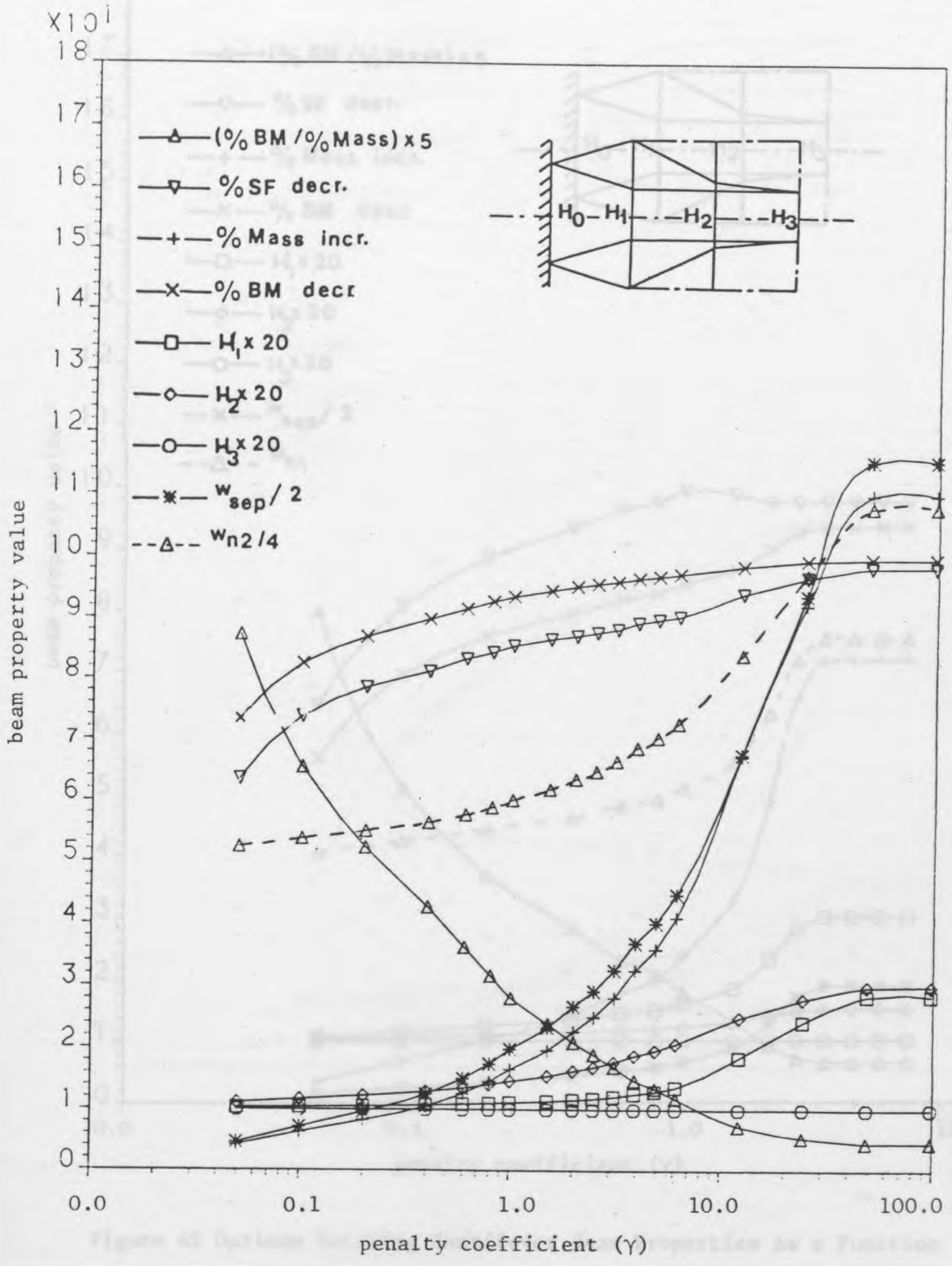

Figure 41 Optimum Non-Rotating Cantilever Beam Properties as a Function of Penalty Coefficient ; 2nd Mode , $w_{si} = 1.34$ and $w_f > w_{\gamma_{02}}$

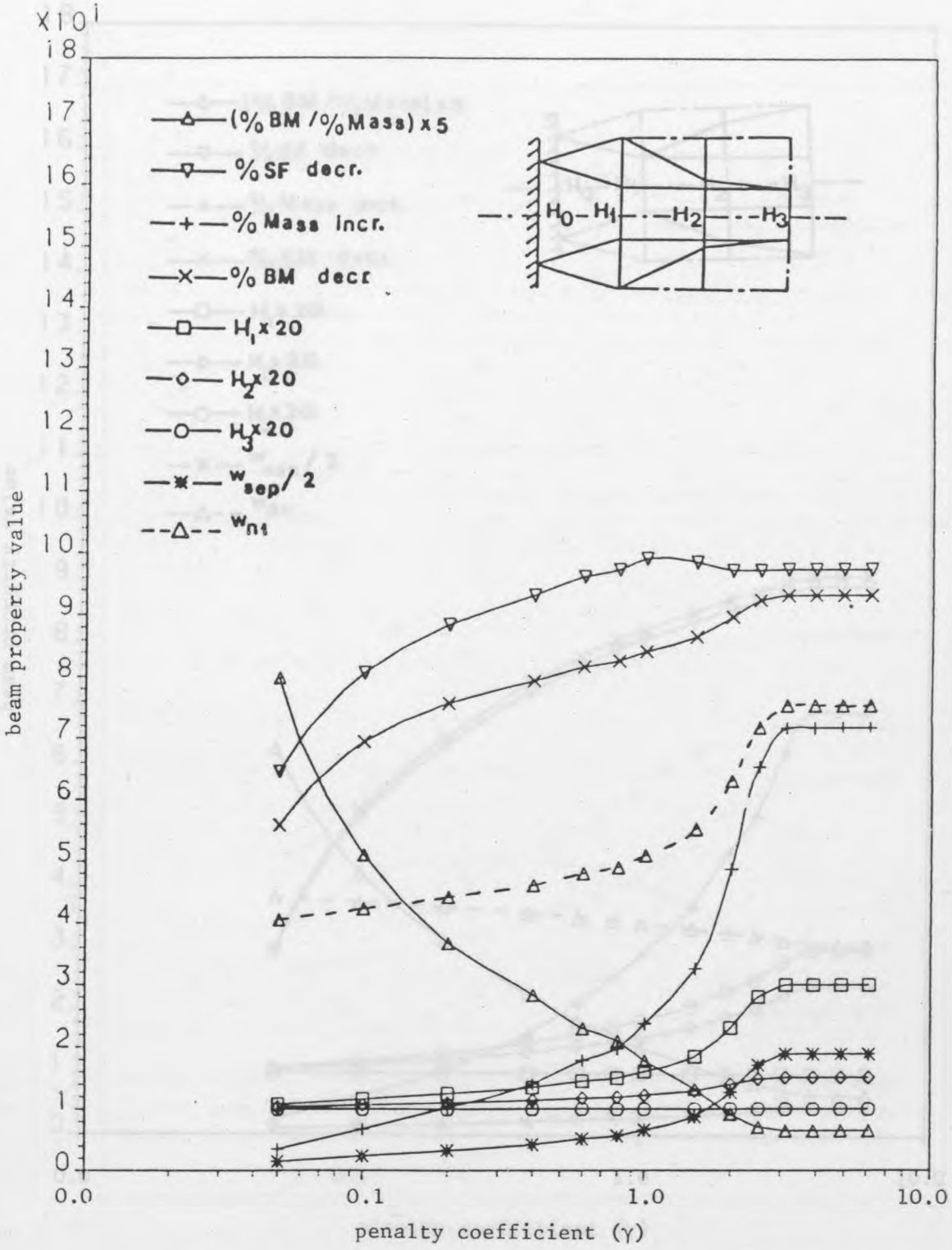

Figure 42 Optimum Rotating Cantilever Beam Properties as a Function of Penalty Coefficient with Rotating Speed Equal to 500 rpm ; (1st Mode) , w_{si} = 1.12 and $w_f < w_{\gamma 01}$

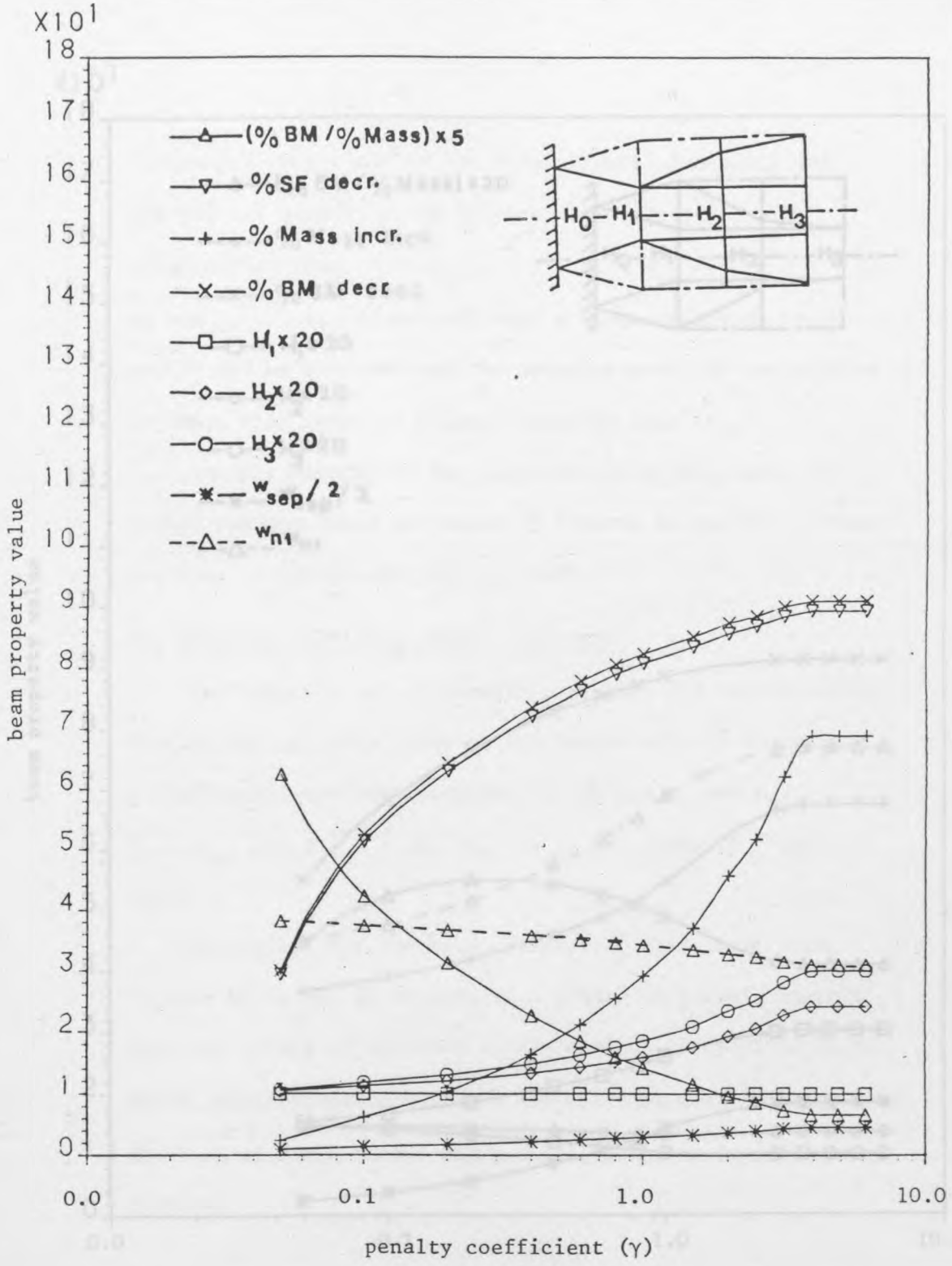

Figure 43 Optimum Rotating Cantilever Beam Properties as a Function of Penalty Coefficient with Rotating Speed Equal to 500 rpm ; - (1st Mode) , w_{si} = 1.38 and $w_f > w_{\gamma 01}$

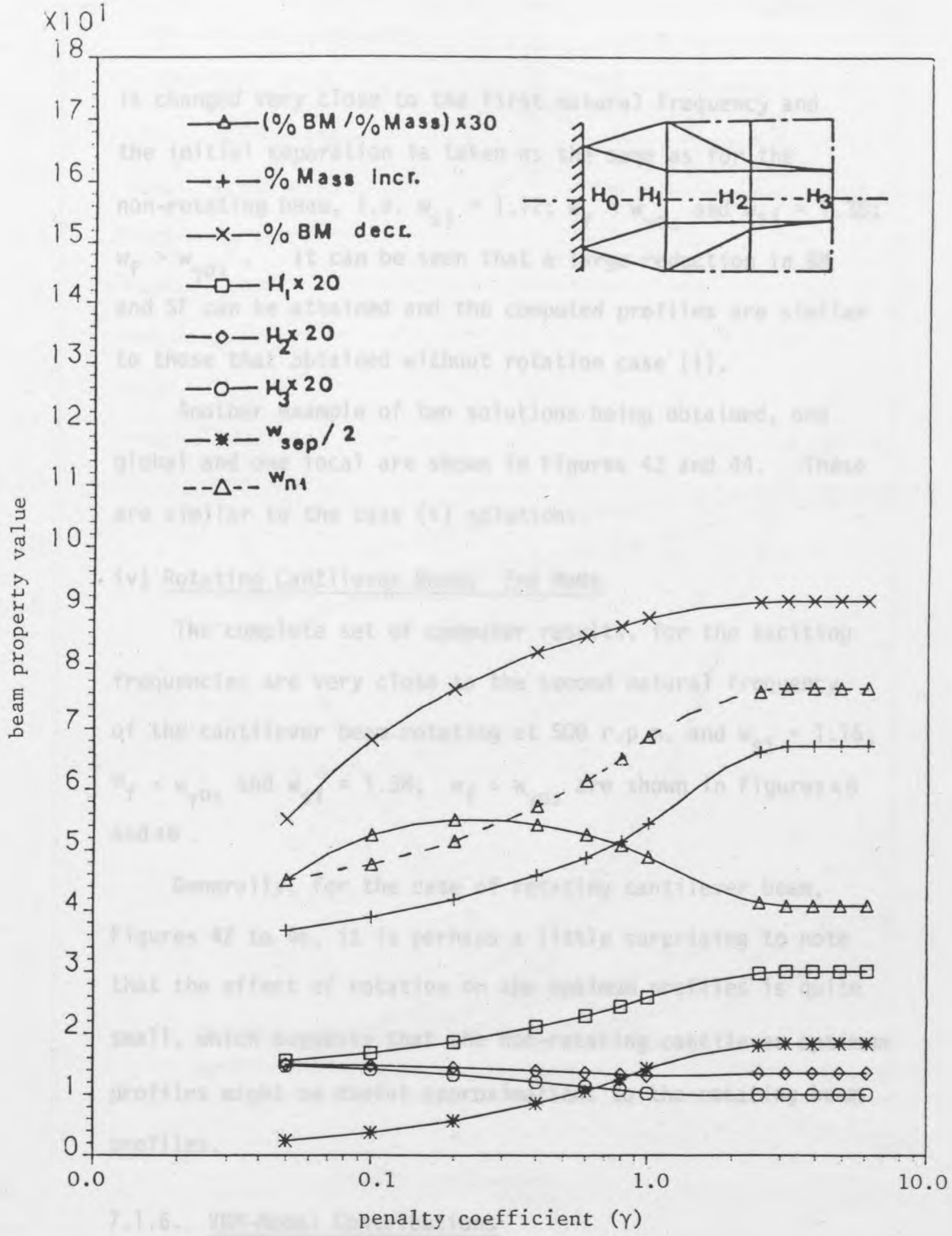

Figure 44 Optimum Rotating Cantilever Beam Properties as a Function of Penalty Coefficient with Rotating Speed Equal to 500 rpm ; (1st Mode) , $w_{si} = 1.38$ and $w_f > w_{\gamma_{01}}$ - Global Minima

is changed very close to the first natural frequency and the initial separation is taken as the same as for the non-rotating beam, i.e. $w_{si} = 1.12$; $w_f < w_{\gamma o_1}$ and $w_{si} = 1.38$; $w_f > w_{\gamma o_1}$. It can be seen that a large reduction in BM and SF can be attained and the computed profiles are similar to those that obtained without rotation case (i).

Another example of two solutions being obtained, one global and one local are shown in Figures 43 and 44. These are similar to the case (i) solutions.

iv) Rotating Cantilever Beam; 2nd Mode

The complete set of computer results, for the exciting frequencies are very close to the second natural frequency of the cantilever beam rotating at 500 r.p.m. and $w_{si} = 1.16$; $w_f < w_{\gamma o_2}$ and $w_{si} = 1.38$; $w_f > w_{\gamma o_2}$ are shown in Figures 45 and 46.

Generally, for the case of rotating cantilever beam, Figures 42 to 46, it is perhaps a little surprising to note that the effect of rotation on the optimum profiles is quite small, which suggests that the non-rotating cantilever optimum profiles might be useful approximations to the rotating beam profiles.

7.1.6. VBM-Modal Contributions

Computations of the vibration bending moment of the cantilever beam for certain situations in which the beam configuration remains constant for an increase in γ

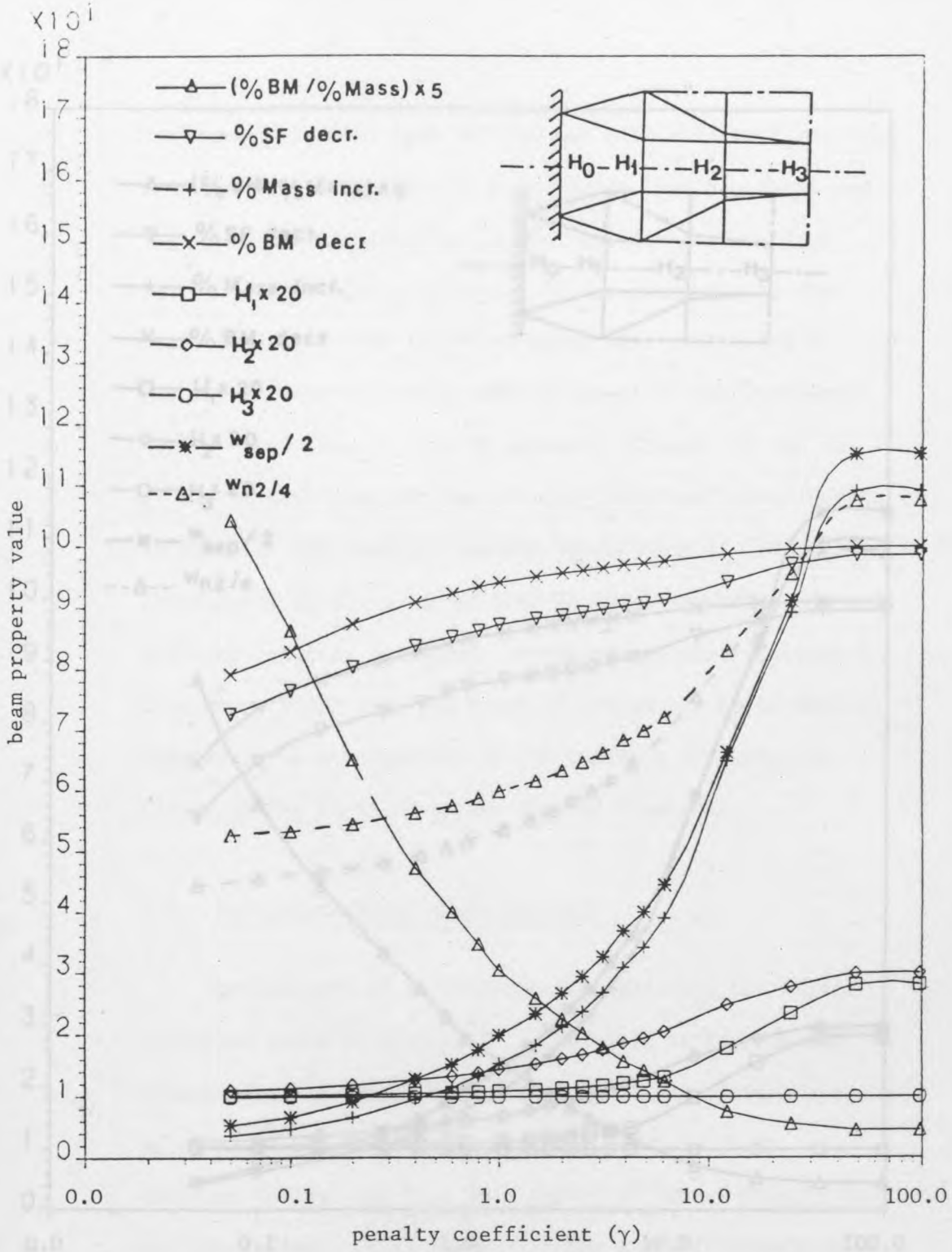

Figure 45 Optimum Rotating Cantilever Beam Properties as a Function of Penalty Coefficient with Rotating Speed Equal to 500 rpm ; (2nd Mode) , w_{si} = 1.16 and $w_f < w_{\gamma 02}$

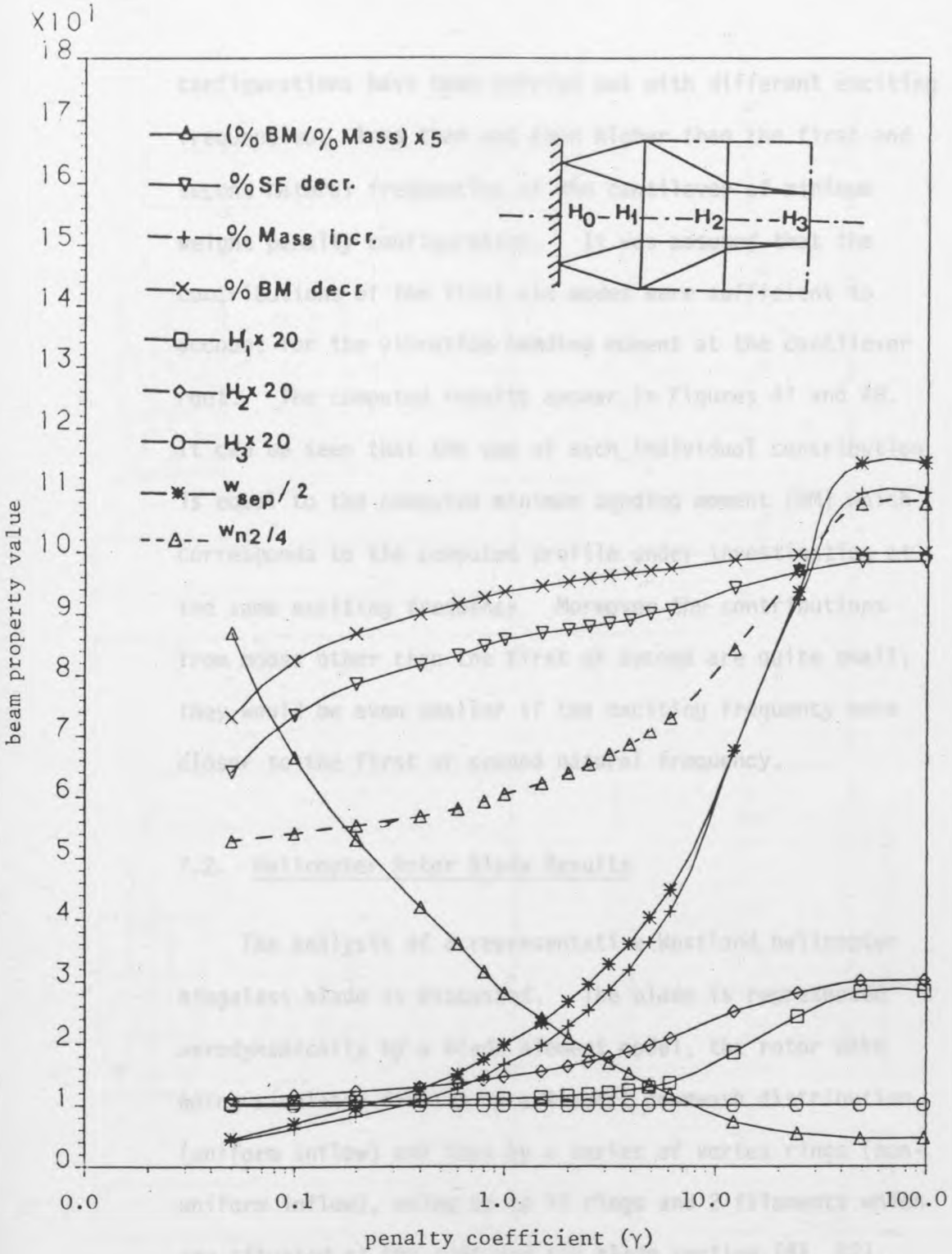

Figure 46 Optimum Rotating Cantilever Beam Properties as a Function of Penalty Coefficient with Rotating Speed Equal to 500 rpm ; (2nd Mode) , $w_{si} = 1.34$ and $w_f > w_{\gamma_{02}}$

configurations have been carried out with different exciting frequencies; less than and then higher than the first and second natural frequencies of the cantilever of minimum weight penalty configuration. It was assumed that the contributions of the first six modes were sufficient to account for the vibration bending moment at the cantilever root. The computed results appear in Figures 47 and 48. It can be seen that the sum of each individual contribution is equal to the computed minimum bending moment (BM) which corresponds to the computed profile under investigation at the same exciting frequency. Moreover the contributions from modes other than the first or second are quite small; they would be even smaller if the exciting frequency were closer to the first or second natural frequency.

7.2. Helicopter Rotor Blade Results

The analysis of a representative Westland helicopter hingeless blade is discussed. The blade is represented aerodynamically by a blade element model, the rotor wake being simulated firstly by a Glauert downwash distribution (uniform inflow) and then by a series of vortex rings (non-uniform inflow), using up to 12 rings and 2 filaments which are situated at the root and tip blade section [81, 82], (vortex ring model "RAE-Farnborough"). Aerofoil section lift was obtained from tabular data ($C_{\ell} = 5.7$). Dynamic stall and three dimensional effects were not included, only

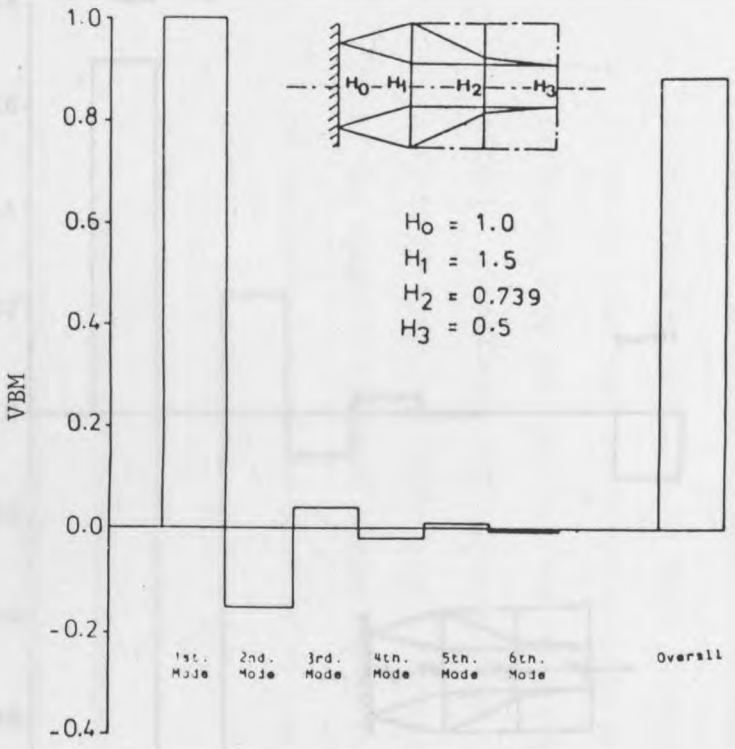

(a) w_{si} = 1.12 , $w_f < w_{\gamma_{01}}$ and γ = 3.13

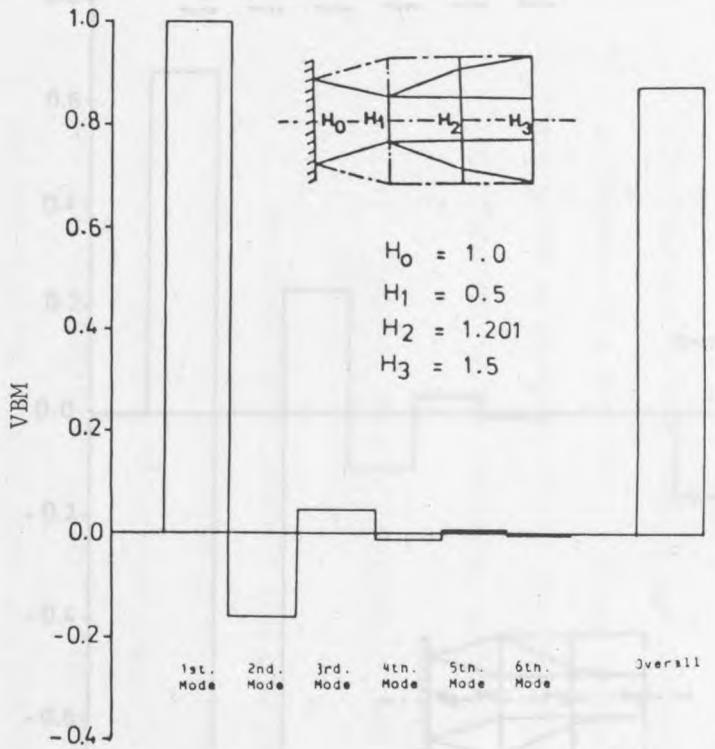

(b) $w_{si} = 1.38$, $w_f > w_{\gamma_{01}}$ and γ = 4.88

Figure 47 Normalized VBM Mode Contributions for the Optimized Cantilever Beam ; Min. Poss Bending Moment , 1st Natural Frequency.

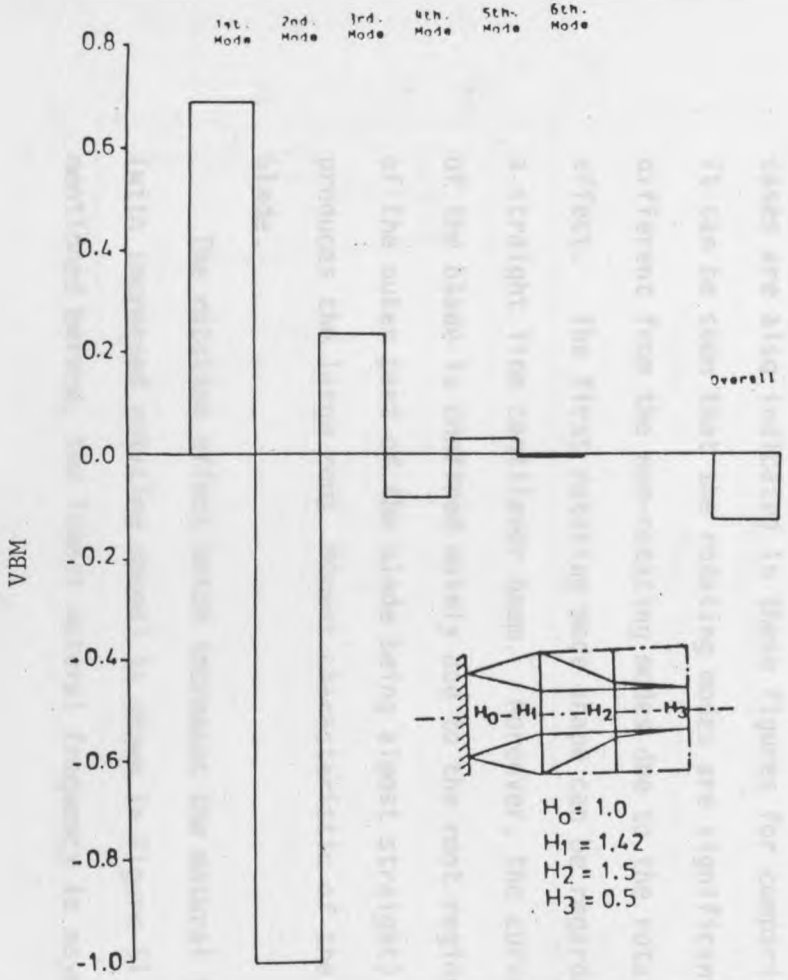

(a) w_{si} = 1.16 , $w_f < w_{\gamma_{02}}$ and γ = 48.83

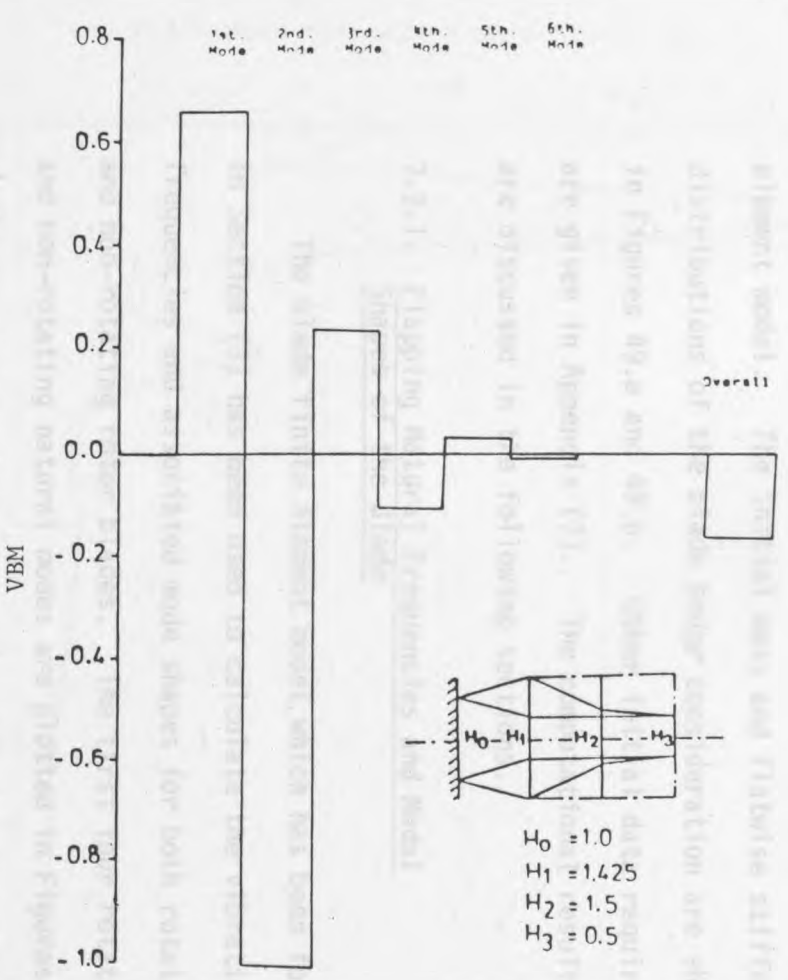

(b) w_{si} = 1.34 , $w_f > w_{\gamma_{02}}$ and γ = 48.83

Figure 48 Normalised VBM Mode Contributions for the Optimized Cantilever Beam ; Min. Poss Bending Moment , 2nd Natural Frequency.

flapping deflection being considered using a 24-finite element model. The initial mass and flatwise stiffness distributions of the blade under consideration are shown in Figures 49.a and 49.b. Other initial data required are given in Appendix (7). The computational results are discussed in the following sections.

7.2.1. Flapping Natural Frequencies and Modal Shapes of the Blade

The blade finite element model which has been formulated in Section (3) has been used to calculate the vibration frequencies and associated mode shapes for both rotating and non-rotating rotor blades. The first four rotating and non-rotating natural modes are plotted in Figures 50.a to 50.d. The resultant natural frequencies for the two cases are also indicated in these figures for comparison. It can be seen that the rotating modes are significantly different from the non-rotating modes due to the rotation effect. The first rotating mode shape can be regarded as a straight line cantilever beam. Moreover, the curvature of the blade is confined mainly due to the root region (most of the outer part of the blade being almost straight). It produces the large root moment characteristic of the hingeless blade.

The rotation effect which increases the natural frequencies (with increased rotating speed) is shown in Figure 51. As mentioned before, the lowest natural frequency is asymptotic

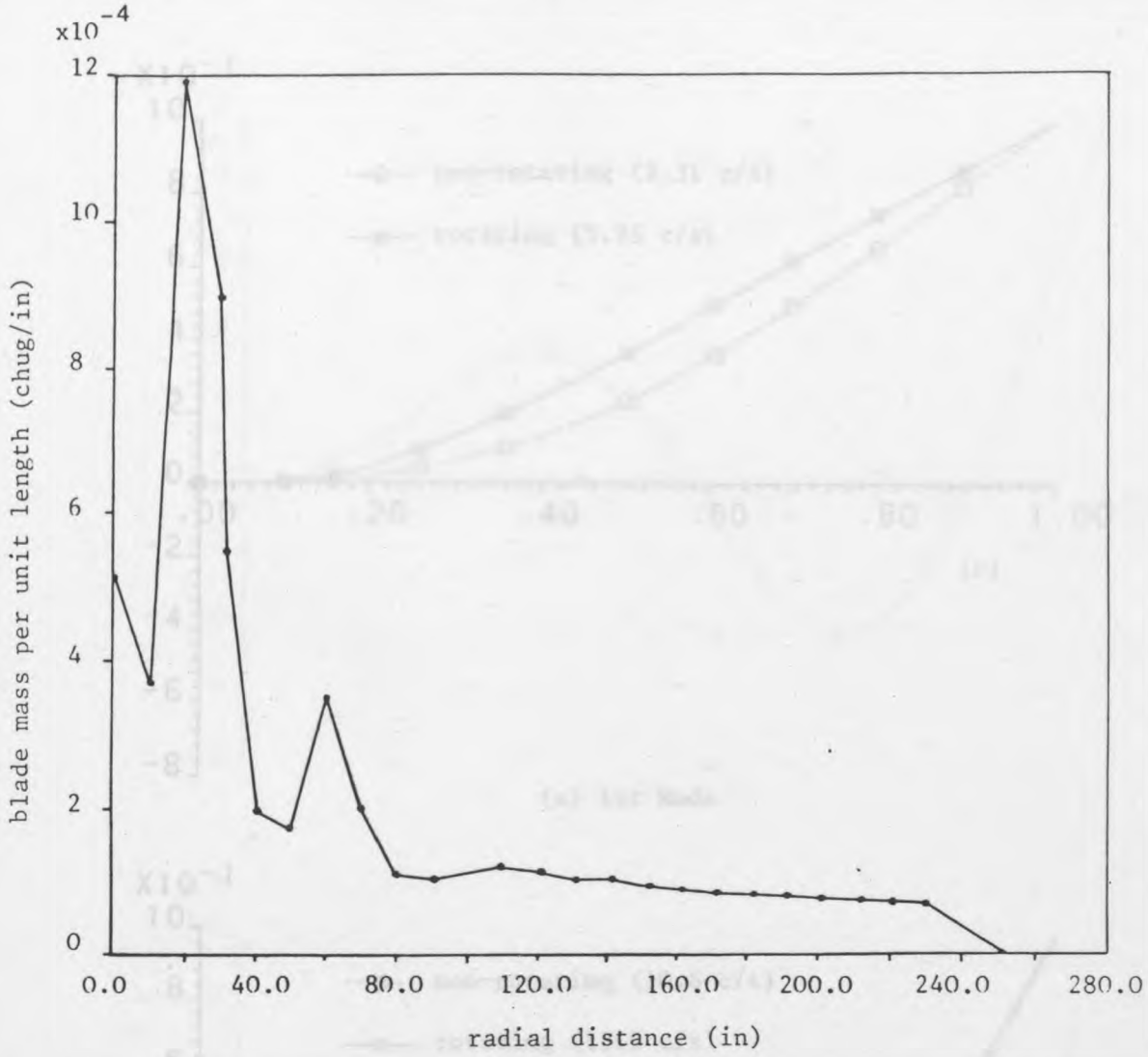

Figure (49.a) Blade Mass Distribution

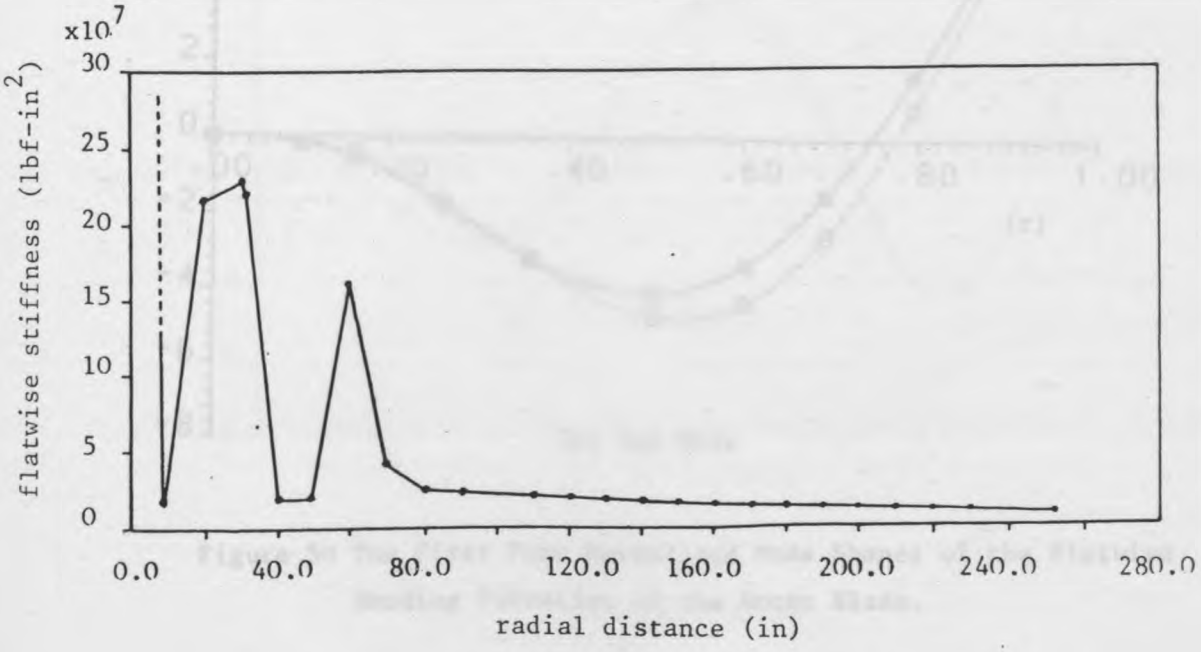

Figure (49.b) Blade Flatwise Stiffness Distribution

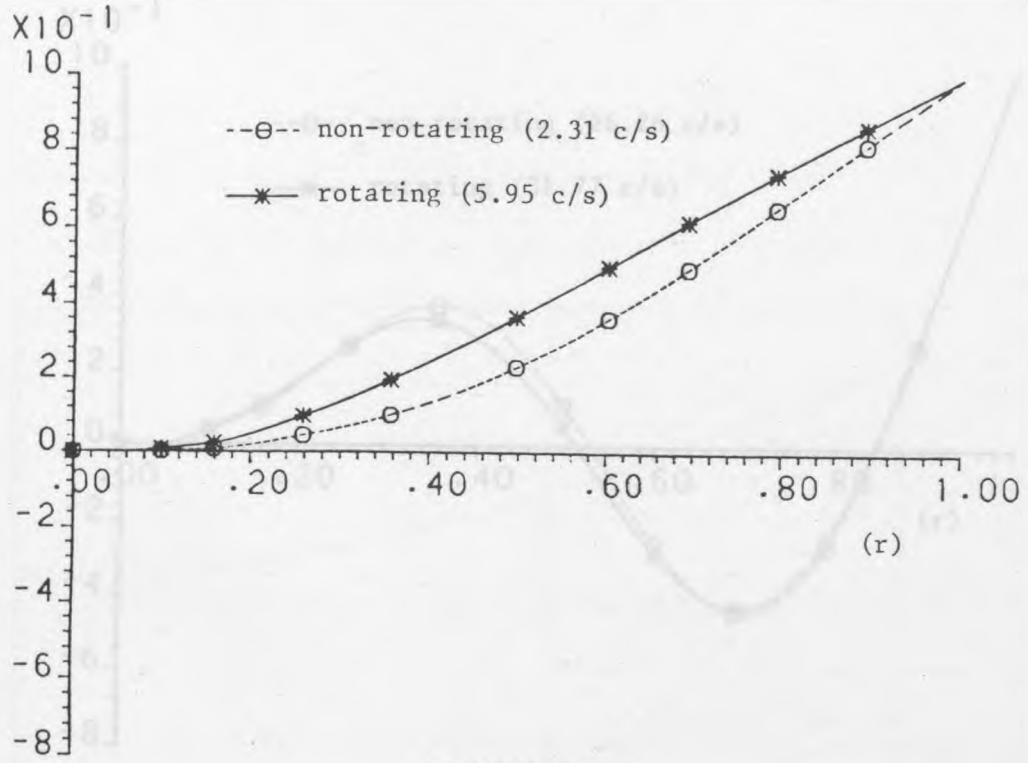

(a) 1st Mode

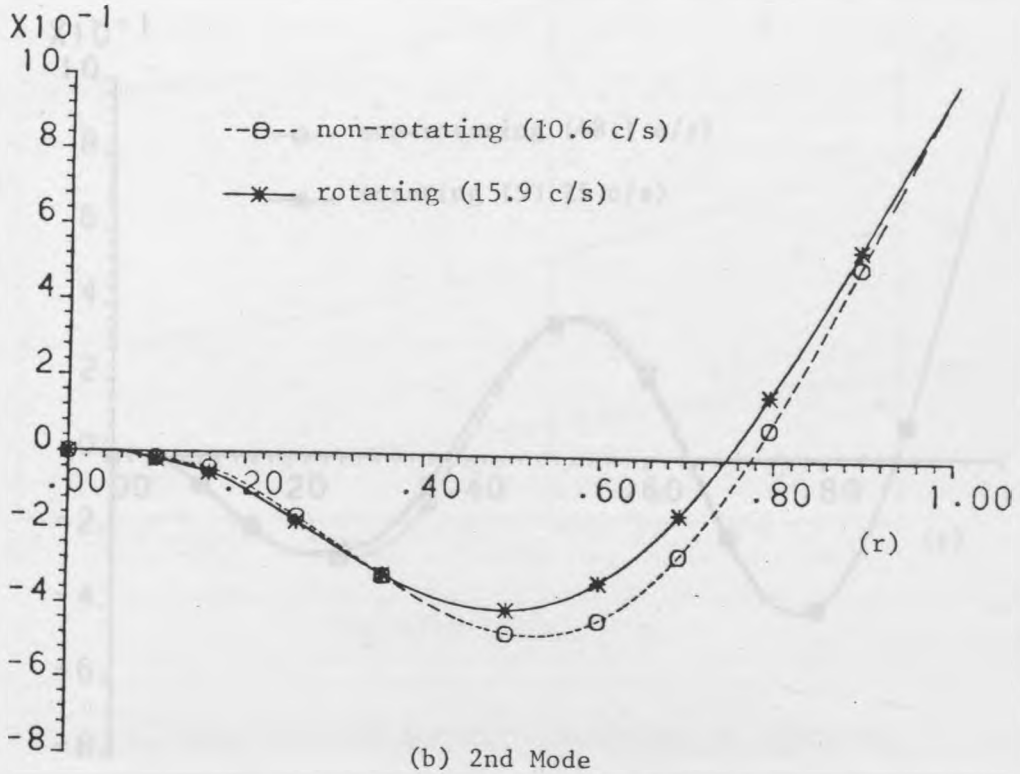

(b) 2nd Mode

Figure 50 The First Four Normalized Mode Shapes of the Flatwise Bending Vibration of the Rotor Blade.

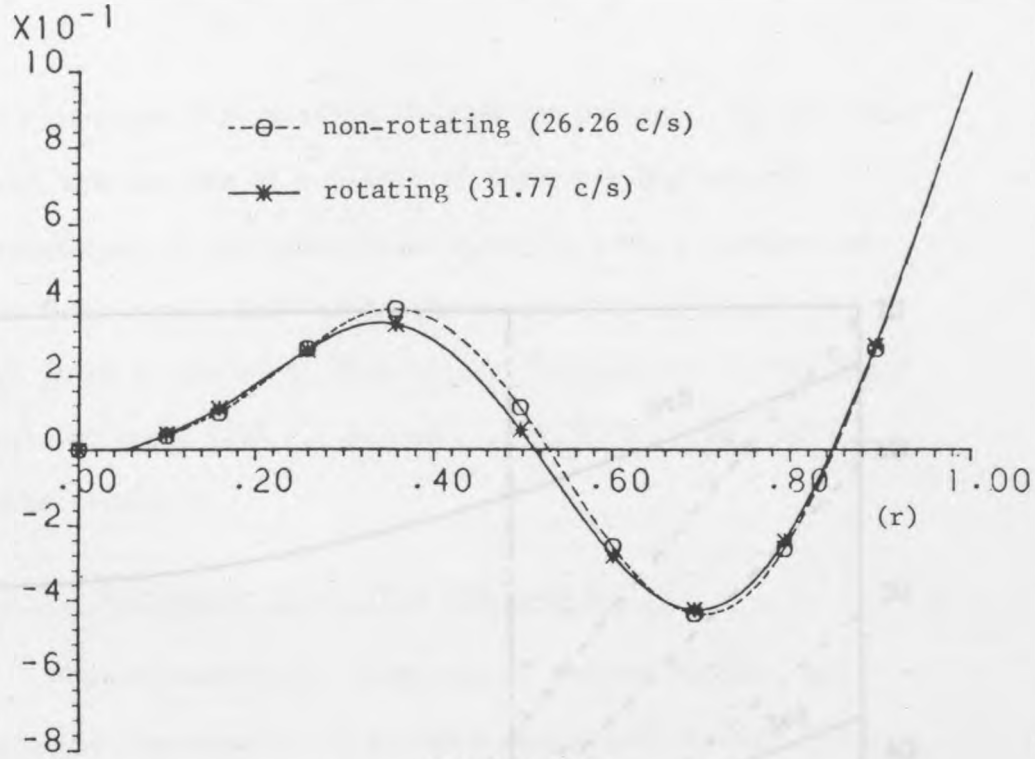

(c) 3rd Mode

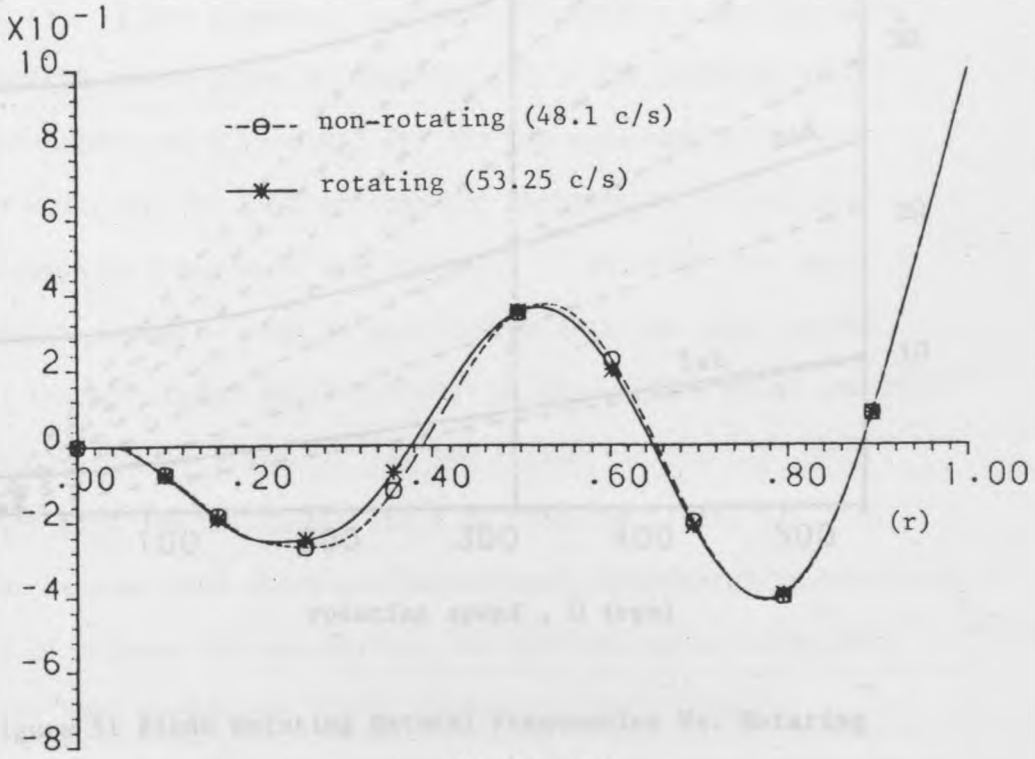

(d) 4th Mode

Figure 50 Cont.

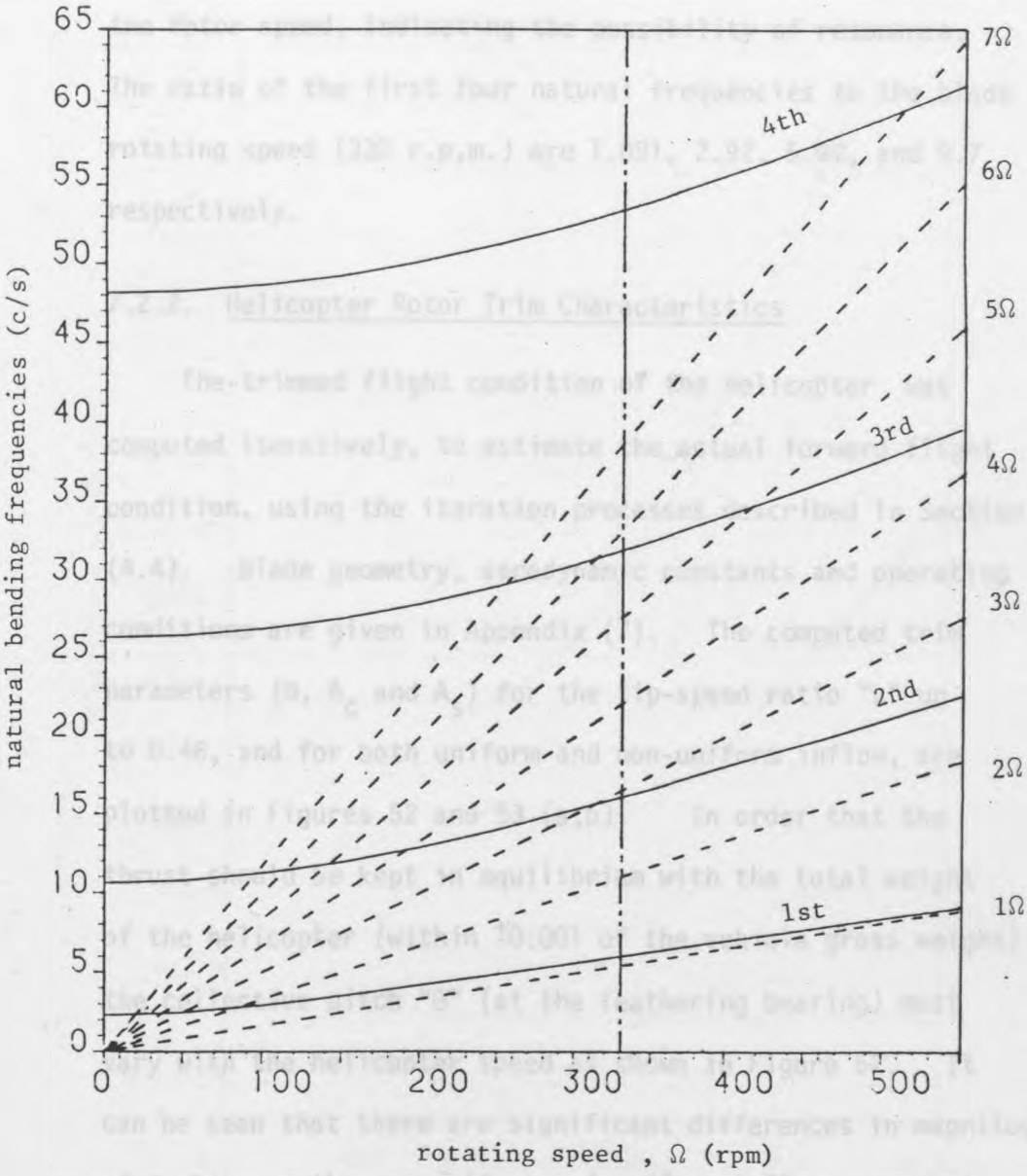

Figure 51 Blade Rotating Natural Frequencies Vs. Rotating Speed.

to a straight line passing through the origin. On the other hand, one can see at a glance if there are any natural frequencies of the blade which coincide with a harmonic of the rotor speed, indicating the possibility of resonance. The ratio of the first four natural frequencies to the blade rotating speed (330 r.p.m.) are 1.091, 2.92, 5.97, and 9.7 respectively.

7.2.2. Helicopter Rotor Trim Characteristics

The trimmed flight condition of the helicopter was computed iteratively, to estimate the actual forward flight condition, using the iteration processes described in Section (4.4). Blade geometry, aerodynamic constants and operating conditions are given in Appendix (7). The computed trim parameters (Θ, A_c and A_s) for the tip-speed ratio "μ" up to 0.48, and for both uniform and non-uniform inflow, are plotted in Figures 52 and 53 (a,b). In order that the thrust should be kept in equilibrium with the total weight of the helicopter (within $\pm$0.001 of the vehicle gross weight) the collective pitch "Θ" (at the feathering bearing) must vary with the helicopter speed as shown in Figure 52. It can be seen that there are significant differences in magnitude of Θ between the non-uniform and uniform inflow cases but they both follow the trend drawn by Bramwell [1].

The variation of amplitudes of lateral cyclic pitch "A_s" and longitudinal cyclic pitch "A_c" required for trim at

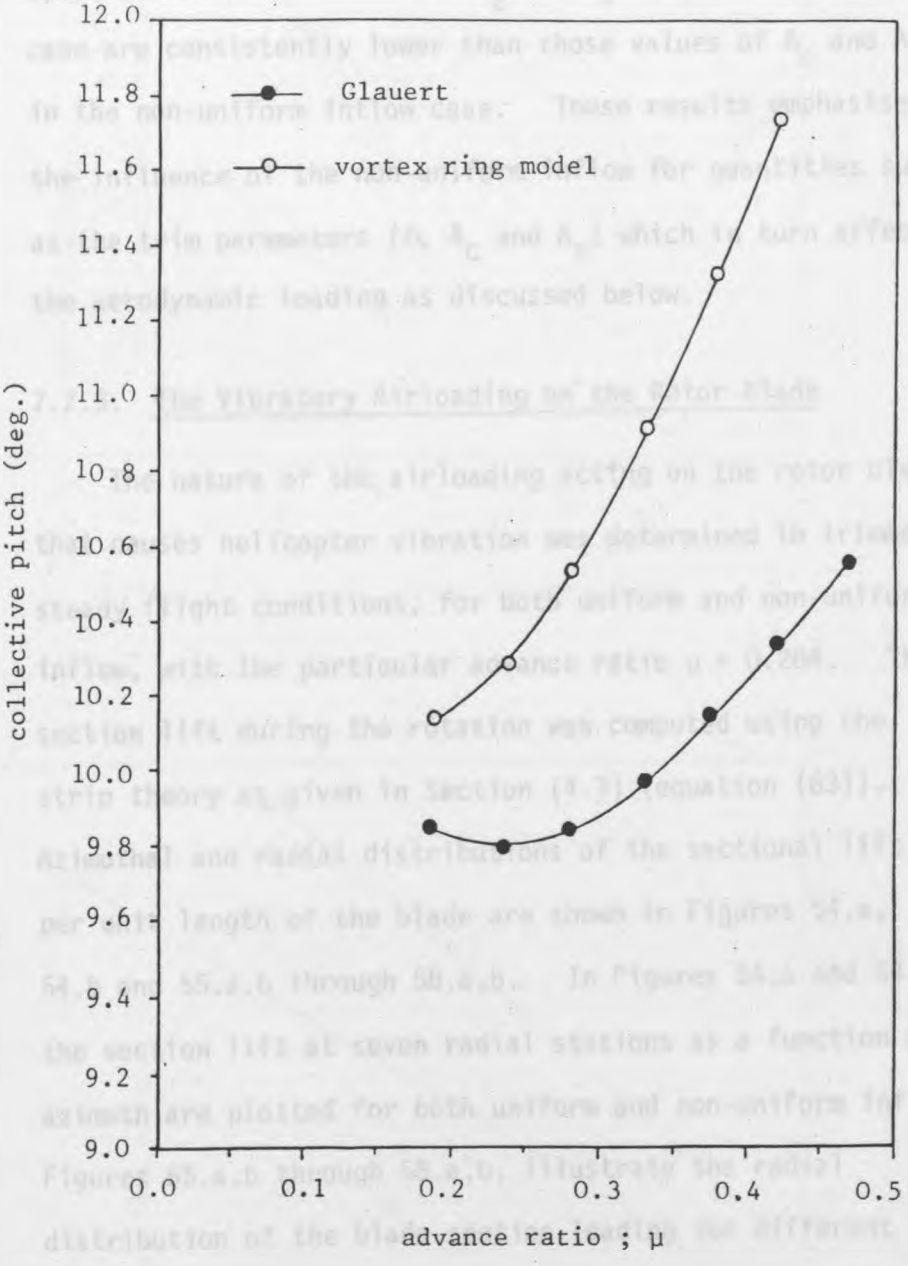

Figure 52 Collective Pitch Variation in Trimmed Flight.

different forward speeds are shown in Figures 53.a and 53.b. It can be observed that A_s varies linearly with the helicopter speed and the values of both A_c and A_s in the uniform inflow case are consistently lower than those values of A_c and A_s in the non-uniform inflow case. These results emphasise the influence of the non-uniform inflow for quantities such as the trim parameters (θ, A_c and A_s) which in turn affect the aerodynamic loading as discussed below.

7.2.3. The Vibratory Airloading on the Rotor Blade

The nature of the airloading acting on the rotor blades that causes helicopter vibration was determined in trimmed steady flight conditions, for both uniform and non-uniform inflow, with the particular advance ratio $\mu = 0.284$. The section lift during the rotation was computed using the strip theory as given in Section (4.3) (equation (63)). Azimuthal and radial distributions of the sectional lift per unit length of the blade are shown in Figures 54.a, 54.b and 55.a,b through 58.a,b. In Figures 54.a and 54.b the section lift at seven radial stations as a function of azimuth are plotted for both uniform and non-uniform inflow. Figures 55.a,b through 58.a,b, illustrate the radial distribution of the blade section loading for different azimuth angles (from 0 to 330^{o}) for the two cases (uniform and non-uniform inflow). It can be seen that there is a reduction in lift in the tip region of the advancing blade

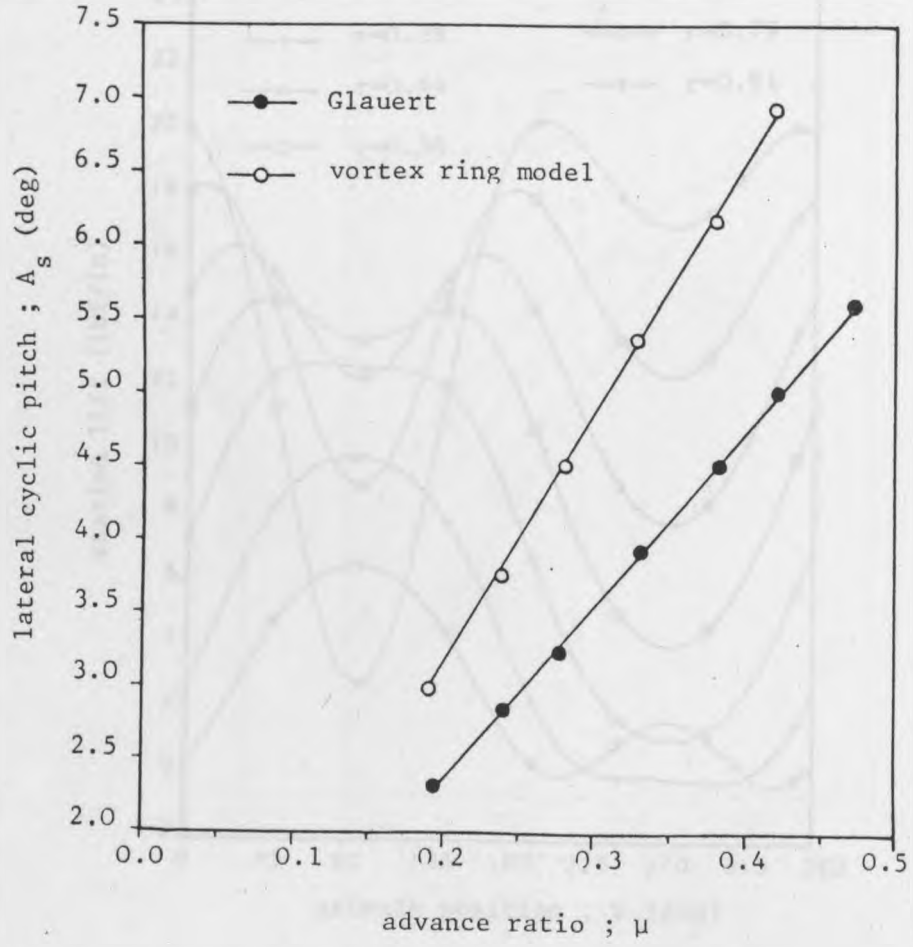

(a) Lateral Pitch Angle to Trim.

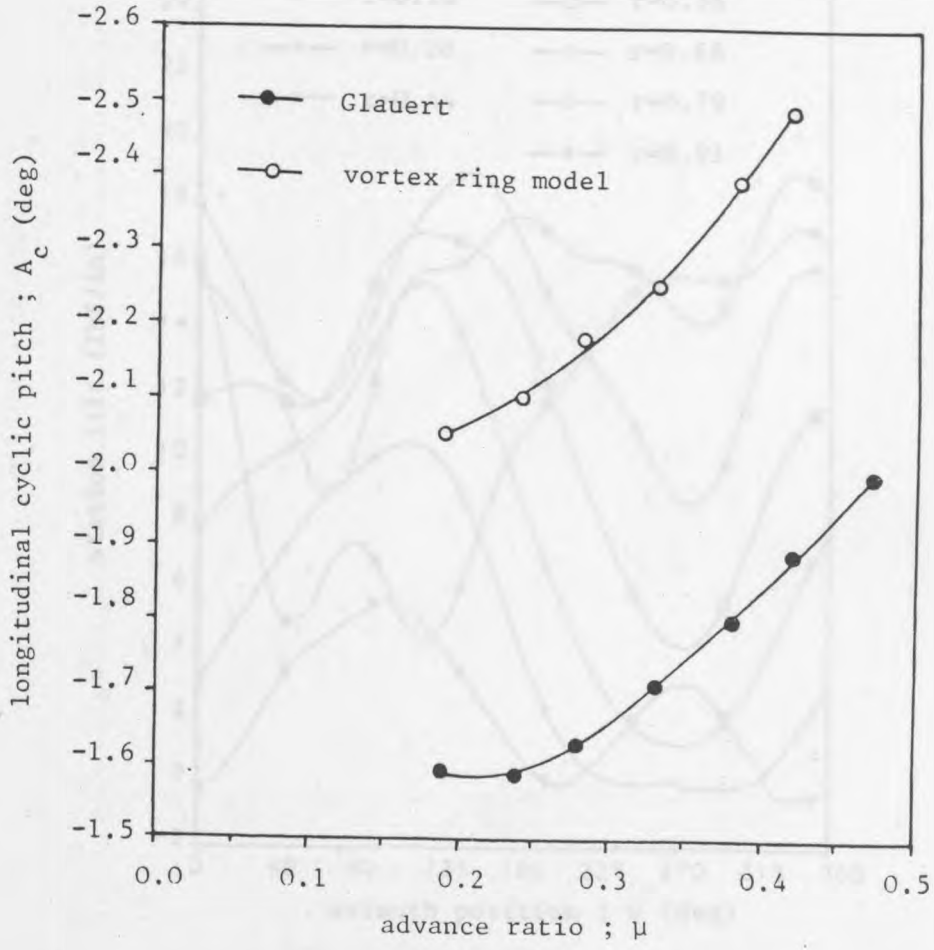

(b) Longitudinal Pitch Angle to Trim.

Figure 53 Cyclic Pitch Variation in Trimmed Flight.

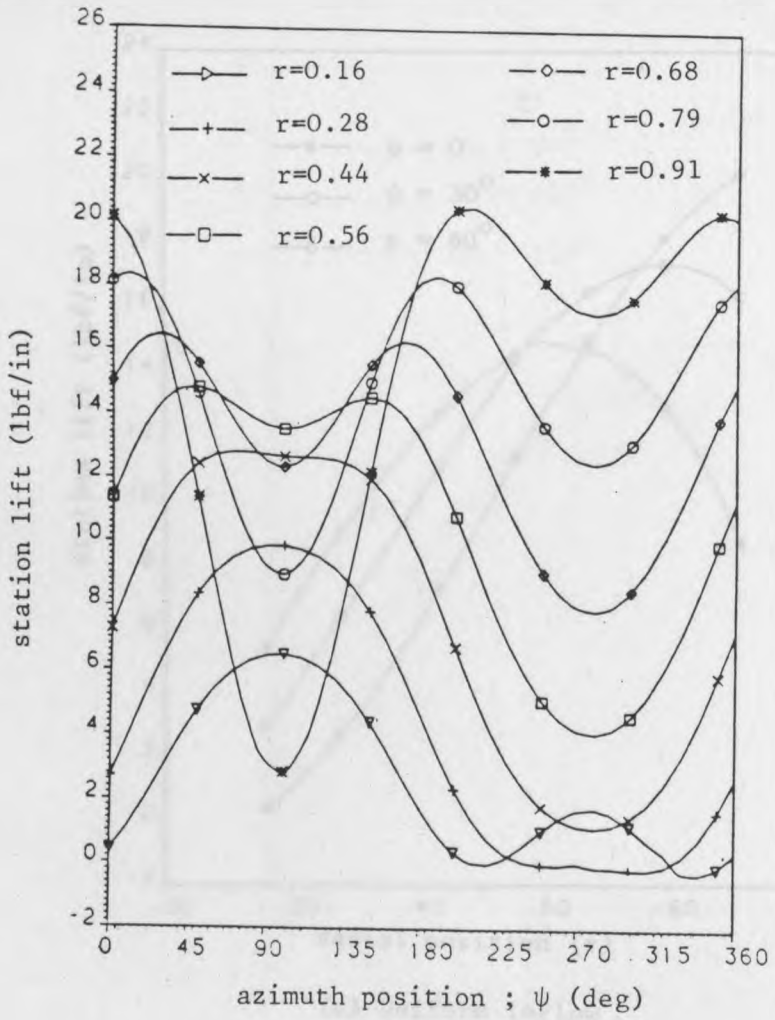

(a) Uniform Inflow

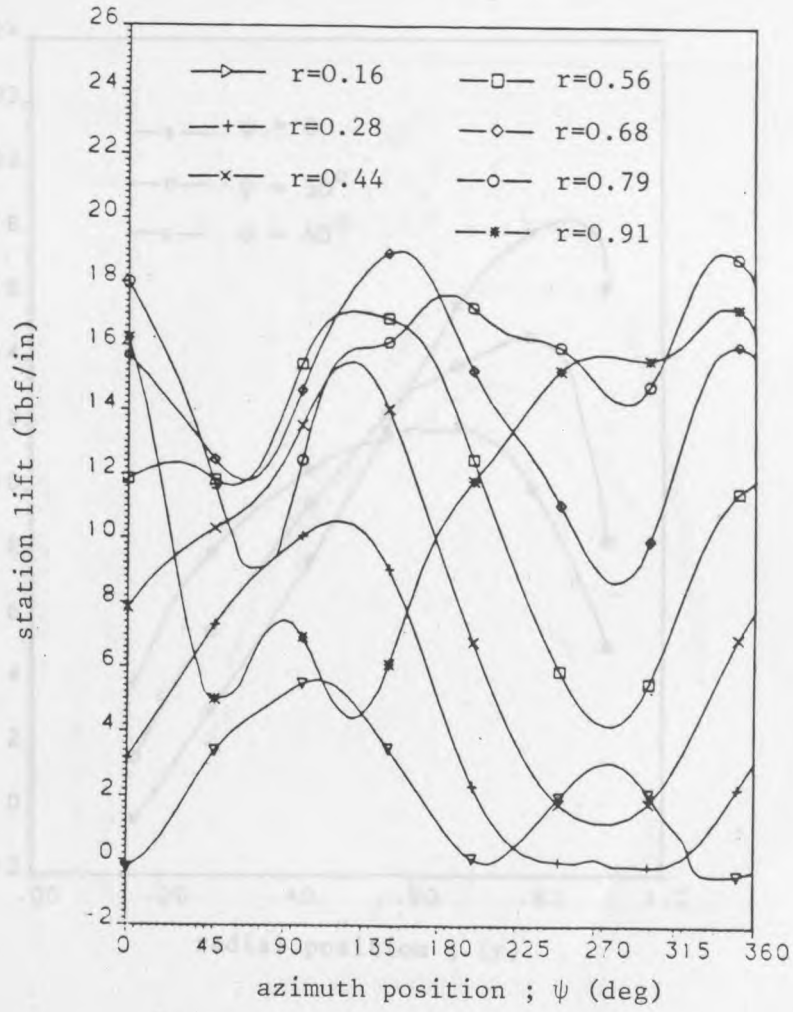

(b) Non-Uniform Inflow

Figure 54 Azimuthal Variation of the Blade Lift for Different Radial Position "r" and $\mu = 0.284$

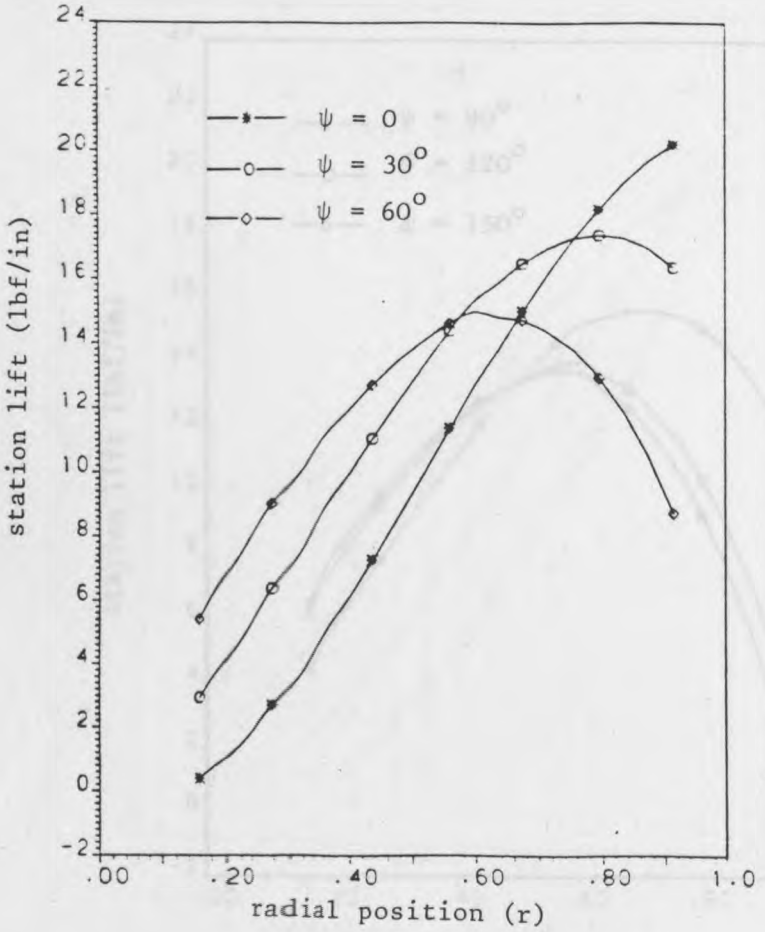

(a) Uniform Inflow

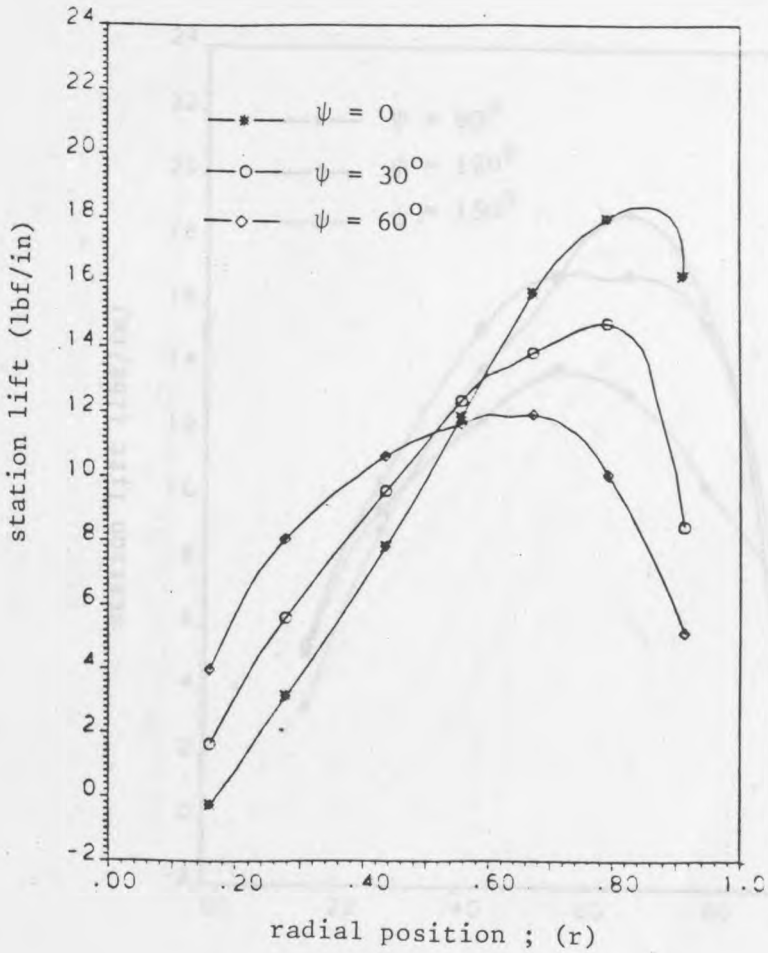

(b) Non-Uniform Inflow

Figure 55 Radial Distribution of the Blade Lift at $\mu = 0.284$, for $\psi = 0$, 30^{o} and 60^{o}

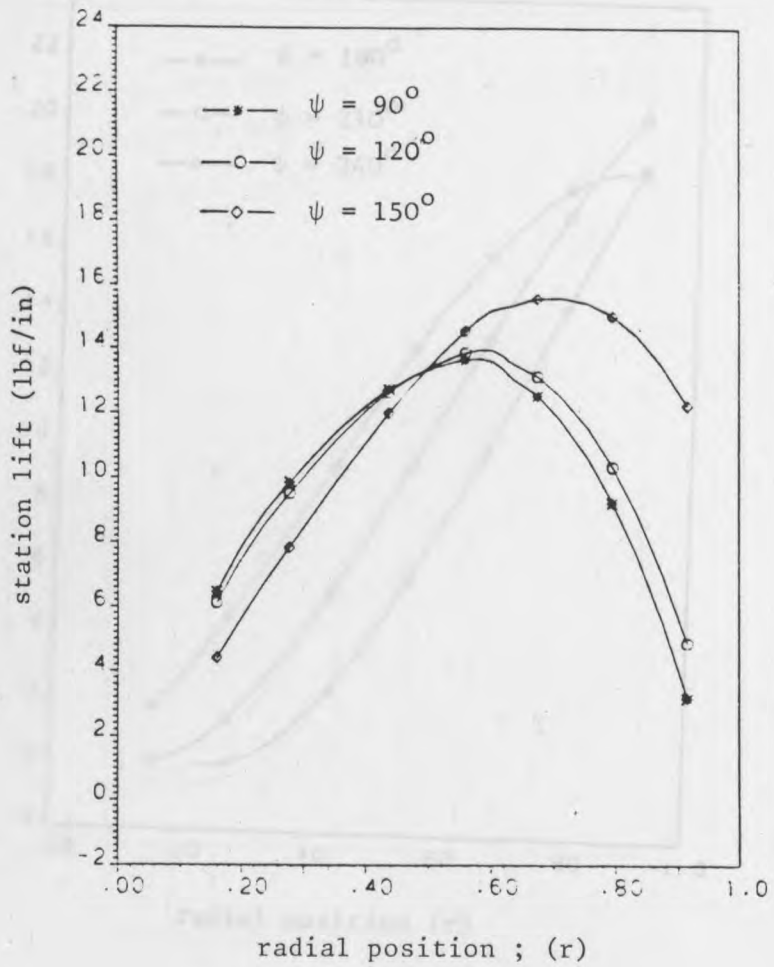

(a) Uniform Inflow

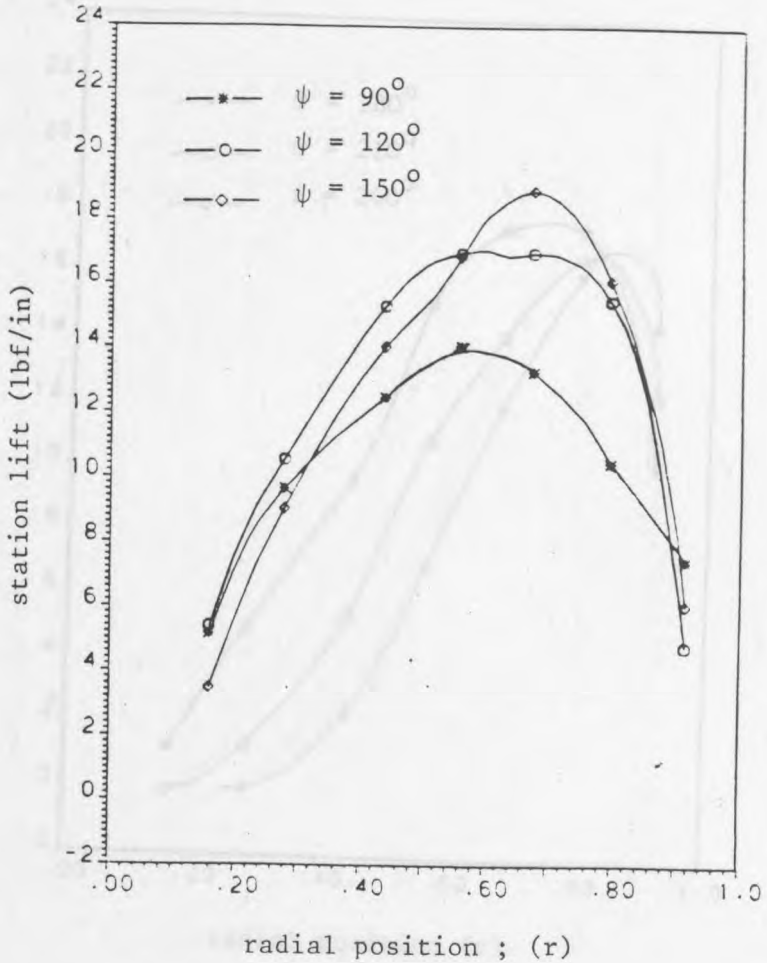

(b) Non-Uniform Inflow

Figure 56 Radial Distribution of the Blade Lift at $\mu = 0.284$, for $\psi = 90^{\circ}$, 120° and 150°

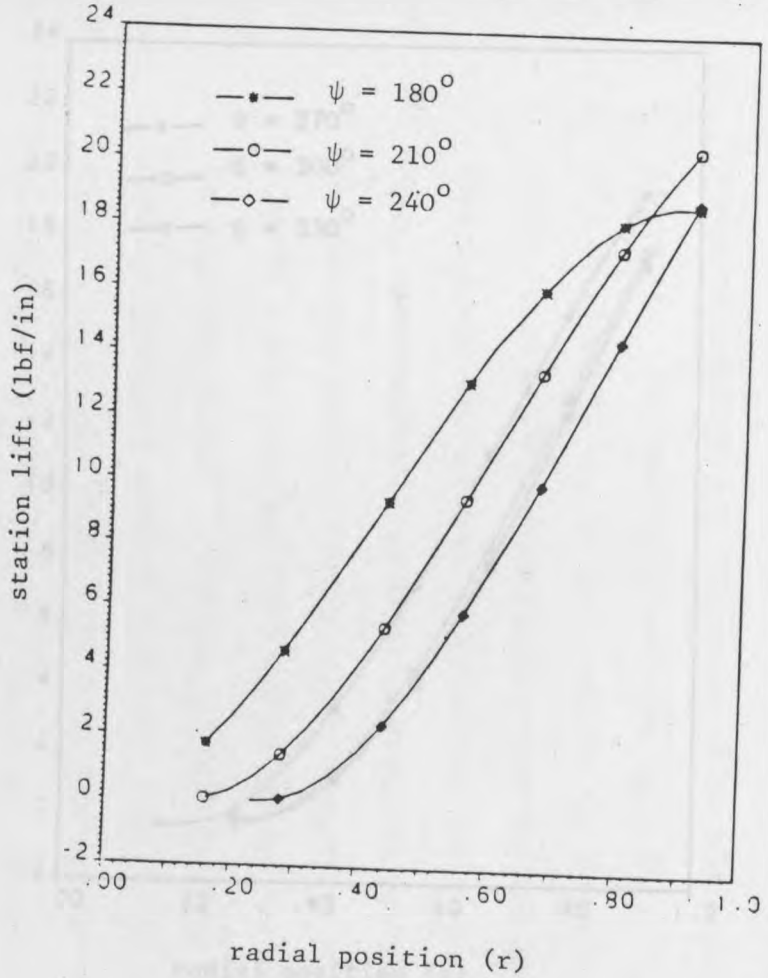

(a) Uniform Inflow

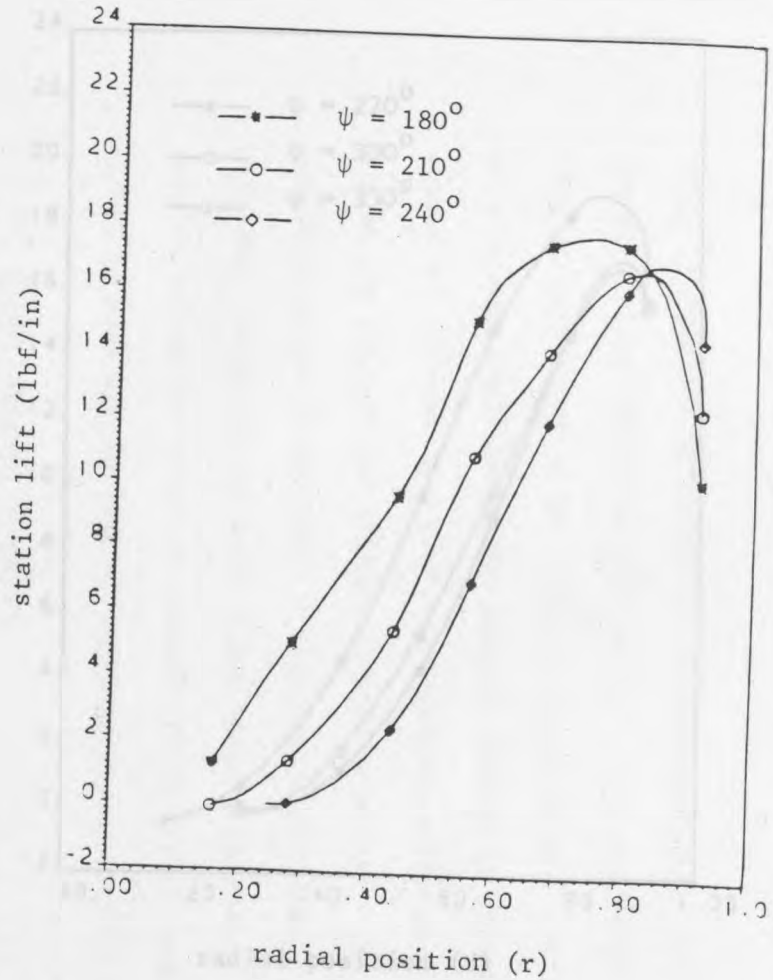

(b) Non-Uniform Inflow

Figure 57 Radial Distribution of the Blade Lift at $\mu = 0.284$, for $\psi = 180^{o}$, 210^{o} and 240^{o}

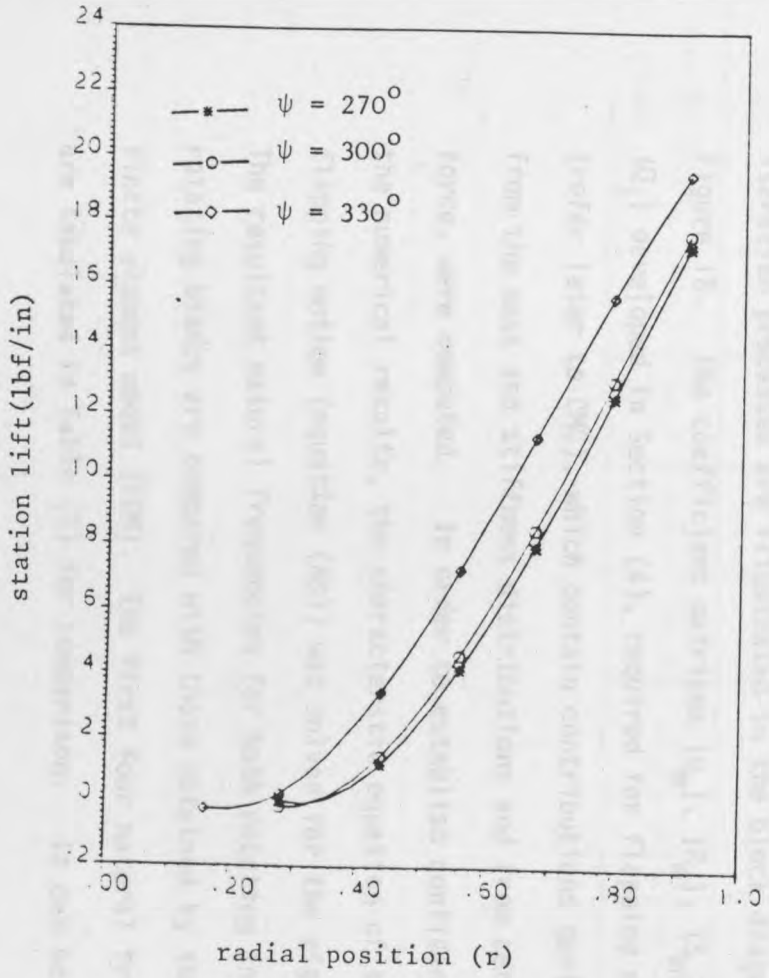

(a) Uniform Inflow

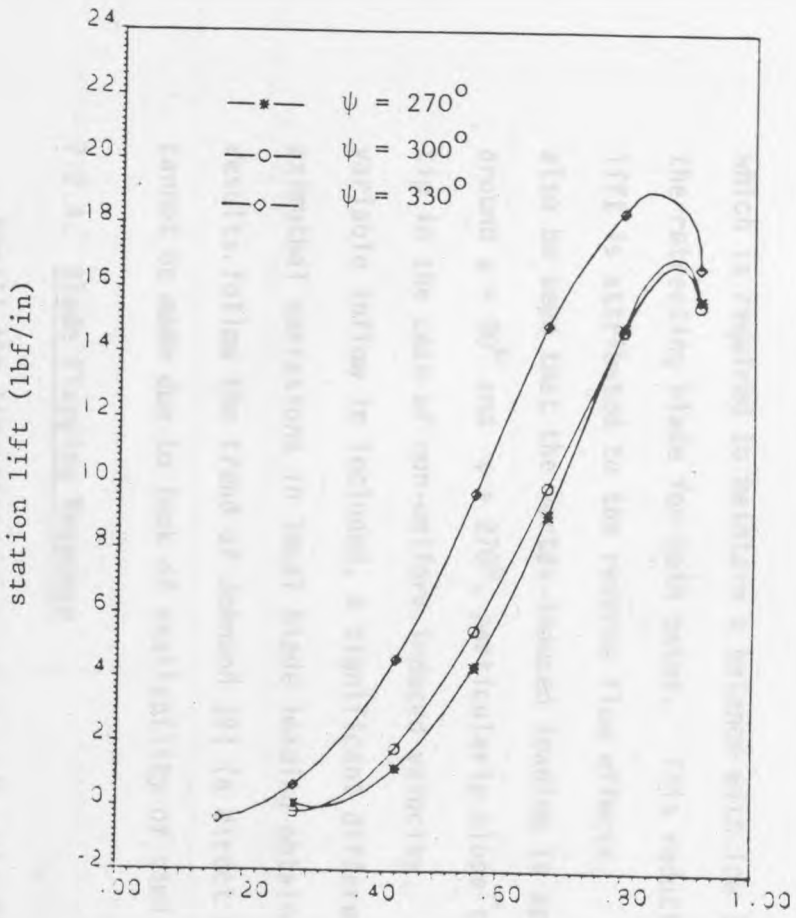

(b) Non-Uniform Inflow

Figure 58 Radial Distribution of the Blade Lift at $\mu = 0.284$, for $\psi = 270^{o}$, 300^{o} and 330^{o}

which is required to maintain a balance with low lift on the retreating blade for both cases. This reduction in lift is attributed to the reverse flow effects. It can also be seen that the vortex-induced loading is apparent around $\psi = 90^{o}$ and $\psi = 270^{o}$, particularly close to the tip in the case of non-uniform induced velocity. So, when variable inflow in included, a significant difference in azimuthal variations in local blade loading obtains. These results follow the trend of Johnson [2] (a direct comparison cannot be made due to lack of availability of similar data).

7.2.4. Blade Flapping Response

Recall the iteration processes to solve the flapping equation of motion described in Section (5.4). These iteration processes are illustrated in the block diagram, Figure 18. The coefficient matrices $[p_m]$, $[R_m]$, $\{S_{mi}\}$ and $\{Q_i\}$ developed in Section (4), required for flapping motion (refer later to CMC), which contain contributions derived from the mass and stiffness distributions and from aerodynamic force, were computed. In order to establish confidence in the numerical results, the characterstic equation of the flapping motion (equation (80)) was solved for the eigenvalues. The resultant natural frequencies for both rotating and non-rotating blades are compared with those obtained by the previous finite element model (FEM). The first four natural frequencies are tabulated in Table (1) for comparison. It can be seen

Table 1 Rotating and Non-Rotating Blade Natural Frequencies.

Values	Blade FEM				CMC of the Blade			
	Natural Frequencies (rad/sec)				Natural Frequencies (rad/sec)			
	w_{n1}	w_{n2}	w_{n3}	w_{n4}	w_{n1}	w_{n2}	w_{n3}	w_{n4}
Rotating Blade	37.7	101.1	200.3	335.3	38.1	100.6	200.6	336.3
Non-Rotating Blade	14.6	66.7	165.0	302.5	14.6	66.7	165.0	302.5

that these frequencies have the same values for the non-rotating case, as those obtained from the previous finite element model. These are due to the loss of accuracy in the numerical integration of the centrifugal contribution $[R_m]$.

The flapping equation of motion was now solved for the generalised co-ordinate $\{q_i\}$, through the first four revolutions of the blade (i.e. $N_{rev} = 4$ in the block diagram, Figure 18). This solution yields the blade response of steady state for each flatwise mode. The results as a function of azimuth, expressed in terms of the blade tip deflection (coning deflection plus mode deflection), are plotted in Figure 59 for both uniform and non-uniform inflow cases. Blade tip deflection mode contributions for both cases are also shown in Figures 60.a and 60.b. It was assumed that the contributions of the first four modes were sufficient to account for the computed blade deflection. It can be seen that such a blade subjected to aerodynamic forces as it moves around the azimuth tends to oscillate up and down (as shown in Figure 59) at its natural frequency, and there is one complete flapping cycle for each revolution of the rotor. It can also be seen that for both uniform and non-uniform inflow the contributions from modes other than the first mode to the blade deflection (Figures 60.a and 60.b) are quite small.

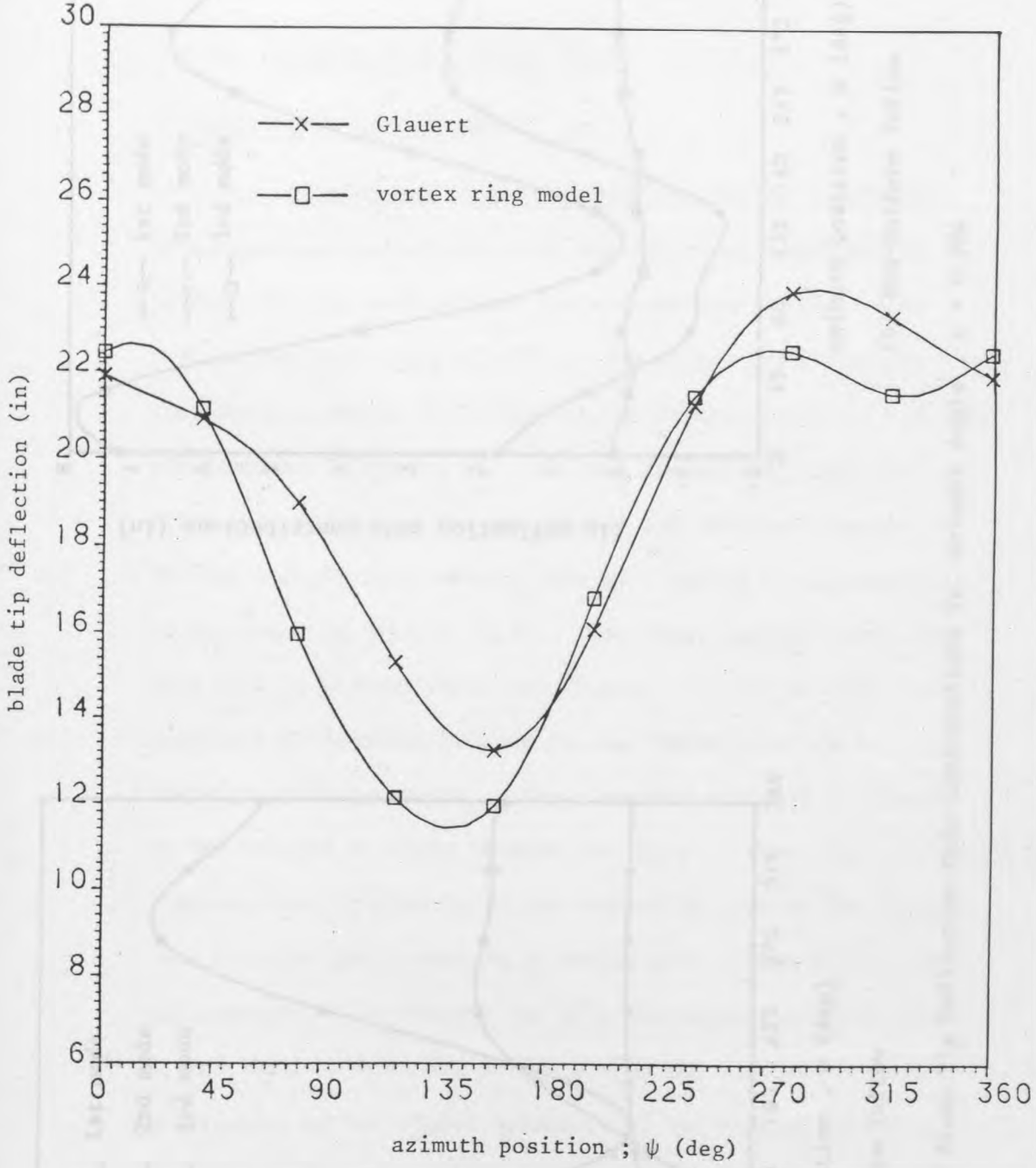

Figure 59 Blade Tip Deflection Vs. Azimuth Angle ,
$\mu = 0.284$

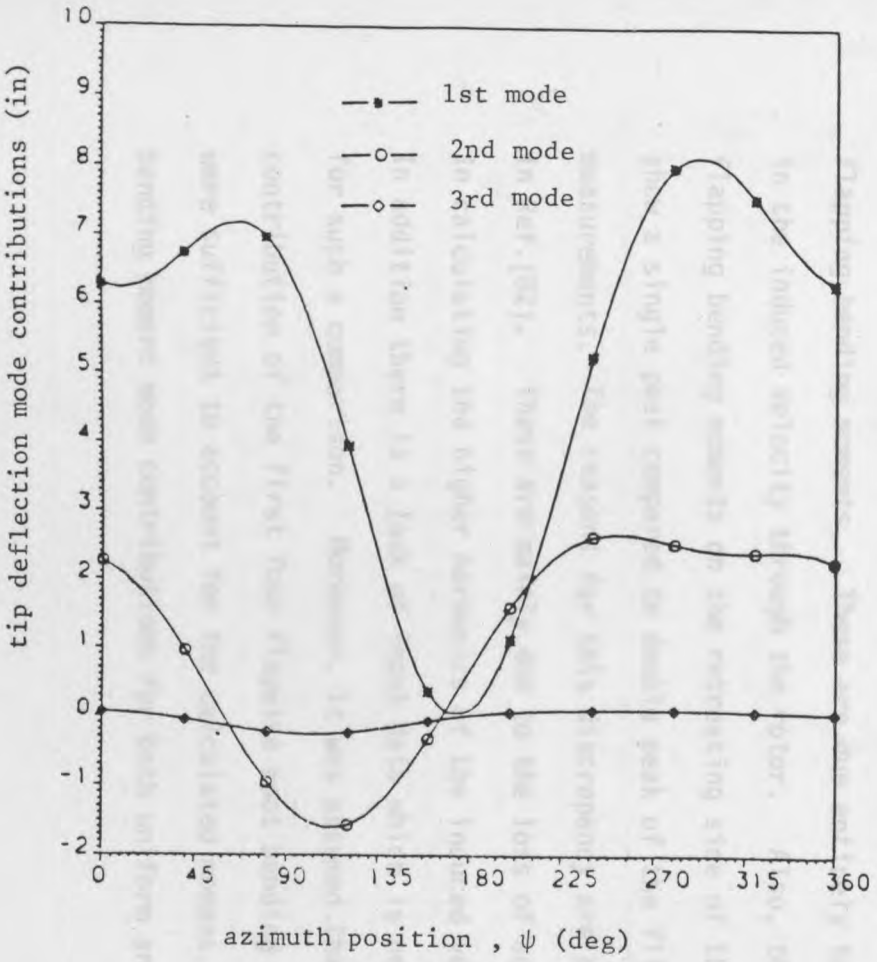

(a) Uniform Inflow

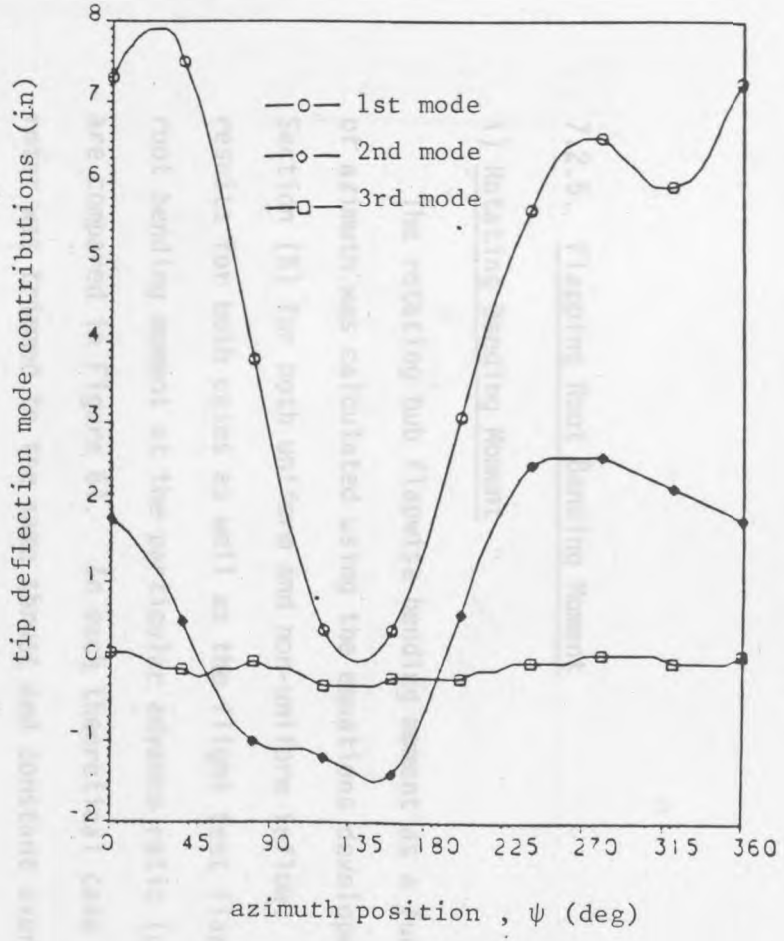

(b) Non-Uniform Inflow

Figure 60 Blade Tip Deflection Mode Contributions Vs. Azimuth Angle , $\mu = 0.284$

7.2.5. Flapping Root Bending Moment

i) Rotating Bending Moment

The rotating hub flapwise bending moment as a function of azimuth was calculated using the equations developed in Section (5) for both uniform and non-uniform inflow. The results for both cases as well as the flight test flapwise root bending moment at the particular advance ratio ($\mu = 0.284$) are compared in Figure 61. In each theoretical case the rotor was trimmed to the same thrust and constant average rolling and pitching moments (due to flapping displacement), as mentioned in Section (5.4). The input control pitch for each case is written below the figure. It can be seen that there are differences between the two theoretical root flapping bending moments. These are due entirely to change in the induced velocity through the rotor. Also, the calculated flapping bending moments on the retreating side of the disc show a single peak compared to double peak of the flight test measurements. The reasons for this discrepancy are discussed in Ref.[82]. These are mainly due to the loss of accuracy in calculating the higher harmonics of the induced velocity. In addition there is a lack of input data which is necessary for such a comparison. Moreover, it was assumed that the contribution of the first four flapwise root bending moments were sufficient to account for the calculated moment. These bending moment mode contributions for both uniform and non-

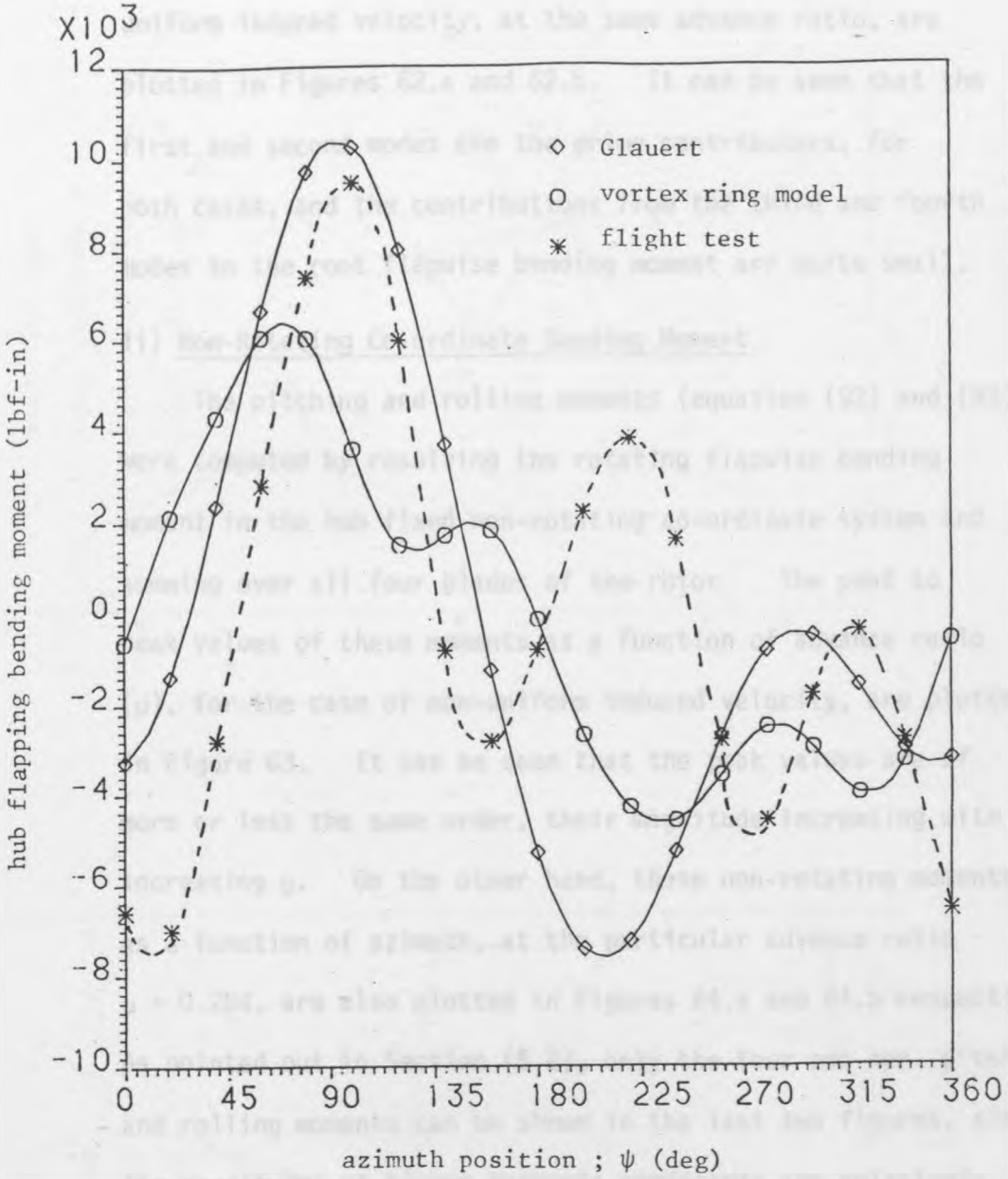

Figure 61 Rotating Hub Flapwise Bending Moment Vs. Azimuth Angle at $\mu = 0.284$;

$\theta_s = 9.84 + 1.64 \cos \psi - 3.25 \sin \psi$ (^{o}) - Glauert

$\theta_s = 10.53 + 2.17 \cos \psi - 4.5 \sin \psi$ (^{o}) - vortex ring

$\theta_s = 14.80 + 0.96 \cos \psi - 5.15 \sin \psi$ (^{o})- flight test

uniform induced velocity, at the same advance ratio, are plotted in Figures 62.a and 62.b. It can be seen that the first and second modes are the prime contributors, for both cases, and the contributions from the third and fourth modes to the root flapwise bending moment are quite small.

ii) Non-Rotating Co-ordinate Bending Moment

The pitching and rolling moments (equation (92) and (93)) were computed by resolving the rotating flapwise bending moment in the hub fixed non-rotating co-ordinate system and summing over all four blades of the rotor. The peak to peak values of these moments as a function of advance ratio (μ), for the case of non-uniform induced velocity, are plotted in Figure 63. It can be seen that the peak values are of more or less the same order, their magnitude increasing with increasing μ. On the other hand, these non-rotating moments as a function of azimuth, at the particular advance ratio $\mu = 0.284$, are also plotted in Figures 64.a and 64.b respectively. As pointed out in Section (5.2), only the four per rev. pitching and rolling moments can be shown in the last two figures, since the magnitudes at higher harmonic components are relatively small. These moments, which are transmitted from the rotating hub system to the fixed fuselage system, where they act as exciting moments at the frequency of 4Ω (four blades), had pitching and rolling peak to peak values of 6000 lbf-in and 5400 lbf-in respectively. Thus, it can be concluded that,

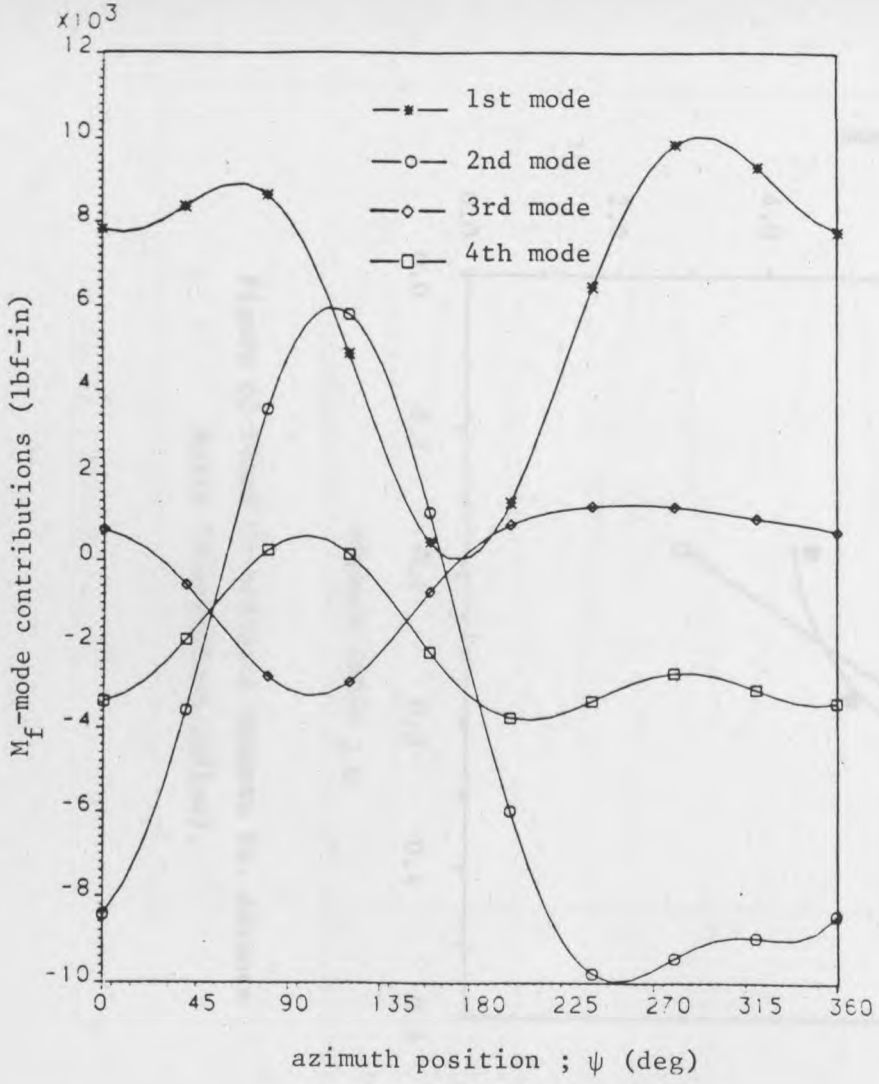

(a) Uniform Inflow

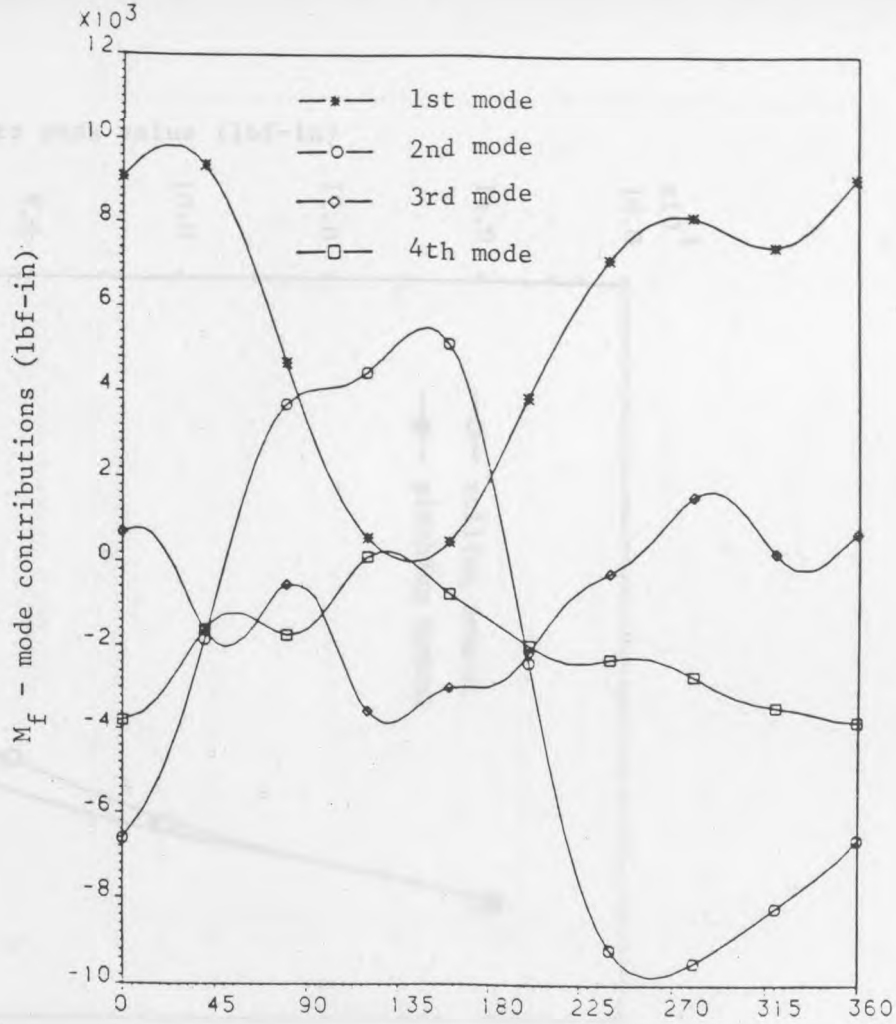

(b) Non-Uniform Inflow

Figure 62 Rotating Hub Flapwise Bending Moment "M_f" Mode Contributions Vs. Azimuth Angle ; $\mu = 0.284$

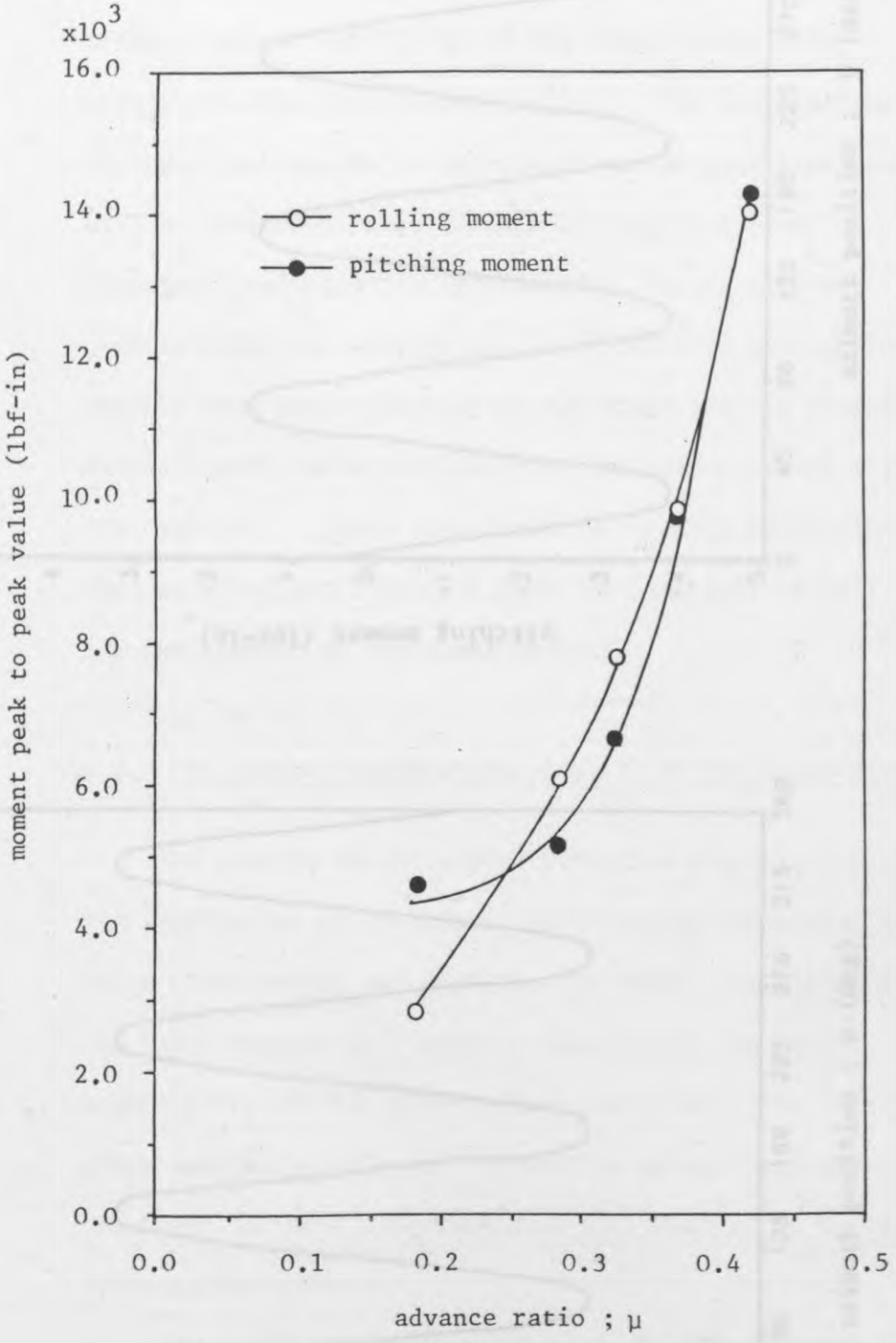

Figure 63 Fixed Co-ordinate Moments Vs. Advance Ratio (Non-Uniform Inflow).

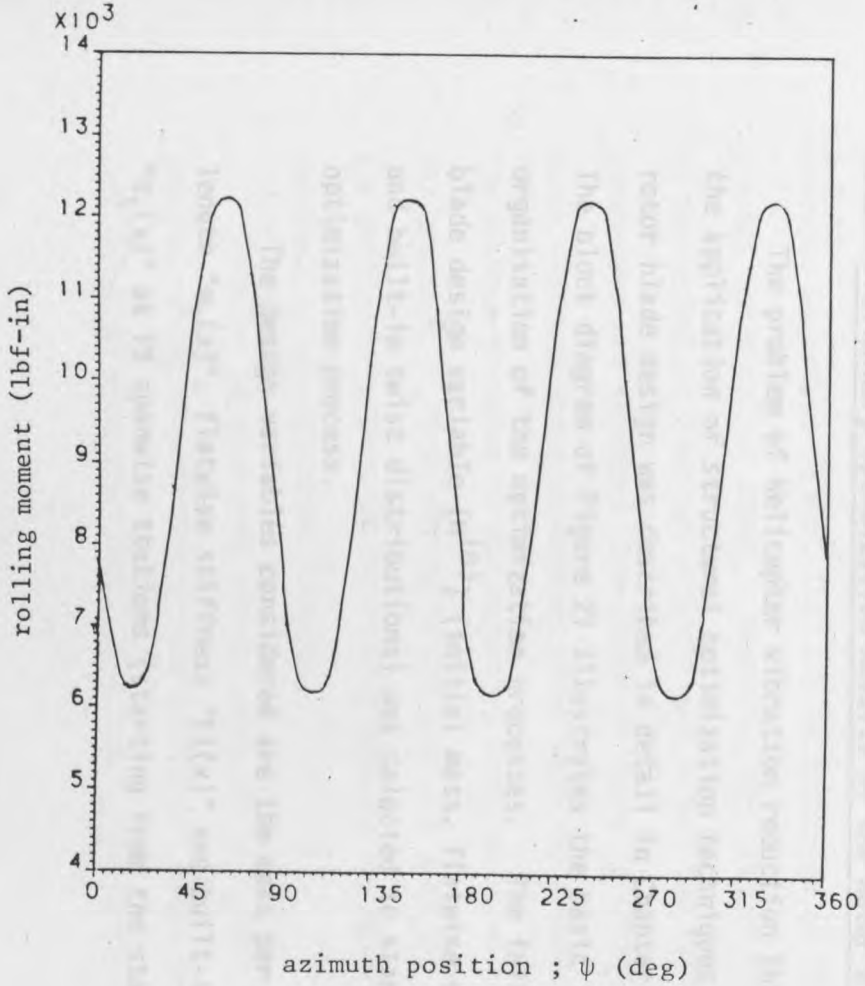

(a) Rolling Moment

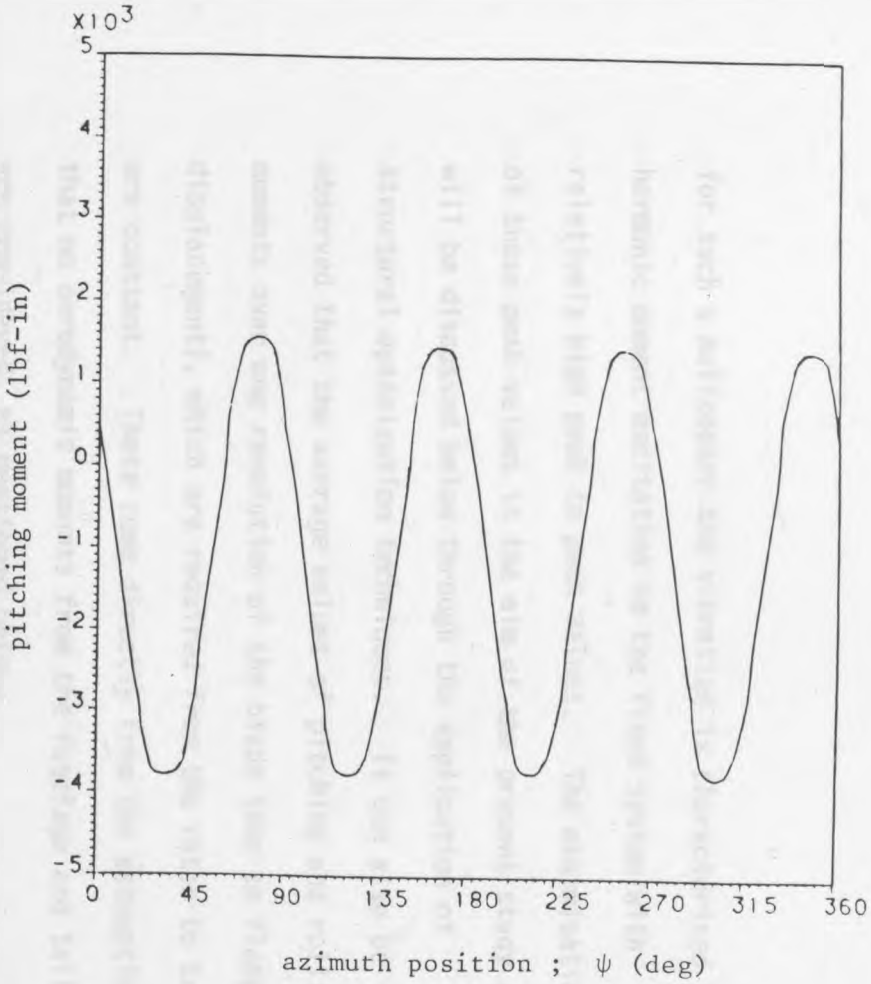

(b) Pitching Moment

Figure 64 Non-Rotating Hub Flapwise Bending Moments Vs. Azimuth Angle ; $\mu = 0.284$

for such a helicopter the vibration is characterised by harmonic moment excitation in the fixed system with relatively high peak to peak values. The minimisation of these peak values is the aim of the present study and will be discussed below through the application of structural optimization techniques. It can also be observed that the average values of pitching and rolling moments over one revolution of the blade (due to flapping displacement), which are required from the rotor to trim, are constant. These come directly from the assumption that no aerodynamic moments from the fuselage and tail are considered, as mentioned before.

7.3. Preliminary Optimization Results of the Rotor Blade

The problem of helicopter vibration reduction through the application of structural optimization techniques to rotor blade design was described in detail in Chapter 6. The block diagram of Figure 21 illustrates the basic organisation of the optimization processes. The initial blade design variable ($\underset{\sim}{H}^{(o)}$) (initial mass, flatwise stiffness and built-in twist distributions) was selected to start the optimization process.

The design variables considered are the mass per unit length "$m_i(x)$", flatwise stiffness "EI(x)" and built-in twist "$\theta_t(x)$" at 19 spanwise stations (starting from the station

just after the feathering bearing) along the blade. Upper and lower bounds on these design variables were prescribed to prevent them from reaching impractical values as mentioned before in Section (6).

The objective function to be minimised is the mathematical representation of rolling and pitching moments. These moments are calculated as described in Section (5).

Unfortunately, the size of such an optimization problem, in terms of the above huge number of design variables, is computationally expensive. It leads to unacceptably long computation times, since the major computational effort is in evaluation of the objective function. Thus, in order to reduce the computational time involved in the mathematical programming approach chosen, some of the approximation concepts described in Ref. [53] are incorporated in the present optimization study. However, the rate of change of the objective function with changes in all the variable parameters was computed (the larger of these "gradients" would indicate those parameters which have the greatest effect). The maximum increase in the objective function occurs along its gradient. Then, moving in the negative gradient direction (as mentioned in Section (6.1)) will produce the maximum decrease in the objective function.

In order to gain some insight into the optimization process, a set of preliminary results for the blade tailoring configuration were generated. The understanding gained from

these preliminary results, in addition to the results obtained from the optimum configurations of the cantilever beam, Section (7.1), led to the development of more refined optimization procedure. The preliminary results presented are organised in the following two distinct sections.

7.3.1. Minimisation of Oscillatory Rolling Moment

In this section, the preliminary results for the optimum blade configurations are presented separately for: (i) blade mass distribution, (ii) blade flatwise distribution, (iii) built-in twist along the blade. The objective function used in generating these results was the peak-to-peak value of oscillatory rolling moment (M_{xp}) in forward flight at only one particular advance ratio (μ = 0.284). In each case the gradient of this objective function at 19 spanwise stations along the blade was computed and the normalised descent direction emanating from the initial design variable $\underset{\sim}{H}^{(o)}$ has been obtained. Three different blade designs with three different descent steplengths along the descent direction were generated.

(i) Optimum Blade Mass Distribution

The preliminary modified blade mass distributions are presented in Figure 65, which are obtained for different descent steplengths $\lambda_{m1} = 0.5*10^{-3}$, $\lambda_{m2} = 0.625*10^{-3}$ and $\lambda_{m3} = 0.125*10^{-2}$ along the computed descent direction. Figures 66 and 67 show, respectively, the corresponding rolling

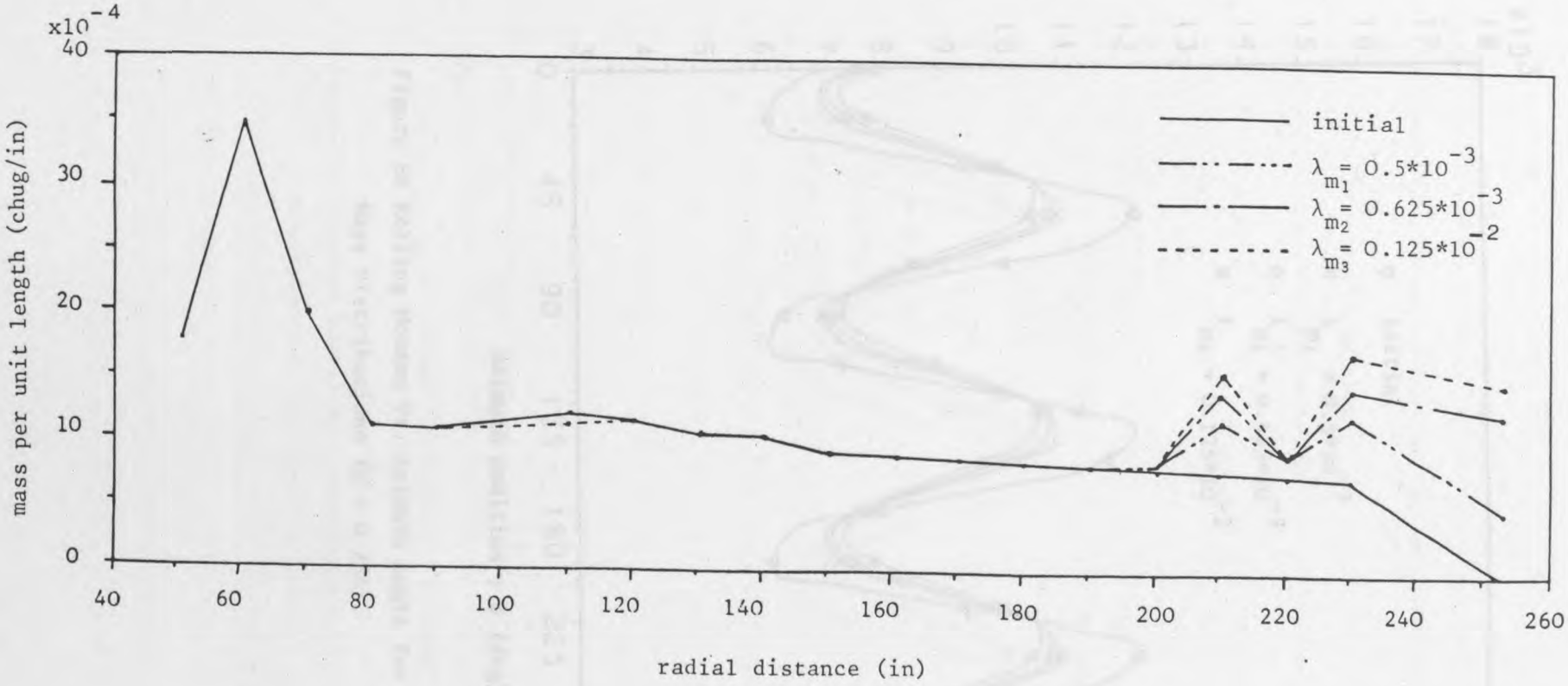

Figure 65 Initial and Modified Blade Mass Distributions for Minimum Rolling Moment ($\mu = 0.284$).

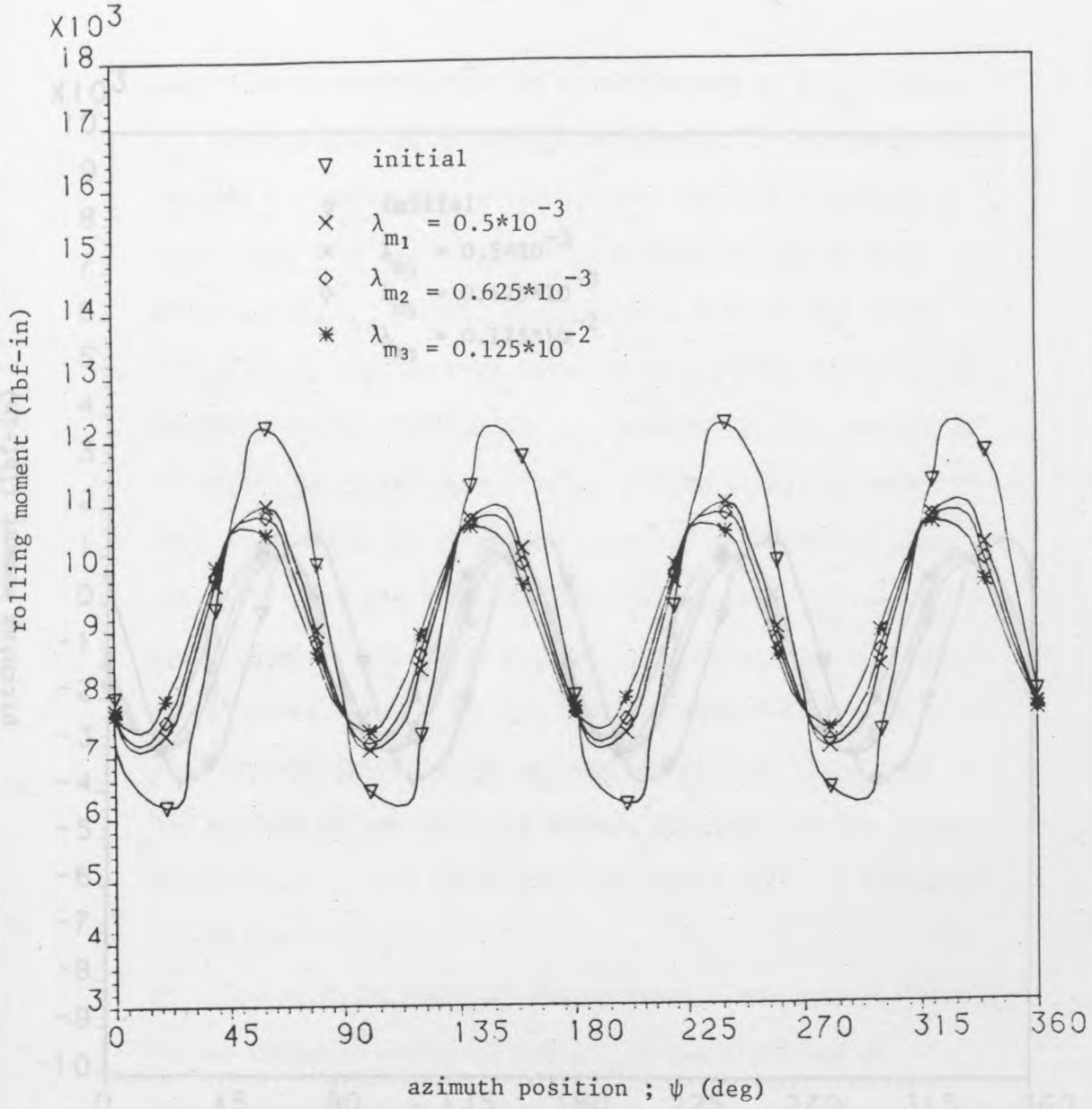

Figure 66 Rolling Moment Vs. Azimuth Angle for Different Blade Mass Distributions (μ = 0.284).

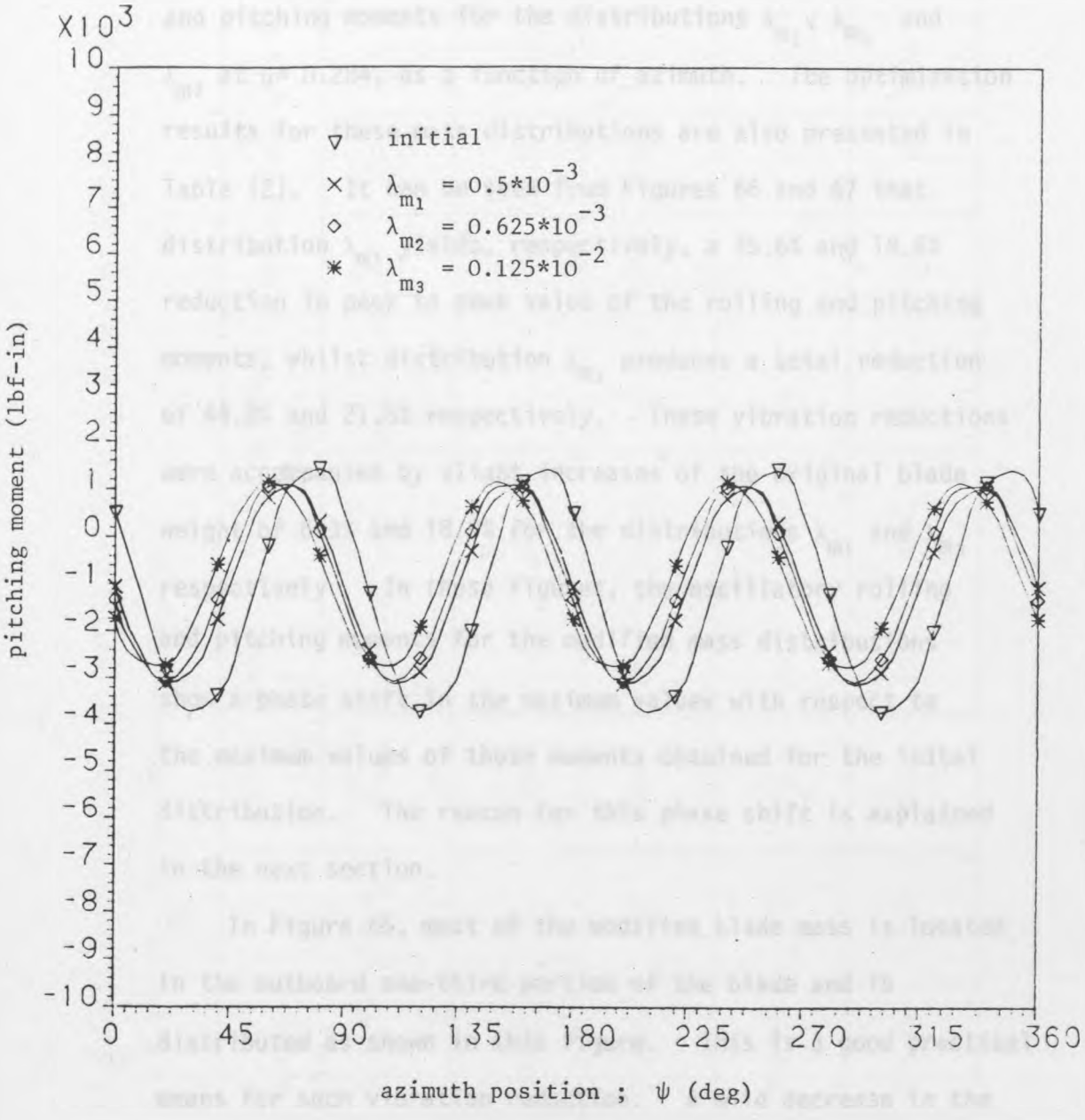

Figure 67 Pitching Moment Vs. Azimuth Angle for Different Blade Mass Distributions ($\mu = 0.284$).

and pitching moments for the distributions λ_{m_1}, λ_{m_2} and λ_{m_3} at $\mu = 0.284$, as a function of azimuth. The optimization results for these mass distributions are also presented in Table (2). It can be seen from Figures 66 and 67 that distribution λ_{m_1} yields, respectively, a 35.6% and 18.6% reduction in peak to peak value of the rolling and pitching moments, whilst distribution λ_{m_3} produces a total reduction of 44.8% and 21.5% respectively. These vibration reductions were accompanied by slight increases of the original blade weight of 6.3% and 18.9% for the distributions λ_{m_1} and λ_{m_3} respectively. In these figures, the oscillatory rolling and pitching moments for the modified mass distributions show a phase shift in the maximum values with respect to the maximum values of those moments obtained for the inital distribution. The reason for this phase shift is explained in the next section.

In Figure 65, most of the modified blade mass is located in the outboard one-third portion of the blade and is distributed as shown in this figure. This is a good practical means for such vibration reduction. A mild decrease in the mass per unit length at the blade radial distance equal 220 in (r = 87%) was evident and there is a substantial increase at the two adjacent stations for the modified distribution of λ_{m_1}, λ_{m_2} and λ_{m_3}. This mass distribution (at the tip region) acts like a "dumb-bell" (see also the modified flatwise stiffness distributions at the blade tip

Table 2. Optimization Results Comparison for the Initial and Modified Blade Mass Distribution at $\mu = 0.284$ (M_{xp} is the objective function).

Values	Blade mass; W_b (lb)	% Incr. in W_b	Rolling Moment M_x (lbf-in)		Pitching Moment My (lbf-in)		Natural Frequency Ratio			
			Peak to peak; M_{xp}	% Reduction in M_{xp}	Peak to peak; M_{yp}	% Reduction in M_{yp}	$\frac{w_{n_1}}{\Omega}$	$\frac{w_{n_2}}{\Omega}$	$\frac{w_{n_3}}{\Omega}$	$\frac{w_{n_4}}{\Omega}$
Initial Distribution	200.15	-	6029	-	5149	-	1.091	2.92	5.97	9.70
Distribution of $\lambda_{m_1} = 0.5*10^{-3}$	212.83	6.3	3880	35.6	4189	18.6	1.048	2.89	5.6	9.16
Distribution of $\lambda_{m2} = 0.625*10^{-3}$	215.99	7.9	3730	38.1	4182	18.8	1.04	2.9	5.59	9.09
Distribution of $\lambda_{m_3} = 0.125*10^{-2}$	231.84	15.8	3327	44.8	4041	21.5	1.01	2.97	5.58	8.89

region next section), which increases the blade inertia and thus affects the blade natural frequencies as well as its mode shapes. These modified mass distributions of the blade for the same descent steplengths λ_{m_1}, λ_{m_2} and λ_{m_3} are also shown in Figure 68 in which the above optimization results were computed at another advance ratio, $\mu = 0.372$. It is interesting to note that the resultant modified mass distributions are more or less the same as those for $\mu = 0.284$ and each distribution in the outboard one-third of the blade acts again as what is called a "dumb-bell". The optimization results corresponding to these modified distributions (λ_{m_1}, λ_{m_2} and λ_{m_3}) in this case, are compared in Table (3) with that of the initial blade distribution. From this comparison it is evident that the peak to peak values of the rolling and pitching moments have decreased substantially, however, the percentage reduction seen in those values are from 40.7% to 54.2% and from 36.2% to 46.3% respectively, and a slight increase (from 5.6% to 13%) of the original blade mass accompanied these vibration reductions. The effects of the modified mass distribution on the blade natural frequencies as well as its modal shapes will be discussed below.

A comparison of the first four modal shapes of the rotating blade, for its initial and modified mass distribution

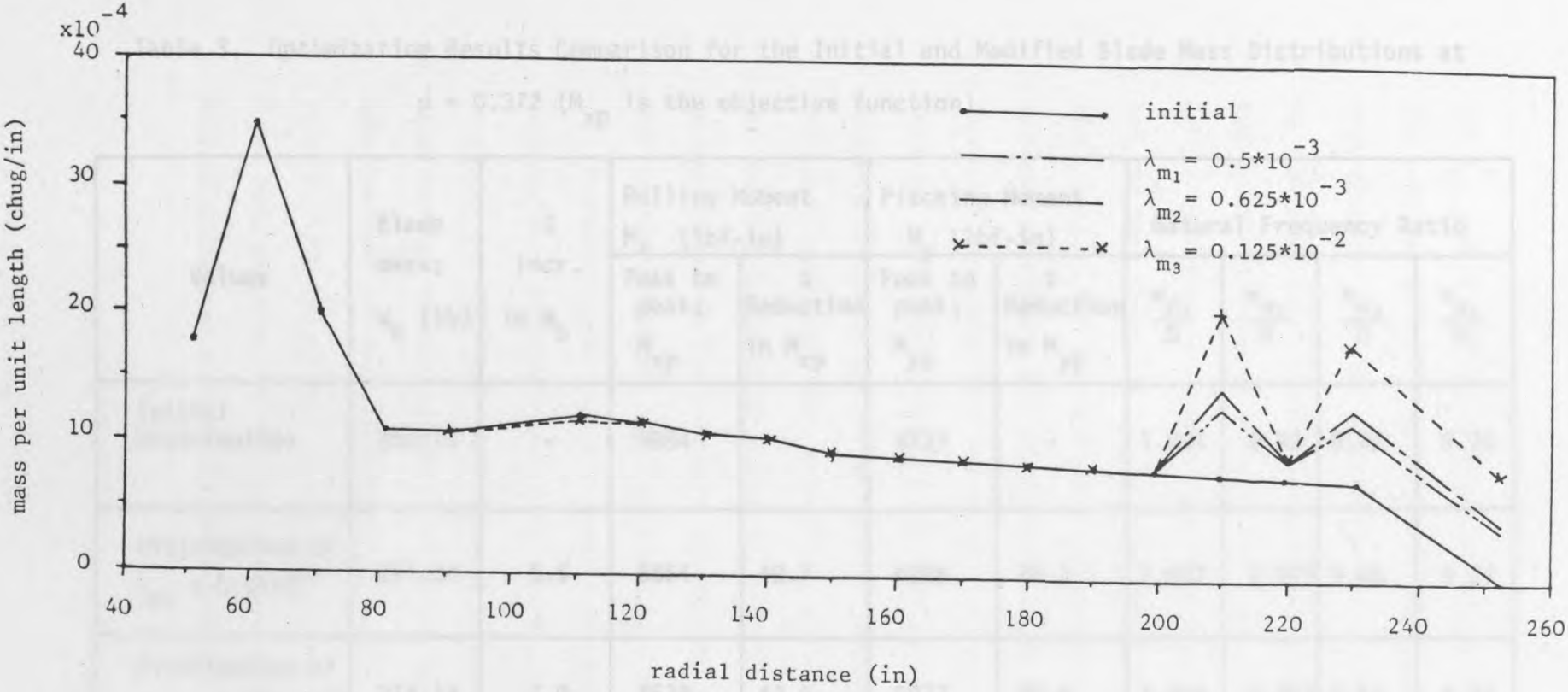

Figure 68 Initial and Modified Blade Mass Distributions for Minimum Rolling Moment (μ = 0.372).

Table 3. Optimization Results Comparison for the Initial and Modified Blade Mass Distributions at $\mu = 0.372$ (M_{xp} is the objective function).

Values	Blade mass; W_b (lb)	% Incr. in W_b	Rolling Moment M_x (lbf-in)		Pitching Moment M_y (lbf-in)		Natural Frequency Ratio			
			Peak to peak; M_{xp}	% Reduction in M_{xp}	Peak to peak; M_{yp}	% Reduction in M_{yp}	$\frac{w_{n_1}}{\Omega}$	$\frac{w_{n_2}}{\Omega}$	$\frac{w_{n_3}}{\Omega}$	$\frac{w_{n_4}}{\Omega}$
Initial Distribution	200.15	-	9884	-	9737	-	1.091	2.92	5.97	9.70
Distribution of $\lambda_{m1} = 0.5*10^{-3}$	211.34	5.6	5854	40.7	6208	36.2	1.057	2.905	5.66	9.27
Distribution of $\lambda_{m2} = 0.625*10^{-3}$	214.14	7.0	5578	43.6	5977	38.6	1.050	2.911	5.65	9.21
Distribution of $\lambda_{m3} = 0.125*10^{-2}$	228.13	13.0	4524	54.2	5233	46.3	1.022	2.97	5.63	8.98

(of λ_{m_3} and μ= 0.284), is shown in Figures 69.a to 69.d. The rotating natural frequencies of the blade for both distributions are also compared in Table (2). It can be seen from these figures that for the second flatwise mode, the amplitude of the antinode (near midspan) is larger than that for the initial blade mass distribution and the node point (at r = 74%) has moved outboard by about 7.3%. For the third and fourth modes, both the antinode amplitudes and the antinode radii have also increased, (Figures 69.c and 69.d). It can also be seen that the additional weight at the node region of the second mode causes the second natural frequency to remain virtually unchanged, and, thereafter, a slight increase was observed as shown in Tables (2) and (3). This is due to the changes in the resultant generalised mass, for the modified distributions (λ_{m_1}, λ_{m_2}, and λ_{m_3}) of this mode.

Vibration modal analysis results for both initial and modified mass distributions of the blade were carried out to obtain the modified blade response. Also, the rotating flapwise root bending moment of the blade and its mode contributions for each modified distribution were performed to understand the effects on the prime contributors to the 4 per rev. pitching and rolling moments. These results will be discussed later in the next section.

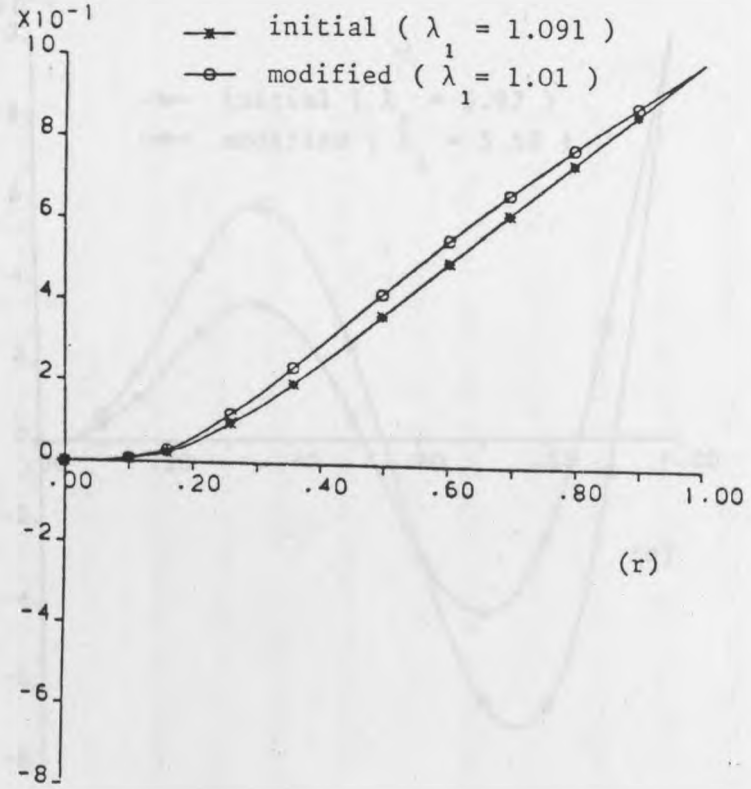

(a) 1st Mode

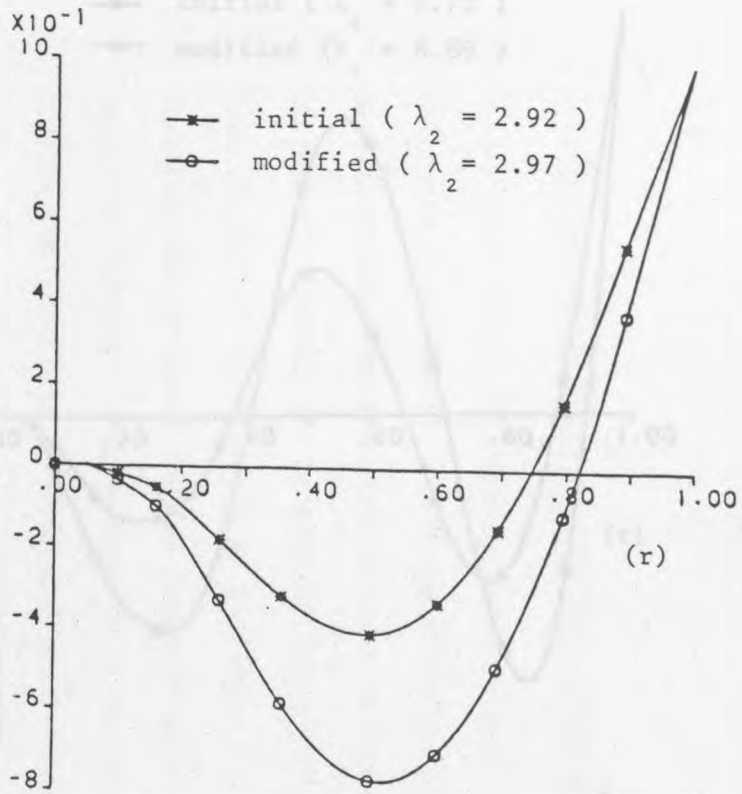

(b) 2nd Mode

Figure 69 The First Four Normalised Flatwise Bending Mode Shapes of the Rotating Blade for Initial and Modified Mass ($\lambda_{m_3=} = 0.125*10^{-2}$) Distributions.

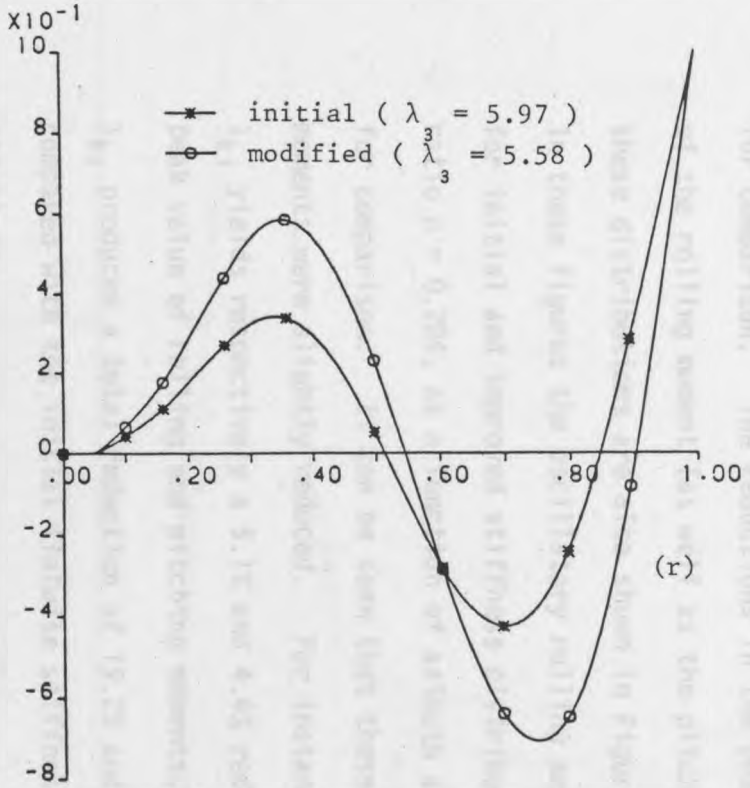

(c) 3 rd Mode

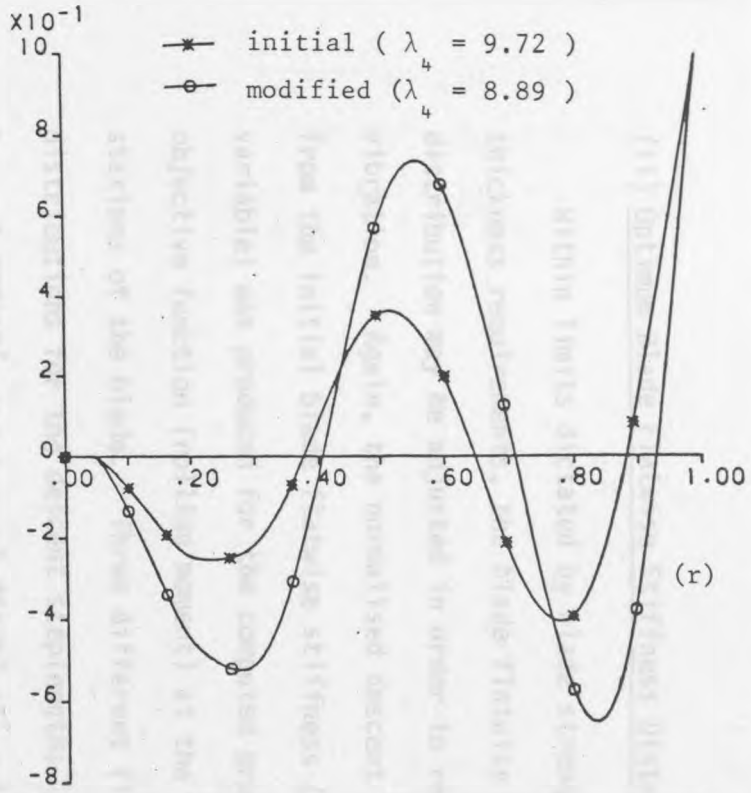

(d) 4th Mode

Figure 69 Cont.

(ii) Optimum Blade Flatwise Stiffness Distribution

Within limits dictated by blade strength and aerofoil thickness requirements, the blade flatwise stiffness distribution may be adjusted in order to reduce helicopter vibration. Again, the normalised descent direction emanating from the initial blade flatwise stiffness (initial design variable) was produced for the computed gradients of the objective function (rolling moment) at the previous spanwise stations of the blade. Three different flatwise stiffness distributions for the descent steplengths $\lambda_{k_1} = 0.5*10^7$, $\lambda_{k_2} = 0.625*10^7$ and $\lambda_{k_3} = 1.25*10^7$ along this descent direction are examined below.

Figure 70 illustrates the initial and resultant modified blade flatwise stiffness distributions (λ_{k_1}, λ_{k_2}, and λ_{k_3}) for comparison. The reductions in the peak to peak value of the rolling moment (as well as the pitching moment) of these distributions are also shown in Figures 71 and 72. In these figures the oscillatory rolling and pitching moments for initial and improved stiffness distributions, at advance ratio $\mu = 0.284$, as a function of azimuth are also plotted for comparison. It can be seen that these oscillatory moments were slightly reduced. For instance, distribution λ_{k_1} yields respectively a 5.1% and 4.4% reduction in peak to peak value of rolling and pitching moments, whilst distribution λ_{k_3} produces a total reduction of 19.2% and 14.6% respectively, compared with the initial flatwise stiffness distribution of the blade.

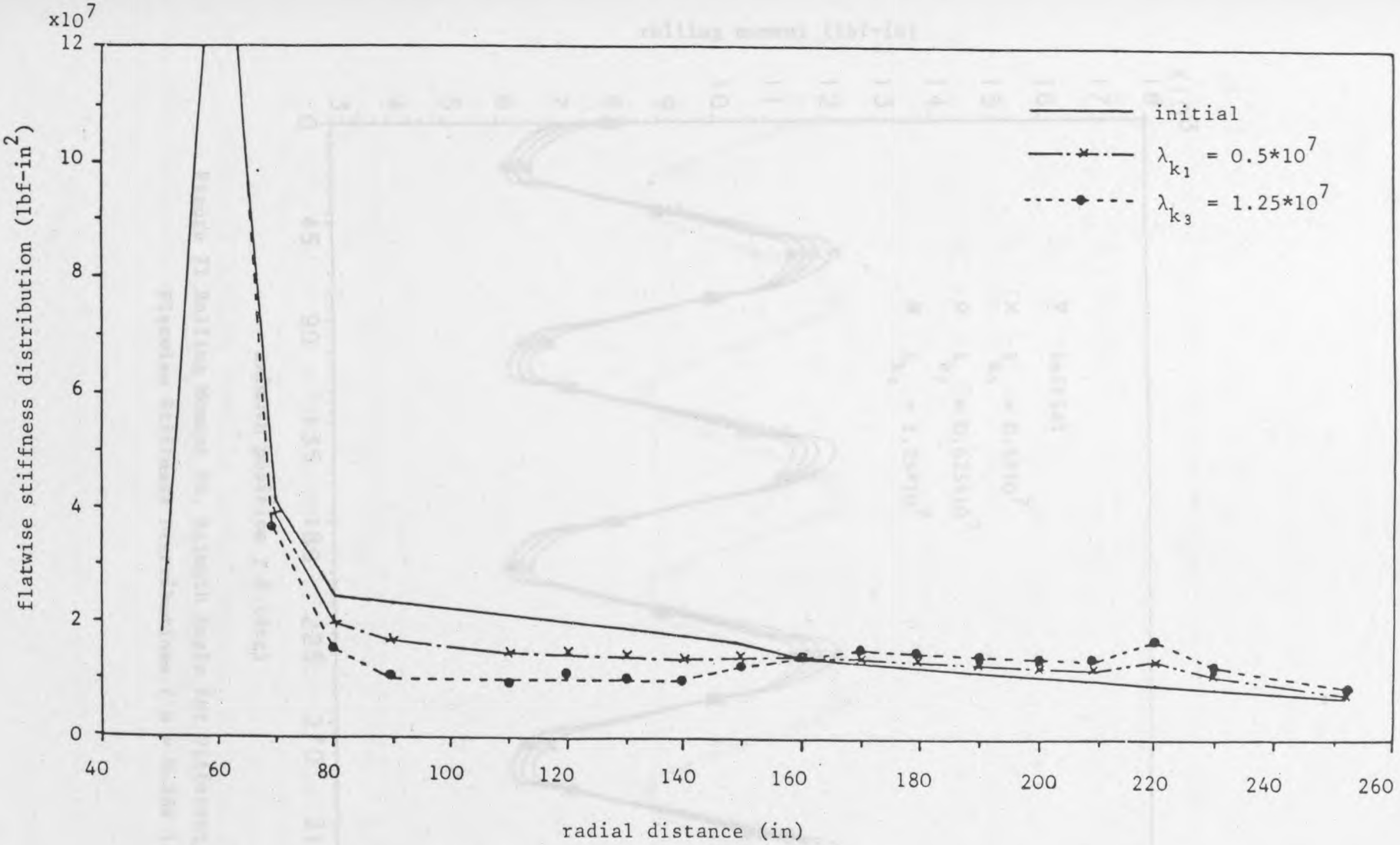

Figure 70 Initial and Modified Blade Flatwise Stiffness Distributions for Minimum Rolling Moment ($\mu = 0.284$).

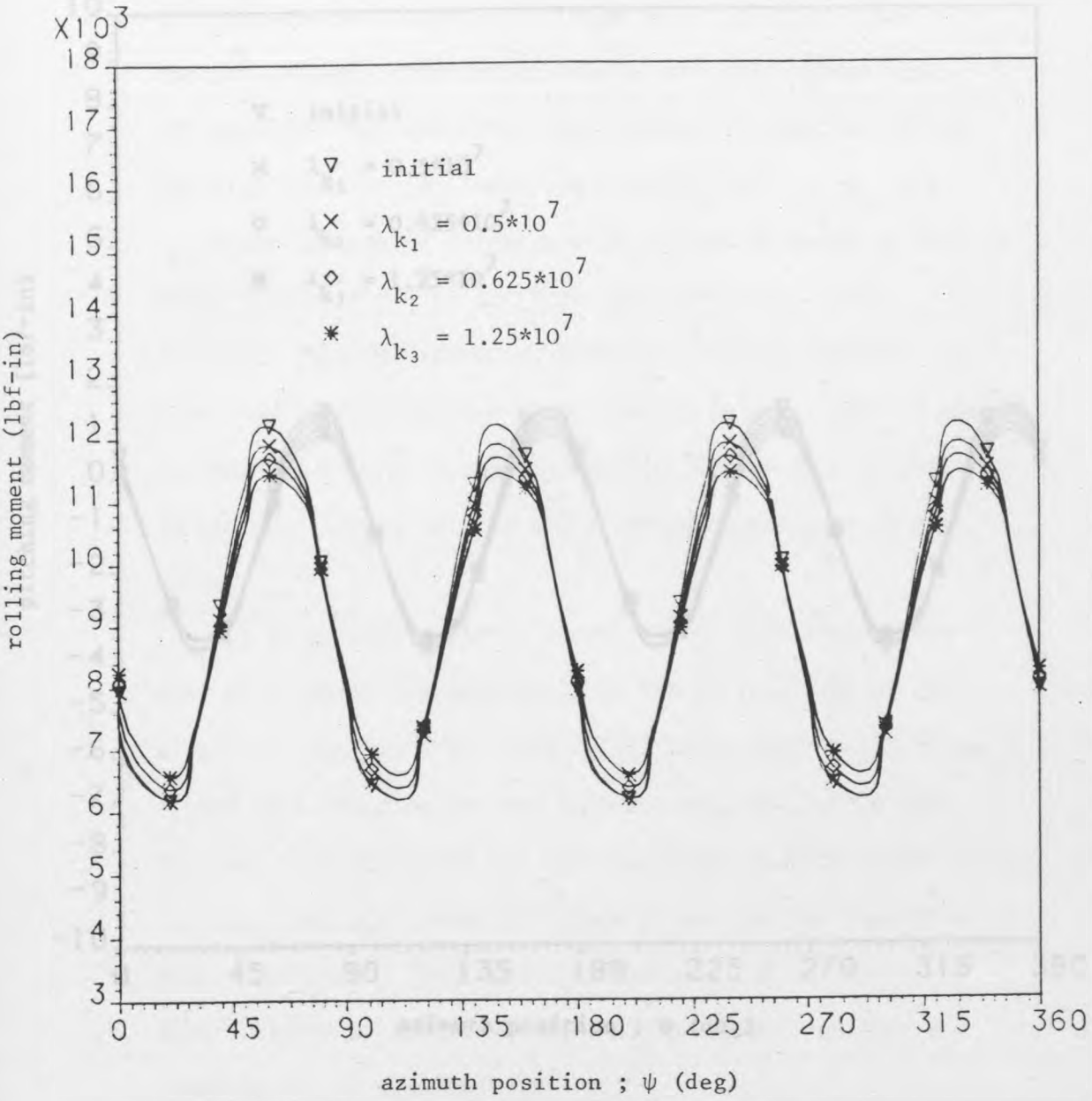

Figure 71 Rolling Moment Vs. Azimuth Angle for Different Blade Flatwise Stiffness Distributions ($\mu = 0.284$).

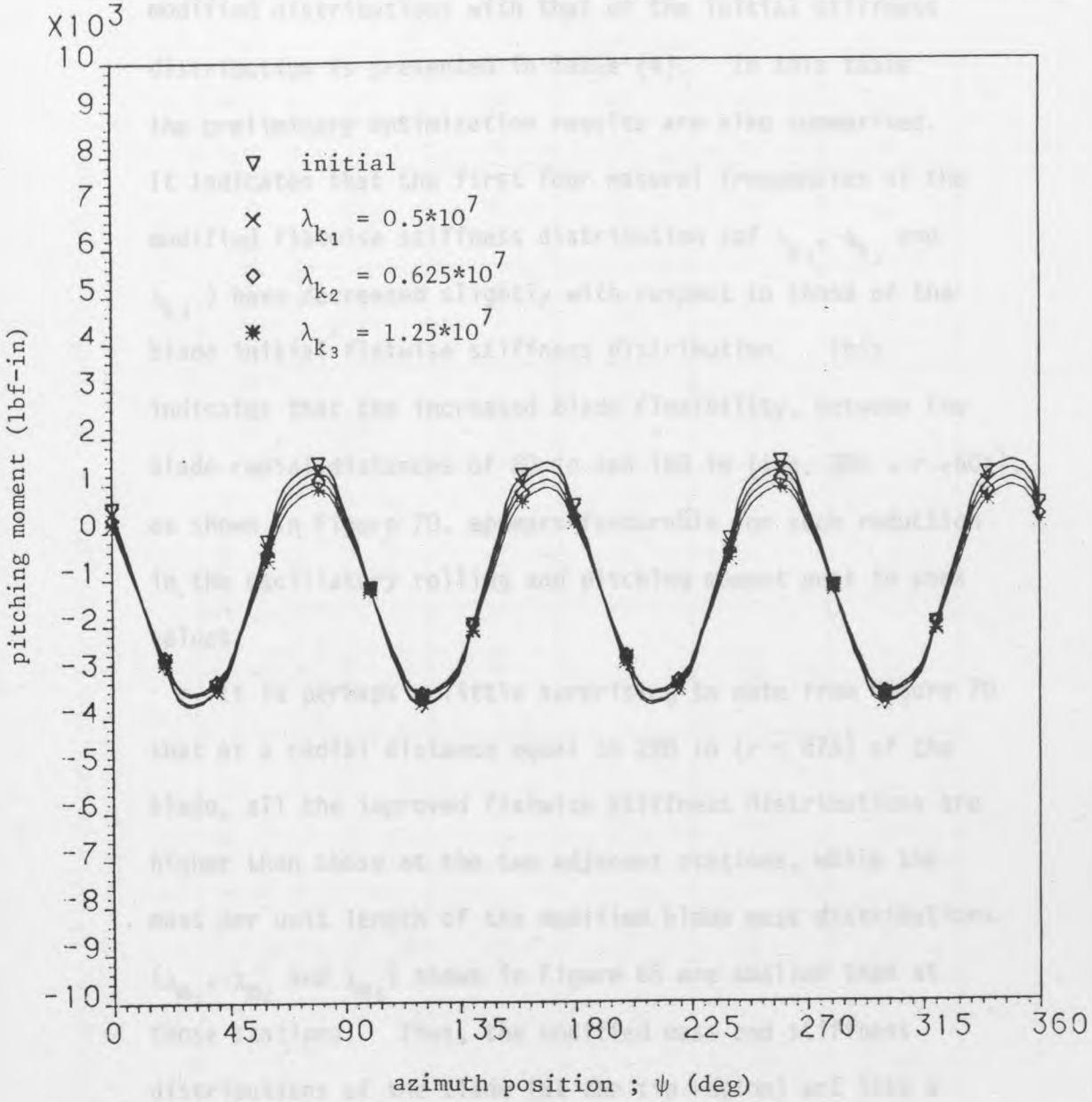

Figure 72 Pitching Moment Vs. Azimuth Angle for Different Blade Flatwise Stiffness Distributions ($\mu = 0.284$)

A comparison of rotating flapping frequencies of the modified distributions with that of the initial stiffness distribution is presented in Table (4). In this table the preliminary optimization results are also summarised. It indicates that the first four natural frequencies of the modified flatwise stiffness distribution (of λ_{k_1}, λ_{k_2} and λ_{k_3}) have decreased slightly with respect to those of the blade initial flatwise stiffness distribution. This indicates that the increased blade flexibility, between the blade radial distances of 80 in and 160 in (i.e. $30\% < r < 60\%$), as shown in Figure 70, appears favourable for such reduction in the oscillatory rolling and pitching moment peak to peak values.

It is perhaps a little surprising to note from Figure 70 that at a radial distance equal to 220 in ($r = 87\%$) of the blade, all the improved flatwise stiffness distributions are higher than those at the two adjacent stations, while the mass per unit length of the modified blade mass distributions (λ_{m_1}, λ_{m_2} and λ_{m_3}) shown in Figure 65 are smaller than at those stations. Thus, the modified mass and stiffness distributions of the blade (at the tip region) act like a "dumb-bell", as mentioned before.

On the other hand, one can conclude that the blade mass distribution, rather than flatwise stiffness distribution is the prime variable in reducing the oscillatory rolling and pitching moments. In order to investigate the cause

Table 4. Optimization Results Comparison for the Initial and Modified Flatwise Stiffness Distributions, at $\mu = 0.284$

Values	Rolling Moment M_x (lbf-in)		Pitching Moment M_y (lbf-in)		Natural Frequency Ratio			
	Peak to peak; M_{xp}	% Reduction in M_{xp}	Peak to peak; M_{yp}	% Reduction in M_{yp}	$\frac{w_{n_1}}{\Omega}$	$\frac{w_{n_2}}{\Omega}$	$\frac{w_{n_3}}{\Omega}$	$\frac{w_{n_4}}{\Omega}$
Initial Distribution	6029	-	5149	-	1.091	2.92	5.79	9.70
Distribution of $\lambda_{k_1} = 0.5*10^7$	5724	5.0	4928	4.25	1.087	2.88	5.74	9.59
Distribution of $\lambda_{k_2} = 0.625*10^7$	5638	6.5	4880	5.2	1.085	2.87	5.72	9.55
Distribution of $\lambda_{k_3} = 1.25*10^7$	4861	19.4	4417	14.2	1.078	2.79	5.57	9.29

of this and to understand the cause of the phase shift in maximum values of rolling and pitching moments (Figures 66 and 67) from the modified mass distributions, a complete set of aeroelastic analyses for both improved mass and stiffness distributions of the blade were carried out. The rotating flapping root bending moment, its modal contributions and steady state responses at the blade tip as a function of azimuth, at advance ratio $\mu = 0.284$, are compared in Figures 73.a and 73.b to 78.a and 78.b for both cases of modified distributions.

In Figures 73.a to 78.a, the above aeroelastic results for the modified blade mass distributions of λ_{m_1}, λ_{m_2} and λ_{m_3} are compared with those of the initial mass distribution of the blade. At the same time the results of the modified blade flatwise stiffness (of λ_{k_1}, λ_{k_2} and λ_{k_3}) distributions are also compared in Figures 73.b to 78.b. It can be seen that the flapping root bending moment "$M_{fi}(\psi)$", its first four mode contributions and the steady state response for the modified blade flatwise stiffness distributions (λ_{k_1}, λ_{k_2} and λ_{k_3}), are almost identical with those of the initial stiffness distribution, whilst these results are considerably different from those of the modified blade mass distributions (λ_{m_1}, λ_{m_2} and λ_{m_3}).

In Figure 73.a, the rotating flapping moment $M_{fi}(\psi)$ at $\mu = 0.284$ is compared for the initial and modified blade mass distributions. It can be seen that the peak to peak value

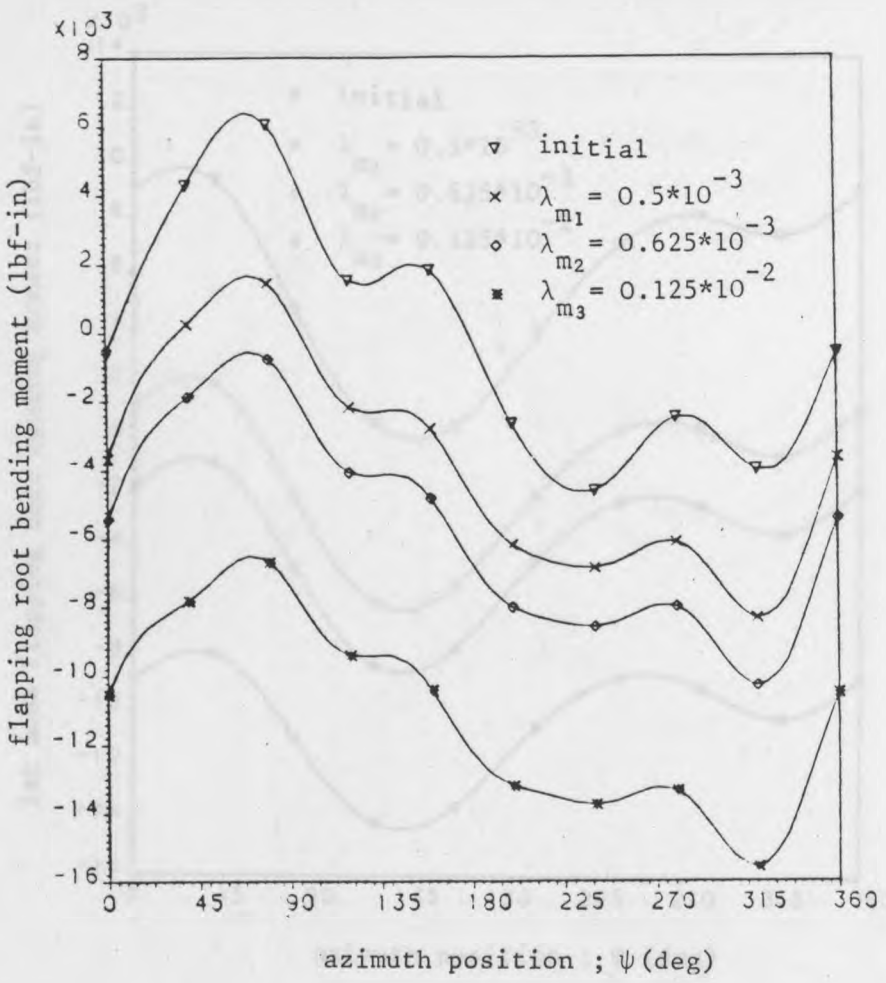

(a)

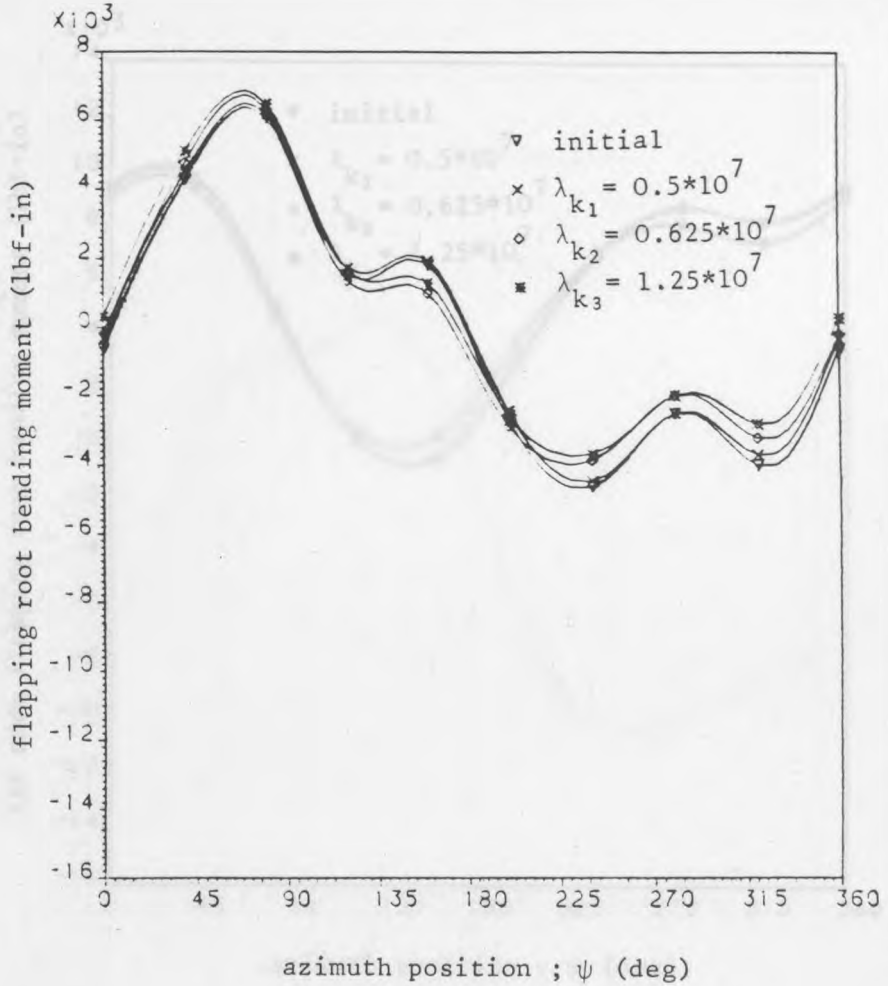

(b)

Figure 73 Blade Flapping Root Bending Moment Vs. Azimuth Angle For : (a) Different Blade Mass Distributions and (b) Different Blade Flatwise Stiffness Distributions.

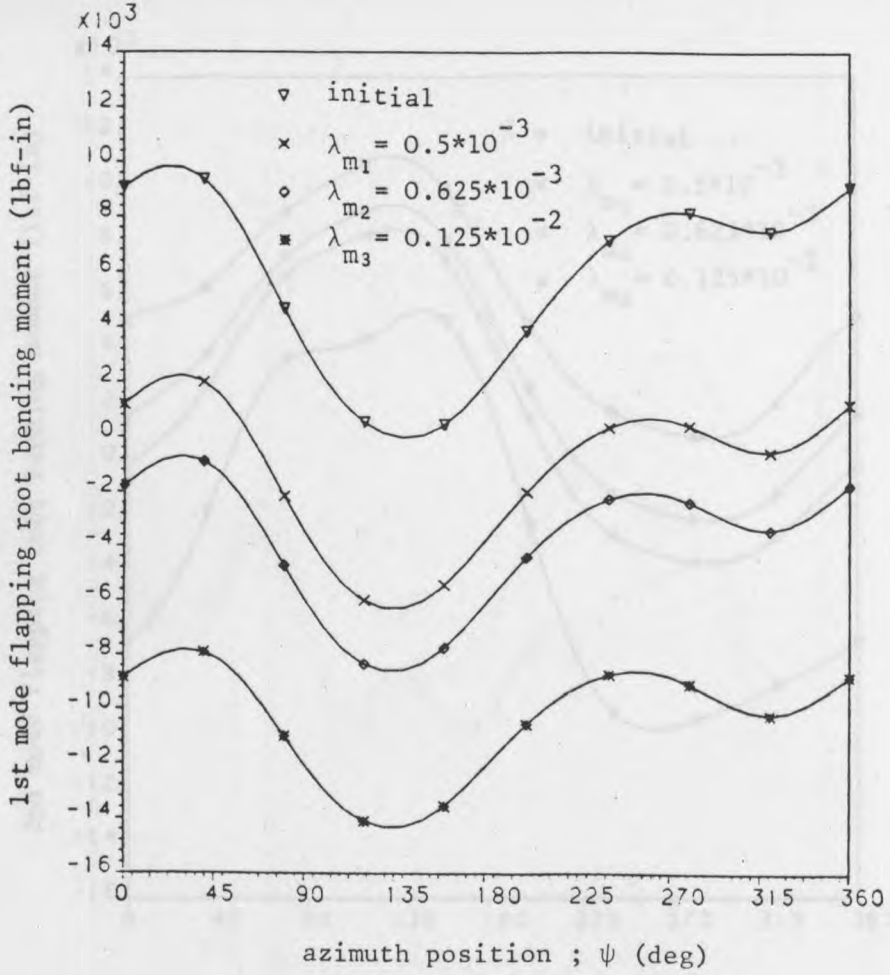

(a)

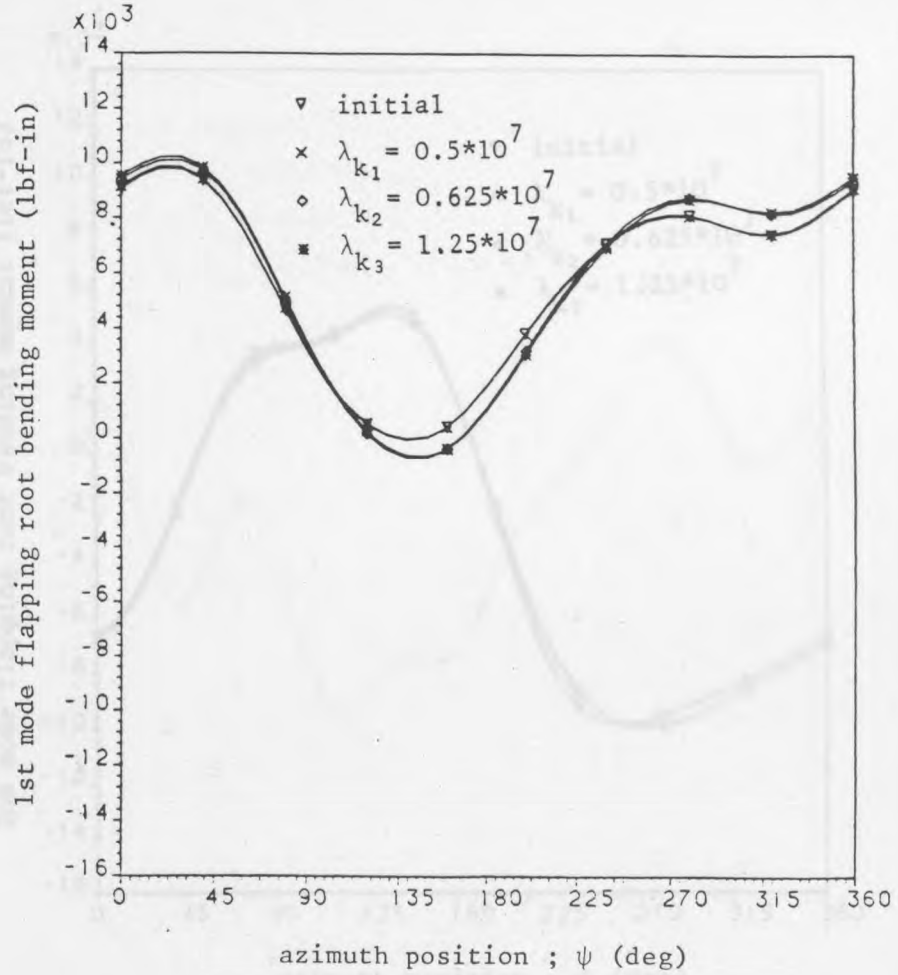

(b)

Figure 74 First Mode Flapping Root Bending Moment Vs. Azimuth Angle For : (a) Different Blade Mass Distributions and (b) Different Blade Flatwise Stiffness Distributions.

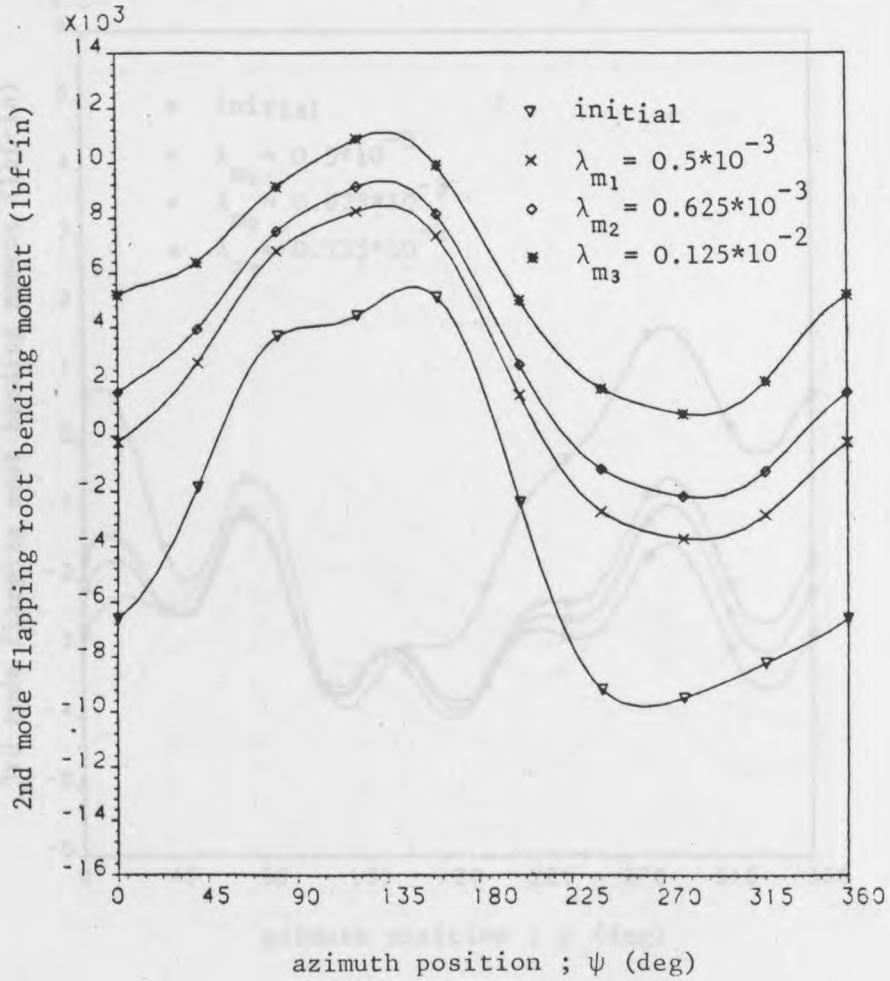

(a)

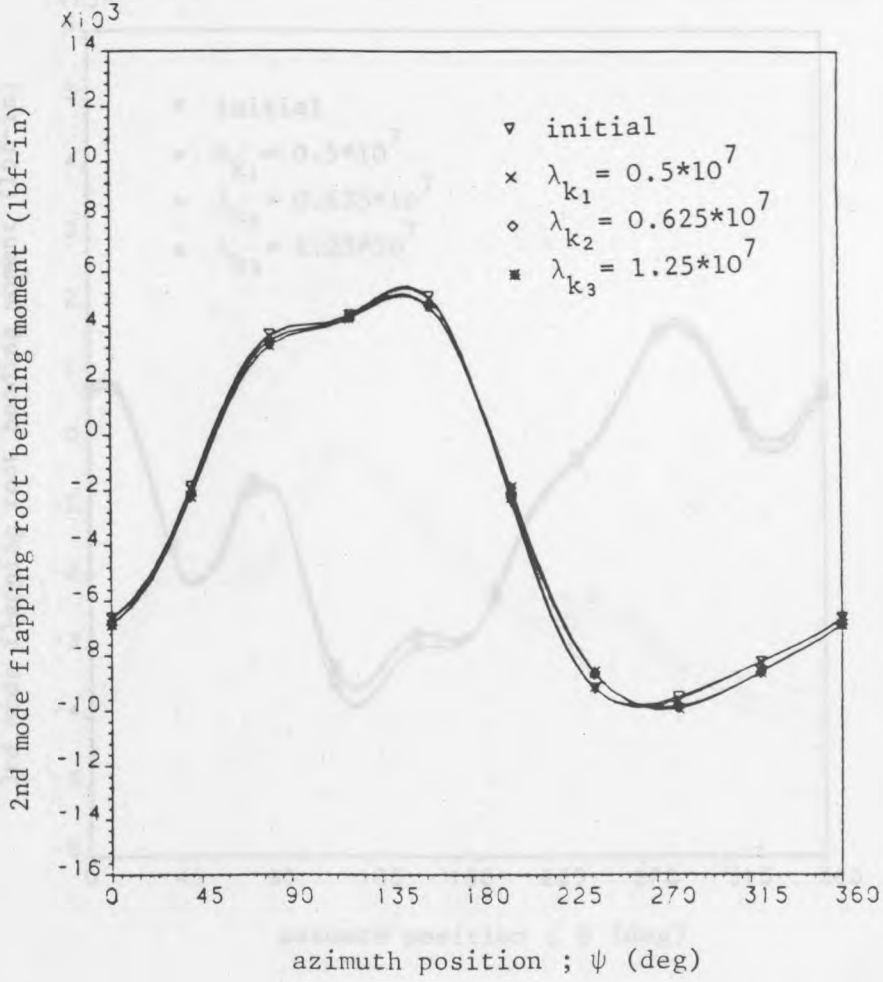

(b)

Figure 75 Second Mode Flapping Root Bending Moment Vs. Azimuth Angle For : (a) Different Blade Mass Distributions and (b) Different Blade Flatwise Stiffness Distributions.

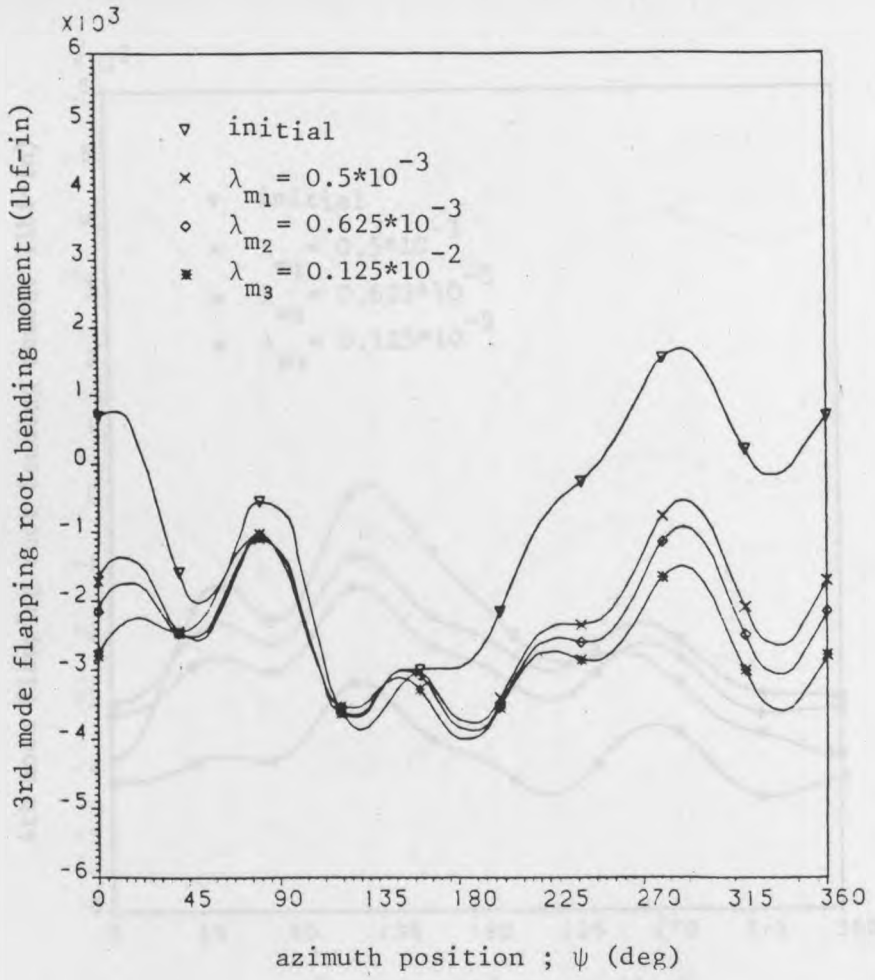

(a)

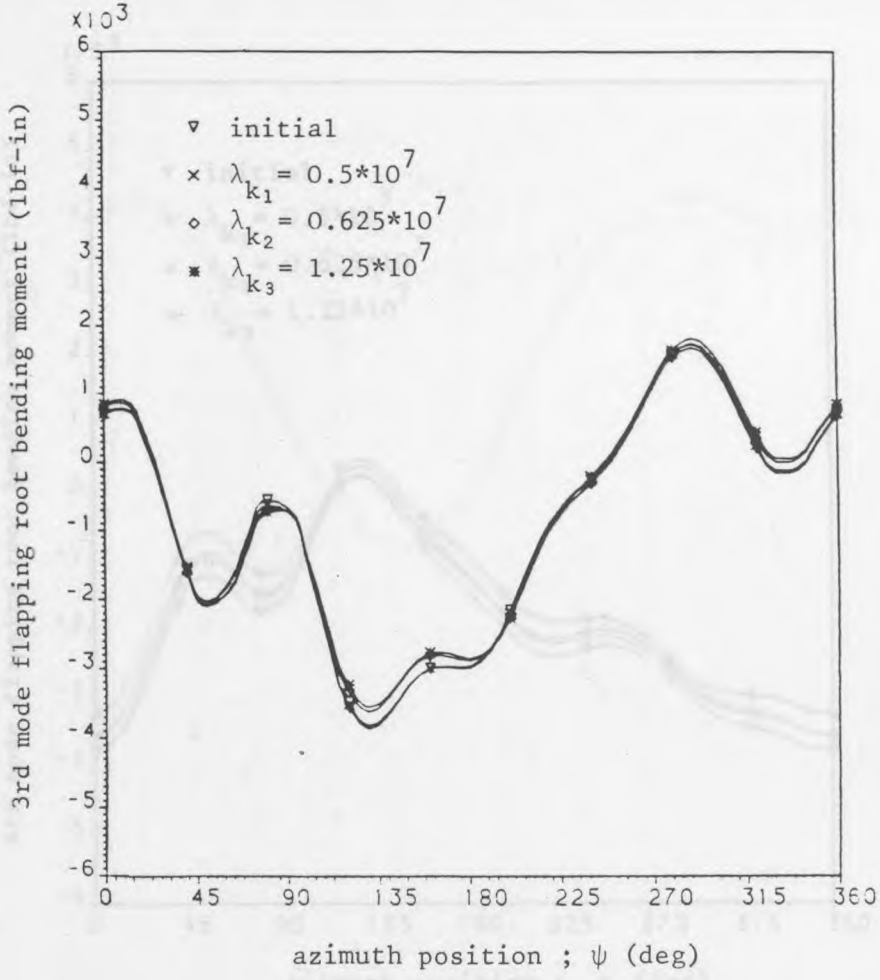

(b)

Figure 76 Third Mode Flapping Root Bending Moment Vs. Azimuth Angle For : (a) Different Blade Mass Distributions and (b) Different Blade Flatwise Stiffness Distributions.

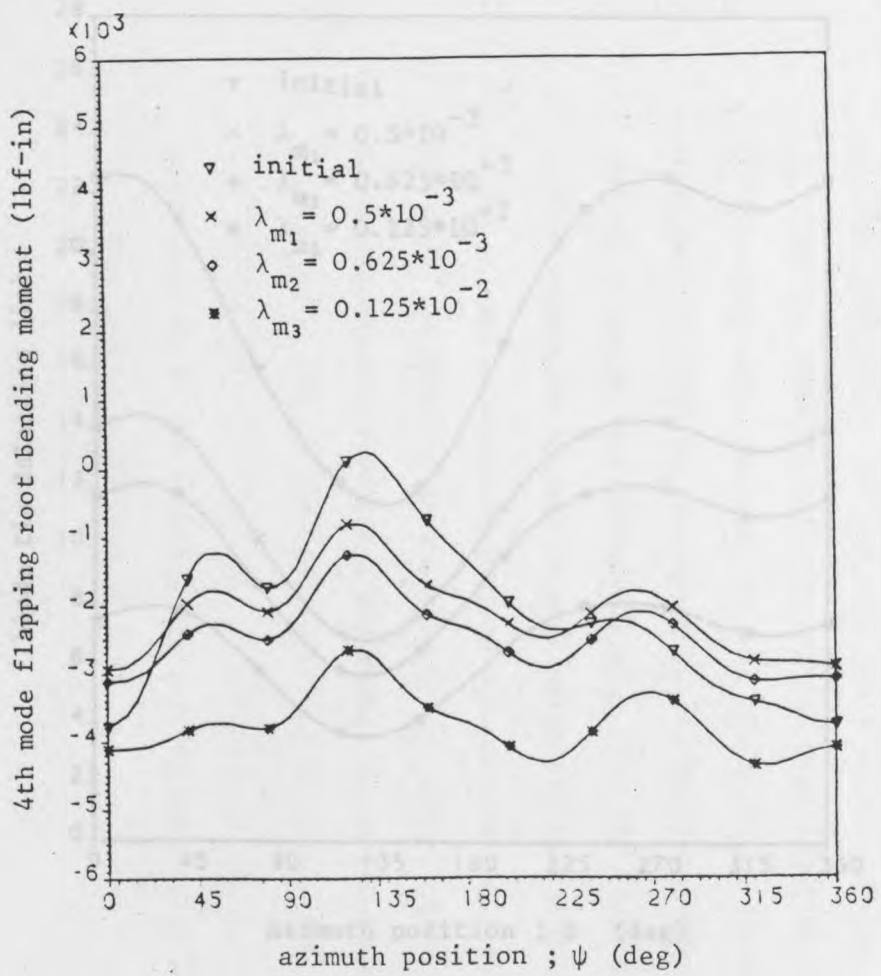

(a)

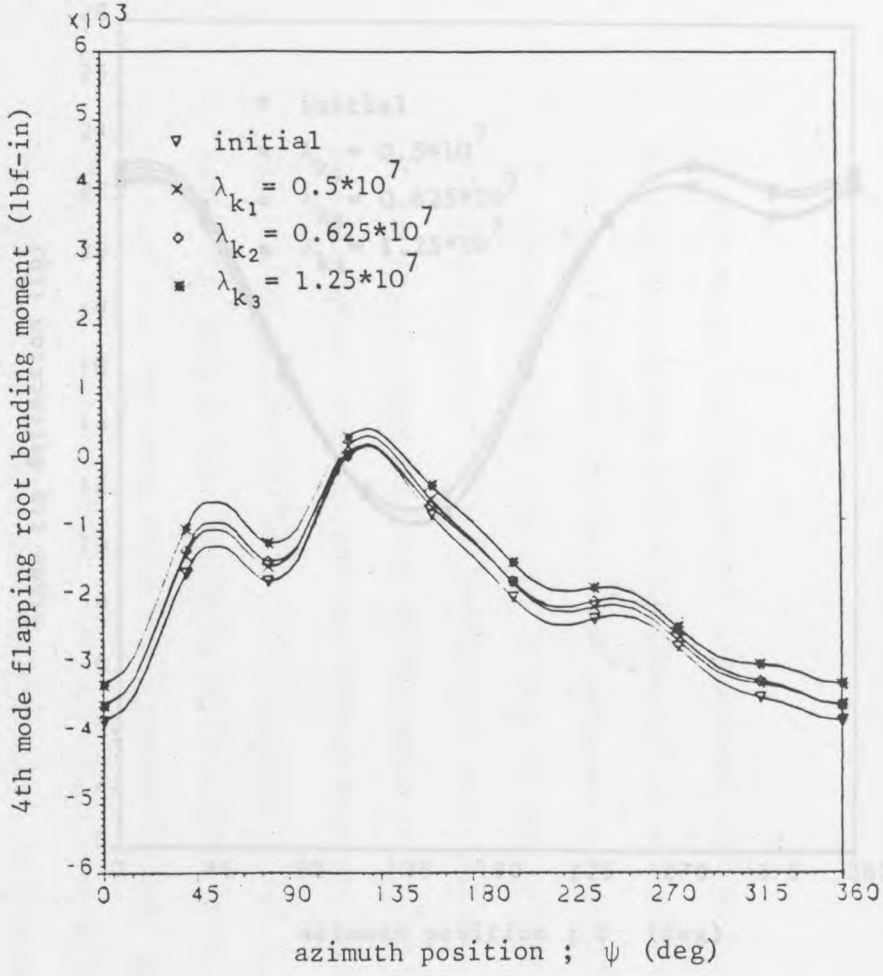

(b)

Figure 77 Fourth Mode Flapping Root Bending Moment Vs. Azimuth Amgle For : (a) Different Blade Mass Distributions and (b) Different Blade Flatwise Stiffness Distributions.

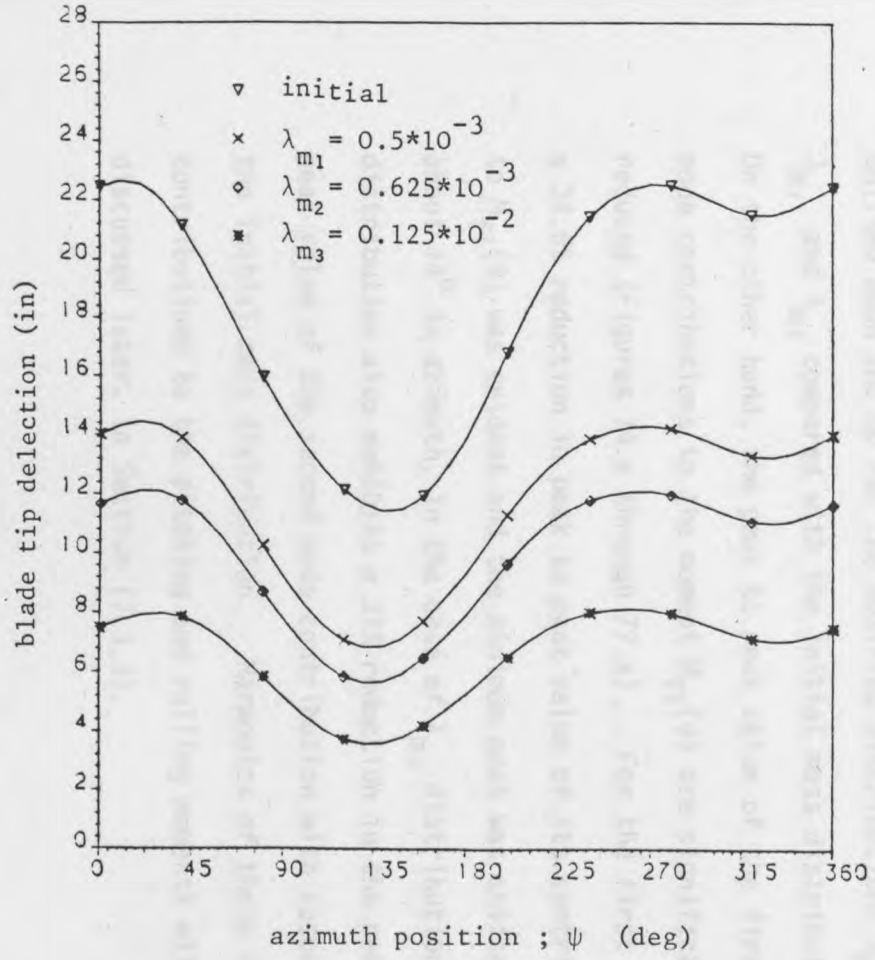

(a)

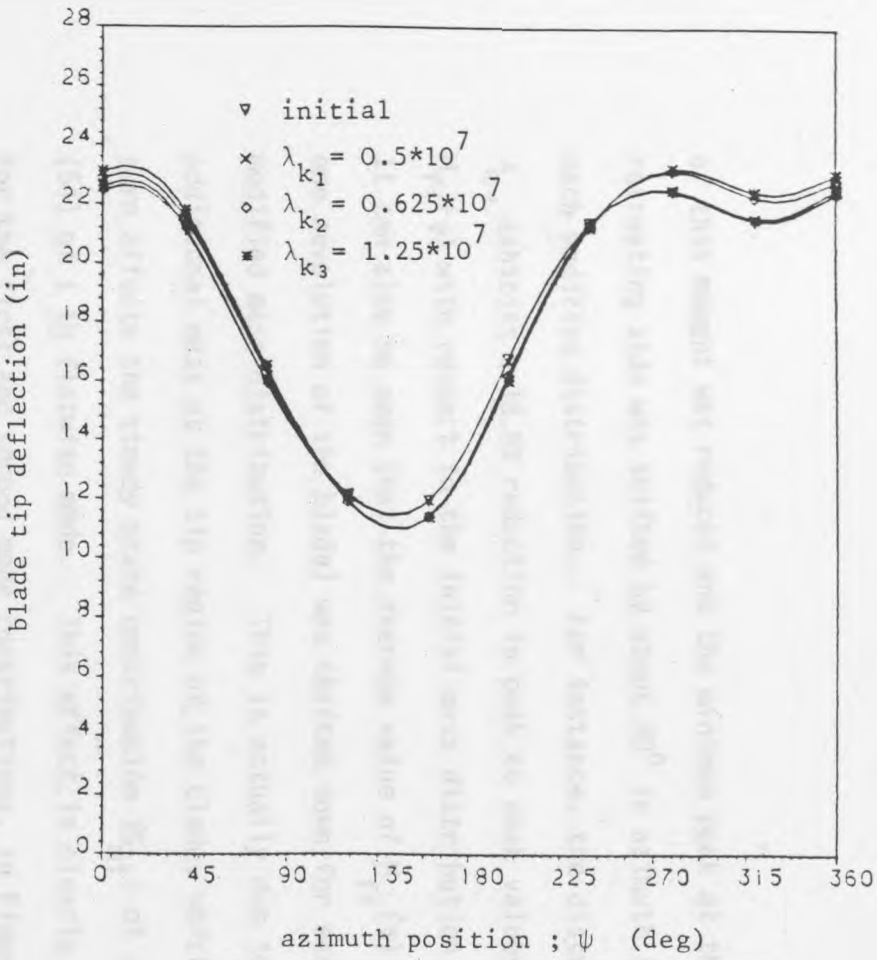

(b)

Figure 78 Blade Tip Deflection Vs. Azimuth Angle For : (a) Different Blade Mass Distributions and (b) Different Blade Flatwise Stiffness Distributions.

of this moment was reduced and the minimum peak at the retreating side was shifted by about 90^{o} in azimuth for each modified distribution. For instance, the distribution λ_{m_3} exhibits a 18.9% reduction in peak to peak values of $M_{fi}(\psi)$ with respect to the initial mass distribution. It can also be seen that the average value of $M_{fi}(\psi)$ (over one revolution of the blade) was shifted down for each modified mass distribution. This is actually due to the additional mass at the tip region of the blade, which in turn affects the steady state contribution $\{S_{mi}\}$ of equation (54) of i th flatwise mode. This effect is clearly shown, for the first and second mode contributions, in Figures 74.a and 75.a respectively. Their average values are shifted down and up for the modified distributions λ_{m_1}, λ_{m_2} and λ_{m_3} compared with the initial mass distribution. On the other hand, the peak to peak value of the first four mode contributions to the moment $M_{fi}(\psi)$ are significantly reduced (Figures 74.a through 77.a). For the first mode, a 34.6% reduction in peak to peak value of its contribution to $M_{fi}(\psi)$ was evident and the minimum peak was shifted by about 14^{o} in azimuth, in the case of λ_{m_3} distribution. This distribution also exhibits a 31% reduction in the peak to peak value of the second mode contribution with respect to the initial mass distribution. Harmonics of these modal contributions to the pitching and rolling moments will be discussed later, in Section (7.3.3).

In Figure 78.a, the steady state responses at the blade tip for the modified mass distributions (λ_{m_1}, λ_{m_2} and λ_{m_3}) are compared with that of the initial mass distribution at the particular advance ratio "μ = 0.284". It can be seen that the responses for these modified distributions are significantly reduced with respect to that of initial mass distribution. For instance, the peak to peak value of the response was reduced by 59%, for the case of λ_{m_3} distribution, and the minimum peak was shifted by an amount of 14^{o} in azimuth, compared with that of the initial distribution. The reason for this reduction will be discussed in Section 7.3.3.

Thus, from the foregoing results the reduction in the peak to peak values of $M_{fi}(\psi)$ in steady state response of the blade and the previous phase shifts, may be the cause of the phase shift of the maximum values of pitching and rolling moments for the modified mass distributions shown in Figures 66 and 67. There is no such phase shift in the case of modified flatwise stiffness distributions (Figures 71 and 72), with respect to those of the initial distributions. This is because the computed quantities $M_{fi}(\psi)$ and the steady state response for each of the modified flatwise stiffness distributions (Figures 73.b through 78.b) are almost identical with that of initial flatwise stiffness distribution.

(iii) Optimum Built-in Twist Distribution Along the Blade

Blade twist may also affect vibratory hub loads and moments by altering the basic airloads applied to the blade. Thus, the rates of change of the objective function (rolling moment) with changes in the built-in twist variable $\theta_t(x)$ at the previous 19 stations along the blade were computed. The baseline of these gradients is taken to be the initial distribution of $\theta_t(x)$ along the blade. The normalised descent direction emanating from this initial design variable was performed, and three different descent steplengths $\lambda_{\theta 1} = 0.01$, $\lambda_{\theta_2} = 0.0125$ and $\lambda_{\theta_3} = 0.025$ along this direction are examined. The preliminary optimization results, at $\mu = 0.284$, for the distributions of $\lambda_{\theta 1}$, $\lambda_{\theta 2}$ and $\lambda_{\theta 3}$ are presented in Table (5) and the modified distribution is compared with the initial distribution in Figure 79. However, the results presented in Table (5) show very little effect from the built-in twist along the blade on the oscillatory rolling and pitching moments. For instance, the modified distribution $\lambda_{\theta 1}$ yields 6.5% and 2.3% reductions in the peak to peak value of pitching and rolling moments respectively, while the distribution $\lambda_{\theta 3}$ yields 16% and 5.8% reductions respectively with respect to the initial distribution. It can also be seen from Figure 79 that the modified distribution $\lambda_{\theta 3}$ has more or less the same values as those of the initial distribution, except in the tip

Table 5. Optimization Results Comparison for the Initial and Modified Built-in Distributions Along the Blade at $\mu = 0.284$

Values	Rolling Moment M_x (lbf-in)		Pitching Moment M_y (lbf-in)	
	Peak to peak; M_{xp}	% Reduction in M_{xp}	Peak to peak; M_{yp}	% Reduction in M_{yp}
Initial Distribution	6029	-	5149	-
Distribution of $\lambda_{\theta 1} = 0.01$	5892	2.3	4823	6.3
Distribution of $\lambda_{\theta 2} = 0.0125$	5858	2.8	4741	7.9
Distribution of $\lambda_{\theta 3} = 0.025$	5682	5.8	4330	15.9

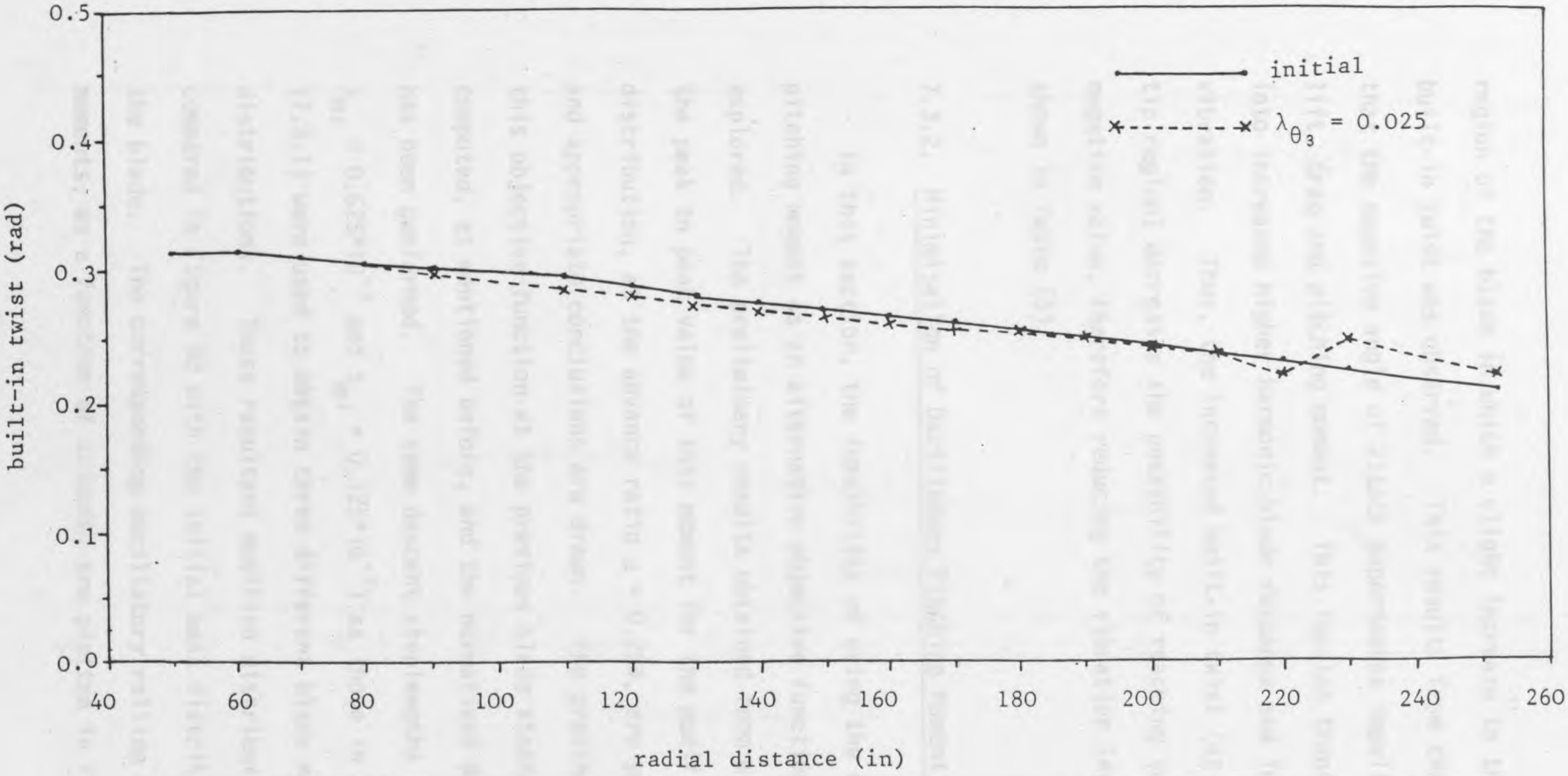

Figure 79 Initial and Modified Built-in Twist Along the Blade for Minimum Rolling Moment (μ = 0.284).

region of the blade in which a slight increase in the built-in twist was observed. This results from the fact that the negative angle of attack experiences impulsive lift, drag and pitching moment. This impulse translates into increased higher harmonic blade response and increased vibration. Thus, the increased built-in twist (at the tip region) decreases the possibility of reaching such a negative value, therefore reducing the vibration level as shown in Table (5).

7.3.2. Minimisation of Oscillatory Pitching Moment

In this section, the feasibility of using the oscillatory pitching moment as an alternative objective function is explored. The preliminary results obtained from minimising the peak to peak value of this moment for the modified mass distribution, at the advance ratio $\mu = 0.284$, are presented and appropriate conclusions are drawn. The gradients of this objective function at the previous blade stations were computed, as mentioned before, and the normalised descent has been performed. The same descent steplengths ($\lambda_{m_1} = 0.5*10^{-3}$ $\lambda_{m_2} = 0.625*10^{-3}$ and $\lambda_{m_3} = 0.125*10^{-2}$) as those in Section (7.3.1) were used to obtain three different blade mass distributions. These resultant modified distributions are compared in Figure 80 with the initial mass distribution of the blade. The corresponding oscillatory rolling and pitching moments, as a function of azimuth, are plotted in Figures 81

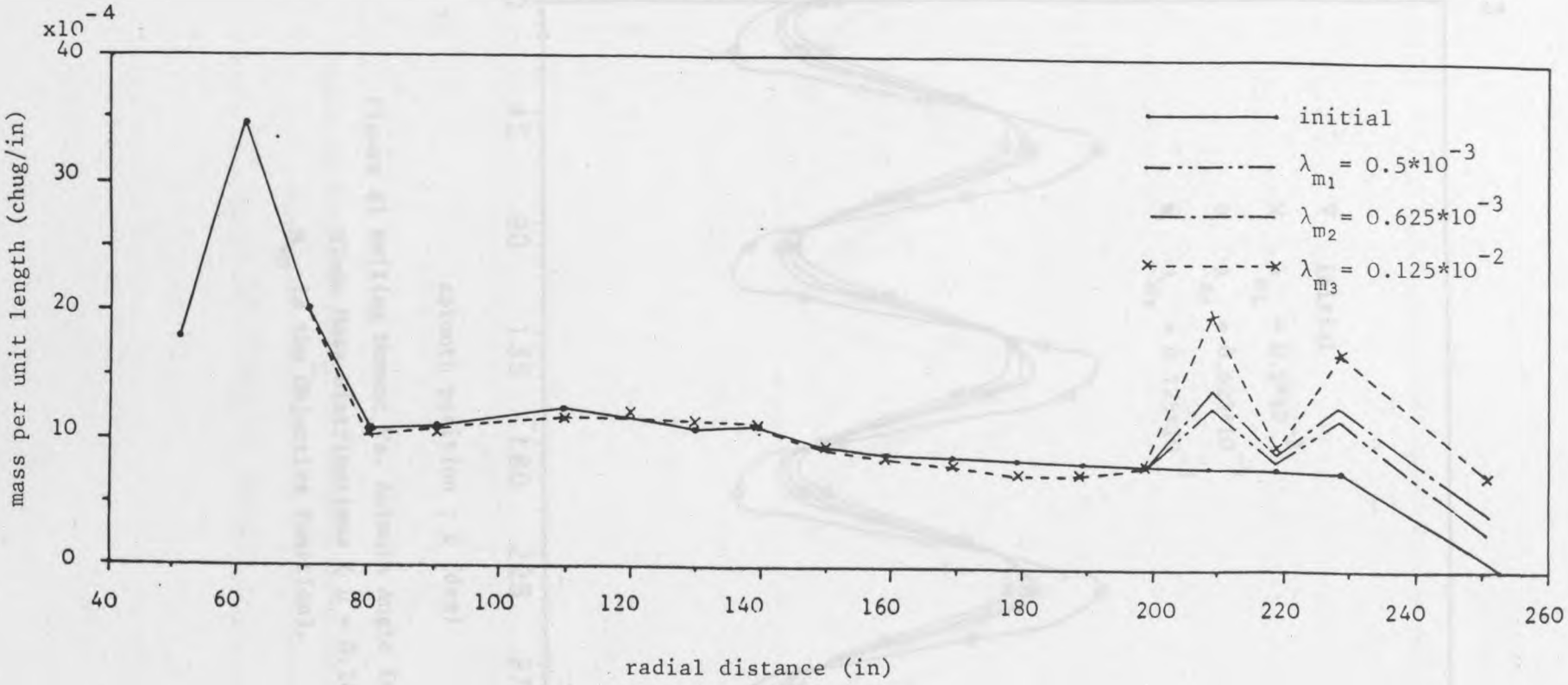

Figure 80 Initial and Modified Blade Mass Distributions for Minimum Pitching Moment ($\mu = 0.284$).

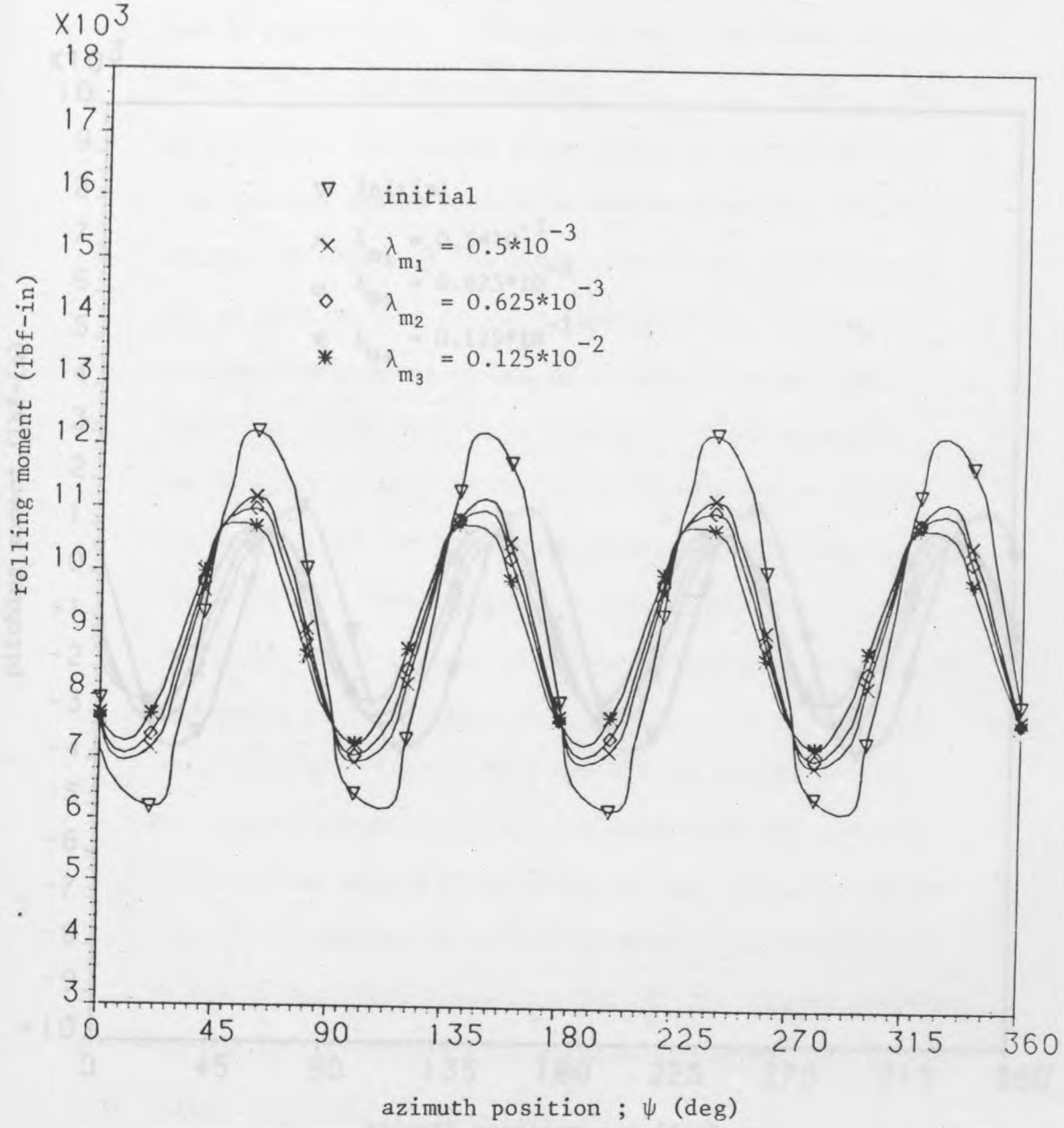

Figure 81 Rolling Moment Vs. Azimuth Angle for Different Blade Mass Distributions (μ = 0.284 and M_{yp} is the Objective Function).

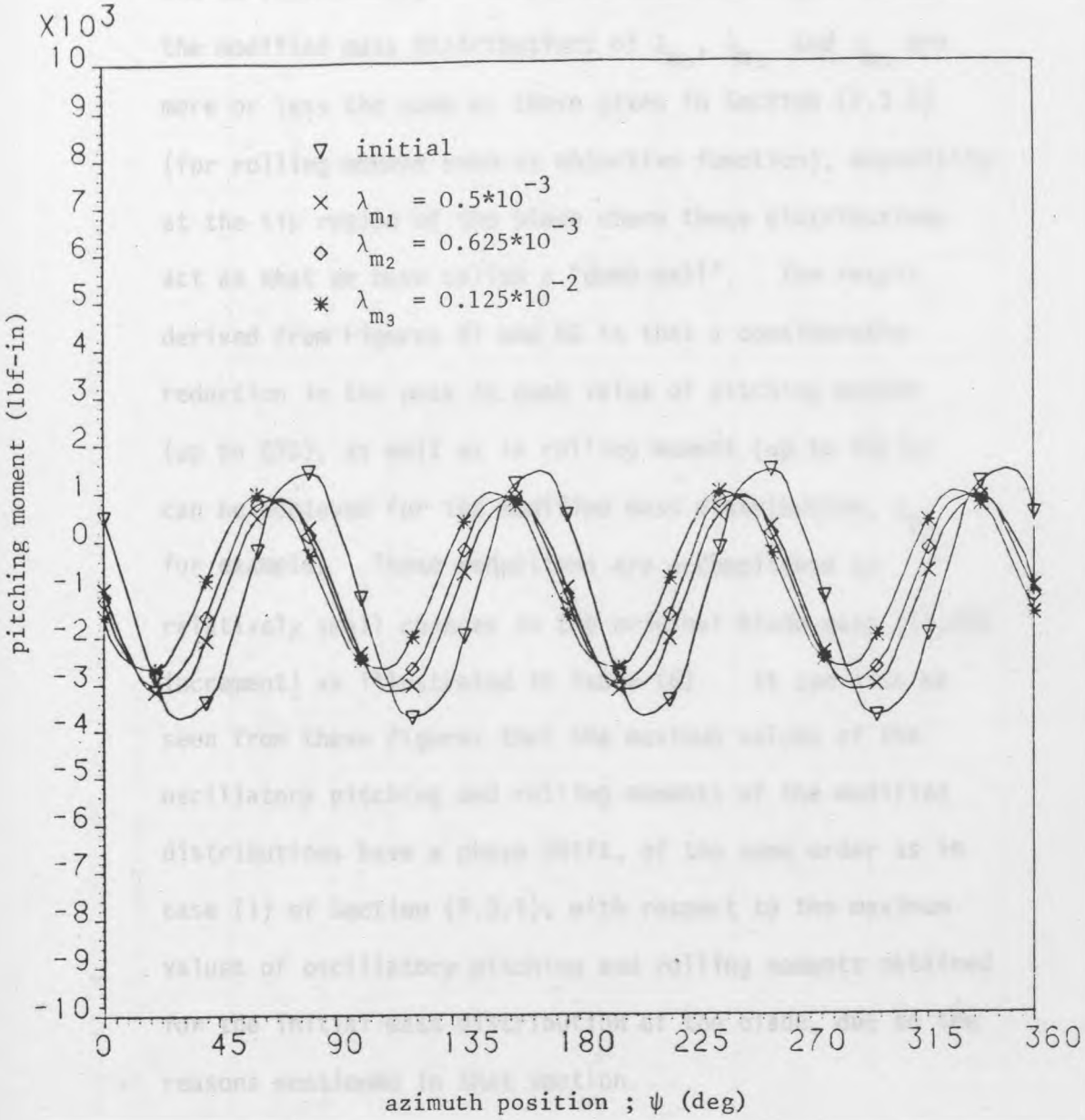

Figure 82 Pitching Moment Vs. Azimuth Angle for Different Blade Mass Distributions (μ = 0.284 and M_{yp} is the Objective Function).

and 82 respectively. It can be seen from Figure 80 that the modified mass distributions of λ_{m_1}, λ_{m_2} and λ_{m_3} are more or less the same as those given in Section (7.3.1) (for rolling moment used as objective function), especially at the tip region of the blade where these distributions act as what we have called a "dumb-bell". The result derived from Figures 81 and 82 is that a considerable reduction in the peak to peak value of pitching moment (up to 29%), as well as in rolling moment (up to 43 %) can be achieved for the modified mass distribution, λ_{m_3} for example. These reductions are accomplished by relatively small changes in the original blade mass (13.25% increment) as illustrated in Table (6). It can also be seen from these figures that the maximum values of the oscillatory pitching and rolling moments of the modified distributions have a phase shift, of the same order as in case (i) of Section (7.3.1), with respect to the maximum values of oscillatory pitching and rolling moments obtained for the initial mass distribution of the blade, due to the reasons mentioned in that section.

In Table (6), the rotating natural frequencies of the modified blade mass distribution are also compared with those of the initial distribution. This indicates that all but the second flapping natural frequencies are decreased slightly, the second remaining virtually unchanged initially, thereafter a slight increment being observed, as discussed in case (i) of Section (7.3.1).

Table 6. Optimization Results Comparison for the Initial and Modified Blade Mass Distribution at $\mu = 0.284$ (M_{yp} is the obective function).

Values	Blade mass; W_b (lb)	% Incr. in W_b	Rolling Moment M_x (lbf-in)		Pitching Moment M_y (lbf-in)		Natural Frequency Ratio			
			Peak to peak; M_{xp}	% Reduction in M_{xp}	Peak to peak; M_{yp}	% Reduction in M_{yp}	$\frac{w_{n_1}}{\Omega}$	$\frac{w_{n_2}}{\Omega}$	$\frac{w_{n_3}}{\Omega}$	$\frac{w_{n_4}}{\Omega}$
Initial Distribution	200.15	-	6029	-	5149	-	1.091	2.92	5.97	9.70
Distribution of $\lambda_{m_1} = 0.5*10^{-3}$	210.77	5.3	4225	29.9	4014	22.0	1.058	2.9	5.67	9.28
Distribution of $\lambda_{m2} = 0.625*10^{-3}$	213.43	6.6	4064	32.6	3979	22.7	1.051	2.9	5.68	9.20
Distribution of $\lambda_{m3} = 0.125*10^{-2}$	226.71	13.3	3431	43.1	3655	29.4	1.023	2.95	5.69	8.96

Other sequences of the above preliminary results, in which the second frequency ratio ($\frac{\omega_{n_2}}{\Omega}$) of the initial blade configurations was reduced to 2.7, were carried out. This frequency ratio was obtained by multiplying the flatwise stiffness, at each station of the original blade, by a factor of 0.675. The above optimization process (with pitching moment peak to peak value used as objective function) was re-run. The optimization results at the same advance ratio $\mu = 0.284$ and same descent steplengths ($\lambda_{m_1} = 0.5*10^{-3}$, $\lambda_{m_2} = 0.625*10^{-3}$ and $\lambda_{m_3} = 0.125*10^{-2}$) are compared in Table (7) with those of the initial mass distribution. The resultant modified distributions are also plotted in Figure 83. It is interesting to note that these modified mass distributions for this special case are again more or less the same as those mentioned above as well as for the foregoing resultant distributions in case (i) of Section (7.3.1). Moreover, the reductions in the peak to peak values of pitching moment (as well as in rolling moment) in this case (Table (7)) are of the same order as for those cases indicated in Tables (2,3 and 6). For instance, reductions in the order of 33.4% and 40.4% in pitching and rolling moment peak to peak values respectively have been achieved, for the modified mass distribution λ_{m_3}. A relatively small change in the original blade weight (up to 17.4% increase) is sacrificed for these reductions.

Table 7. Optimization Results Compariosn for the Initial and Modified Blade Mass Distributions at $\mu = 0.284$ (especial case for $\frac{w_{n_2}}{\Omega} = 2.7$ and M_{yp} is the objective function)

Values	Blade mass; W_b (lb)	% Incr. in W_b	Rolling Moment M_x (lbf-in)		Pitching Moment M_y (lbf-in)		Natural Frequency Ratio			
			Peak to peak; M_{xp}	% Reduction in M_{xp}	Peak to peak; M_{yp}	% Reduction in M_{yp}	$\frac{w_{n_1}}{\Omega}$	$\frac{w_{n_2}}{\Omega}$	$\frac{w_{n_3}}{\Omega}$	$\frac{w_{n_4}}{\Omega}$
Initial Distribution	200.15	-	6029	-	5149	-	1.091	2.92	5.97	9.70
Distribution of $\lambda_{m_1} = 0.5*10^{-3}$	214.1	6.8	2799	38.8	4872	23.5	1.010	2.68	5.01	7.86
Distribution of $\lambda_{m_2} = 0.625*10^{-3}$	217.6	8.7	2756	39.8	4716	26.0	1.003	2.68	5.0	7.80
Distribution of $\lambda_{m_3} = 0.125*10^{-2}$	235.0	17.4	2726	40.4	4247	33.4	0.975	2.72	5.04	7.67

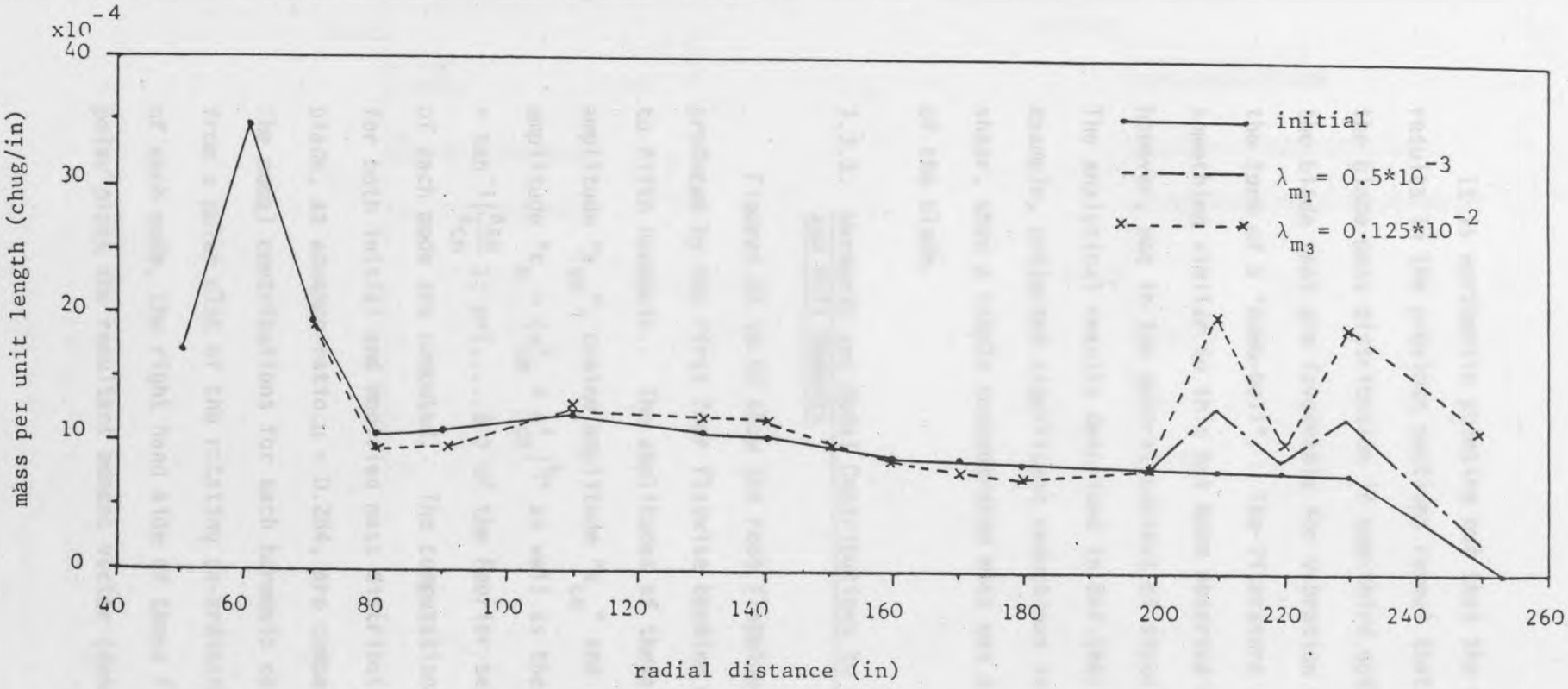

Figure 83 Initial and Modified Blade Mass Distributions for Minimum Pitching Moment , $\mu = 0.284$ (especial case for $(w_{n_2}/\Omega) = 2.7$).

It is worthwhile pointing out that the optimization results in the previous sections reveal that additions to the blade mass distribution in one-third outboard span of the blade that are favourable for vibration reduction take the form of a "dumb-bell". The literature shows that something similar to this has been observed before, but, however, not in the general context of structural optimization. The analytical results described in Ref.[66] and [67], for example, projected significant reductions in 4P vertical root shear, when a simple concentrated mass was added to the tip of the blade.

7.3.3. Harmonic and Modal Contributions to Pitch and Roll Moments

Figures 84 to 88 show the root flapping bending moment produced by the first four flatwise bending modes at the first to fifth harmonic. The amplitudes of these harmonics (sine amplitude "a_{sn}", cosine amplitude "a_{cn}" and the resultant amplitude "$c_n = (a_{sn}^2 + a_{cn}^2)^{\frac{1}{2}}$" as well as the phase angle ($\phi_n = \tan^{-1}(\frac{a_{sn}}{a_{cn}})$; n=1,....5) of the Fourier series representation of each mode are computed. The computational results obtained for both initial and modified mass distributions (λ_{m_3}) of the blade, at advance ratio $\mu = 0.284$, are compared in these Figures. The modal contributions for each harmonic can be clearly seen, from a polar plot of the rotating co-ordinate moment vector of each mode, the right hand side of these figures. In these polar plots the resultant moment vector (denoted by R) which

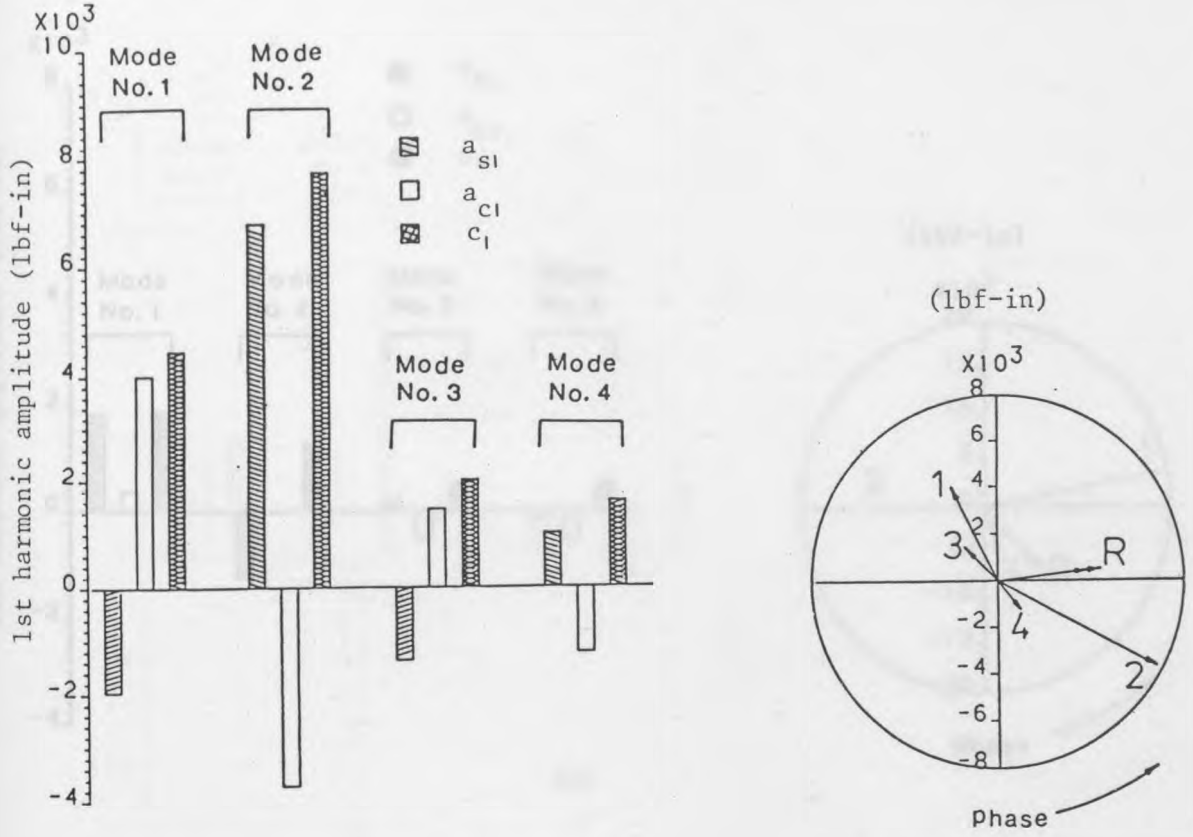

(a)

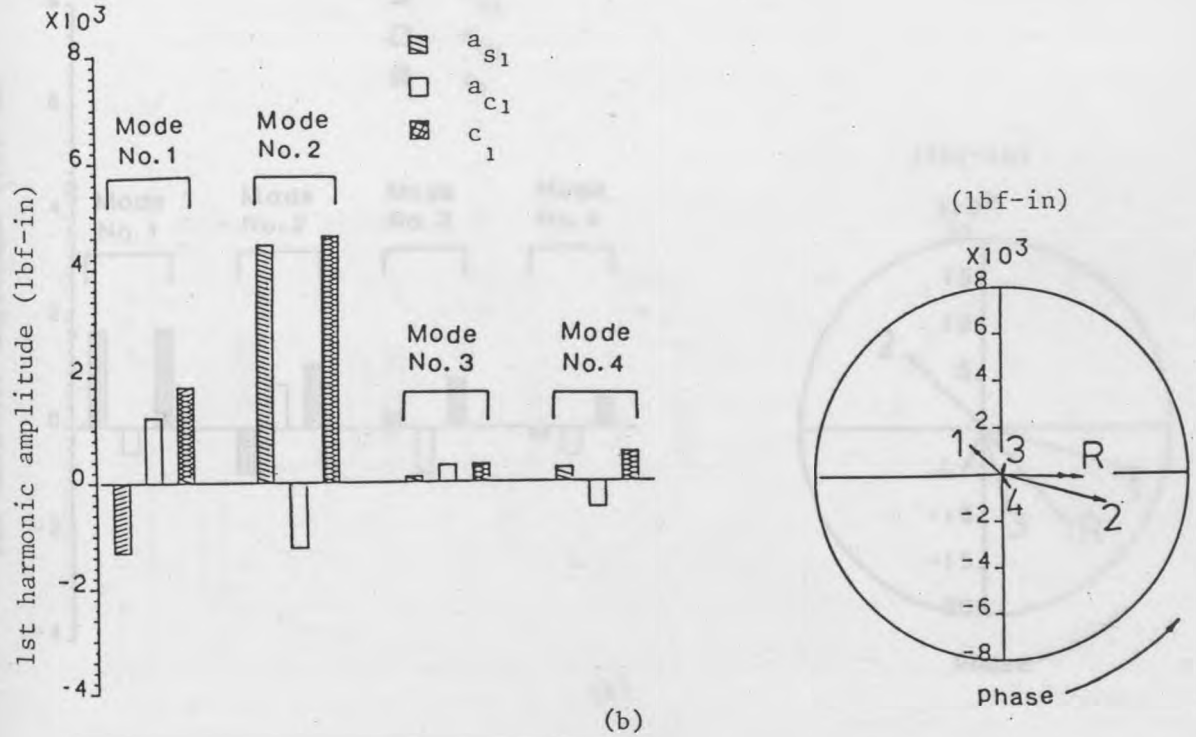

(b)

Figure 84 1st Harmonic Amplitudes and Phase of Fourier Series Representation of $M_{fi}(\psi)$-Mode Contributions For :

(a) Initial Blade Mass Distribution

(b) Modified Blade Mass Distribution (λ_{m_3}).

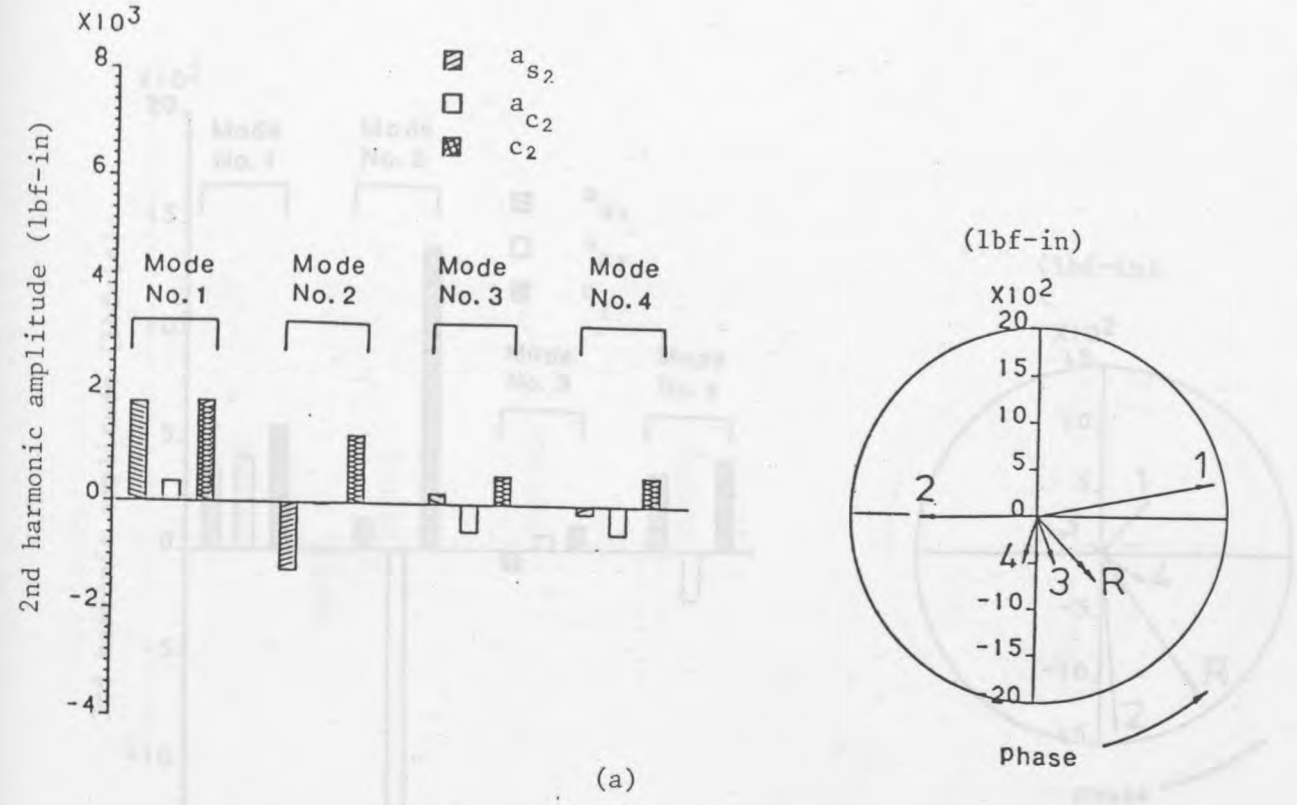

(a)

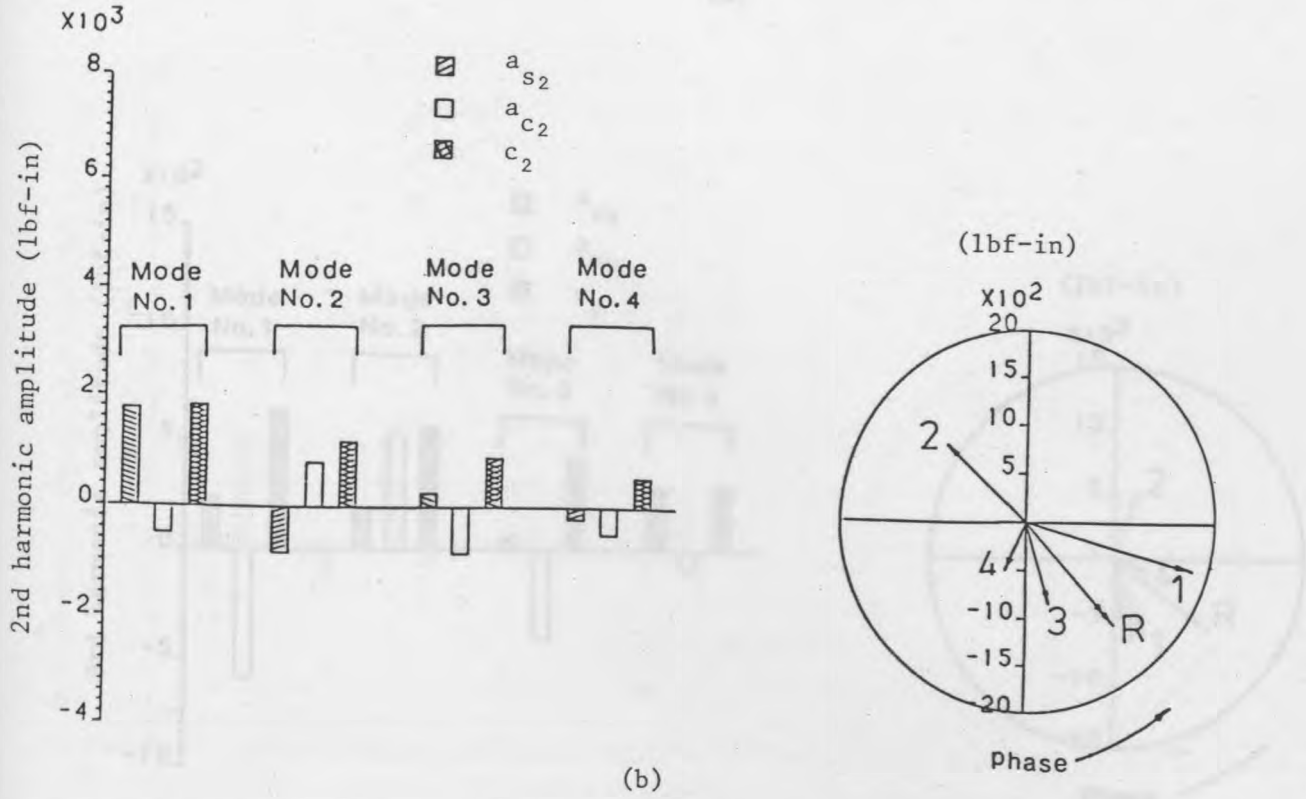

(b)

Figure 85 2nd Harmonics Amplitudes and Phase of Fourier Series Representation of $M_{fi}(\psi)$-Mode Contributions for :

(a) Initial Blade Mass Distribution

(b) Modified Blade Mass Distribution (λ_{m_3})

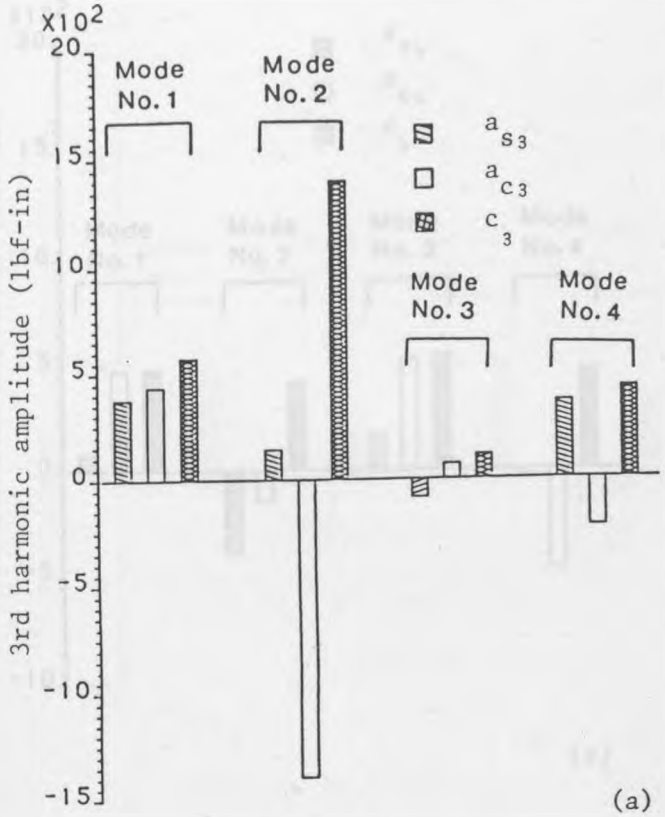

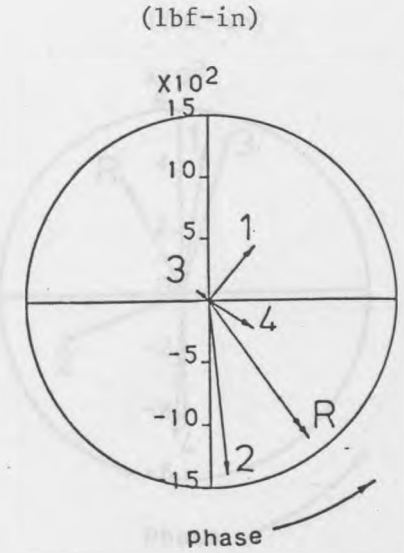

(a)

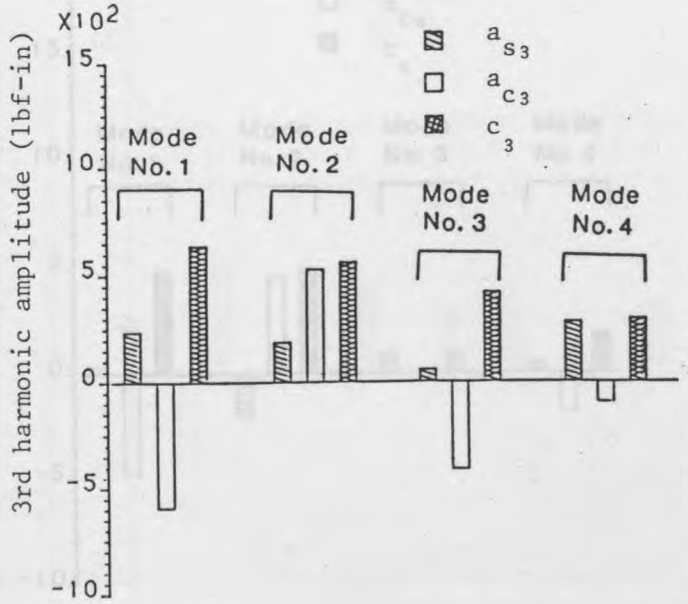

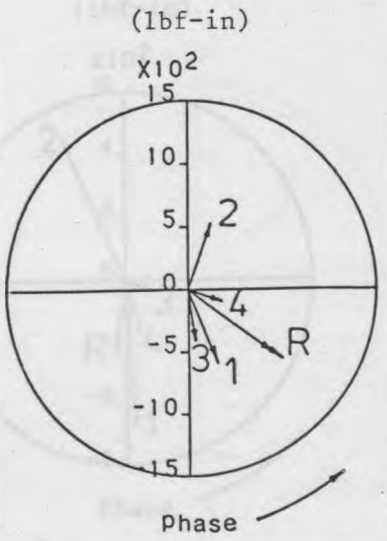

(b)

Figure 86 3rd Harmonic Amplitudes and Phase of Fourier Series Representation of $M_{fi}(\psi)$-Mode Contributions for :
(a) Initial Blade Mass Distribution
(b) Modified Blade Mass Distribution (λ_{m_3})

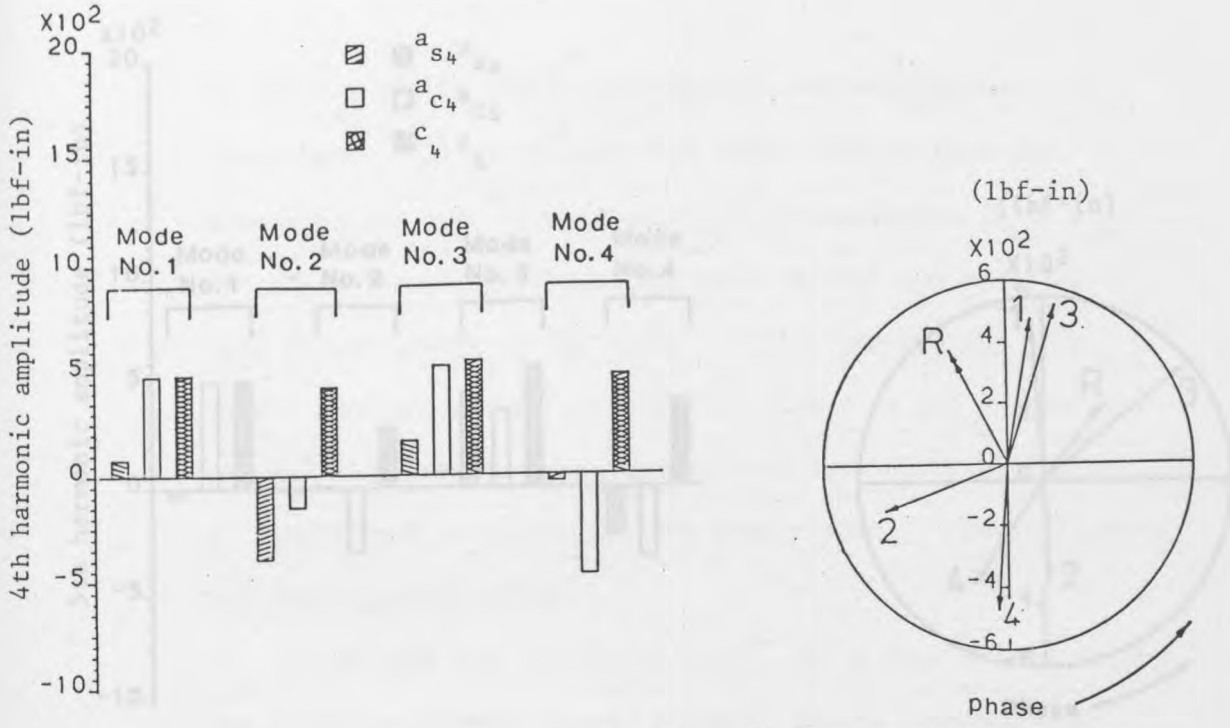

(a)

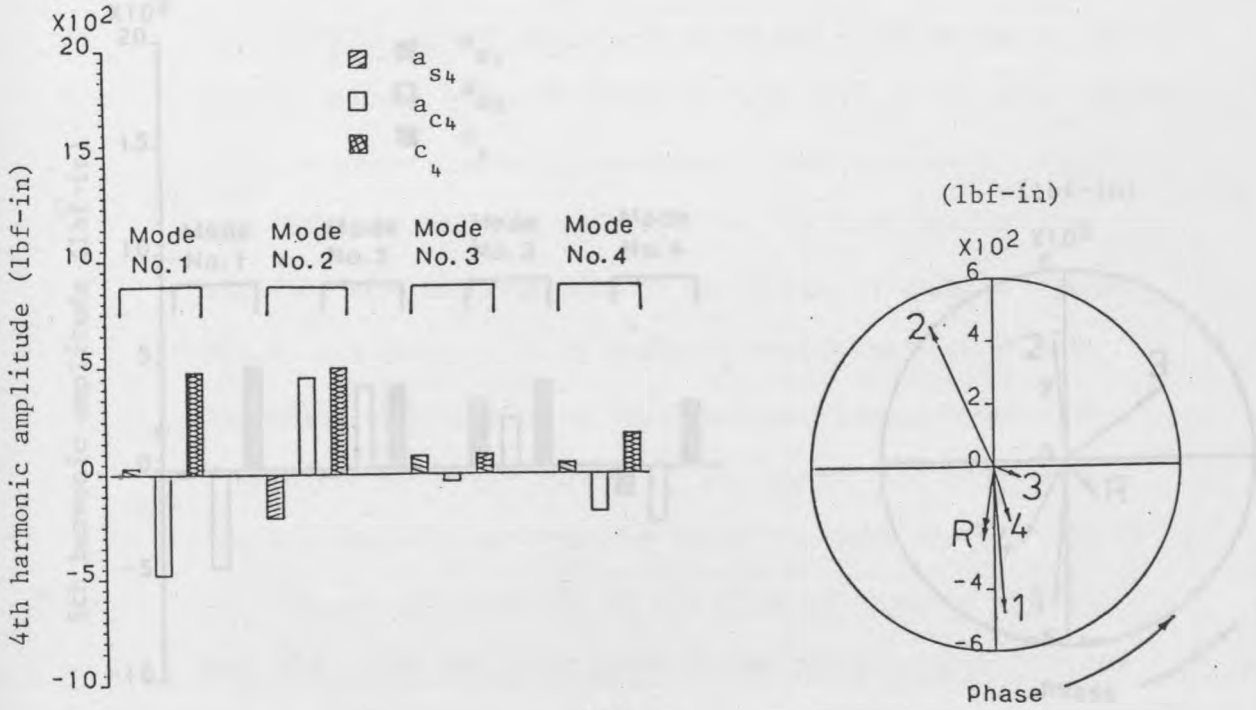

(b)

Figure 87 4th Harmonic Amplitudes and Phase of Fourier Series Representation of $M_{fi}(\psi)$-Mode Contributions for :

(a) Initial Blade Mass Distribution

(b) Modified Blade Mass Distribution (λ_{m_3})

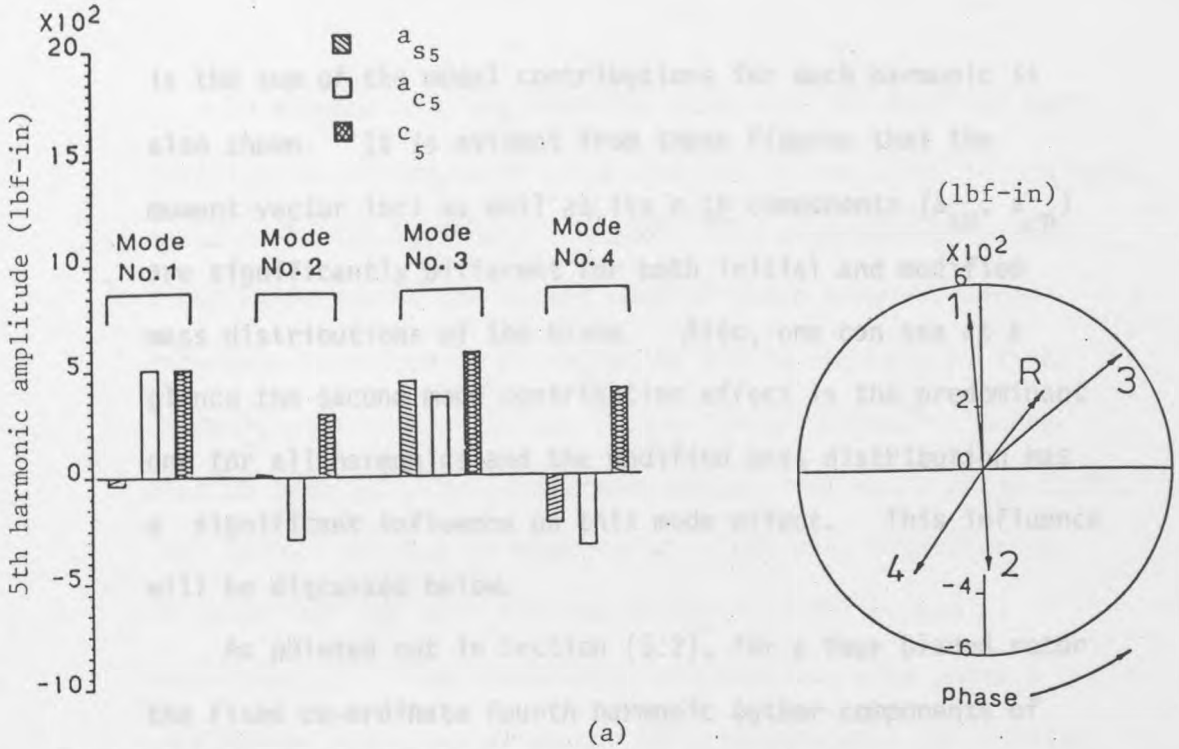

(a)

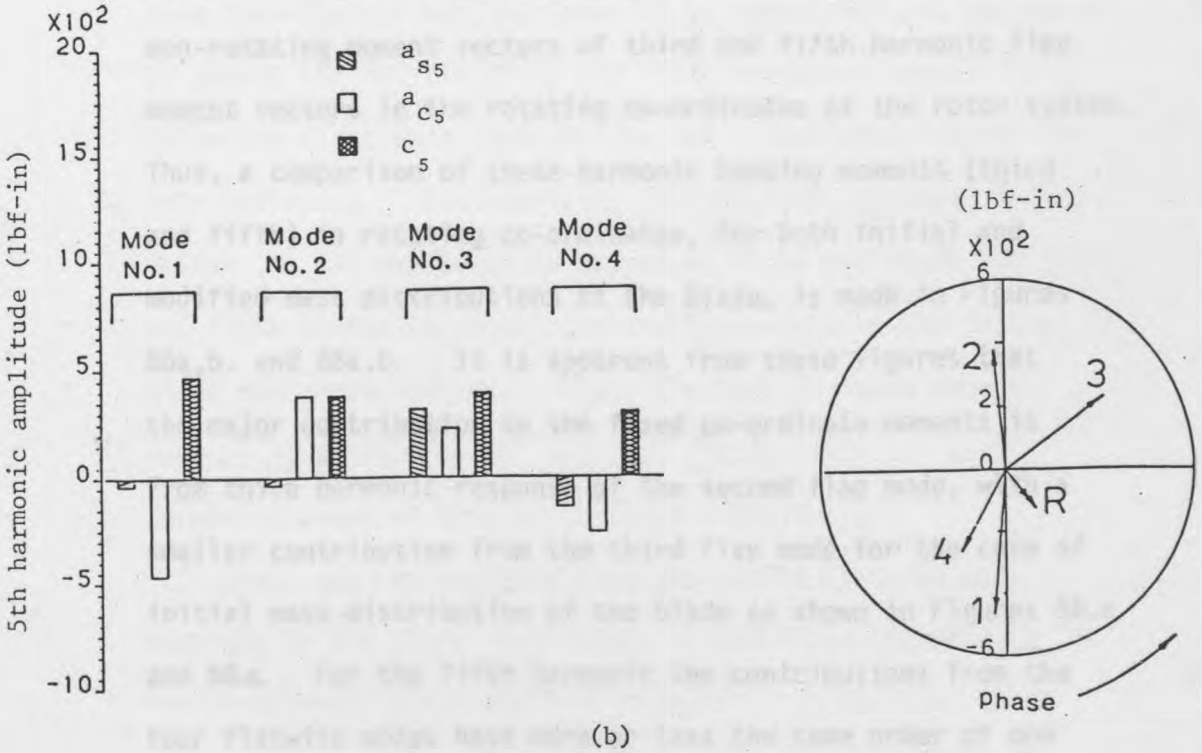

(b)

Figure 88 5th Harmonic Amplitudes and Phase of Fourier Series Representation of $M_{fi}(\psi)$-Mode Contributions for :

(a) Initial Blade Mass Distribution

(b) Modified Blade Mass Distribution (λ_{m_3})

is the sum of the modal contributions for each harmonic is also shown. It is evident from these Figures that the moment vector loci as well as its n th components (a_{sn}, a_{cn}) are significantly different for both initial and modified mass distributions of the blade. Also, one can see at a glance the second mode contribution effect is the predominant one for all harmonics and the modified mass distribution has a significant influence on this mode effect. This influence will be discussed below.

As pointed out in Section (5.2), for a four bladed rotor the fixed co-ordinate fourth harmonic (other components of diminishing order at eighth harmonic, twelfth harmonic and so on are neglected) pitch and roll moments are the resultant non-rotating moment vectors of third and fifth harmonic flap moment vectors in the rotating co-ordinates of the rotor system. Thus, a comparison of these harmonic bending moments (third and fifth) in rotating co-ordinates, for both initial and modified mass distributions of the blade, is made in Figures 86a,b. and 88a,b. It is apparent from these figures that the major contribution to the fixed co-ordinate moments is from third harmonic response of the second flap mode, with a smaller contribution from the third flap mode for the case of initial mass distribution of the blade as shown in Figures 86.a and 88.a. For the fifth harmonic the contributions from the four flatwise modes have more or less the same order of one third of third harmonic second flap mode contribution.

In Figures 86.b and 88.b,the effect of the modified mass distribution on the major contributions to the fixed co-ordinate moments is clearly shown. However this distribution yields a 60% reduction in the second mode of third harmonic while this mode increases by an amount of 20% in the case of fifth harmonic with respect to the initial distribution. It can also be seen that the second mode vector loci has a phase shift, with respect to that of the initial blade mass distribution, of about 150^{o} and 175^{o} for the third and fifth harmonics respectively. The fourth mode contribution also shows a significant reduction of amount 30% compared with the initial distribution for both harmonics. On the other hand, the third mode contribution has increased by an amount 60% and decreased by amount 45% for the third and fifth harmonics respectively, while the first mode contribution has a negligible change for both harmonics. Consequently, the resultant rotating moment vector (R) has decreased by amount of 30.5% and 46.2% for third and fifth harmonics respectively with respect to the initial blade mass distribution. Also, the loci of these moment vectors is shifted by 10^{o} and 110^{o} respectively for both harmonics compared with the initial distribution.

Thus, one can conclude that the second flatwise mode response is the prime contributor to the fixed co-ordinate fourth harmonic pitch and roll moments. It is clear that the modified mass distribution has a significant influence on this second mode contribution, especially the third harmonic content of the fixed co-ordinate moments.

To understand the reasons for the observed vibration reduction in the major contributor to the pitching and rolling moments (i.e. the third harmonic bending moment of the second flatwise mode, Figure 86), it is helpful to consider the vibratory airloads which are applied to the blade at the exciting frequency w_f. The generalised response of this mode, to sinusoidal excitation at w_f, is characterised by the ratio of generalised force to generalised mass, the aerodynamic damping and the frequency separation (separation of the damped natural frequency from the forcing frequency "w_f"). Each of these will be discussed below.

The amplitudes of the third harmonic (a_{s_3}, a_{c_3} and c_3) of the Fourier series representation of the airload $F_\ell(x)$, equation (62.a) are computed. The computational results obtained for both initial and modified mass distributions of the blade, at $\mu = 0.284$, are compared in Figures 89.a and 89.b. The ratio of generalised modal airload (product of $F_\ell(x)$ times the displacements at x in the second flatwise mode) to generalised mass are also plotted, for comparison, in Figure 90. Moreover the aerodynamic damping is estimated for both initial and modified blade mass distributions. These damping calculations are given in Appendix (8).

In Figures 89.a and 89.b, it is observed that the effect of the modified blade mass distribution on the 3/rev airload ($F_\ell(x)$) is not very noticeable; however it does have a significant effect on both the generalised modal force and

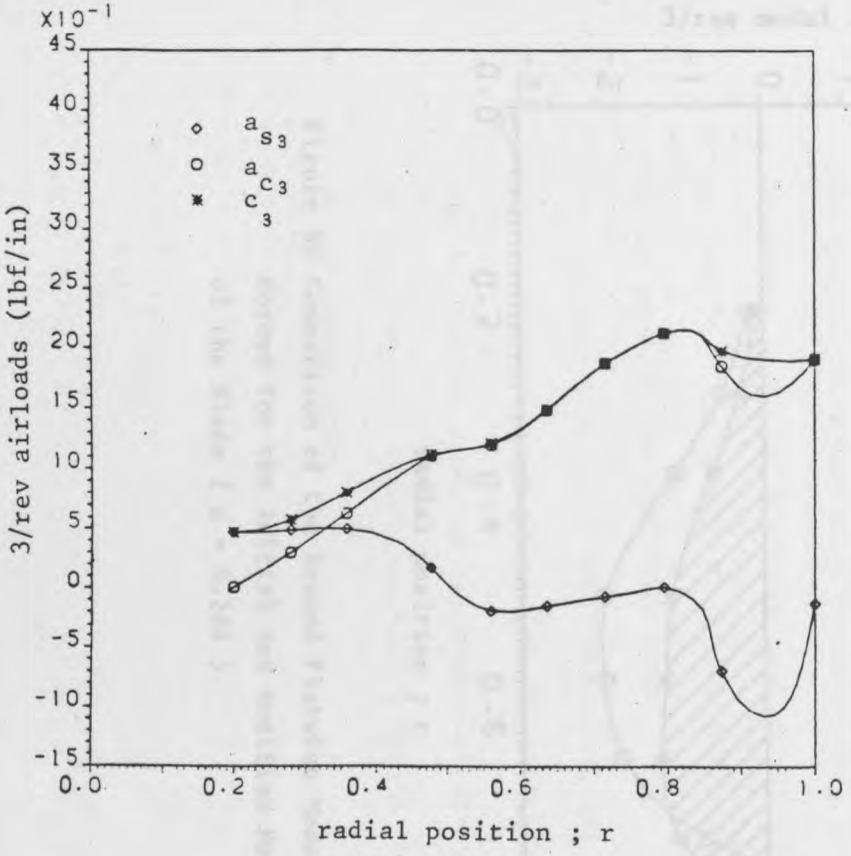

(a) Initial Distribution

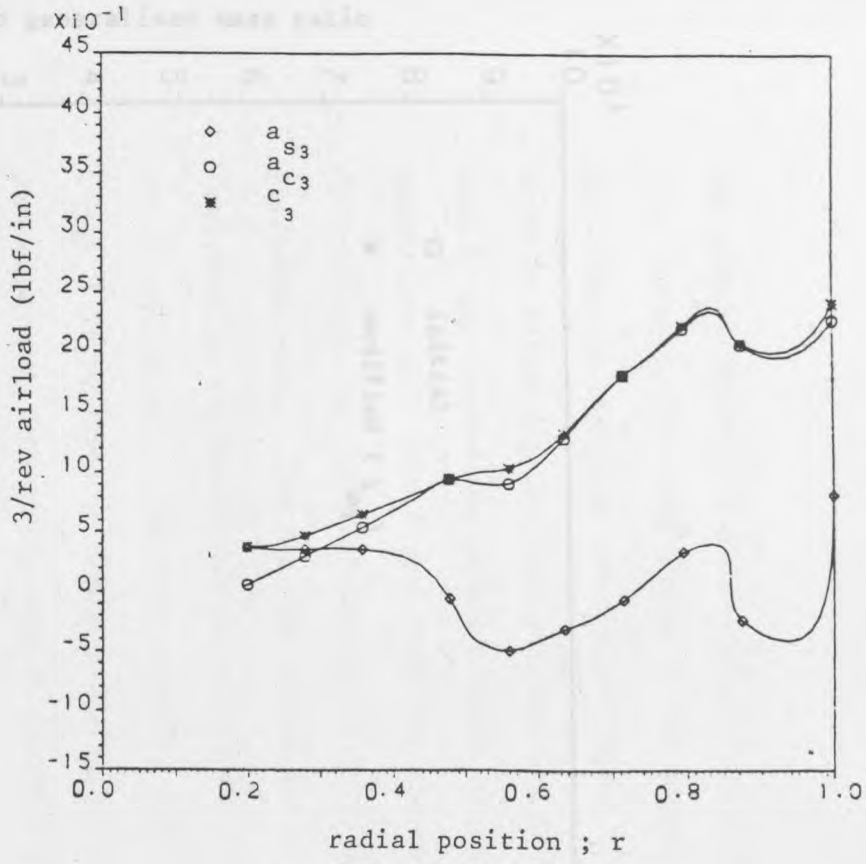

(b) Modified Distribution (λ_{m_3})

Figure 89 Third Harmonic of the Vibratory Airloads for both Initial and Modified Blade Mass Distributions ($\mu = 0.284$).

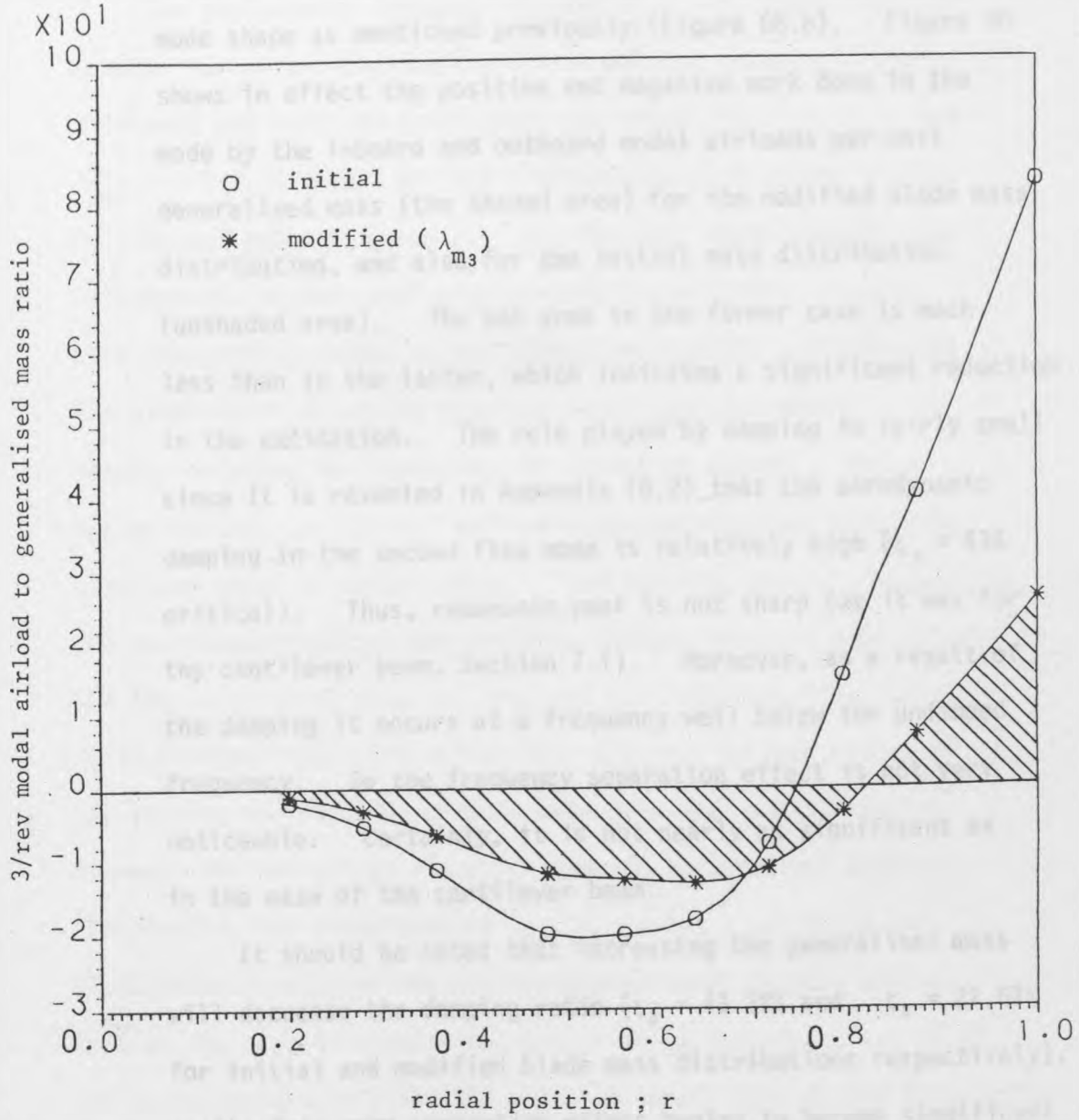

Figure 90 Comparison of the Second Flatwise Mode-3/rev Generalised Forces for the Initial and Modified Mass Distributions of the Blade ($\mu = 0.284$).

the generalised mass (equation (83.a)) as shown in Figure 90. This is due to the large change in the second flatwise bending mode shape as mentioned previously (Figure 68.b). Figure 90 shows in effect the positive and negative work done in the mode by the inboard and outboard modal airloads per unit generalised mass (the shaded area) for the modified blade mass distribution, and also for the initial mass distribution (unshaded area). The net area in the former case is much less than in the latter, which indicates a significant reduction in the excitation. The role played by damping is fairly small since it is revealed in Appendix (8.2) that the aerodynamic damping in the second flap mode is relatively high (ζ_2 = 43% critical). Thus, resonance peak is not sharp (as it was for the cantilever beam, Section 7.1). Moreover, as a result of the damping it occurs at a frequency well below the undamped frequency. So the frequency separation effect is not very noticeable. Certainly, it is not nearly as significant as in the case of the cantilever beam.

It should be noted that increasing the generalised mass will decrease the damping ratio (ζ_2 = 43.22% and ζ_2 = 21.61% for initial and modified blade mass distributions respectively), so the frequency separation effect begins to become significant in the latter case.

7.3.4. Refined Optimization Results of the Blade Configurations

The preliminary results, presented so far, imply that for greater refinement the modified distributions of mass, flatwise stiffness and built-in twist along the blade (for λ_{mi}, λ_{ki}, and $\lambda_{\theta i}$; i = 1,2,3) should be used simultaneously to obtain minimum rolling and pitching moments. To this end, these moments were re-computed, at the same advance ratio (μ = 0.284), firstly with the rolling moment as the objective function and then with the alternative objective function being pitching moment. The results obtained are summarised in Tables (8 and 9). These tables contain the initial and modified distributions resulting after one stage of optimization. The rotating natural frequencies, the oscillatory rolling and pitching moments (peak to peak values) and the total blade mass are compared for both objective functions. It is evident from these tables that the peak to peak values of the rolling and pitching moments have decreased substantially. However, the percentage reduction seen in these values obtained, for example, for distributions λ_{m3}, λ_{k3} and $\lambda_{\theta 3}$ are 48.5% and 28.8% respectively for the rolling moment (peak to peak values) used as the objective function, whilst these reductions are 45.7% and 34.1% respectively for the pitching moment used as the alternative objective function. It is interesting to note that the reduction in the peak values are somewhat higher than those of cases of the modified blade mass only distributions shown in Tables (2) and (6). However, these differences are quite small (less than 8%).

Table 8. Refined Optimization Results Comparison for the Initial and Modified Blade Mass, Flatwise Stiffness and Built-in Twist Distributions at $\mu = 0.284$ (M_{xp} is the objective function).

Values	Blade mass; W_b (lb)	% Incr. in W_b	Rolling Moment M_x (lbf-in)		Pitching Moment M_y (lbf-in)		Natural Frequency Ratio			
			Peak to peak; M_{xp}	% Reduction in M_{xp}	Peak to peak; M_{yp}	% Reduction in M_{yp}	$\frac{w_{n_1}}{\Omega}$	$\frac{w_{n_2}}{\Omega}$	$\frac{w_{n_3}}{\Omega}$	$\frac{w_{n_4}}{\Omega}$
Initial Distribution	200.15	-	6029	-	5149	-	1.091	2.91	5.79	9.70
Distribution of λ_{m_1}, λ_{k_1}, & λ_{θ_1}	212.83	6.3	3707	38.5	3934	23.6	1.044	2.86	5.57	9.12
Distribution of λ_{m_2}, λ_{k_2}, & λ_{θ_2}	215.99	7.9	3547	41.2	3908	24.1	1.035	2.86	5.55	9.03
Distribution of λ_{m_3}, λ_{k_3}, & λ_{θ_3}	231.84	15.9	3105	48.5	3667	28.8	0.999	2.89	5.5	8.71

Table 9. Refined Optimization Results Comparison for the Initial and Modified Blade Mass, Flatwise Stiffness and Built-in Twist Distributions at $\mu = 0.284$ (M_{yp} is the objective function).

Values	Blade mass; W_b (lb)	% Incr. in W_b	Rolling Moment M_x (lbf-in)		Pitching Moment M_y (lbf-in)		Natural Frequency Ratio			
			Peak to peak; M_{xp}	% Reduction in M_{xp}	Peak to peak; M_{yp}	% Reduction in M_{yp}	$\frac{w_{n_1}}{\Omega}$	$\frac{w_{n_2}}{\Omega}$	$\frac{w_{n_3}}{\Omega}$	$\frac{w_{n_4}}{\Omega}$
Initial Distribution	200.15	-	6029	-	5149	-	1.091	2.91	5.79	9.70
Distribution of λ_{m_1}, λ_{k_1} & λ_{θ_1}	210.77	5.3	4007	33.5	3708	28.0	1.054	2.86	5.65	9.22
Distribution of λ_{m_2}, λ_{k_2} & λ_{θ_2}	213.43	6.6	3828	36.5	3647	29.2	1.046	2.858	5.63	9.14
Distribution of λ_{m_3}, λ_{k_3} & λ_{θ_3}	226.71	13.3	3273	45.7	3302	34.1	1.015	2.86	5.58	8.77

Although the moment peak values have decreased, the corresponding values of the total blade mass have the same values as those for modified blade mass distributions shown in Tables (3) and (7); also the rotating natural frequencies are slightly decreased due to the increased blade flexibility shown in Figure 70. It can be concluded that the oscillatory hub rolling moment is a better objective function because it results in a greater maximum reduction in vibration level (see Tables (9) and (10)).

CONCLUSIONS

The conclusions presented in this section are divided into two distinct categories; firstly, those associated with the complete optimization leading to minimisation of the vibration bending moment at the cantilever root of the plain cantilever beam, and secondly, those associated with the hingeless helicopter rotor blade configurations which minimise the non-rotating rolling and pitching moment at the rotor head.

The main conclusions for the optimum configurations of the cantilever beam that minimise the root vibration bending moment are as follows:

1. The minimum vibration bending moment (as well as minimum shearing force) at the cantilever root were obtained using a sequential unconstrained minimisation technique incorporating an algorithm based on the steepest descent method [89]. The optimization proceeded without complication and the results indicate a satisfactory sequence which has led to a reduction in some cases of 92% in bending moment, although a rather heavy weight penalty (in added cantilever weight of about 70%) is paid for this reduction.
2. The ability to obtain a global minimum did not seem to be a problem; it does however depend on the actual starting value of the design parameters so human operator experience enters into the picture.

3. It is perhaps a little surprising to note that the effect of rotation on the computed profiles is quite small which suggests that the optimum non-rotating cantilever profiles might provide useful approximations in the estimation of the rotating cantilever beam profiles.

The conclusions for the hingeless rotor blade configurations in forward flight are summarised below. These conclusions should be viewed in the framwork of the assumptions made in the analysis. The theoretical analysis employed has demonstrated its potential to give a detailed definition of the rotor's aeroelastic behaviour in steady flight conditions. Based on the computed aerodynamic quantities in the preceding sections the following conclusions are drawn:

4. Inevitably, errors in the magnitude and distribution of the aerodynamic loading arise, shown up in particular by the comparison of theoretical flapwise root bending moment and flight test measurements, due to a lack of fully detailed data for oscillating aerofoils. The definition of downwash, even the vortex ring model (non-uniform inflow) is a simplified model of the actual downwash and this may have a significant effect on the harmonic response of the higher order modes. Similarly, interference effects with the airframe, tail rotor and vortices shed from the rotor hub may influence the response of these modes.

5. The first and second flatwise bending modes are the prime vibration contributors whilst the contributions from the third and fourth modes to the root flapwise bending moment are quite small.

6. The second flatwise mode response plays an important role in the vibration response of rotor blades. It is a predominant contributor to the fixed co-ordinate fourth harmonic pitch and roll moments. These moments have relatively high peak to peak values (they act as exciting moments) which increases with increasing advance ratio. The minimisation of these peak values through the application of structural optimization technique is the aim of the present study.

7. Optimization of a blade configuration at chosen advance ratio offers very good potential for vibration reduction. By selecting a completely arbitrary initial blade configuration a very dramatic gain could have been obtained by the optimization process. However, it is more consistent with good engineering practice to try and improve on what is already a satisfactory design.

8. The optimization technique results in realistic designs by locating mass distributed in the outboard one-third portion of the blade and by adding stiffness near the nodepoint of the second flatwise mode, providing a "dumb-bell" effect.

9. The mass distribution, rather than flatwise stiffness or built-in twist distribution along the blade is the prime variable in reducing the oscillatory rolling and pitching moments.

10. The optimization results show very little effect of the built-in twist along the blade on the fixed co-ordinate moments (rolling and pitching moments).

11. A 48.5% and 28.8% reduction in the peak to peak value of the oscillatory rolling and pitching moments respectively can be achieved with relatively minor modifications of the original blade configuration (mass distribution, flatwise stiffness distribution and built-in twist distribution). These vibration reductions are accompanied by an increase in the original blade weight of 15.9%. With up to 44.8% and 21.5% reductions respectively occurring in the stage of using modified mass distribution only, while the remaining reduction (3.7% and 6.3% respectively) is achieved by introducing the modified flatwise stiffness and built-in twist distributions as well.

12. The percentage reductions in vibration amplitude were achieved at both advance ratios of $\mu = 0.284$ and $\mu = 0.372$, and also at both second mode rotational frequency ratios of $\frac{w_{n2}}{\Omega} = 2.92$ and $\frac{w_{n2}}{\Omega} = 2.7$.

13. The comparison of rotating natural frequencies of the modified blade distributions with those of the initial

distribution indicates that all the second flapping natural frequencies are decreased slightly, the second remaining virtually unchanged for the shorter optimization steplength whilst a slight increase occurred for longer steplengths.

14. The choice of rolling moment as the objective function produces a larger overall reduction in the vibration level than that resulting from choosing the hub pitching moment.

15. Higher levels of vibration reduction can be expected for the complete sequence of the structural optimization process, i.e. many steps in appropriate directions until convergence is achieved.

16. Structural optimization should be considered as a method that is complementary to other philosophies and devices, e.g. higher harmonic control, in the overall aim of reducing vibration in helicopters. It provides significant alleviation of vibration with small penalty, and it could well be incorporated into the normal design process used by the helicopter industry.

REFERENCES

1. BRAMWELL, A.R.S., Helicopter Dynamics, Edward Arnold, London, (1976).

2. JOHNSON, W., Helicopter Theory, Princeton University Press, (1980).

3. REICHERT, G., "Helicopter Vibration Control - A Survey", Sixth European Rotorcraft and Power Lift Aircraft Forum, Sept.16-19, Bristol, England, (1980).

4. DONE, G.T.S.,"Recent Advances in Helicopter Vibration Control", The Shock and Vibration Digest, Vol.12, No.1, Jan.(1980).

5. DONE, G.T.S.,"Further Advances in Helicopter Vibration Control", The Shock and Vibration Digest, Vol.15, No.2., Feb.(1983).

6. SHIPMAN, D., "Nodalization Applied to Helicopters", SAE Trans., 730 894, (1973).

7. KIDD, D.L., BALKE,R.W., WILSON, W.F. and WERNICKE, R.K., "Recent Advances in Helicopter Vibration Control", 26th Annual National Forum of the American Helicopter Society, June (1970).

8. FLANNELLY, W.G., "The Dynamic Antiresonance Vibration Isolator", 22nd Annual National Forum of American Helicopter Society, (1966).

9. BARTLETT, F.D., and FLANNELLY, W.G., "Application of Antiresonance Theory to Helicopters", presented at the AHS/NASA- Ames Specialists Meeting on Rotorcraft Dynamics Feb.13-15, (1974).

10. RITA, A.D., McGARVEY, J.H., and JONES, R., "Helicopter Rotor Isolation Evaluation Utilising the Dynamics Antiresonance Vibration Absorber", 32nd Annual National Forum of A.H.S., No.1030, (1976).

11. DESJARDINS, R.A. and HOOPER, W.E., "Rotor Isolation of the Hingeless Rotor", 2nd European Rotorcraft and Power Lift Aircraft Forum, No.13, Sept.20-22, (1976).

12. DESJARDINS, R.A. and HOOPER, W.E., "Antiresonance Rotor Isolation for Vibration Reduction", J.of American Helicopter Society, Vol.25, July, (1980).

13. JONES, R., "Control of Helicopter Vibration Using the Dynamic Antiresonance Vibration Isolator", SAE Trans. 730 894, (1973).

14. HALWES, D.R., "LIVE - Liquid Inertia Vibration Eliminator", 36th Annual National Forum of the A.H.S., Paper No.80-22, (1980).

15. BRAUN, D., "Development of Antiresonance Force Isolator for Helicopter Vibration Reduction", Sixth European Rotorcraft and Power Lift Aircraft Forum, Sept.16-19, Bristol, England (1980).

16. HARDENBERG, P.W. and SALTANIS, P.B., "Preliminary Development of an Active Transmission Isolation System", 27th Annual National Forum of A.H.S., May (1971).

17. KUCZYNSKI, W.A. and MADDEN, J. "The RSRA Active Isolation/ Rotor Balance System", J.of American Helicopter Society, Vol.25, April (1980).

18. DEN HARTOG, J.P., Mechanical Vibration, New York, McGraw-Hill Book Co.Inc., Fourth Edition, pp.219-222, (1959).

19. PAUL, W.F., "Development and Evaluation of the Main Rotor Bifilar Absorber", 25th Annual National Forum of the A.H.S., Paper No.354, (1969).

20. TAYLOR, R.B. and TEAR, P.A., "Helicopter Vibration Reduction with Pendulum Absorbers", 30th Annual National Forum of the A.H.S., May, (1974).

21. WACHS, M.A., "The Main Rotor Bifilar Absorber and its Effect on Helicopter Reliability/Maintainability", SAE Trans. 730 894, (1973).

22. MOUZAKIS, T., "Monofilar - A Dual Frequency Rotor Head Absorber", American Helicopter Society National Specialists' Meeting on Helicopter Vibration, Hartford, CT., Nov. (1981).

23. VISWANATHAN, S.P. and McCLURE, R.D., "Analytical and Experimental Investigation of Bearingless Hub-Absorber", J.of American Helicopter Society, July, (1983).

24. WHITE, R.W., "A Fixed Frequency Rotor Head Vibration Absorber Based on G.F.R.P. Springs", Fifth European Rotorcraft and Power Lift Aircraft Forum, Sept.4-7, Amsterdam,(1979).

25. O'LEARY, J.J., "Reduction in Vibration of CH 47C Helicopter Using a Variable Tuning Vibration Absorber", Shock and Vibration Bulletin, 40, Pt.5, December, (1969).

26. DESJARDINS, R.A. and SANKEWITSCH, U., "Integrated Floor/ Fuel Isolation System for the Model 234 Commercial Chinook", Fifth European Rotorcraft and Power Lift Aircraft Forum, No.39, Sept.4-7, Amsterdam (1979).

27. SISSINGH, G.J. and DONHAM, R.E., "Hingeless Rotor Theory and Experiment on Vibration Reduction by Periodic Variation of Conventional Controls", NASA SP-352, February (1974).

28. YEN, J.G.,"Vibration Reduction with Higher Harmonic Blade Feathering for Helicopters with Two-Bladed Teetering and Four-Bladed Hingeless Rotors", 36th Annual National Forum of the A.H.S., No.80-69, May (1980).

29. SHAW, J. and ALBIN, N., "Active Control of the Helicopter Rotor for Vibration Reduction", J.of American Helicopter Society, 26 (3), (1981).

30. TAYLOR, R.B. and FARRAR, F.A., "An Active Control System for Helicopter Vibration Reduction by Higher Harmonic Pitch", 36th Annual National Forum of the A.H.S., No. 80-71, May, (1980).

31. HAMMOND, C.E., "Wind Tunnel Results showing Rotor Vibratory Loads Reduction Using Higher Harmonic Blade Pitch", J.of American Helicopter Society, January (1983).

32. VENKAYYA, V.B., "Structural Optimization; A Review and Some Recommendations", Int.J.for Numerical Methods in Engineering, 13, pp.203-228, (1978).

33. PIERSON, B.L., "A Survey of Optimal Structucal Design Under Dynamic Constraints", Int.J.for Numerical Methods in Engineering, Vol.3., pp.491-499, (1972).

34. RANACHARYULU, M.A.V. and DONE, G.T.S., "A Survey of Structural Optimization Under Dynamic Constraints", The Shock and Vibration Digest, Vol.11, No.12, December, (1979).

35. TURNER, M.J., "Design of Minimum Mass Structures with Specified Natural Frequencies", AIAA J., 5, pp.406-412, (1967).

36. RUBIN, C., "Minimum Weight Design of Complex Structures Subject to a Frequency Constraint", AIAA J., Vol.8, No.5, pp.923-927, (1970).

37. FOX, R.L. and KAPOOR, M.P., "Structural Optimization in Dynamic Response Regime: A Computational Approach", AIAA J., Vol.8, (10), pp.1798-1803, (1970).

38. TAYLOR, J.E., "Minimum Mass Bar for Axial Vibration at Specified Natural Frequency", AIAA J, Vol.5,(10), pp.1911-1913, (1967).

39. ZARGHAMEE, M.S., "Optimum Frequency of Structures", AIAA J., Vol.6, pp.749-750, (1968).

40. McCART, R.R. HAUG, E.J. and STREETER, T.D., "Optimal Design of Structures with Constrains Natural Frequency", AIAA J., Vol.8, (6), pp.1012-1019, (1970).

41. ELWANY, M.H.S. and BARR, A.D.S., "Optimal Design of Beams under Flexural Vibration", J.of Sound and Vibration,88 (2), pp.175-195, (1983).

42. ELWANY, M.H.S. and BARR, A.D.S., "Some Optimization Problems in Torsional Vibration", J.of Sound and Vibration, 57 (1), pp.1-33, (1978).

43. ELWANY, M.H.S. and BARR, A.D.S., "Minimum Weight Design of Beams in Torsional Vibration with Several Frequency Constraints", J.of Sound and Vibration, 62 (3), pp.411-425, (1979).

44. JOSEPH, S. and LUCIEN, A.S., "Frame Optimization including Frequency Constrains", J.of the Structural Division (1), pp.283-291 (1975).

45. NIORDSON, F.I., "On the Optimal Design of Vibrating Beam", Quart.of App.Maths., 23, pp.47-53, (1965).

46. PIERRE, D.A., Optimization Theory with Application, John Wiley, New York, (1969).

47. JACOBY, S.L.S., KOWALIK, J.S. and PIZZO, J.T., Iteration for Non-Linear Optimization Problems, Prentice-Hall Inc., Englewood Cliffs, (1972).

48. MOE, J., "Fundamentals of Optimization", Computer and Sturctures, Vol.4, pp.95-113, (1974).

49. DONE, G.T.S., "Adjustment of a Rotor Model to Achieve Agreement Between Calculated and Experimental Natural Frequencies", J.of Mech.Eng. Science, 21, pp.389-396, (1979).

50. KIM, K.O., ANDERSON, W.J. and SANDSTROM, R.E., "Non-linear Inverse Perturbation Method in Dynamic Analysis", AIAA J., Vol.21, No.9, pp.1310-1316, (1983).

51. STETSON, K.A., "Perturbation Method of Structure Design Relevant to Holographic Vibration Analysis", AIAA J., Vol.13, No.4, pp.457-459, (1975).

52. STETSON, K.A. and PALMA, G.E., "Inversion of First-Order Perturbation Theory and Its Application to Structural Design", AIAA J., Vol.14, No.4., pp.454-460, (1976).

53. DONE, G.T.S., "Vibration Control by Passive Means Other than Using Damping", Dynamika, Maszyn, Ossolineum, pp.75-76, (1978).

54. SCIARRA, J.J., "Vibration Reduction by Using Both the Finite Element Strain Energy Distribution and Mobility Techniques", The Shock and Vibration Bulletin, No.44., Pt.2., (1974).

55. DONE, G.T.S.and HUGHES, A.D., "The Response of Vibrating Structure as a Function of Structural Parameters", J.of Sound and Vibration, 38, pp.255-266, (1975).

56. VINCENT, A.H., "A Note on Properties of Variation of Structural Response with respect to a Single Structural Parameter when plotted in Complex Plane", Westland Helicopters Report, GEN/DYN/RES/010R (1973).

57. DONE, G.T.S., HUGHES, A.D. and WEBBY, J., "The Response of Vibrating Structural Parameters - Application and Experiment", J.of Sound and Vibration, 49, pp.149-159, (1976).

58. WALKER, W.R., "An Investigation of a Structural Vibration Technique", Royal Aircraft Establishment, TMS 953, July, (1979).

59. DONE, G.T.S. and HUGHES, A.D., "Reducing Vibration by Structural Modification", Vertica, 1 (1), pp.31-38, (1976).

60. DONE, G.T.S. and RANGACHARYULU, M.A.V., "Use of Optimization in Helicopter Vibration Control by Structural Modification", 5th European Rotorcraft and Power Lift Aircraft Forum, Paper No.68, Sept.4-7, (1979).

61. HANSON, H.W. and CALAPODAS,N.J., "Evaluation of Practical Aspects of Vibration Reduction Using Structural Optimization Techniques", J.of Helicopter Society, July, (1980).

62. SOBEY, A.J., "Helicopter Vibration Reduction through Structural Manipulation", 6th European Rotorcraft and Power Lift Aircraft Forum, Paper No.17, Sept.16-19, (1980).

63. DONE, G.T.S., "Use of Optimization in Helicopter Vibration Control by Structural Modification", The Amer.Helicopter Society National Specialists Meeting on Helicopter Vibration, No.44., November (1981).

64. WANG, B.P., KITS, L, PILKEY, W.D. and PALAZZOLO, A.B., "Helicopter Vibration Reduction by Local Structural Modification", J.of the American Helicopter Society, July, (1982).

65. KING, S., "The Modal Approach to Structural Modification", J.of the American Helicopter Society, April, (1983).

66. HIRSCH, H., HUTTON,R.B. and RASUMOFF, A., "Effect of Spanwise and Chordwise Mass Distribution on Rotor Blade Cyclic Stress", J.of American Helicopter Society, Vol.1, No.2., pp.37-45, (1956).

67. TAYLOR, R.B., "Helicopter Vibration Reduction by Rotor Blade Modal Shaping", 38th Annual Forum of the American Helicopter Society, May, (1982).

68. BLACKWELL, R.H., "Blade Design for Reduced Helicopter Vibration", J.of the American Helicopter Society, July, (1983).

69. BENNET, R.L., "Optimum Structural Design", 38th Annual Forum of the A.H.S., May, (1982).

70. FRIEDMANN, P.P. and SHANTHAKUMARAN, P., "Optimum Design of Rotor Blades for Vibration Reduction in Forward Flight", 39th Annual Forum of the A.H.S., May (1983).

71. MANSFIELD, E.H. and SOBEY, A.J., "The Fibre Composite Helicopter Blade", Aeronautical Quarterly, pp.413-449, May, (1979).

72. NATH, N., Fundamentals of Finite Elements for Engineers, The Athlone Press, London Univ. (1974).

73. HOA, S.V., "Vibration of Rotating Beam with Tip Mass", J.of Sound and Vibration, 67 (3), pp.369-381, (1979).

74. GIBBONS, M.P. and DONE, G.T.S., "Automatic Generation of Helicopter Rotor Aeroelastic Equations of Motion", 8th European Rotorcraft Forum, Paper No.33, Aug.31-Sept.3, (1982).

75. LYTWYN, R.T., "Aeroelastic Stability Analysis of Hingeless Rotor Helicopters in Forward Flight using Blade and Airframe Normal Modes", 36th Annual National Forum of the A.H.S., May (1980).

76. TIMOSHENKO, S. and GOODIER, J.N., Theory of Elasticity, McGraw-Hill Book Co.Inc., (1951).

77. BRAMWELL, A.R.S., "A Method for Calculating the Stability and Control Derivatives of Helicopters with Hingeless Rotor", Res.Memo.Aero.69/4, The City Univ. London, (1969).

78. FRIEDMANN, P. and SHAMIE, J., "Aeroelastic Stability of Trimmed Helicopter Blades in Forward Flight", Vertica, The Int.J.of Rotorcraft & Power Lift Aircraft, Vol.1, Pt.3., (1975).

79. JOHNSON, W., "Comparison of Calculated and Measured Helicopter Rotor Lateral Flapping Angles", J.of the American Helicopter Society, April (1981).

80. YOUNG, M.I., "A Simplified Theory of Hingeless Rotors with Application to Tandem Helicopters", Proc. 18th Annual National Forum of the A.H.S., pp.38-45, (1962).

81. COOK, C.V., "Induced Flow Through a Helicopter Rotor in Forward Flight", Westland Helciopter Ltd. Paper No. 374, January (1970).

82. YOUNG, C., "Development of the Vortex Ring Wake Model and its Influence on the Prediction of Rotor Loads", AGARD-CP334, pp.11.1-11.13.

83. MEIROVITCH, L., Analytical Methods in Vibrations. The Macmillan Press, London, (1967).

84. SADLER, S.G., "Development and Application of a Method for Predicting Rotor Free Wake Positions and Resulting Rotor Blade Airloads", NASA CR-1911, December (1971).

85. HANSFORD, R.E., "A Comparison of Predicted and Experimental Rotor Loads to Evaluate Flap-Lag Coupling with Blade Pitch", 34th Annual National Forum of the A.H.S., May, (1978).

86. BIELAWA, R.L., "Blade Stress Calculations - Mode Deflection vs Force Integration", The American Helicopter Symposium on Rotor Tech., Aug.11-13 (1976).

87. TIMOSHENKO, S. and YOUNG, D.H., Vibration Problems in Engineering, D.Van Nostrand Co.Inc. (1956).

88. CASSIS, J.H. and SCHMIT, L.A., "On Implementation of the Extended Interior Penalty Function", Int.J.for Numerical Methods in Engineering, Vol.10, pp.3-23, (1976).

89. CURRY, H.B., "The Method of Steepest Descent for Non-linear Minimisation Problems", Quar.App.Maths., Vol.2., pp.258-261, (1944).

90. ROSENBROCK, H.H., "An Automatic Method for Finding the Greatest or Least Value of a Function", Computer Journal, Vol.3., pp.175-184, (1960).

APPENDIX 1

A.1. Strain Energy Expression for a Slender Pre-twisted Blade

The blade considered is initially pre-coned away from the plane of rotation about the rotor axis. It has pre-twist (getting less outboard) and applied pitch (which is actually time varying).

The flapping deflection $f_\beta(x)$ in the plane of pre-cone, the twisting deflection about a local axis $f_\theta(x)$ and the lagging deflection $f_\zeta(x)$ normal to the flapping plane are elastic deformations considered.

To obtain the strain energy, an axis system is set up on intermediate positions of the strained and unstrained blade. This axis system is given in Ref. [74]. The displacement field $\{u\} \equiv \{u,v,w\}$ can be obtained by subtraction of these two position vectors and it would be related to the local blade axes, i.e.:

$$\{u\} = [T_{40}]^T[T_2][T_3][T_4] - [I]\{r\}$$
$$+[T_{40}]^T[T_2]\begin{bmatrix} x \\ (-\frac{1}{2}\int\zeta(x)^2dx) \\ 0 \\ f_\zeta(x) \\ 0 \end{bmatrix} + [T_{40}]^T\begin{bmatrix} x \\ (-\frac{1}{2}\int\beta(x)^2dx) \\ 0 \\ 0 \\ f_\beta(x) \end{bmatrix} \tag{1.1}$$

in which the rotational matrices and symbols are as in the text (equations (27) to (33)). The matrix $[T_{40}]$ is equal $[T_4]$ with elastic twist excluded,

$$[T_3] = \begin{bmatrix} \cos \zeta(x) & -\sin \zeta(x) & 0 \\ \sin \zeta(x) & \cos \zeta(x) & 0 \\ 0 & 0 & 1 \end{bmatrix}$$

and [I] is the unit diagonal matrix,

where $f_\zeta(x)$, $f_\beta(x)$ and $f_\theta(x)$ are lag, flap and twist elastic deflections respectively, and

$$\zeta(x) = f'_\zeta(x)$$
$$\beta(x) = f'_\beta(x)$$

The rotation part of the {u} vector, of a point of interest $\{r\} \equiv \{o,y,z\}$ is:

$$[A^*]\{r\} = [T_{40}]^T[T_2][T_3][T_4]-[I]\begin{bmatrix} o \\ y \\ z \end{bmatrix} \qquad (1.2)$$

By successive matrix multiplication the matrix [A*] can be written as:

$$[A^*] = \begin{bmatrix} 0 & (-\zeta(x)\cos\theta_o - \beta(x)\sin\theta_o) & (\zeta(x)\sin\theta_o - \beta(x)\cos\theta_o) \\ (\zeta(x)\cos\theta_o + \beta(x)\sin\theta_o) & 0 & -f_\theta(x) \\ (-\zeta(x)\sin\theta_o + \beta(x)\cos\theta_o) & f_\theta(x) & 0 \end{bmatrix}$$

(1.3)

The displacement part of the {u} vector, equation (1.1), can be found to the 1st order:

$$[T_{40}]^T[T_2]\begin{bmatrix} 0 \\ f_\zeta(x) \\ 0 \end{bmatrix} + [T_{40}]^T \begin{bmatrix} 0 \\ 0 \\ f_\beta(x) \end{bmatrix}$$

and in this case $[T_2] \rightarrow [I]$ so it gives:

$$[T_{40}]^T \begin{bmatrix} 0 \\ f_\zeta(x) \\ f_\beta(x) \end{bmatrix} = \begin{bmatrix} 1 & 0 & 0 \\ 0 & \cos\theta_o & \sin\theta_o \\ 0 & -\sin\theta_o & \cos\theta_o \end{bmatrix} \begin{bmatrix} 0 \\ f_\zeta(x) \\ f_\beta(x) \end{bmatrix}$$

$$= \begin{bmatrix} 0 \\ f_\zeta(x)\cos\theta_o + f_\beta(x)\sin\theta_o \\ -f_\zeta(x)\sin\theta_o + f_\beta(x)\cos\theta_o \end{bmatrix} \quad (1.4)$$

Therefore, the displacement field vector {u} can be rewritten as:

$$\begin{bmatrix} u \\ v \\ w \end{bmatrix} = \begin{bmatrix} (-f'_\zeta(x)\cos\theta_o - f'_\beta(x)\sin\theta_o)y + (f'_\zeta(x)\sin\theta_o - f'_\beta(x)\cos\theta_o)z \\ -f_\theta(x)z + (f_\zeta(x)\cos\theta_o + f_\beta(x)\sin\theta_o) \\ f_\theta(x)y + (-f_\zeta(x)\sin\theta_o + f_\beta(x)\cos\theta_o) \end{bmatrix}$$

(1.5)

Accordingly:

$$\frac{\partial u}{\partial x} = (-f''_{\zeta}(x)\cos\theta_o - f''_{\beta}(x)\sin\theta_o)y + (f''_{\zeta}(x)\sin\theta_o - f''_{\beta}(x)\cos\theta_o)z$$

$$\frac{\partial u}{\partial y} = (-f'_{\zeta}(x)\cos\theta_o - f'_{\beta}(x)\sin\theta_o)$$

$$\frac{\partial u}{\partial z} = (f'_{\zeta}(x)\sin\theta_o - f'_{\beta}(x)\cos\theta_o)$$

$$\frac{\partial v}{\partial x} = -f'_{\theta}(x)z + f'_{\zeta}(x)\cos\theta_o + f'_{\beta}(x)\sin\theta_o$$

$$\frac{\partial v}{\partial y} = 0$$

$$\frac{\partial v}{\partial z} = -f_{\theta}(x)$$

$$\frac{\partial w}{\partial x} = f'_{\theta}(x)y - f'_{\zeta}(x)\sin\theta_o + f'_{\beta}(x)\cos\theta_o$$

$$\frac{\partial w}{\partial y} = f_{\theta}(x)$$

$$\frac{\partial w}{\partial z} = 0$$

which leads to the following strains [76]:

i) non-zero strains:

$$\varepsilon_{xx} = \frac{\partial u}{\partial x} = (-f''_{\zeta}(x)\cos\theta_o - f''_{\beta}(x)\sin\theta_o)y + (f''_{\zeta}(x)\sin\theta_o - f''_{\beta}(x)\cos\theta_o)z$$

$$\gamma_{xz} = \frac{\partial u}{\partial z} = f'_{\zeta}(x)\sin\theta_o - f'_{\beta}(x)\cos\theta_o$$

$$\gamma_{xy} = \frac{\partial u}{\partial y} + \frac{\partial v}{\partial x} = -f'_{\theta}(x)z$$

ii) zero strains:

$$\gamma_{yz} = \frac{\partial v}{\partial z} + \frac{\partial w}{\partial y} = 0$$

$$\varepsilon_{yy} = \frac{\partial v}{\partial y} = 0$$

$$\varepsilon_{zz} = \frac{\partial w}{\partial z} = 0$$

These zero strains actually due to the chordwise sections being assumed rigid.

The strain energy stored in any section of volume dv is given by:

$$u = \tfrac{1}{2} \int_{vol} \{\varepsilon\}^T [D] \{\varepsilon\} \, dv \qquad (1.6)$$

where

[D] is the elastic matrix

and

$$\{\varepsilon\} = \{\varepsilon_{xx}, \gamma_{xz}, \gamma_{xy}\}^T \qquad (1.7)$$

ε_{yy} and ε_{zz} are zero, therefore ε_{xx} cannot be affected by σ_{yy} and σ_{zz} through Poisson's ratio thus:

$$[D] = \text{diag } [E,G,G]$$

Substituting the above matrix [D] and the strain vector (equation (1.7)) into equation (1.6) the strain energy can be written as:

$$S.E. = \tfrac{1}{2}\{\int_0^L [(EI_{zz}\,(f''_\zeta(x)\cos\theta_o + f''_\beta(x)\sin\theta_o)^2$$

$$- 2EI_{zy}(f''_\zeta(x)\cos\theta_o + f''_\beta(x)\sin\theta_o)(f''_\zeta(x)\sin\theta_o - f''_\beta(x)\cos\theta_o)$$

$$+ EI_{yy}(f''_\zeta(x)\sin\theta_o - f''_\beta(x)\cos\theta_o)^2$$

$$+ GJ\, f'_\theta(x)]\, dx\} \qquad (1.8)$$

where

$$I_{zz} = \int\int y^2 dydz$$

$$I_{zy} = \int\int yzdydz$$

$$I_{yy} = \int\int z^2 dydz$$

$$J = \int\int (y^2 + z^2)dydz$$

We assume symmetry for the blade cross-section and hence the yy-principle axis coincides with blade chord (the zz-axis coincides with that of the blade). It is also assumed that there is no twisting flexibility along the blade (i.e. $f_\theta(x) = 0$). Then, the strain energy becomes:

$$S.E. = \tfrac{1}{2}\{\int_0^L [EI_{zz}(f''_\zeta(x)\cos\theta_o + f''_\beta(x)\sin\theta_o)^2$$

$$+ EI_{yy}(f''_\zeta(x)\sin\theta_o - f''_\beta(x)\cos\theta_o)^2]dx\} \qquad (1.9)$$

Pure flapping response (i.e. $f_\zeta(x) = 0$) gives:

$$S.E. = \tfrac{1}{2}\{\int_0^L [EI_{zz} f''_\beta(x)^2 \sin^2\theta_o + EI_{yy} f''_\beta(x)^2 \cos^2\theta_o]dx\} \quad (1.10)$$

Typically I_{zz} is higher order than I_{yy}; the effect of the relative size of the two terms of the above equation is discussed as follows. For lower modes and especially the first flap, the curvature is greatest inboard of the blade, where θ_o is zero. Thus, approximately, the strain energy is given by:

$$S.E. = \tfrac{1}{2} \int_0^L EI_{yy} f''_\beta(x)^2 dx \quad (1.11)$$

For higher modes, the blade itself provides a relatively larger contribution to the strain energy (i.e. the contribution to stiffness from I_{zz} is significant). Thus, pure flapping will not happen. Nevertheless, for a uniform beam (assuming symmetry at any cross-section) the "flatwise" and "edgewise" modes will be uncoupled. Thus, from equation (1.9) a flatwise mode (effect of I_{zz} is zero) is such that:

$$f''_\zeta(x)\cos\theta_o + f''_\beta(x)\sin\theta_o = 0$$

i.e.

$$f_\zeta(x) = -f_\beta(x)\tan\theta_o$$

Substituting the above equation into equation (1.9) leads:

$$S.E. = \tfrac{1}{2} \int_0^L [EI_{yy} f''_\beta(x)^2 / \cos^2\theta_o] dx \qquad (1.12)$$

Similarly, an edgewise mode is such that:

$$f''_\zeta(x) \sin\theta_o - f''_\beta(x) \cos\theta_o = 0$$

i.e.

$$f_\beta(x) = f_\zeta(x) \tan\theta_o$$

The strain energy in this case is given by:

$$S.E. = \tfrac{1}{2} \int_0^L [EI_{zz} f''_\zeta(x)^2 / \cos^2\theta_o] dx \qquad (1.13)$$

Consequently, if the strain energy for pure flapping (equation (1.10)) is used, it will be overestimated for those modes involving significant curvature of the blade itself, i.e. higher modes, compared with what happens in practice, where these modes tend to be flatwise (equation (1.12)).

Thus, the rotor and blade motion is computed assuming flapping deflections only, the strain energy and hence the structural stiffness terms being more applicable to flatwise deformations.

Since, θ_o is normally moderately small, and moreover varies according to the trim situation being considered, a further approximation is to take $\cos\theta_o = 1$. This approximation

will lead to an underestimate in the strain energy, and in this case equation (1.12) becomes:

$$S.E. = \tfrac{1}{2} \int_0^L [EI_{yy} f''_\beta(x)^2 dx] \qquad (1.14)$$

APPENDIX 2

A.2. Contribution to Matrices; $[p_m]$, $[R_s]$ and $[R_m]$

A2.1. General Expressions

The elemental i th and j th mode shape function, equation (23) can be written as:

$$f_{\beta i}(x) = A_1 + A_2 x + A_3^2 x + A_4^3 x$$

$$f_{\beta j}(x) = B_1 + B_2 x + B_3^2 x + B_4^3 x \qquad (2.1)$$

where $(A_1 \ldots . A_4)$ and $(B_1 \ldots . . B_4)$ are respectively the unknown constants of the i th and j th mode shape of the element under consideration.

The first and second derivatives of the above equations are:

$$f'_{\beta i}(x) = A_2 + 2A_3 x + 3A_4 x^2$$

$$f'_{\beta j}(x) = B_2 + 2B_3 x + 3B_4 x^2 \qquad (2.2)$$

and

$$f''_{\beta i}(x) = 2A_3 + 6A_4 x$$

$$f''_{\beta j}(x) = 2B_3 + 6B_4 x \qquad (2.3)$$

The product of the i th and j th mode gives:

$$\begin{aligned} f_{\beta i}(x) f_{\beta j}(x) = {} & (A_1 B_1) + (A_1 B_2 + A_2 B_1) x + (A_1 B_3 + A_2 B_2 + A_3 B_1) x^2 \\ & + (A_1 B_4 + A_2 B_3 + A_3 B_2 + A_4 B_1) x^3 \\ & + (A_2 B_4 + A_3 B_3 + A_4 B_2) x^4 + (A_3 B_4 + A_4 B_3) x^5 + (A_4 B_4) x^6 \end{aligned} \qquad (2.4)$$

$$f'_{\beta i}(x)f'_{\beta j}(x) = (A_2 B_2) + (2A_2 B_3 + 2A_3 B_2)x + (3A_2 B_4 + 4A_3 B_3 + 3A_4 B_2)x^2 + (6A_3 B_4 + 6A_4 B_3)x^3 + (9A_4 B_4)x^4 \quad (2.5)$$

$$f''_{\beta i}(x)f''_{\beta j}(x) = (4A_3 B_3) + (12A_3 B_4 + 12A_4 B_3)x + (36A_3 B_4)x^2 \quad (2.6)$$

The constant coefficients of the above equations can be written as:

$$C_2 = (A_1 B_1)$$

$$C_3 = (A_1 B_2 + A_2 B_1)$$

$$C_4 = \S_1 A_1 B_3 + \S_2 A_2 B_2 + \S_3 A_3 B_1$$

$$C_5 = \S_4 A_1 B_4 + \S_5 A_2 B_3 + \S_6 A_3 B_2 + \S_7 A_4 B_1$$

$$C_6 = \S_8 A_2 B_4 + \S_9 A_3 B_3 + \S_{10} A_4 B_2$$

$$C_7 = \S_{11} A_3 B_4 + \S_{12} A_4 B_3$$

$$C_8 = \S_{13} A_4 B_4$$

where

the factors $\{\S\} = \{\S_1 \ldots\ldots \S_{13}\} = 1$ for the case of a zero derivative product,

$$\S_1 = \S_3 = \S_4 = \S_7 = 0$$

$$\S_2 = 1$$

$$\S_5 = \S_6 = 2$$

$$\S_8 = \S_{10} = 3$$

$$\S_{11} = \S_{12} = 6$$

$\S_9 = 4$

$\S_{13} = 9$ for the case of a 1st derivative product,

and

$\S_8 = \S_{10} = 0$

$\S_9 = 4$

$\S_{11} = \S_{12} = 12$

$\S_{13} = 36$ for the case of a 2nd derivative product.

Thus the product of the i <u>th</u> and j <u>th</u> mode shape becomes:

$$f_{\beta i}(x)f_{\beta j}(x) = C_2 + C_3 x + C_4 x^2 + C_5 x^3 + C_6 x^4 + C_7 x^5 + C_8 x^6 \quad (2.8)$$

$$f'_{\beta i}(x)f'_{\beta j}(x) = C_4 + C_5 x + C_6 x^2 + C_7 x^3 + C_8 x^4 \quad (2.9)$$

$$f''_{\beta i}(x)f''_{\beta j}(x) = C_6 + C_7 x + C_8 x^2 \quad (2.10)$$

It should be noted that the constants $[C_2 \ldots\ldots C_8]$ must be calculated for both the k <u>th</u> element and the i <u>th</u> and j <u>th</u> mode shape of the blade, e.g.:

$$C_2(k,i,j) = A(k,1,i) * A(k,1,j)$$

Similarly,

$$C_3(k,i,j) = [A(k,1,i)*A(k,2,j)] + [A(k,2,i)*A(k,1,j)], \ldots$$

Accordingly, the constants $[C_2 \ldots\ldots C_8]$ are easily computed and hence the previous integrations which are required to form respective contributions to matrices can be performed.

A2.2. Inertia Matrix $[p_m]$

Substituting equations (12) and (2.8) into equation (51) and carrying out the indicated integration, the matrix $[p_m]$ is given as:

$$[p_m(i,j)] = [\sum_{k=1}^{N_E} p_{m_{17}}(k,i,j)] \tag{2.11}$$

where

$$\begin{aligned} p_{m_{17}}(k,i,j) = &[m_L^{(k)} C_2(k,i,j) L(k)] + \tfrac{1}{2}[\gamma(k) C_2(k,i,j) + \\ &m_L^{(k)} C_3(k,i,j)] L^2(k) + \tfrac{1}{3}[\gamma(k) C_3(k,i,j) + \\ &m_L^{(k)} C_4(k,i,j)] L^3(k) + \tfrac{1}{4}[\gamma(k) C_4(k,i,j) + \\ &m_L^{(k)} C_5(k,i,j)] L^4(k) + \tfrac{1}{5}[\gamma(k) C_5(k,i,j) + \\ &m_L^{(k)} C_6(k,i,j)] L^5(k) + \tfrac{1}{6}[\gamma(k) C_6(k,i,j) + \\ &m_L^{(k)} C_7(k,i,j)] L^6(k) + \tfrac{1}{7}[\gamma(k) C_7(k,i,j) + \\ &m_L^{(k)} C_8(k,i,j)] L^7(k) + \tfrac{1}{8}\gamma(k) C_8(k,i,j) L^8(k) \end{aligned}$$

A2.3. Structural Stiffness Matrix $[R_s]$

Substituting equations (8) and (2.10) into equation (57) and performing the indicated integration leads to:

$$[R_s(i,j)] = [\sum_{k=1}^{N_E} R_{s_{14}}(k,i,j)] \tag{2.12}$$

where

$$R_{S_{14}}(k,i,j) = s_L^{(k)} C_6(k,i,j)L(k) + \tfrac{1}{2}[\alpha(k)C_6(k,i,j) + s_L^{(k)} C_7(k,i,j)]L^2(k) + \tfrac{1}{3}[\alpha(k)C_7(k,i,j) + s_L^{(k)} C_8(k,i,j)]L^3(k) + \tfrac{1}{4}[\alpha(k)C_8(k,i,j)]L^4(k)$$

A2.4. Centrifugal Stiffness Matrix $[R_m]$

Substituting equation (2.9) into equation (53) the matrix $[R_m]$ can be rewritten as:

$$[R_m] = [\Omega^2 \int_0^L m(x^*)x^* f_1(x^*)dx^*] \tag{2.13}$$

where

$$f_1(x^*) = \int_0^x C_{48}^{(k)}(x)dx \tag{2.14}$$

in which

$$C_{48}^{(k)}(x) = C_4(k,i,j) + C_5(k,i,j)x + C_6(k,i,j)x^2 + C_7(k,i,j)x^3 + C_8(k,i,j)x^4 \tag{2.15}$$

and k,i,j denote the k th element, i th and j th mode shape respectively.

The integration of equation (2.13) is carried out numerically, as shown in the block diagram given in Figure 91, using the standard NAG-library routine (D01GAF). Thus the matrix $[R_m]$ becomes:

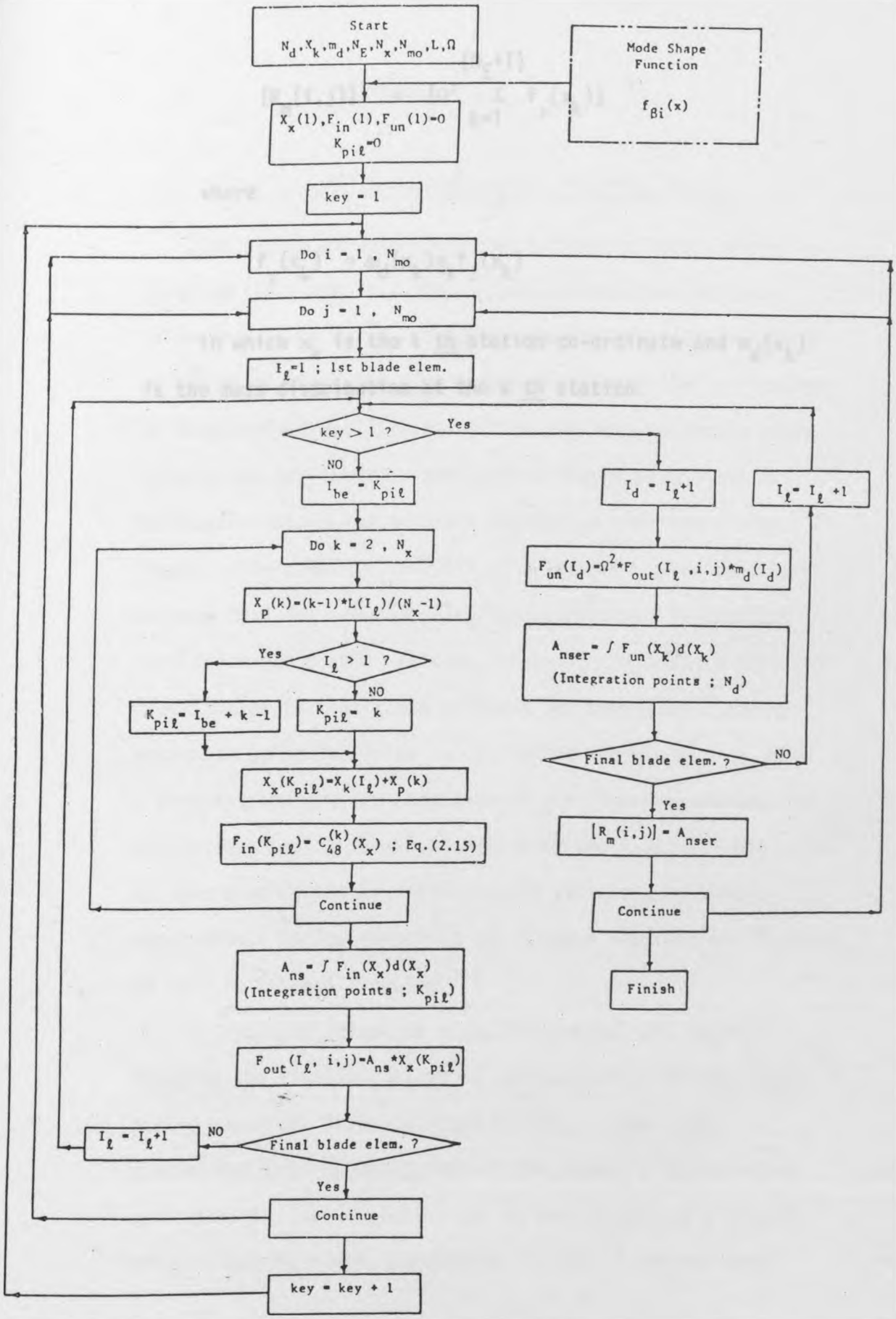

Figure 9| Block Diagram Of Iteration Process to Compute the Centrifugal Matrix $[R_m]$.

$$[R_m(i,j)] = [\Omega^2 \sum_{k=1}^{(N_E+1)} f_2(x_k)]$$

where

$$f_2(x_k) = m_d(x_k) x_k f_1(x_k)$$

in which x_k is the k th station co-ordinate and $m_d(x_k)$ is the mass distribution at the k th station.

APPENDIX 3

A.3. Rotor Lateral and Longitudinal Flapping Angles

The blades of an articulated helicopter rotor have a hinge at the blade root that allows out-of-phase motion (flapping). In forward flight a once-per-revolution motion of the blade about the flap hinge is produced that corresponds to longitudinal and lateral tilt of the rotor tip-path plane relative to the shaft. Such motion occurs with hingeless helicopter rotors due to blade bending at the root of the blade. The simplest analysis of helicopter rotor behaviour assumes that the induced velocity distribution is constant over the rotor disc. In fact, however, the induced velocity distribution is highly non-uniform, and the rotor flapping motion is quite sensitive to the inflow distribution. With a hingeless rotor, the magnitude of the flapping response to non-uniform inflow is not greatly affected [79], but the phase of the response can be significantly affected, so that a longitudinal inflow variation can produce longitudinal flapping as well as lateral flapping.

In order to calculate such longitudinal and lateral flapping the hingeless blade is represented by a rigid blade having an offset flapping hinge [77,80]. Thus, the fundamental bending mode shape of the blade is approximated by a straight line. This leads to the concept of a virtual offset flapping hinge, permitting the use of conventional

analytical methods for articulated rotors with offset flapping hinge. A typical fundamental rotating bending mode shape of the hingeless blade under consideration, which is calculated by the previous finite element model, is shown in Figure 92. Accordingly, an offset flapping hinge "e" of amount 20% has been obtained.

The generalised co-ordinate q_i is a periodic function of (ψ). It represents the flapping deflection of the i th mode at the blade tip. Therefore, one may write $(\Sigma q_i/L)$ in a Fourier series, so the flapping angle relative to the shaft can be written as:

$$f'_\beta(L) = \beta_o + (A_o + \beta_s \sin\psi + \beta_c \cos\psi) + \text{higher harmonics}) \qquad (3.1)$$

where

β_s is the 1st harmonic lateral flapping angle,

β_c is the 1st harmonic longitudinal flapping angle,

and

$$\beta^*_o = \beta_o + A_o \qquad (3.2)$$

is the equivalent coning angle.

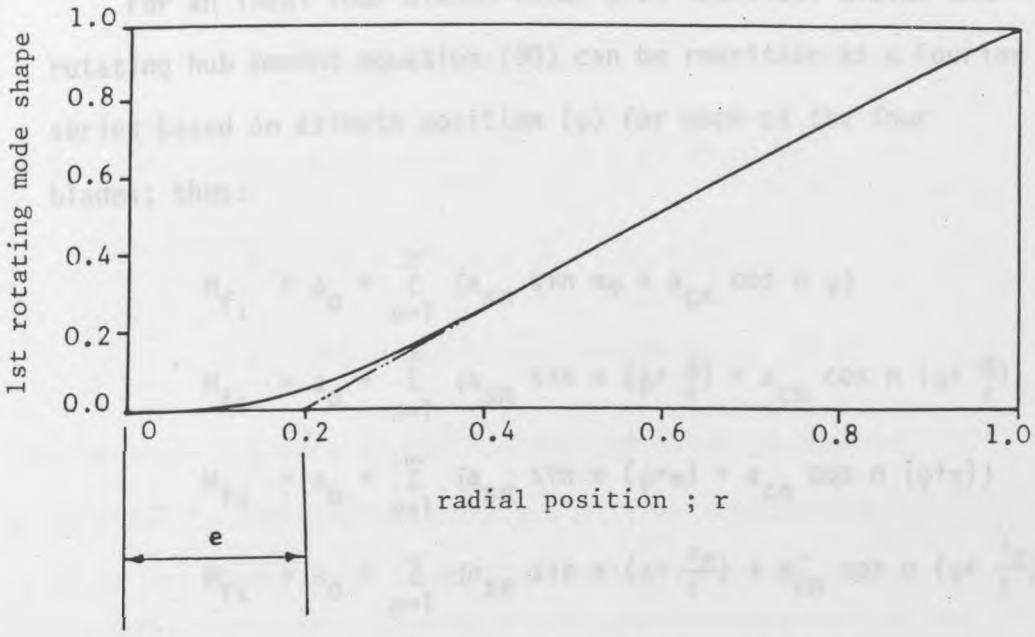

Figure 92 Equivalent Offset Flapping Hinge
Fundamental Mode Approximation.

APPENDIX 4

A.4. Harmonic Content of the Rolling and Pitching Moments

For an ideal four bladed rotor with identical blades the rotating hub moment equation (90) can be rewritten as a Fourier series based on azimuth position (ψ) for each of the four blades; thus:

$$M_{f_1} = a_o + \sum_{n=1}^{\infty} \{a_{sn} \sin n\psi + a_{cn} \cos n\psi\}$$

$$M_{f_2} = a_o + \sum_{n=1}^{\infty} \{a_{sn} \sin n(\psi + \tfrac{\pi}{2}) + a_{cn} \cos n(\psi + \tfrac{\pi}{2})\}$$

$$M_{f_3} = a_o + \sum_{n=1}^{\infty} \{a_{sn} \sin n(\psi + \pi) + a_{cn} \cos n(\psi + \pi)\}$$

$$M_{f_4} = a_o + \sum_{n=1}^{\infty} \{a_{sn} \sin n(\psi + \tfrac{3\pi}{2}) + a_{cn} \cos n(\psi + \tfrac{3\pi}{2})\}$$

Substituting the above equations into equations (92) and (93) in the text, the rolling moment M_{fx} and pitching moment M_{fy} can be obtained.

$$\begin{aligned} M_{fx} = \sum_{n=1}^{\infty} [& a_{sn} \cos\psi \{\sin n\psi \cos n\tfrac{\pi}{2} + \cos n\psi \sin n\tfrac{\pi}{2} \\ & - \sin n\psi \cos n\tfrac{3\pi}{2} - \cos n\psi \sin n\tfrac{3\pi}{2}\} \\ & + a_{cn} \cos\psi \{\cos n\psi \cos n\tfrac{\pi}{2} - \sin n\psi \sin n\tfrac{\pi}{2} \\ & - \cos n\psi \cos n\tfrac{3\pi}{2} + \sin n\psi \sin n\tfrac{3\pi}{2}\} \\ & + a_{sn} \sin\psi \sin n\psi \{1 - \cos n\pi\} \\ & + a_{cn} \sin\psi \cos n\psi \{1 - \cos n\pi\}] \end{aligned} \qquad (4.1)$$

and

$$M_{fy} = \sum_{n=1}^{\infty} [a_{sn} \sin\psi \{\cos n\tfrac{\pi}{2} \sin n\psi + \sin n\tfrac{\pi}{2} \cos n\psi - \cos n\tfrac{3\pi}{2} \sin n\psi - \sin n\tfrac{3\pi}{2} \cos n\psi\}$$

$$+ a_{cn} \sin\psi \{\cos n\tfrac{\pi}{2} \cos n\psi - \sin n\tfrac{\pi}{2} \sin n\psi - \cos n\tfrac{3\pi}{2} \cos n\psi + \sin n\tfrac{3\pi}{2} \sin n\psi\}$$

$$- a_{sn} \cos\psi \sin n\psi \{1 - \cos n\pi\}$$

$$- a_{cn} \cos\psi \cos n\psi \{1 - \cos n\pi\}] \quad (4.2)$$

The harmonic contents of the rolling and pitching moments can be obtained by substituting n=1,2,..... into equation (4.1) and (4.2). The results are summarised in the following Table.

harmonic order	rolling moment M_{fx}	pitching moment M_{fy}
1	$2a_{s_1}$	$-2a_{c_1}$
2	0	0
3	$-2a_{s_3}\cos4\psi+2a_{c_3}\sin4\psi$	$-2a_{s_3}\sin4\psi-2a_{c_3}\cos4\psi$
4	0	0
5	$2a_{s_5}\cos4\psi -2a_{c_5}\sin4\psi$	$-2a_{s_5}\sin4\psi-2a_{c_5}\cos4\psi$
6	0	0
7	$-2a_{s_7}\cos8\psi+ 2a_{c_7}\sin8\psi$	$-2a_{s_7}\sin8\psi -2a_{c_7}\cos8\psi$
8	0	0
9	$2a_{s_9}\cos8\psi +2a_{c_9}\sin8\psi$	$-2a_{s_9}\sin8\psi -2a_{c_9}\cos8\psi$

APPENDIX 5

A.5. Cantilever Beam Vibration Bending Moment Calculation

A5.1. Modal Analysis

Let the cantilever beam under consideration be excited by an external harmonic force of constant amplitude at its tip. Then the differential equations of motion of the viscously damped system are:

$$[m]\ddot{\underset{\sim}{\delta}} + [C]\dot{\underset{\sim}{\delta}} + [K]\underset{\sim}{\delta} = \{F\} \qquad (5.1)$$

where

[m] and [K] are the overall assembly mass and stiffness matrices respectively (calculated using the finite element method described in Section (3)),

[C] is the damping coefficient matrix,

and $\{F\}$ is the exciting force vector.

The normal modes associated with an undamped free vibration system can be used as a transformation matrix to uncouple the above equation (the eigenproblem may be solved as mentioned in Section (3.4)).

The uncoupled equation, for the j th mode is:

$$[M]\ddot{\underset{\sim}{Y}} + 2\zeta_j w_{nj}[M]\dot{\underset{\sim}{Y}} + [K]\underset{\sim}{Y} = F^{(j)} \qquad (5.2)$$

in which

$$\underset{\sim}{\delta} = [\phi]\underset{\sim}{Y}$$

and

$$\left.\begin{aligned} [\phi]^T\,[m]\,[\phi] &= [\ulcorner M \urcorner] \\ [\phi]^T\,[k]\,[\phi] &= [\ulcorner K \urcorner] \end{aligned}\right\} \text{a diagonal matrix}$$

, $F^{(j)} = F_o{}^{(j)}\, e^{iw_f t}$ is the generating force vector, and ζ_j is the damping ratio corresponding to the j th mode shape (assumed to be constant for all modes and approximately equation to 1%).

The steady amplitude of the uncoupled vibratory system is given by:

$$Y_o{}^{(j)} = (F_o{}^{(j)}/K_{jj})/\{[1 - (w_f/w_{nj})^2]^2 + [2\zeta_j w_f/w_{nj}]^2\}^{\frac{1}{2}} \qquad (5.3)$$

which leads to the generalised amplitude vector:

$$\{Y_o\} = \{Y_o{}^{(1)}, Y_o{}^{(2)}, \ldots\ldots\}^T \qquad (5.4)$$

The nodal amplitude vector (translational and rotational) can be determined as:

$$\{\delta_o\} = [\phi]\{Y_o\} \qquad (5.5)$$

A5.2. Vibration Response of the Cantilever Beam

The cantilever amplitude matrix $[\delta_o]$ can be set up for different exciting frequencies; say,

$$[\delta_o] = \{\delta_o{}^{(1)}, \delta_o{}^{(2)}, \ldots\ldots\}$$

where $\{\delta_o^{(j)}\}$ is the amplitude vector corresponding to the j th exciting frequency.

Using equation (5.5) and then rearranging $\{\delta_o^{(j)}\}$, in the same way as in Section (3.5), the corresponding elemental unknown constant vector (equation (22)) can be obtained, say $\{A_i^{*(j)}(x)\}$. Equation (1) of Section (3) is used to calculate the vibration response at distance x along the cantilever, i.e.:

$$\{Z_i^{(j)}(x)\} = \{1 \quad x \quad x^2 \quad x^3\} \{A_i^{*(j)}(x)\} \qquad (5.6)$$

which corresponds to the i th element and the j th exciting frequency.

The computer subroutine (GAUSEL) which was used to compute the mode shape function $\{f_{\beta i}^{(j)}(x)\}$ (equation (23)) is also used to compute the vibration response function $\{Z_i^{(j)}(x)\}$ of the above equation in which j relates to the j th natural mode and j th exciting frequency respectively.

A5.3. Vibration Bending Moment for the Cantilever Beam

The usual relationship between the bending moment and curvature is given by:

$$M_{bo} = EI(x) \frac{d^2Z(x)}{dx^2} \qquad (5.7)$$

and the shearing force is:

$$F_s = \frac{dM_{bo}}{dx} \qquad (5.8)$$

By twice differentiating the vibration response function, equation (5.6), to determine the curvature, the vibration bending moment M_{bo} and shearing force F_s can be calculated.

A5.4. Vibration Bending Moment Modes Contribution

The contribution from the i th mode to the vibration bending moment, at distance x on the cantilever considered, can be calculated by the previous section in conjunction with the estimated mode shape function $\{f_{\beta i}{}^{(j)}(x)\}$, equation (23). The steady state response may be described as a superposition of the normal modes. Thus, the bending moment can be written as:

$$M_b(x,t) = \sum_{j=1}^{m_o} [\lambda_{ij}]; \qquad i = 1,\ldots.N_E \tag{5.9}$$

where

$$[\lambda_{ij}] = [EI(x).\ \{f''_{\beta i}{}^{(j)}(x)\}.\{Y_o(t)\}] \tag{5.10}$$

is a matrix of order $(N_E * m_o)$ and can be written as:

$$[\lambda_{ij}] = \begin{array}{c} \begin{array}{cc} \text{1st mode} & \text{2nd mode} \ \cdots\cdots \rightarrow \end{array} \\ \left[\begin{array}{cc} \lambda_{11} & \lambda_{12} \ \cdots\cdots \rightarrow \\ \lambda_{21} & \lambda_{22} \ \cdots\cdots \rightarrow \\ \vdots & \vdots \\ \downarrow & \downarrow \end{array}\right] \end{array}$$

Substituting equation (5.4) into equation (5.10) the contribution of the j th mode to vibration bending moment of the cantilever root (i.e. x = 0) can be computed using the same procedure as given in Section (5).

APPENDIX 6

A.6.1. Dynamic Testing Equipment

The equipment used for the dynamic testing of the cantilever beam model, which is shown in the block diagram, Figure 25, consists of the following instruments:

- Automatic Vibration Exciter Control (Type 1025);
  frequency range 5 Hz to 10 kHz.
- Power Amplifier (Model PA300);
  frequency range 3 Hz to 10 kHz.
- Electrodynamic Vibrator (of 400 series vibrator)
  frequency range 1.5 Hz to 9 kHz.
  The maximum exciting force 98N (22 lbf).
- Force Transducer (9301A); sensitivity 3.66 PC/N
  Resonance frequency ≃ 90 kHz.
- Charge Amplifier (CA/04);
  frequency range 2 Hz to 12 kHz.
- DC - 5 kHz Carrier Frequency Bridge Amplifier (Model 3C66).
- Cathode Ray Oscilloscope (Model 3A74); DC - 2 MHz.
- Piezoelectric Accelerometer (233 E); sensitivity 59.3 PC/g.
- Gain Phase Meter (Model 3575 A).
- X-Y Plotter (Type 26000 A).

A6.2. Static Calibration of the Strain Gauge Load Cell

The cantilever beam, Figure 24, was loaded by a dead weight, in steps, and strain gauge outputs were recorded on the oscilloscope. The results are plotted in Figure 93 from which a good linearity with practically no hysteresis in the range of the test can be observed. The VBM (in N.mm) is given by multiplying the oscilloscope signal (sd) by the factor (9.8*580)/2.5/1.63.

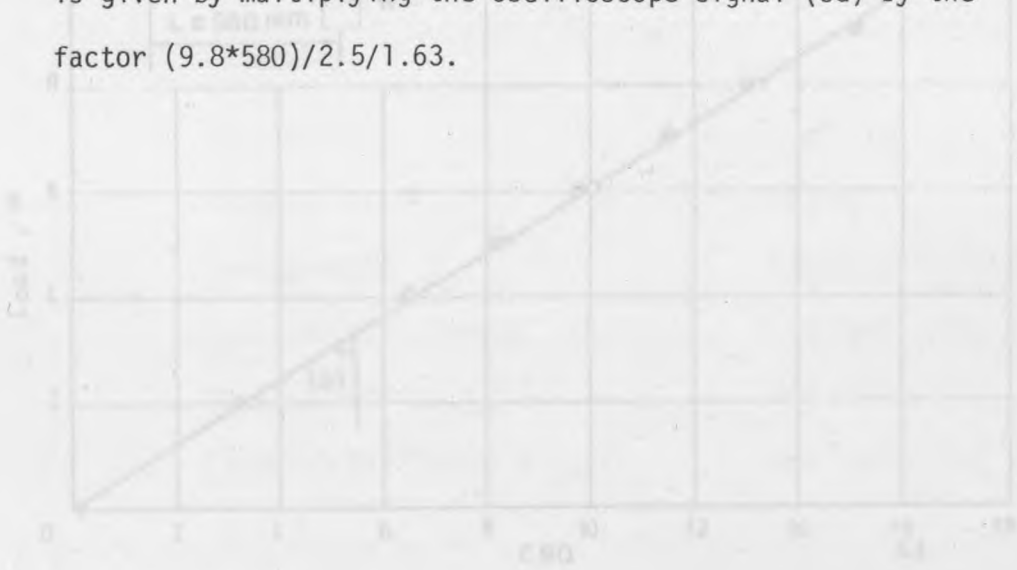

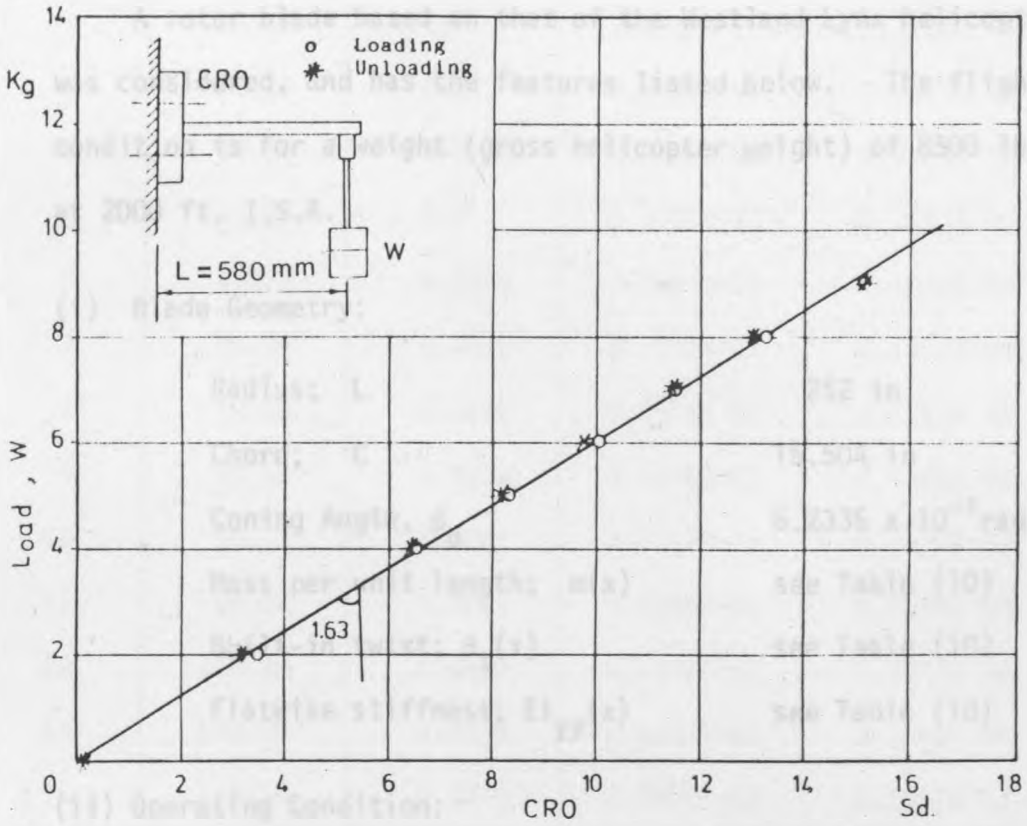

Figure 93 Static Calibration Curve for the Strain Gauge Load Cell.

APPENDIX 7

A.7.1. The Hingeless Rotor Blade

A rotor blade based on that of the Westland Lynx helicopter was considered, and has the features listed below. The flight condition is for a weight (gross helicopter weight) of 8500 lbs at 2000 ft. I.S.A.

(i) Blade Geometry:

Radius; L	252 in
Chord; C	15.504 in
Coning Angle, β_o	5.2336×10^{-2} rad.
Mass per unit length; m(x)	see Table (10)
Built-in twist; $\theta_t(x)$	see Table (10)
Flatwise stiffness; $EI_{yy}(x)$	see Table (10)

(ii) Operating Condition:

Rotor speed; Ω	330 r.p.m.
Helicopter flight speed; V_f	122 (or 160) knots

(iii) Aerodynamic Constants:

Air density; ρ	0.002241 slug/ft^3
Lift Slope; C_ℓ	5.7

Table 10 Blade Station Properties.

Station No.	Blade Radius (in)	Built-in Twist (rad)	Mass Per Unit Lenth (chug/in)	Flatwise Stiffness (Ibf-in^2)
1	0.0	0.0	0.5179E-02	0.1000E 13
2	10.05	0.0	0.3722E-02	0.2288E 08
3	20.10	0.0	0.1190E-01	0.2168E 09
4	30.15	0.0	0.8981E-02	0.2289E 09
5	31.55	0.0	0.5508E-02	0.2192E 09
6	40.22	0.3192	0.1960E-02	0.1870E 08
7	50.00	0.3192	0.1797E-02	0.1779E 08
8	60.08	0.3158	0.3549E-02	0.1613E 09
9	70.16	0.3102	0.2036E-02	0.4080E 08
10	80.23	0.3046	0.1112E-02	0.2470E 08
11	90.02	0.2992	0.1096E-02	0.2344E 08
12	110.20	0.2880	0.1204E-02	0.2085E 08
13	120.20	0.2825	0.1186E-02	0.1965E 08
14	130.30	0.2770	0.1065E-02	0.1853E 08
15	141.00	0.2715	0.1046E-02	0.1741E 08
16	151.70	0.2659	0.9389E-03	0.1632E 08
17	160.20	0.2603	0.9062E-03	0.1465E 08
18	170.00	0.2549	0.8746E-03	0.1377E 08
19	180.00	0.2493	0.8419E-03	0.1249E 08
20	190.20	0.2437	0.8093E-03	0.1176E 08
21	200.20	0.2381	0.7964E-03	0.1092E 08
22	210.00	0.2327	0.7856E-03	0.1032E 08
23	220.10	0.2271	0.7744E-03	0.9703E 07
24	230.20	0.2215	0.7633E-03	0.9087E 07
25	252.00	0.2094	0.5220E-07	0.8740E 07

A7.2. The Cantilever Beam

The cross-sectional properties and dimensions of the cantilever beam (steel) considered are as follows:

cross-section depth*width	0.88 * 2.36 in
cantilever length	23.6 in
material density	0.282 lb/cu.in
Young's Modulus	$0.3016*10^{11}$ lbf/in^2

APPENDIX 8

A8.1. Aerodynamic Damping Estimation

The estimation of the aerodynamic damping contribution to the flapping equation of motion is described in this section. This contribution is given in Ref. [74] as:

$$\{Q_a\} = \int \left(\frac{\partial \{R\}}{\partial q_i}\right).\left(\frac{\partial \{F\}}{\partial \dot{q}_j}\right) ds \qquad (8.1)$$

Inspection of the above equation shows that an aerodynamic damping coefficient is given by the integral of the elemental surface ds times the dot product of two vectors. One is a certain differential of {R} and the other is a particular differential of the pressure vector {F} with reference to fixed axes (the component of pressure vector {p} w.r.t. local blade axes are shown in Figure 14 in the text). The required transformation between {F} and {p} is made through the matrix [A] of equation (26) in Section 4. Therefore, equation (8.1) becomes:

$$\{Q_a\} = \int \left\{\frac{\partial \{p\}}{\partial q_j}\right\}^T \{D^{01}\} \, ds \qquad (8.2)$$

where the $\{D^{01}\}$ elements are given in equation (60).

Now, using equation (61) the vector $\frac{\partial \{p\}}{\partial q_j}$ can be written as:

$$\left\{\frac{\partial \{p\}}{\partial \dot{q}_j}\right\} = \begin{bmatrix} 0 \\ \left(\frac{\partial L}{\partial \dot{q}_j} \sin\alpha + L\cos\alpha \frac{\partial \alpha}{\partial \dot{q}_j}\right) \\ \left(\frac{\partial L}{\partial \dot{q}_j} \cos\alpha - L\sin\alpha \frac{\partial \alpha}{\partial \dot{q}_j}\right) \end{bmatrix}$$

In general, using (') to indicate the derivative $\frac{\partial}{\partial \dot{q}_j}$ (e.g. $\frac{\partial v}{\partial \dot{q}_j} = v'$, $\frac{\partial L}{\partial \dot{q}_j} = L'$.....), for small angle approximation (i.e. $\cos\alpha \cong 1$, $\sin\alpha \cong \alpha$) the above equation can be rewritten as:

$$\frac{\partial \{p\}}{\partial \dot{q}_j} = \begin{bmatrix} 0 \\ (\alpha L' + L\alpha') \\ (L' - L\alpha\alpha') \end{bmatrix} \qquad (8.3)$$

Referring to equation (64), v_y is normally -ve, so the incidence angle α can be written as:

$$\alpha \cong \frac{v_z}{v_y}$$

Thus,

$$\alpha' = \frac{1}{v_y}(v_z' - \alpha v_y') \qquad (8.4)$$

$$v' = \frac{1}{v}(v_y v_y' + v_z v_z') \qquad (8.5)$$

From equation (63):

$$L' = \tfrac{1}{2}\rho C\, C_\ell\, v\,(2\alpha v' + v\alpha') \qquad (8.6)$$

therefore:

$$\alpha L' + L\alpha' = \tfrac{1}{2}\rho\, C\, C_{\ell}\, v\, (2\alpha^2 v' + 2v\alpha\alpha')$$

Substituting equations (8.4) and (8.5) into the above equation yields:

$$\alpha L' + L\alpha' = \tfrac{1}{2}\rho\, C\, C_{\ell} v\, [2\alpha^2 - \frac{v_y v'_y}{v} + 2\alpha^2 \frac{v_z v'_z}{v}$$

$$+ 2\alpha \frac{v v'_z}{v_y} - 2\alpha^2 \frac{v v'_y}{v_y}]$$

Assuming $v \cong -v_y$ (since $\alpha \cong \frac{v_z}{v_y}$) and neglecting the higher order in α, the above equation becomes:

$$\alpha L' + L\alpha' = \tfrac{1}{2}\rho\, C\, C_{\ell}\, v\, \{-2\alpha v'_z\} \qquad (8.7)$$

Similarly:

$$L' - L\alpha\alpha' = \tfrac{1}{2}\rho\, C\, C_{\ell}\, v\, \{-2v'_z\} \qquad (8.8)$$

Substituting equations (8.7) and (8.8) into equation (8.3) gives:

$$\frac{\partial \{p\}}{\partial \dot{q}_j} = \tfrac{1}{2}\rho\, C\, C_{\ell}\, v \begin{bmatrix} 0 \\ -2\alpha v'_z \\ -2\, v'_z \end{bmatrix} \qquad (8.9)$$

From equation (68)

$$v'_z = \frac{\partial v_z}{\partial \dot{q}_j} = -\cos\theta(x)\, \cos\beta(x)\, f_{\beta j}(x)$$

$$\cong -f_{\beta j}(x)$$

Then, equation (8.9) can be rewritten as:

$$\frac{\partial\{p\}}{\partial \dot{q}_j} = \tfrac{1}{2}\rho\ C\ C_\ell\ v \begin{bmatrix} 0 \\ -2\alpha f_{\beta j}(x) \\ -2f_{\beta j}(x) \end{bmatrix} \qquad (8.10)$$

Substituting the above equation and equation (60) (Section 4) into equation (8.2) and carrying out the indicated matrix multiplication the estimated aerodynamic damping (for small $\beta(x)$ and $\theta(x)$) of the j <u>th</u> mode can be written as:

$$\{Q_a{}^{(j)}\} \cong \int_0^L \rho C\ C_\ell\ v\ \{f_{\beta j}(x)\}^2\ dx\} \qquad (8.11)$$

A8.2. <u>Damping Estimation in Second Flap Mode of the Blade</u>

The damping in second flap mode, for both initial and modified blade (mass distributions), will be calculated below. In these calculations, only the non-periodic part of the aerodynamic damping $\{Q_a{}^{(j)}\}$ (non-periodic part of the relative velocity v_y of equation (68)) is considered for the sake of simplicity and obtaining an approximate result.

Thus, equation (8.11) becomes:

$$\{Q_a{}^{(j)}\} = \rho\ C\ C_\ell \Omega \int_0^L x\ \{f_{\beta j}(x)\}^2 dx \qquad (8.12)$$

Recalling the results of the blade mode shape $f_{\beta 2}(x)$ and corresponding undamped natural frequency w_{n_2} in the text as well as the aerodynamic constants (ρ, C_ℓ) and blade chord (C)

given in Appendix (7) we obtain:

(i) For Initial Blade

damping coefficient; $Q_a^{(2)} = 2.071$ lbf/in/sec

damping ratio; $\zeta_2 = \dfrac{Q_a^{(2)}}{2w_{n2}M_2} = 43.22\%$

(ii) For Modified Blade (of λ_{m3})

damping coefficient; $Q_a^{(2)} = 3.24$ lbf/in/sec

damping ratio; $\zeta_2 = \dfrac{Q_a^{(2)}}{2w_{n2}M_2} = 21.61\%$

Computer program
(Appendix 9, pp. 301-331)
has been removed for
copyright reasons